Ollscoil na hÉireann, Corcaigh
National University of Ireland, Cork

ucc
Coláiste na hOllscoile Corcaigh, Éire
University College Cork, Ireland

Micro cameras as adjunct tools in biomedical applications

Thesis presented by
Lorenzo Niemitz

ORCID: 0000-0002-5261-7040

for the degree of
Doctor of Philosophy

University College Cork
Tyndall National Institute

Head of Department: Fatima Gunning
Supervisor: Stefan Andersson-Engels
Co-supervisor: Ray Burke
Co-supervisor: Simon Sørensen

2024

Micro cameras as adjunct tools in biomedical applications

© 2024 Lorenzo Niemitz
All rights reserved

Biophotonics@Tyndall
Tyndall National Institute
University College Cork, UCC
Ireland

For my family.

Abstract

Biomedical imaging is one of the most impactful periprocedural tools and is used across a wide range medical applications. The eyes of the clinician are a key component in surgical decision making, and an image is often the first step in both diagnostic and interventional procedures. With the miniaturisation of CMOS image sensors, micro-cameras are being investigated for use in biomedical imaging and the development of biomedically specific sensors has begun.

This thesis makes several important contributions to the use of these micro-cameras as adjunct tools that meet a number of unmet clinical needs in a variety of interventional procedures. To achieve this integration capabilities are demonstrated and a micro-camera based technology platform is developed. The micro-camera is integrated at the tip of various devices, along with multi-spectral fibre illumination, automated readout, control, and image processing; into a compact format suitable for clinical use.

The technology is then applied to a number of applications, with the system tailored to the specific use cases. The verification of procedural success in a cardiovascular intervention is investigated. A micro-camera based 2.30 mm catheter device is developed and tested on an animal model. It is shown to be able to image in the challenging environment of the blood field. Here the procedure can be recorded and we are able to extract physiological information in a step toward verification of device placement as well as success of ablation procedures in the heart. The dimensions are pushed to 1.19 mm to navigate into the peripheral lung. This achieves imaging deeper than with a traditional bronchoscope, while maintaining the ability to provide multi-spectral illumination via fibre optics. This is demonstrated on *ex-vivo* tissue.

The micro-camera platform makes an impact on breast conserving surgery procedures, where for the first time the periprocedural imaging of micro-calcifications is investigated. This enables the intra-surgical detection of micro-calcifications up to 2.00 mm in the resection margin. To do this a multi-spectral diffuse optical imaging technique for surgical guidance is proposed, and used to detect micro-calcifications. A rigorous co-registration method is developed to validate the data, and image processing techniques proposed to aid the automated detection.

Finally, polarisation resolved imaging is investigated using the micro-camera. Here the platform offers a solution for flexible polarisation resolved imaging systems. An initial prototype of both a miniature and benchtop system is presented along with images on optical elements and bulk tissue samples. Line of sight to tissue imaging, and to investigate multi-spectral polarisation resolved imaging is discussed.

List of Publications

This thesis is based on the following papers, which will be referred to by their Roman numerals in the text.

I **Microcamera Visualisation System to Overcome Specular Reflections for Tissue Imaging**
Niemitz, Lorenzo and van der Stel, Stefan D and Sørensen, Simon and Messina, Walter and Venkata Sekar, Sanathana Konugolu and Sterenborg, Henricus JCM and Andersson-Engels, Stefan and Ruers, Theo JM and Burke, Ray.
Micromachines **14(5)**, 1062– (2023).

II **Real-time peri-operative microcalcification detection in superficial breast tissues**
van der Stel, Stefan D and Niemitz, Lorenzo, and Sørensen, Simon and Feenstra, Lianne and Sterenborg, Henricus JCM and Andersson-Engels, Stefan and Ruers, Theo JM and Burke, Ray.
Submitted to Translational Medicine Communications **-**, under review (submitted: Sep 2023).

III **Towards a flexible polarimetric camera-on-tip miniature endoscope for 3×3 Mueller matrix measurements of biological tissue**
Niemitz, Lorenzo and Sørensen, Simon and Wang, Yineng and Messina, Walter and Burke, Ray and Andersson-Engels, Stefan.
1262733– (2023) *European Conference on Biomedical Optics.*

IV **Camera-on-tip Angioscope for in-vivo Cardiovascular Diagnostics and Surgical Guidance**
Sørensen, Simon and Messina, Walter, and Niemitz, Lorenzo, and O'Dowling, Claire, and Buszman, Piotr and Andersson-Engels, Stefan, and Burke, Ray.
– (submitted: Mar 2024) *Submitted to Journal of Biomedical Optics.*

V **Design and assembly of miniature diagnostic catheter imaging systems based on an angioscope study**
Messina, Walter and Niemitz, Lorenzo and Sørensen, Simon and O'Dowling, Claire and Buszman, Piotr and Andersson-Engels, Stefan and Burke, Ray.
– (to be submitted: Mar 2024) *Target journal: IEEE Transactions on Biomedical Engineering.*

VI **Open-source compact and customisable multi-LED platform for biophotonics applications**
Yavari, Hasti and Niemitz, Lorenzo and Wang, Yineng, and Burke, Ray, and Andersson-Engels, Stefan, and Sørensen, Simon. (Manuscript in editing process. To be submitted: 2024) *Target journal: Biomedical Optics Express.*

VII **Multi-spectral in-vivo FPGA-based surgical imaging**
Alsharari, Majed and Niemitz, Lorenzo and Sørensen, Simon and Woods, Roger and Burke, Ray and Engels, Stefan Andersson and Reaño, Carlos and Mai, Son T.
International Symposium on Applied Reconfigurable Computing **LNCS 13569**, 103–117 (2022).

Abbreviations

ADC	Analog to Digital Converter
ASIC	Application Specific Integrated Circuit
CCD	Charge Coupled Device
CMOS	Complementary metal–oxide–semiconductor
CIS	CMOS Image Sensor
DAQ	Data acquisition system
DCIS	Ductal Carcinoma in Situ
DRS	Diffuse Reflectance Spectroscopy
GRIN	Graded index
HSV	Hue Saturation Value
ID	Inner Diameter
IR	Infrared
FPGA	Field Programmable Gate Array
FLIM	Fluorescence Lifetime Imaging
LED	Light Emitting Diode
LOG	Laplacian of Gaussians
LSCI	Light Speckle Contrast Imaging
NIR	Near Infrared
OD	Outer Diameter
OR	Operating Room
PSA	Polarisation State Analyser
PSG	Polarisation State Generator
RGB	Red Green Blue
SPAD	Single Photon Avalance Diode
SWIR	Short Wave Infrared

Contents

Abstract **v**

Acknowledgements **xv**

1 Introduction **1**
1.1 Optics Technology in Medicine . . . 1
1.2 The Role of the Micro-camera . . . 2
1.3 Structure of the Thesis . . . 4

2 Background and Theory **7**
2.1 Light Tissue Interactions . . . 7
2.1.1 Biomedical Optics . . . 7
2.1.2 Absorption and Scattering . . . 8
2.1.3 Diffuse Imaging and Reflection . . . 10
2.1.4 Polarisation . . . 11
2.2 Camera Technology . . . 13
2.2.1 Fundamentals . . . 13
2.2.2 Micro-Image Sensors . . . 13
2.3 Image Processing . . . 17
2.3.1 Feature Detection . . . 17
2.3.2 Image Transformations . . . 19
2.3.3 Contrast Enhancement and HDR . . . 20
2.3.4 Colour Analysis . . . 20
2.4 Summary . . . 21

3 Integration and Assembly **23**
3.1 Research Objective . . . 23
3.2 Clinical Requirements . . . 23
3.3 Chip-on-tip Systems . . . 25
3.4 Design Considerations . . . 26
3.4.1 Alignment . . . 26
3.4.2 Light delivery and numerical aperture . . . 26
3.4.3 Materials and tolerances . . . 27
3.5 Assembly . . . 30
3.6 Polariser Integration . . . 34
3.7 Small Diameter Systems . . . 36
3.8 Back-end illumination . . . 38
3.9 Image Acquisition . . . 40

4 Miniature *in-* and *ex vivo* Applications **43**
4.1 Research Objective . . . 43
4.2 *in vivo* Study for Intraluminal Cardiovascular Imaging . . . 44
4.2.1 Intravascular imaging . . . 44
4.2.2 System and Navigation . . . 45
4.2.3 Data Analysis . . . 48
4.3 Miniaturised Device for *ex vivo* Lung Imaging . . . 51
4.3.1 Endoscopy in the Lung . . . 51
4.3.2 Miniature Lung Endoscope . . . 51
4.4 Discussion and Conclusion . . . 53

5 Micro-cameras in Breast Conserving Surgery **57**
5.1 Research Objective . . . 57
5.2 Micro-calcifications and DCIS . . . 57
5.3 Handheld Tissue Visualisation System . . . 58
5.4 Specular Reflections . . . 59
5.4.1 Multi-flash . . . 59
5.4.2 Cross-polarisation . . . 61
5.5 Measurement Protocol . . . 63
5.6 Clinical Validation . . . 65

5.7 Feature Detection 67
5.8 Results 71
5.9 Outlook 73

6 Miniaturised Polarisation Imaging **75**
6.1 Research Objective 75
6.2 Introduction 75
6.3 Methods 77
6.4 Benchtop Imaging System 77
6.5 Miniaturisation 80
6.6 Results 81
6.7 Discussion and Future Work 83

7 Conclusion **85**

Comments on the Papers **89**

Reflection and Perspectives **93**

References **97**

Papers

I	**Microcamera Visualisation System to Overcome Specular Reflections for Tissue Imaging**	**115**
II	**Real-time peri-operative microcalcification detection in superficial breast tissues**	**135**
III	**Towards a flexible polarimetric camera-on-tip miniature endoscope for 3×3 Mueller matrix measurements of biological tissue**	**155**
IV	**Camera-on-tip Angioscope for in-vivo Cardiovascular Diagnostics and Surgical Guidance**	**161**
V	**Design and assembly of miniature diagnostic catheter imaging systems based on an angioscope study**	**187**
VI	**Open-source compact and customisable multi-LED platform for biophotonics applications**	**197**
VII	**Multi-spectral in-vivo FPGA-based surgical imaging**	**211**

Acknowledgements

It would clearly not have been possible to perform this work without help, and I would therefore like to thank a number of people. I also want to gratefully acknowledge the funding agency SFI once again for supporting me and my work through grants SFI/15/RP/2828, SFI-12/RC/2276_P2, and SFI-22/RP-2TF/10293.

First of all, I would like to thank my supervisors Stefan Andersson-Engels and Ray Burke and Simon Sørensen. I have great appreciation for the effort you put into teaching and mentoring, and into supporting me in my work and future career. Your open door policies, and motivational talks have time and time again reignited my passion for the work. I have found your help and advice invaluable, and I could not have done this without you. Walter Messina, thank you for teaching me so much and for being so approachable and helpful. I could not have been so successful at the integration without your help. Not only is your work of fantastic quality, you are also an absolute joy to work with. Thank you also to the entire Biophotonics group and anybody not mentioned by name who helped me along the way.

A huge thank you also to Noreen Nudds for helping with some very delicate assembly tasks and most importantly for being a fantastic desk neighbour who always provided me with sweets, food, and good humour. Thank you also to Paul Tassie without whose help I could not have achieved the polariser dicing required for this work. Thank you to Marc Rensing for advice on integration. Thank you to Andreas Amann, for taking time to meet me personally when I had mathematical questions. Even though the interaction was relatively brief and once off, it has stuck with me as a fantastic reflection of what working a multi-disciplinary institution should look like. In the same vein I must thank Guangbo Hao, for taking the time to meet me to consult about mechanical actuation in a catheter. These interactions, however brief, have left a lasting positive impression on me.

A big thank you to all clinical collaborators, large and small. Your help, assistance, and expertise has made much of this work possible and given it meaning. To the surgeons at the Netherlands Cancer Institute, a special thank you for allowing me into the OR to gain incredible experience and for being so patient with my inability to remember medical terminology. To Theo Ruers and Dick Sterenborg, a huge thank you for hosting me and for your advice and guidance to make the collaborative work the best it can be.

Thank you to my friends at Tyndall for making my time here so memorable and so enjoyable, despite the large amount of money spent on getting coffee.

A final special thank you also to Liz and to my family, my mother, my sister, and my grandparents. For sticking with me, supporting me, helping me, cooking for me, doing all those things a family does, and being a constant in my life. No words can express the appreciation I have for you.

Chapter 1

Introduction

Chapter 1 introduces the important role light plays in medicine, with a particular focus on micro-camera technology in the context of translational biomedical applications, and outlines the objectives of this thesis. An overview of the structure of the thesis is also presented.

1.1 Optics Technology in Medicine

Optical technologies have become widespread in the last century, and the medical field is no different[1]. The market valuation of optics in medicine exceeds $100 billion a year, and is more than twice as large as the radiological market share [1]. Biomedical optics forms the fundamental science behind the devices and technologies that form this market, with optical biophotonic technology having applications ranging from the nano to the macro scale [2]. These technologies span from ophthalmology [3, 4] to microscopy [5–7]; from the pulse oximeter [8] to more involved spectroscopic techniques [9–12]; and from wide field-of-view imaging to endoscopy applications [13–18]. Medical applications range from *in vivo* and intraoperative surgical tools, to wound monitoring [19, 20], to screening [21], through to *ex vivo* and *in vitro* diagnostics and pathology [22]. Especially interesting in the context of this thesis are endoluminal imaging, as well as cancer imaging [23] and diagnostic techniques [24]. The non-ionising nature of visible and infrared light promises a safer tool-set that can be implemented *in vivo* for diagnostics and image guidance. Novel imaging techniques have great potential to provide label-free image contrast [25] in surgery and assist with *in vivo* tumour margin assessment, with the potential to provide real-time wide field-of-view imaging [26].

Aside from the diagnostic potential of light, the optical toolkit also lends itself miniaturisation. Optical fibre offers light delivery in a small footprint [27] and the miniaturisation of sensors [28] and light sources allows for more compact devices. Camera sensor technology has consistently evolved [29], and imaging has become more ubiquitous. This miniaturisation potential of optics allows for integration of optical technologies into existing tools [30], as well as the development of novel platforms [31] that can have transformative impact on medical care [2], provided the challenges of clinical translation can be overcome [32]. The work in this thesis focuses on optical imaging of biological tissue using miniature camera sensors, and their integration into tools that are used in *ex* and *in vivo* studies of tissue.

[1] That successful surgical procedures have been completed for thousands of years prior to the availability of such technology is simply astounding.

1.2 The Role of the Micro-camera

The aim of this thesis is to investigate miniature image sensors or "micro-cameras" as shown in Figure 1.1 and their applications in a biomedical context. This includes developing an integration process to build miniature imaging systems that combine imaging and multi-spectral illumination that are suitable for clinical use, analysing the readout of the micro-cameras and extracting relevant physiological parameters in novel clinical use cases, and investigating the future potential of image sensors in novel sensing modalities.

This thesis presents micro-camera based imaging systems that act as adjunctive tools in medical procedures. Such tools compliment and supplement the current clinical standard of care, but do not aim to replace the work of the clinician. Instead, the adjunctive tool provides additional information, ideally intra-operatively, which can assist in decision making and ultimately improve patient outcome. The small footprint of the micro-camera enables integration with other technologies, as well as endoluminal examination in difficult to access parts of the body, where size matters. The term micro-camera, as it is used in this work, refers to a camera that near or smaller than 1000 μm in footprint, when packaged. This small footprint is not always necessary, in particular in traditional endoscopic applications. There are certainly occasions where using a micro-camera would be disadvantageous, such as when a high resolution wide field-of-view image of a large surface is required. However, increasingly more small footprint applications are emerging in biomedical imaging. So there are circumstances when a micro-camera is the only way to obtain an image in a small lumen of the body; or, when only the micro-camera meets the footprint requirements to integrate it with another technology and provide vision of a procedure[2]. The micro-camera can be thought of as an enabling technology, which allows for relatively straightforward and cheap integration with a variety of technologies, at small footprints. It allows for a full image processing toolkit to be implemented, in places where previously no image existed, and can be used alongside a variety of optical techniques.

[2] This could be a DRS probe, a fluorescence probe, a surgical tool, among others.

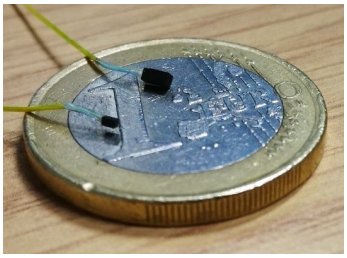

Figure 1.1. *Size comparison of micro-cameras with a 1 Euro coin.*

In a system, a sensor is usually mounted on the end of the device. This contrasts to techniques where the light is transferred through air or glass to a large sensor that sits proximally, away from the patient. The terms "chip-on-the-tip", "chip-on-tip", and "camera-on-tip" are often used interchangeably to describe systems where the image sensor is mounted distally. This technology has been enabled by developments in CMOS image sensor technology, of which the micro-cameras described in this work are a derivative. Some of the earliest descriptions of the chip-on-tip approach originated over two decades ago [33, 34]. The technology eliminates the image carrying optical fibres of traditional systems, and additionally allows for a disposable business model due to the low cost and mass producible nature of the sensors. Such a disposable business model has recently re-gained popularity, in part due to potential risks associated with reprocessing of bronchoscopes in treatment of acute respiratory illnesses [35], where use of disposable endoscopes has been recommended [36]. A shift towards the disposable camera on the tip endoscopes is seen, and expected to continue across endoluminal imaging devices. This shift towards the disposable may reverse again towards reusable devices in the near futur. Camera imaging remains applicable in that case. A micro-camera device itself is not limited to be used solely in a standalone endoscopic imaging system, but due to its small size, can also be integrated into other tools. One can therefore image a number of "chip-on-tip" tools that aside from performing a primary task, are also capable of providing an image at location.

Compact chip-on-tip endoscopes [37] have in recent years seen use in,

and been proposed for, ear nose and throat applications [38–40], gastroenterology [41], pulmonology [42], urology [43], cardiovascular applications [44–46], arthroscopy [47, 48], and other minimally invasive procedures [49]. Some of these have been integrated alongside other technologies such as haptics in [45], and biospy needles in [42].

Aside from chip-on-tip devices, miniaturisation of imaging technology is pervasive. The technology competes with the likes of fibre image guides [50], OCT [51], and scanning fibre endoscopes [14, 16, 17]. Many of the footprints of chip-on-tip endoscopes have, until now, not been truly competitive when compared to other technologies such as OCT or scanning fibre endoscopes. This thesis aims to investigate even smaller sensors of 1 mm and 650 μm, which can achieve dimensions of approximately 3 Fr[3]. Integration at such a scale for medical applications faces challenges around illumination using compact sources and delivery methods capable of multi-spectral illumination in a small footprint. With limited sensor area and pixel size, the best image quality must be achieved. Therefore, addressing the specific reflection challenges associated with tissue imaging is important. Optical components must be integrated into the small dimensions, and adequately aligned to achieve this. The sensitivity of the sensor, rapid real-time read-out and device control, and effective and efficient powering all play a role in usability of the device as a biomedical optic tool. Different challenges arise depending on application, from clearing the blood field, to extremely small dimensions, to complex co-registration challenges in medical data. These are addressed on a case by case basis. The core questions of the thesis are focused on where micro-cameras fit in to the clinical applications; and how to best integrate them, create imaging contrast, and analyse the data readout. Where can micro-cameras add value to existing procedures, and how can do they compare and compete with existing technologies?

[3] The French (Fr) is a unit that is commonly used to measure the size of a catheter. It measures the outer diameter (OD) of the catheter with one Fr being defined as a third of a millimeter.

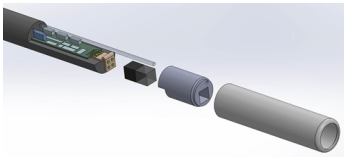

Figure 1.2. *Early design concept of a micro camera imaging system designed specifically for biomedical applications with optical communication and powering links and ASICs.*

In this thesis the integration challenges associated with such small devices when used in real-world scenarios are explored. Their potential as an adjunct tool in diffuse tissue imaging and breast conserving surgery is demonstrated in Paper **I** and Paper **II**, their potential to assist in flexible polarimetric measurements of tissue is discussed in Paper **III**, and their applications in endo lumial imaging of the cardiovascular space is shown in Paper **IV** and Paper **V**. Potential of the devices to be integrated into compact clinically ready systems is demonstrated, and supported by Paper **VI** and Paper **VII**.

The work in this thesis also informs part of a wider project, which funded the work undertaken in this PhD thesis, in which a custom camera sensor is being developed. The sensor is designed particularly with biomedical applications in mind, retaining the micro-camera footprint, maximising framerate for fast applications, and including optical communication and powering. It is intended to feature the world's smallest ADC for an image sensor. Optical communication and powering allows the sensor to be completely electrically isolated, and for an even more compact backend. It also allows for an increased datarate, with unbalanced datarate challenges being solved by the communications team involved. The design concept is shown in Figure 1.2. An ASIC board processes micro-camera data and feeds it to a reflective electro-absorption modulator which has been proposed for the communication scheme. Powering is handled using on-chip PV cells and dedicated powering circuitry that is being developed by collaborators. The work presented in this thesis helped to inform applications and requirements of this sensor. It informs the illumination considerations such as illumination profile and wavelengths, and investigates target applications such as in the cardiovascular space, and in breast conserving surgery. It also informs image processing considerations.

While a micro-camera is, at its most fundamental, a camera which

provides an image, the applications go beyond simple visualisation of tissue. By integrating the micro-camera into a system — that is, combining it with illumination sources, image processing algorithms, and different optical components such as polarisers — the role of the micro-camera is expanded. Using multi-spectral imaging, an image stack can be created which can be used to increase contrast of certain physiological features. Colour information can be used to extract physiological parameters such as heart rate and respiratory rate. The addition of polarising optics can enable polarimetry measurments and provides information about the structure of the visualised tissue. NIR illumination allows for diffuse imaging below the tissue surface. Image processing can help extract and enhance features of interest. In this way the micro-camera fits into the minimally invasive medical ecosystem, providing a valuable and additional resource in a variety of procedures. The small footprint of the micro-camera demonstrates the ability to achieve this even at the smallest scale.

1.3 Structure of the Thesis

The general aims of the thesis are outlined below.

(i) To investigate the potential of miniature image sensors as adjunctive tools in a variety of biomedical applications.

(ii) To develop and integrate systems using a miniature image sensor that are ready to use in a clinical environment.

This work was carried out as part of the Biophotonics@Tyndall group, based at Tyndall National Institute in Ireland, and kindly supported by Science Foundation Ireland (SFI) grants SFI/15/RP/2828, SFI-12/RC/2276_P2, and SFI-22/RP-2TF/10293.

The thesis is based on 7 Publications which will be referred to by their Roman numerals as Papers **I**–**VII**, respectively, in the text. There are 5 main chapters, the content of which is outlined below.

Chapter 2 examines the fundamental underlying principles of the work conducted as part of this thesis. Light as a physical phenomenon is introduced and relevant properties such as absorption, scattering, and polarisation, are discussed. Light tissue interactions, and thereby the core principles of biophotonics, are examined. Camera technology, pertaining to micro image sensors, is also reviewed, alongside common image analysis techniques which will feature in this work. Finally, the reader is introduced to fundamental medical concepts pertaining to the application spaces of the technology.

Chapter 3 explores the integration challenges of miniature image sensors into clinically relevant devices and systems. Clinical requirements are discussed which bound the design choices, and set out the need for a systems based approach to effective clinical translation. Some optical limitations and design considerations are discussed, before the assembly and integration process is demonstrated for a number of systems. This includes integration of polarisers, micro-camera, fibres for illumination, and the packaging of the whole system in a protective sleeve that allows application specific use. The smallest integration to date of a camera into a catheter system with illumination is shown, and images from the same from an *ex vivo* study are shown. The custom built light sources and control systems that enable real-time imaging are described.

Chapter 4 sees the micro-camera integrated into small diameter systems for *in vivo* applications. The focus is on a novel angioscope designed to detect hypoxia and assist with ablation and device placement *in vivo*. The system integrates a flush channel, camera sensor, and fibre illumination into a 2.1 mm OD catheter. Integration and imaging challenges are discussed, and results from an *in vivo* porcine animal trial where the device is guided into the beating heart are shown. The device is able to image the heart wall, and video analysis can extract physiological parameters such as heart-rate and respiratory rate of the animal. Further small diameter applications are also explored in this chapter such as potential use in peripheral lung applications, and in oral cavity examination.

Chapter 5 introduces two more manuscripts of the thesis, in work related to imaging of breast cancer tissue using a handheld tool. Direct specular reflections from glossy, wet, tissue surfaces can result in areas with saturated pixels diminishing the image quality of a system. Two methods for reducing the specular reflection in images are explored and their efficacy in the context of an adjunctive tissue imaging probe are discussed. The multi-flash method uses multiple illumination points and a software algorithm to remove specular reflections, while the static cross-polarised method uses the phenomenon of polarisation maintaining reflections to filter out any non-diffuse light. Images of tissue mimicking phantoms demonstrate the ability to image features at some depth, while a tissue image verified the efficacy of the specular reflection removal techniques on human tissue.

The cross polarised tissue visualisation tool is then used in an *ex vivo* human tissue study to image micro-calcifications in breast lumpectomies. This is the first time micro-calcifications are imaged without an x-ray. Locations are co-located with the x-ray ground truth, and image processing techniques are used to detect the micro-calcifications, and separate them from any remaining specular reflections. The handheld tool shows promise for real-time peri-operative imaging of micro-calcifications which may help localise further diagnostic techniques in minimally invasive breast conserving surgery for ductal carcinoma *in situ* (DCIS).

Chapter 6 introduces a miniature flexible polarimetry system at a 5 mm diameter, which uses a micro-camera and rotating linear polariser as polarisation state analyser, and optical fibres with distally mounted polarisers as the polarisation state generator. The system demonstrates the ability to integrate a polarimetry system into a small flexible footprint. The initial design is shown, as well as the first polarimetry image captured using a micro-camera. Problems with the current design and future work are also discussed.

To conclude, **Chapter 7** summarises the results contained in this thesis, and future work is discussed.

Finally, a reflective statement is offered at the end of this thesis.

Chapter 2

Background and Theory

This Chapter details the core technical concepts that form the foundation for the work in this thesis. Fundamentals of biomedical optics and light tissue interaction are reviewed in order to establish an understanding of what happens in the context of imaging of tissue. Reflections and polarisation are examined with this same lens. State-of-the-art micro-camera technology and image analysis is also introduced.

Light interacts with tissue, tissue interacts with light.

2.1 Light Tissue Interactions

2.1.1 Biomedical Optics

Two fundamental processes govern the interaction of tissue and light, absorption and scattering. These occur fundamentally on a microscopic or molecular, however are often described in terms of their bulk properties in tissue, and given as absorption coefficient [cm^{-1}], and scattering coefficient [cm^{-1}]. The coefficients are defined as the probability coefficients for absorption/scattering per unit path length of light in the tissue. Biological tissue is a complex structure consisting of many different structures built on various molecular compositions. They are mostly heterogeneously distributed, and each interact with light in different ways. The picture of tissue changes depending on the scale used to examine it, from molecular processes, to cellular structures, to more macroscopic features. The composition of tissue is inhomogeneous, and this results in variations in the optical density described by the local refractive index. These variations in the local refractive index are the origin of light scattering in tissue. All these components influence the way light travels through tissue which has been studied extensively [52]. Biomedical optics is the study of these light-tissue interactions, and their applications and translation [2].

These light tissue interactions, absorption and scattering, prove convenient for tissue recognition, analysis and treatment, since different types of tissue present with different properties, resulting in different light-tissue interaction effects. If an absorption, or an inelastic scattering event takes place, this can be described by an energy transfer. Such energy transfers result, for example, in the heating of tissue. This phenomenon is used in laser ablation procedures to heat and kill tissue in the irradiated area [53]. Light of certain frequencies can target light sensitive molecules called photosensitisers which can be used to treat diseases through the production of reactive oxygen species [54, 55]. High

frequency light, in the UV and beyond, can ionise atoms and cause significant damage to DNA and tissue [56, 57]. Tissue can have an effect on the polarisation state of light [58–60]. An absorption event can lead to re-emission of a fluorescence photon of a different frequency, changing the colour of light. These differences in light tissue interaction depending on tissue type also allow for differentiation between healthy, and malignant tissue, for example by determining the optical properties of tissue using techniques like diffuse reflectance spectroscopy [11, 61]. Absorption and re-emission may be a one photon, or a multiple photon process as is the case with upconversion. Upconverting nanoparticles for example may in the future have widespread uses in biomedical applications [62]. Some components of tissue may also exhibit fluorescence, emitting light for some duration (fluorescence lifetime) after excitation [63]. As light propagates through tissue and scatters, the angle of propagation of the light changes. Inelastic scattering can lead to Raman shifted light which has a multitude of applications in medicine [64].

However, the highly scattering nature of tissue, along with its heterogeneity, poses challenges. A signal that is sent into tissue, must return to the sensor in order to be detected. Different tissue components mean different local tissue optical properties, and as light propagates through tissue it randomly changes direction [65]. It is difficult to determine where a photon has been, and therefore, to know exactly where some change to detected light has occurred. When imaging tissue, resolving features at depth is difficult as the path of the light through tissue is uncertain and there is a depth weighting to the returning photons [2, 66]. Different wavelengths of light interact differently with tissue, forming the basis for biophotonic techniques and applications. Simply holding a white LED to your thumb and observing the diffuse red glow is evidence of these fundamental interactions between light and tissue.

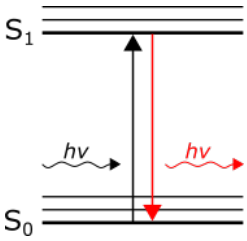

Figure 2.1. *Jablonski diagram showing a scattering event. A photon is absorbed (black) and the immediate re-emission of a photon is shown (red) between energy levels S_0 and S_1. Vibrational levels for both the S_0 and S_1 electronic levels of the molecule are indicated.*

2.1.2 Absorption and Scattering

A more in depth examination of absorption and scattering helps lay the foundations for understanding how light interacts with tissue. It also sets the scene for understanding diffuse imaging and reflection, discussed in the next section. Boudoux [67] provides us with a very targeted biomedical perspective on light tissue interactions, with other books [68–70] helping to provide a comprehensive picture of scattering in particular. Tissue consists of microscopic non-uniformities that result in refractive index changes. In order to form an understanding of the effect of light on tissue and vice-versa, the dual wave and photon model of light is adopted. In this view energy is quantised, however the probabilistic nature of events is not fully captured.

Tissue is made up of atoms and molecules, which can be excited by incident electromagnetic radiation. When an electromagnetic wave interacts with atoms and molecules in the tissue, electric dipole oscillations are induced as bound electrons are vibrating in the electromagnetic field. When the frequency of the light resonates with the transition energy of an atom or molecule in the tissue (a tissue absorber), a photon of light can be absorbed. The energy of the photon is then transferred to the atom or molecule. In tissue such an absorber is often decribed as a chromophore. This transition can be represented graphically using a Jablonski diagram (Fig. 2.1), where the incident photon results in an energy level transition from ground state S_0 to an excited state S_1. Similarly, relaxation into a lower energy state results in the emission of the photon. The frequency (ν) of this photon is given by the energy difference between the two states, $\Delta E = h\nu$, where h is Planck's constant[1]. Absorption is described in bulk

[1] Such excitation and relaxation of molecules and atoms is, however, not limited to the absorption of a photon. Mechanical, thermodynamic, electrical, and chemical effects can all result in energy level transitions.

tissue in terms of its macroscopic quantity the absorption coefficient:

$$\mu_a = \rho\sigma_a \tag{2.1}$$

This parameter is dependent on the absorption cross section σ_a and molecular density ρ in units of molecules per unit volume.

When the frequency of incident light is non-resonant with matter, scattering may occur. Despite the frequency not being resonant, an oscillation will still be induced in the electron clouds. With a microscopically varying refractive index in the tissue, these oscillations will vary spatially. These oscillating dipoles will in turn result in the emission of photons. However, there is no atomic or molecular energy transition. In the corresponding Jablonski diagram for scattering (Fig. 2.2), the virtual state (V) is introduced. This state is extremely short lived. The scattering event can be elastic, meaning there is no energy change, or in-elastic as is the case with Raman scattering for example. In this work, however, we almost exclusively deal with results of elastic scattering events in bulk tissue.

Mie theory describes scattering from spherical particles and is used extensively in the approximation of light transport through biological tissue. Rayleigh scattering is a subset of Mie scattering, where the particles are much smaller than the wavelength of light [65]. In the Rayleigh case, the scattering cross section is inversely proportional to the wavelength to the fourth power. This means that in the Rayleigh case blue light is scattered about 10 times more strongly than red light. As the particle size exceeds the wavelength, scattering becomes more wavelength independent[2].

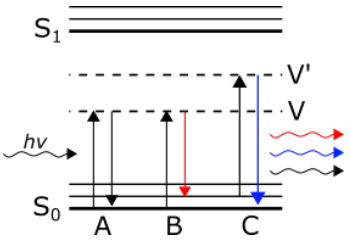

Figure 2.2. *Jablonski diagram of scattering events. A is an elastic scattering event. B and C are in-elastic scattering events.*

[2] Were this a textbook, this section is also where one would find the obligatory explanation as to why the sky is blue and the sunset red.

Treating each scatterer in the medium as a source of individual spherical wavelets allows for an intuitive understanding of scattering. As the wavelets interact they will interfere constructively and destructively, depending on the density of the scatterers.

In the bulk tissue scattering is described macroscopically, similar to the absorption coefficient in terms of scattering cross section, σ_s, and scatter density, ρ:

$$\mu_s = \rho\sigma_s \tag{2.2}$$

Scattering is anisotropic, its intensity varies with the angle of scattering. This is described by the anisotropy factor g.

$$g = \langle \cos\theta \rangle \tag{2.3}$$

In a dense homogenous medium scatterers are very close together, and so the constructive interference in the forward direction dominates, while destructive interference takes place predominantly in the other directions[3]. Hence, most of the scattering takes place in the forward direction. From the anisotropy factor, the reduced scattering coefficient can be calculated as:

$$\mu_s' = (1-g)\mu_s \tag{2.4}$$

[3] In the case of widely spaced scatterers the wavelets are more independent of each other in the non-forward directions and little interference is seen.

It can be interpreted as the average distance a photon travels before it can be considered as having been isotropically scattered. Examining μ_s' can be used to determine if a material's interaction with light is scattering-dominated ($\mu_a << \mu_s'$) or absorption dominated ($\mu_a \geq \mu_s'$).

Different tissue types will naturally have different absorption and scattering coefficients, as both absorption and scattering is frequency and material dependent. Chromophores require an allowed energy transition to absorb, and scattering is dictated by the refractive index and size of the scattering particle relative to the light wavelength. One can imagine the complex nature of tissue consisting of very many refractive index changes distributed throughout the medium in a non-homogeneous manner. NIR light proves useful when trying to image biological tissue at some depth

due its lower value of the scattering coefficient and therefore deeper penetration depth. Certain wavelength ranges also prove more preferential than others as they avoid the strong absorption of chromophores such as hemoglobin, fat, and melanin. This region is also referred to as the tissue optical window, with multiple windows throughout the VIS/NIR and SWIR having been identified since its conception [66, 71, 72].

2.1.3 Diffuse Imaging and Reflection

To form an image of biological tissue, we detect light that has interacted with tissue in some way. In this case, the light almost always originates from a source outside of the tissue, interacts with the tissue, and returns to our sensor. Since the end goal is to image *in vivo*, the source and detector are in reflectance mode - that is, they are both on the same side of the target to be imaged, and there is no imaging through the target (in transmission mode) taking place. Incident light may directly reflect from the surface of the tissue, which is referred to as a specular reflection. These specular reflections are mirror-like. A rough surface may result in many individual rays reaching the sensor in a multitude of directions. It may also take some path through the tissue, potentially interacting with components of that tissue along the way, and re-emerge on to the sensor. This is referred to as diffusely reflected light. Real-world materials usually exhibit reflection containing both specular and diffuse reflected components. This is especially apparent on biological tissue, which displays a complex heterogeneous morphology of different material composition. Tissue, additionally, is often wet, coated with mucus or saliva or water; adding an additional smooth surface with a high specular reflection component. In the case of imaging with a camera, in particular one limited in the number of its pixels, specular reflection is an undesirable artefact. It provides little information about the underlying tissue, and can result in erroneous feature identification both by human and machine observers [73]. When imaging tissue, in particular with features that may be embedded at some depth in the tissue, measuring only the diffuse component is advantageous.

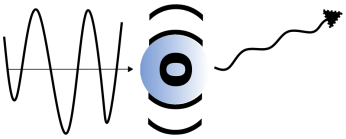

Figure 2.3. *Incident wave induces a dipole oscillation and a scattering event takes place.*

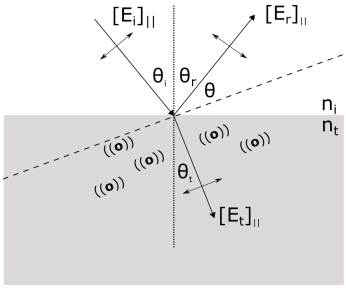

Figure 2.4. *Electron-oscillators and an example of Brewster's Law. The incident wave is parallel to the plane of incidence in this case. The reflected wave vanishes entirely when $\theta = 0$, i.e. the angle between reflected ray and dipole axis is zero.*

To examine reflection in more detail the electron-oscillator model proves to provide a convenient picture of the phenomenon of polarised light and reflections[4]. Recall that an electromagnetic wave oscillates perpendicular to the direction of propagation. This oscillation in the electric field interacts with charges around the atom or molecule, setting them in motion. Imagine an electromagnetic wave that is linearly polarised, incident on a medium. The electromagnetic wave will induce a dipole in the electron cloud of each scatterer (Fig. 2.3). The oscillating dipole has a directional radiation pattern, which results in a polarisation effect. In the direction of the oscillation no radiation is emitted, whereas a maximum is emitted orthogonal to the oscillation direction. The scattered light is linearly polarised in the direction of the dipole axis [70]. It follows that the induced electric dipole will oscillate along the direction of polarisation and the reflected ray maintains its polarisation. However, the direction of polarisation compared to the plane of incidence also plays an important role. When the incident light oscillates perpendicular to the plane of incidence, behaviour is as expected and described above. When the polarisation is in plane with the plane of incidence the dipoles will oscillate in plane with the oscillation of the refracted wave, which now differs from that of the incident oscillation due to geometry. There is now an angular difference between the dipole axis and the reflected wave. This angular difference results in a reduction of power of the reflected wave. Once a critical angle is reached the reflected wave disappears. This angle is referred to as the Brewster angle (Fig. 2.4).

[4] Hecht [68] notes that this picture is incomplete, failing to account for magnetic non-conducting materials [74]. These, however, are deemed irrelevant in this biomedical context.

The key takeaway, is that direct reflections will maintain their polarisation. Hence, polarising the incident beam linearly in one direction, and polarising the detector orthogonal to the incident beam can filter out direct reflections. Due to the loss of polarisation state with continual scattering events in tissue, diffusely reflected light can still be detected, and diffuse imaging can be achieved[5]. Of course, in practice, not all incident light will be perfectly polarised. In Paper **I** and Paper **II** it is demonstrated that this effect is sufficient to improve image quality in biomedical imaging captured using a micro-camera sensor.

[5] In the cross-polarisation work conducted in this thesis the orientation of the polarisers in relation to the surface of the tissue is irrelevant. Removing specular reflections through cross polarisation or due to Brewsters law converges to the same outcome.

2.1.4 Polarisation

Examining polarisation in more detail has advantages beyond its convenient properties related to reflection. In their book, editors Ramella-Roman and Novikova [75] provide a fantastic summary of polarised light and its applications in biomedical imaging.

To establish a theoretical understanding of polarisation, we treat light as a wave travelling in $\hat{z}$ through time, t.

$$\vec{E}(z,t) = \mathrm{Re}\left[\vec{\psi} e^{i(kz-wt)}\right] \tag{2.5}$$

Due to the superposition principle any light wave can be represented as a combination of waves oscillating in the $\hat{x}$ and $\hat{y}$ directions, such that $\vec{\psi} = \psi_1\hat{x} + \psi_2\hat{y}$. Beginning with the monochromatic case, assume a plane wave is propagating in $\hat{z}$ with:

$$\vec{E}_x = E_{0x}\cos(\omega t - kz) \tag{2.6}$$

$$\vec{E}_y = E_{0y}\cos(\omega t - kz) \tag{2.7}$$

Where $E_{0x} = \mathrm{Re}\left[\tilde{E}_x e^{i\delta_x}\right]$ and $E_{0y} = \mathrm{Re}\left[\tilde{E}_y e^{i\delta_y}\right]$, with $\tilde{E}_x$ and $\tilde{E}_y$, and δ_x and δ_y, being the amplitudes and phases of the oscillations along the $\hat{x}$ and $\hat{y}$ directions, respectively. While the so called Jones vectors only represent the $\vec{E}$ field of monochromatic plane waves which are fully polarised and coherent, the Stokes vector fully describes the polarisation state of all light regardless of degree of polarisation. In the monochromatic case the Stokes vector is given by:

$$\tilde{\mathbf{S}} = \begin{bmatrix} I \\ Q \\ U \\ V \end{bmatrix} = \begin{bmatrix} I_x + I_y \\ I_x - I_y \\ I_{45^\circ} - I_{-45^\circ} \\ I_{\mathrm{left}} - I_{\mathrm{right}} \end{bmatrix} = \begin{bmatrix} s_0 \\ s_1 \\ s_2 \\ s_3 \end{bmatrix} \longrightarrow \begin{cases} s_0 = & E_{0x}^2 + E_{0y}^2 \\ s_1 = & E_{0x}^2 - E_{0y}^2 \\ s_2 = & 2E_{0x}E_{0y}\cos(\delta) \\ s_3 = & 2E_{0x}E_{0y}\sin(\delta) \end{cases} \tag{2.8}$$

We can describe polarisation of light in terms of the polarisation ellipse (Fig. 2.5) with orientation angle Ψ and ellipticity angle χ where

$$\tan(2\Psi) = \frac{s_2}{s_1} \tag{2.9}$$

$$\tan(2\chi) = \frac{s_3}{s_0} \tag{2.10}$$

The degree of polarisation (DOP) describes how polarised light is and has values between $0 \leq \mathrm{DOP} \leq 1$. At a value of 1 the light is fully polarised, at a value of 0 is it completely unpolarised. Partially polarised states are assigned a value between 0 and 1.

$$\mathrm{DOP} = \frac{\sqrt{s_1^2 + s_2^2 + s_3^2}}{s_0} \tag{2.11}$$

The polarisation state of light can be represented graphically using the Poincaré Sphere (Fig. 2.6), where the last three stokes parameters

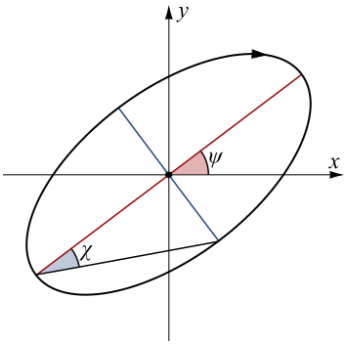

Figure 2.5. *The polarisation ellipse.*

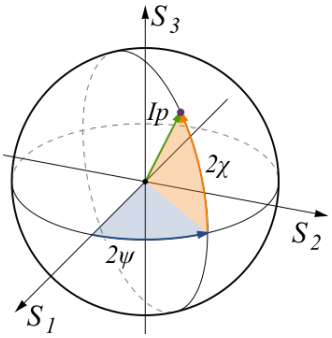

Figure 2.6. *The Poincaré Sphere can be used to represent the polarisation states of light.*

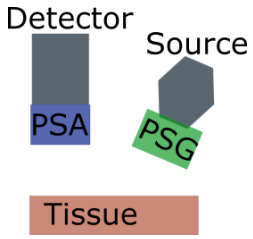

Figure 2.7. *Schematic diagram of a polarimetry system in reflectance mode, showing PSA, PSG, and sample.*

(s_1, s_2, s_3) form the bases of the space. Fully polarised light on the surface of the sphere, unpolarised light at the origin, and partial polarisation in between the two.

Various optics can be used to manipulate the polarisation state of light. The simplest of these is the polariser, which will linearly polarise light. The wave plate allows introduction of a phase shift effectively delaying one of the orthogonal components of the superposition of the wave. A quarter wave plate will introduce a quarter wave shift, and when passing a beam of light through both a linear polariser and a quarter wave plate, circular polarisation can be achieved. In this way the polarisation of light can be manipulated. In practice, a polarimetry system consists of a polarisation state generator (PSG) and a polarisation state analyser (PSA), and may be constructed in either transmission or reflectance mode (Fig. 2.7). The PSG polarises the incident light, while the PSG applies a polarising filter to detected light. In this way a set of incident and detected Stokes vectors are known, and the polarisation properties of the sample can be reconstructed.

These polarisation properties are captured using the Mueller matrix, **M**. It is a 4x4 matrix, however when excluding circularly polarised light it is sometimes reduced to a 3x3 sub-matrix [76]. This matrix is the polarisation transfer function of a medium and is useful in describing polarisation properties of tissue. Where the Stokes vector is a full description of the polarisation state of light, the Mueller matrix is a complete description of polarimetric properties of some sample. By measuring the intensities of light, the matrix can be reconstructed and polarisation properties of the sample determined.

$$\vec{S}_{\text{out}} = \mathbf{M}\vec{S}_{\text{in}} = \begin{bmatrix} m_{00} & m_{01} & m_{02} & m_{03} \\ m_{10} & m_{11} & m_{12} & m_{13} \\ m_{20} & m_{21} & m_{22} & m_{23} \\ m_{30} & m_{31} & m_{32} & m_{33} \end{bmatrix} \vec{S}_{\text{in}} \tag{2.12}$$

A Mueller matrix can be further decomposed into matrices of fundamental polarisation properties, retardance (R), diattenuation (D), and depolarisation (Δ) [76–78]. In other words the terms refer to: the change of phase during propagation, the attenuation depending on the polarisation state of incident light, and the loss of degree of polarisation during propagation, respectively.

$$\mathbf{M} = \mathbf{M_D}\mathbf{M_R}\mathbf{M_\Delta} \tag{2.13}$$

These properties can be used to separate the different effects of the medium on the polarisation state of light[6]. Similar to optical elements which change the polarisation state of light, tissue structures have an effect on polarisation. It is well known that in a dense turbid medium, light will lose its polarisation state [79]. Therefore, as light undergoes multiple scattering events in tissue, the polarisation of the light is eventually randomised [80, 81]. Tissue structures which affect scattering events, and which have a birefringent effect, for example, will result in different interactions with polarised light. In this way, polarised light provides another dimension along which to examine tissue, with potential to add structural tissue contrast to images. Current advances in polarisation in the context of biomedical imaging is explored further in Chapter 6. The micro-camera may prove a key enabling technology for clinical translation. A flexible polarimetry device using a micro-camera sensor on the tip is presented in Paper **III**.

[6] A diffuser, for example, is expected to be highly depolarising due to the presence of many scatters. An LCD screen uses retardance to adjust the polarisation state of light. A polariser is a perfect example of diattenuation.

2.2 Camera Technology

2.2.1 Fundamentals

The fundamental properties of light are translated into images via sensors and imaging optics. Two primary ways to do this for camera imaging is using a charged coupled device (CCD) or using compound metal oxide semiconductor (CMOS) to collect a photon and generate an electric charge. Modern third generation CMOS image sensors (CIS) combine the full package of analog pixel array and analog output amplifier with digital driving circuitry, ADCs, and signal processing into one chip.

The image sensor is made up of a number of pixels, of a certain pixel size, arranged in a matrix. The separation of each pixel, called the pixel pitch, dictates how many pixels are present in the area of the sensor. The pixel active area is the area of the pixel which is sensitive to light, i.e. which will induce an electrical response when struck with a photon. The ratio of light sensitive area to total area of the pixel is also known as the fill factor of the pixel. It depends on the active area in relation to readout electronics which take up space in the pixel[7]. The fill factor will also play a large role in light sensitivity of the pixel, as more photons will be able to strike the active area. Atop the pixel sits a micro-lens array to focus light onto the pixel. In order to introduce colour sensitivity, a colour filter may be integrated between the pixel and this microlens array. These filters are usually red, green, and blue (RGB) colour filters and are patterned in what is referred to as a Bayer pattern (Fig. 2.9) on the pixel array.

The charge induced due to the incoming photons in the integration period of the sensor, is stored and then read out using the imager readout electronics. Readout takes place either in a rolling shutter, where pixels are read out row by row; or a global shutter configuration. A global shutter can read out all pixels simultaneously and eliminates motion distortion caused by sequential row-by-row readout. However, global shutter requires readout electronics on each pixel, rather than at the end of the row - resulting in larger pixel pitches and reduced fill factor. As a result current micro-camera technology, where pixel pitch is very important for overall footprint, relies on the traditional rolling shutter readout configuration.

The single photon avalanche diode (SPAD) has also been successfully integrated into an imaging pixel array in the form of a SPAD camera, including a SPAD micro-image sensor with a footprint of 1.4 mm square. [82, 83] This type of sensor allows for time resolved measurements as each photon is time gated. The timing electronics, however, increase pixel size. Technology such as this may find its place in bio-medicine through miniature fluorescence lifetime imaging (FLIM) applications.

[7] In recent years 3D stacked technology allows for much of the readout electronics to be placed on layers below the top pixel layer, with back-side illumination creating even more space efficient pixels.

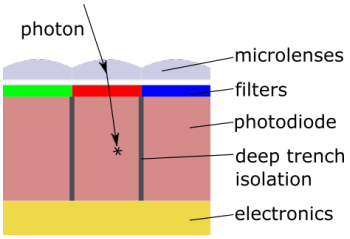

Figure 2.8. *A back-side illuminated pixel absorbs a photon which travels through its active area.*

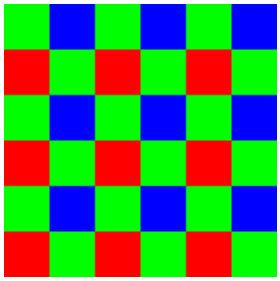

Figure 2.9. *Example of a Bayer pattern. Each 4x4 cell contains two green pixels, one blue pixel, and one red pixel.*

2.2.2 Micro-Image Sensors

In the last two decades much of the advancements in CIS stem from smartphone camera development[8]. The overarching focus of the market is to deliver high quality images, often of people, in a small footprint that fits onto the device in your pocket. Driven by the large technological advancements in CIS, a number of companies have adopted the pixel technology and developed miniature sensors targeting the medical technology market. The two primary manufacturers of CIS chips in this space are *Omnivision* (OV) and *ams OSRAM* (AMS), with their flagship packages for medical applications the OVMed, and the AMS NanEYE product ranges. These are available as either a bare sensor, or as a packaged solution complete with lens. Table 2.1 shows a selection of currently commercially available, packaged, micro image sensor options. There is

[8] Here, pixel count has been a marketable quality for the consumer, even though, as previously discussed, pixel count is not always indicative of a better sensor.

a very large range of camera sensors of all types on the market, but inclusion in Table 2.1 was limited to models most suitable to this thesis, due to both the footprint and the intended medical application space[9]. Unfortunately, the *Omnivision* models OCHTA10 and OCHFA10 were unobtainable from the manufacturer, and as a result have not been analysed in this thesis, however, are still deemed relevant for inclusion in this comparison. It should also be noted that the NanEye2D sensors are now obsolete and replaced entirely by the NanEyeC/M product line.

[9] Camera technology is evolving continually and rapidly, and it is expected that this list will be dated sooner rather than later.

Model	Manufacturer	Colour Modes	FOV	F#	Max Framerate	Pixel Size	Footprint	Resolution	NIR Sensitivity	Output
			deg		fps	μm	mm	pixels		
NanEye2D	ams OSRAM	Mono + RGB	90-160	2.7-4	68	3.000x3.000	1.00x1.00	249x250	Y	digital
NanEyeC/M	ams OSRAM	Mono + RGB	120	4	38	3.000x3.000	1.00x1.00	249x250	Y	digital
OV6948	Omnivision	RGB	120	2.8	30	1.750x1.750	0.65x0.65	208x208	Y	analog
OV6946	Omnivision	RGB	90-120	4/5	30	1.750x1.750	1.10x1.10	400x400	Y	analog
OCHTA10	Omnivision	RGB	120	2.8	30	1.008x1.008	0.65x0.65	400x400	Y	analog
OCHFA10	Omnivision	RGB	123	5	30@720x720 40@600x600 60@400x400	1.008x1.008	1.10x1.10	720x720	Y	analog

Table 2.1. *Comparison of relevant commercially available micro image sensors modules. Key parameters such as FOV and F# of the lens, footprint, available colour modes, maximum frame-rate, pixel resolution and technology, and output are compared. All cameras feature no IR cut-off filter.*

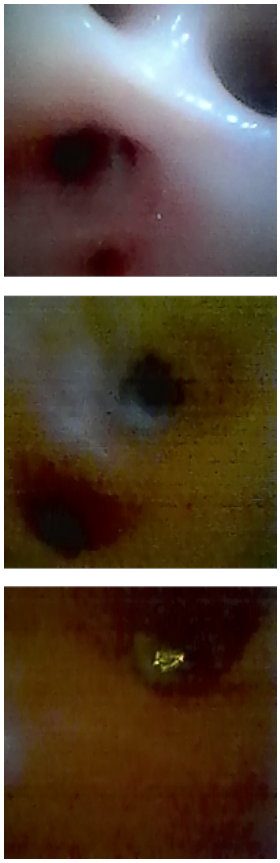

Figure 2.10. *Deterioration of image quality of OVM6948 camera sensor integrated into a 1.19 mm diameter catheter package with illumination, over the course of an ex vivo lung re-inflation experiment.*

The sensors differ in pixel size, resolution, frame-rate, footprint, and output signaling. The different parameters are important considerations when selecting sensors for biomedical application. Beyond the aforementioned parameters, robustness of the package, ease of integration, and ease of control are all parameters that must be considered. The NanEye sensors usually win out in this regard, in particular the 90°and 120° FOV models with low F# which tend to form the best images with good stability, packaging, and control.

All sensors feature no NIR cut-off filter, a desirable feature in biomedical application extending the wavelength range into the more deeply penetrating NIR. The NanEye models feature an optional monochrome version, where the colour filters are not present. In normal applications, on chip colour vision is the standard and desired. However, when maximising pixels and where raw data that is free from pre-processing is of interest, a monochrome sensor may be advantageous. Such a sensor offers more pixels across the VIS-NIR spectrum than the RGB version. No monochrome version of the *Omnivision* sensors are commercially available at the moment.

In order to form an image on the sensor, some lens is mounted in front which dictates the field of view and F# of the system. Table 2.1 shows different FOV and F# values that are commercially available. Of course custom designed lenses can give flexibility beyond the manufacturer provided specifications, however these were out of the scope for this work. GRIN lenses remain the current favourite for microendoscopic imaging systems, in large part due to their widespread availability and simplicity [84]. However, custom multi-element lens systems allow for more design flexibility, with 3D printed monolithic doublet and triplet lenses are emerging as effective alternatives to the traditionally used GRIN lens, especially at short working distances [85]. *ams OSRAM* and their NanEye product line, for example, have recently moved from a single element GRIN lens to a multi-element lens for better performances at close distances with reduced distortion.

The output signal is an important consideration for biomedical micro image sensors, as signal stability is a concern. Often a signal must be transmitted over some distance, as is the case in a catheter application.

The digital LVDS signal of the *ams OSRAM* sensors is a clear advantage over the analog *Omnivision* output, offering a much more robust communication protocol over distance. Robustness in packaging may also differ between products, and the physical connections play a large role in the stability of the devices. It has been noticed, for example, that the OVM6948 device deteriorates in image quality over the course of an *ex vivo* lung experiment, as shown in Figure 2.10. This deterioration is likely due to combination of analog signaling, and poor wire connections, which are strained over the course of the experiment. In particular the wires are easily separated from the very small bond pads.

Resolution and Contrast

The resolution of the imaging system is of interest as it will determine the minimum features that are detectable in the clinical applications. The imaging systems considered in this thesis are not diffraction limited. Rather the lens or the pixel size limit the resolution of the system. Naively, the resolution of the imaging system refers to the minimum dimension of a feature that is discernible given a sensor, illumination, and lens. More accurately, however, it is quantified using a spatial frequency quantity - line pairs per millimeter ($\frac{\text{lp}}{\text{mm}}$). A line pair is a pair of black and white lines of equal size, repeated at a given frequency. In practice, the resolution of the imaging system is not perfect, and there is some ambiguity in when two objects are effectively resolved. That is, there is some blurring at the edges which overlaps as two objects come closer together. This in turn results in varying intensity values detected on the sensor across the boundary. There is no step function transition from a black line to a white line in the captured image even if there is a step function transition in reality.[10]

[10] Light diffracts when passing through a finite circular aperture, resulting in a diffraction pattern called an airy disk. Two airy disks overlapping eventually reduce the contrast enough to make distinguishing a clear boundary impossible.

Resolution must therefore be defined at some image contrast in order to have meaning. This value is the contrast percentage, C%, defined as:

$$\text{C\%} = \frac{I_{\max} - I_{\min}}{I_{\max} + I_{\min}}\%,$$

where I is the pixel intensity. A contrast value of 20% is a commonly selected [86]. It was observed that the vertical contrast and horizontal contrast values often differed for the sensors. The contrast criterion was amended to only require one of these directions to have a contrast of 20%, rounded up. Since this grayscale contrast is a result of the imaging system as a whole, it depends on the sensor, the corresponding lens, and the illumination used. The modulation transfer function, or MTF, is a curve which relates contrast and frequency [87]. It is useful in describing characterising a lens system at a specific working distance and can be used to compared different systems. In this case however, we are simply most interested in the minimum resolvable object size of the camera systems used.

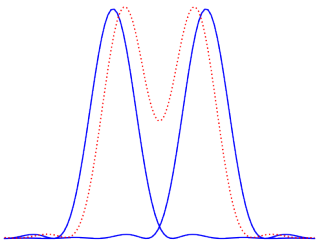

Figure 2.11. *When two imaged spots (blue lines) come closer together their corresponding diffraction patterns interfere constructively (dotted red line) and the central region is blurred.*

Compared are the off the shelf NanEye2D, NanEyeM, and OV6948 modules, with manufacturer lenses. To experimentally measure the resolution, a USAF1951 resolution test target standard is used. In this case illumination intensity and sensor integration time was adjusted to obtain optimal contrast. Distance to the target was adjusted to resolve the minimum feature size with good focus. This is at the minimum focal distance, which is approximately 4 mm for the NanEye2D sensor, and closer at 1.5 mm and 2 mm for the NanEyeM and OV6948 sensors respectively due to their differently designed lenses. The USAF1951 resolution target is imaged, and a line profile is taken across the line-pairs, from which a contrast ratio is calculated. Important to note is that these resolution values only inform us about these complete imaging systems. They do not inform us about the smallest theoretically possible object resolution,

and a different, custom lens solution could provide a much better spatial resolution for these microcamera sensors.[11]

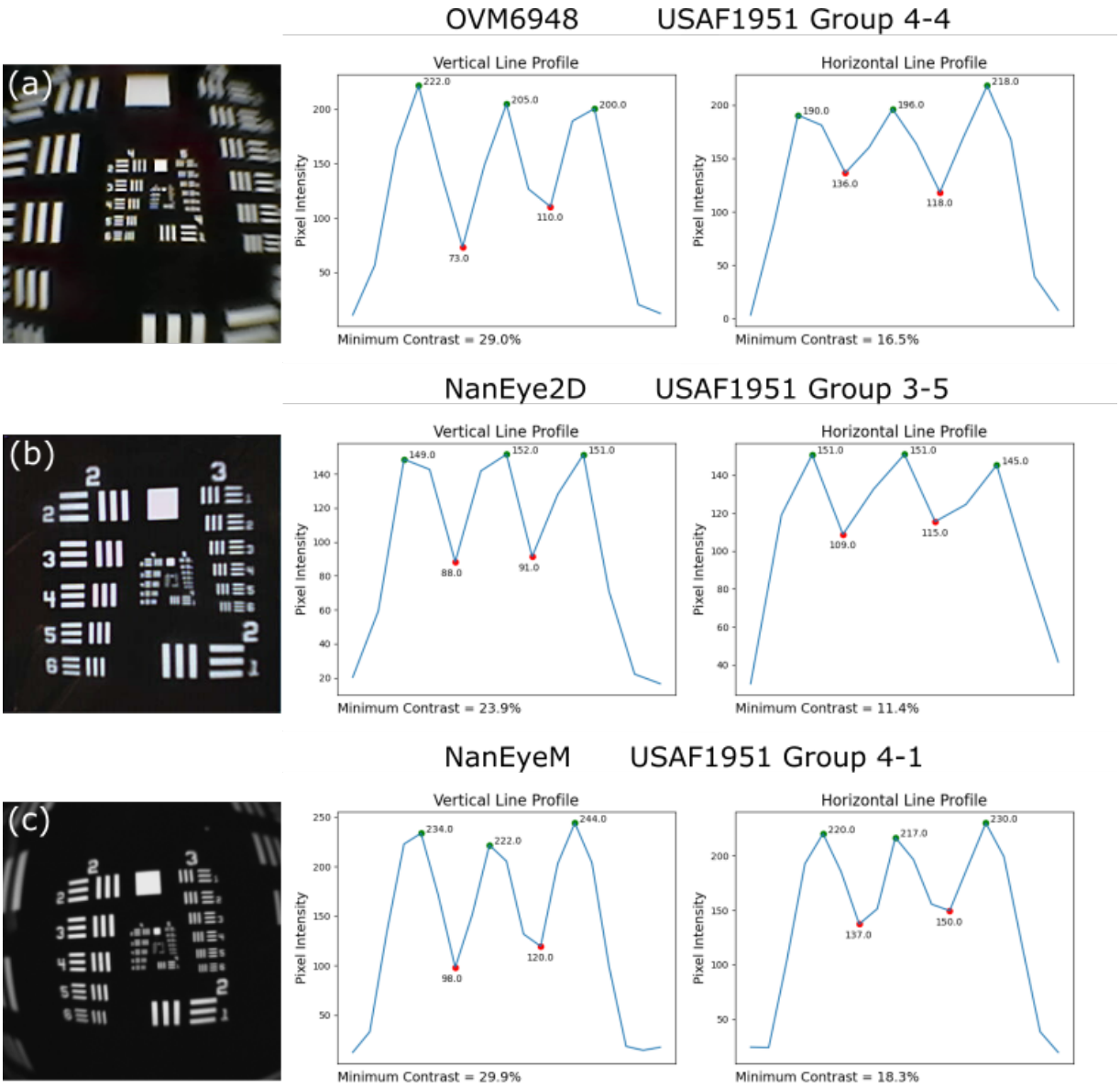

Figure 2.12. *Selection of vertical and horizontal line-profiles for different groups of the USAF1951 resolution target are shown, captured with different 120° FOV micro-camera packages. Local maxima and minima are indicated, and the minimum contrast percentages are shown below each plot.*

[11] Of course designing a custom lens comes with other considerations, such as size, application, packaging, etc. and is out of the scope of this thesis.

In Fig. 2.12 the images of the on the USAF1951 resolution target are shown along with the line profiles of relevant group on resolution target. In order to analyse the line pairs, a horizontal line is drawn across the line pairs and a profile is plotted. From this profile the contrast percentage can be established, and the resolution can be determined. In each case the vertical performance of the lenses is better than the horizontal performance, and that value is selected for evaluation of resolution.

The OVM6948 camera module is able to distinguish Group 4-4 of the target at a 20% contrast threshold. This equates to a measured resolution of 22.62 $\frac{\text{lp}}{\text{mm}}$, where each white line is separated by a black line width of 0.22 μm.

It is clear that both the OVM6948 and the NanEyeM sensors have better performance than the NanEye2D sensor.

Distortion

Due to the lenses on the imaging systems not being perfect, some distortion is introduced. This distortion stretches (pincushion distortion) or compresses (barrel distortion) the outer field imaged by the system.

Images (Fig. 2.13) of a ruled target with 2 mm squares are captured at a distance of 10 mm above the target using the micro-camera modules. Using a diagonal line drawn from the central point to the corner a predicted distance and observed distance are calculated, from which the distortion percentage is estimated (Tab. 2.2).

Model	Distortion %
NanEyeM	+2.5%
NanEye2D	−41.1%
OVM6948	−23.8%

Table 2.2. *Estimated distortion values of the 120°FOV camera lenses for three micro-camera packages, at approximately 10 mm working distance. Note the error in these measurements is expected to be very high, and values should be primarily used for qualitative comparison.*

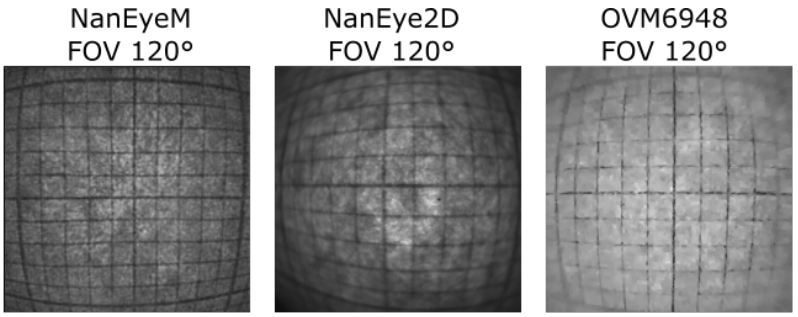

Figure 2.13. *Uncorrected grayscaled images of a ruled target imaged with three micro-cameras with the same diagonal FOV. Each small grid square is 2 mm square.*

Due to the small dimensions of the micro-cameras and short working distances, errors in positioning of the cameras have a much greater effect on measurements. Hence, quantifying the exact distortion of the lenses proved difficult and these results should be treated qualitatively rather than quantitatively. This highlights one of the primary difficulties when working with micro-cameras, their small size.

Since distortion, unlike aberration error which may result in blurring, only shifts the position of objects within the image, it can theoretically be corrected for in a post processing step[12]. For this the lens needs to be well characterised. In the projects related to this thesis, due to sub-optimal illumination conditions, often only the central region of the camera is used for imaging, and this distortion correction is not performed.

[12] Yet another thing our smartphones do all the time without telling us.

2.3 Image Processing

Capturing images allows for the application of a number of image processing techniques. These can improve the visuals of the image, extract or highlight features, or create overlays that display clinically relevant information[13]. A number of parameters can be used when examining these images algorithmically, from intensity changes within a single image, to different feature contrast in a multi-spectral image stack, and colour variations over time in a video. In this work, analysis of image and video data is performed using Matlab and Python, primarily using the Python scikit-image and opencv libraries.

[13] Worth noting is that, similar to the advancements the consumer smartphone market has made to the camera hardware, a large amount of image processing software development over the past two decades, much of it proprietary to each manufacturer, ensures that the images taken with your smartphone are of desirable quality.

2.3.1 Feature Detection

Fundamentally an individual image is a matrix of intensities, I. Another way to think about this is in the form of a surface, where the image has many troughs and peaks where the intensity varies. A feature is formed by a distinctive pattern of intensities. In our surface-like representation we can view it like a distinctive 3D dimensional shape - a blob is like a

[14] This representation of an image is akin to a map with mountains, valleys, and flat areas.

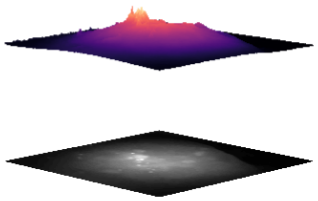

Figure 2.14. *2D gray-scale image mapped to a surface. The more intense areas are mapped to more red and yellow colours.*

Eigenvalues		Pattern
λ_1	λ_2	
N	N	noisy
L	H-	bright tubular structure
L	H+	dark tubular structure
H-	H-	bright blob structure
H+	H+	dark blob structure

Table 2.3. *Eigenvalues and corresponding 2-dimensional patterns found in images. Results depend on the value of the eigenvalue, with H=high, L=low, N=noisy, and the +/- sign indicating the sign of the eigenvalue. Eigenvalues are ordered such that $|\lambda_1| \leq |\lambda_2|$. Table reproduced from [89].*

mountain or a crater; a vessel is like a valley or a ridge[14]. These patterns of intensities can be detected mathematically, for example by taking first and second derivatives along the different axes of the image, and can be interpreted intuitively as examining the rates of change of intensities along the surface that is formed by the image. An edge, for example, will feature a change in intensity with can be detected using a filter such as the Canny edge detector [88].

This technique of examining changes in the image mathematically, has been applied to the automated detection of vessel-like structures in two and three-dimensional images. The method involves convolution of the image with the second derivative of a Gaussian. A Gaussian as shown in (2.14) has some scale, s, which determines the feature size that it is able to detect.

$$G = \frac{1}{2\pi s} e^{-\frac{x^2+y^2}{2s}} \tag{2.14}$$

With multi-scale filtering structures over a broad range of sizes can be detected [89]. Vessel-like structures present as either brighter or darker areas on an image. Let us assume that due to the presence of absorbing haemoglobin the vessel presents as a slightly darker area. This means the surrounding tissue registers brighter intensities than the centre of the vessel, with some intensity change in the transition. The vessel now looks like a valley, deep and flat along its length, with steep sides where it transitions to surrounding tissue. This gives a distinctive feature that can be detected mathematically. A Hessian matrix of a function, f, is constructed as follows in 2 dimensions:

$$\mathbb{H} = \begin{bmatrix} \frac{\partial^2 f}{\partial x^2} & \frac{\partial^2 f}{\partial x \partial y} \\ \frac{\partial^2 f}{\partial x \partial y} & \frac{\partial^2 f}{\partial y^2} \end{bmatrix} \tag{2.15}$$

This matrix represents derivatives of the image is every direction. By calculating the eigenvalues of this matrix patterns or features within the image can be detected, with the value and sign of the eigenvalues informing the type of pattern or feature (Tab. 2.3).

Automated vessel detection has been extensively explored in retinal images [90, 91] and in tubular structure detection in 3D imaging [92, 93]. The vessel detection algorithm used in Figure 2.15 has been adapted from [91]. Figure 2.15 shows the adaptation of the Hessian matrix based vessel detection algorithm to an *in vivo* micro-camera image. In a traditional RGB image the largest contrast between vessels and surrounding tissue exists in the green component. Therefore, the green image is extracted and used for further analysis. A Gaussian blur can help smooth

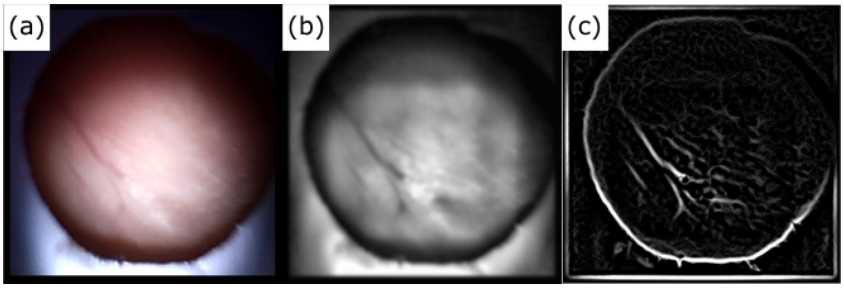

Figure 2.15. *Hessian matrix based vessel detection algorithm adapted to a micro-camera image inside of a canine heart during an animal trial, captured using the NanEye2D RGB 120° FOV sensor. Note that the image is captured in a liquid field, reducing the effective FOV from 120°. The original image is shown in (a); (b) shows the extract green colour channel after Gaussian filtering and CLAHE contrast enhancement; (c) shows the output of the vesselness algorithm, with vessel-like structures highlighted.*

edges before processing, and contrast enhancement can further improve the visibility of the vessel. The vessel detection algorithm successfully detects the primary blood vessel visible in the image, as well as picking out harder to see features surrounding this primary vessel. The catheter wall, due to its gradient, is erroneously detected. Additionally, this implementation of the algorithm also detects smaller vessel-like features in the image which are not visible to the human eye. However, the true nature of these could not be determined in this experiment due to lack of a ground truth in the *in vivo* experiment. The processing of these algorithms can be conducted efficiently on an FPGA platform, in real-time, as demonstrated in Paper **VII**.

Similarly to vessel detection, where we search for positive second derivatives in one direction, and a close to zero second derivatives in the other; blobs are another useful feature which might be desirable to detect automatically in biomedical images. Blobs present as positive or negative second derivatives in both directions. Micro-calcifications, as discussed in publication Paper **II**, present as blob-like features. These can be detected using similar mathematical techniques by taking the Laplacian of a Gaussian[15] and convolving with image, I.

[15] This is the trace of the Hessian. Defined as the sum of elements on the main diagonal of the matrix.

$$\nabla^2 G * I \tag{2.16}$$

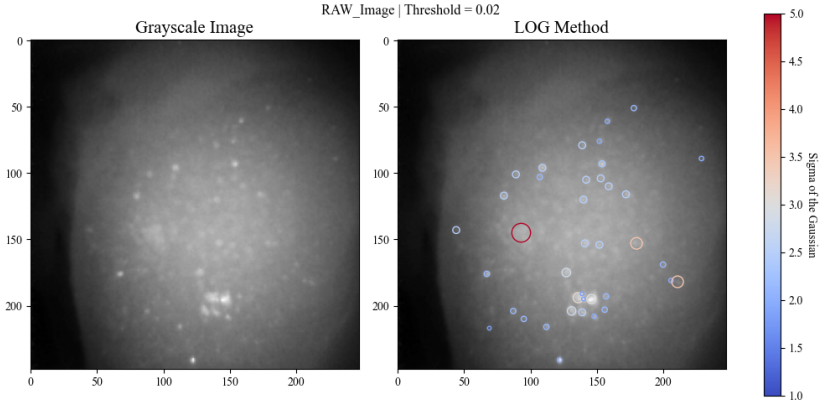

Figure 2.16. *Example of blob detection using the LOG method implemented using Python's scikit-image library. Different colour circles indicate blobs of different scale factors.*

An example is shown in Fig. 2.16 where specular reflection light features, and some larger blob features are detected on a tissue image. The sigma of the Gaussian determines the scale of feature detected. By employing a multi-scale approach features of different sizes are detected and identified.

2.3.2 Image Transformations

On occasion it is useful to perform perspective transformations on images. This is the case in Paper **II** where images must be co-located with an x-ray image in order to validate results.

Homography accounts for perspective. Affine transformation preserves parallelism. These transformations can be captured using a transformation matrix.

$$\mathcal{H} = \begin{bmatrix} h_{11} & h_{12} & h_{13} \\ h_{21} & h_{22} & h_{23} \\ h_{31} & h_{32} & h_{33} \end{bmatrix} \tag{2.17}$$

2.3.3 Contrast Enhancement and HDR

Pre-processing of images before displaying can improve perceived image quality especially when viewed by a human observer. Image contrast can be enhanced using algorithms such as Contrast Limited Adaptive Histogram Equalisation (CLAHE). This CLAHE method computes histogram equalisations locally instead of globally in small regions. Contrast limiting helps to reduce noise amplification by clipping histogram bins to some limit and redistributing the values across the histogram [94]. High dynamic range (HDR) imaging can also be employed in images where the difference between light areas and dark areas is large. This is often the case in micro-camera images due to the illumination pattern and distortion. Traditionally the exposure is varied such that the dark areas are exposed perfectly in one image, the bright areas exposed perfectly in another, and some images in the middle of the two exposures are captured. This results in an image stack of 3-5 images that are used in the HDR algorithm to reconstruct a HDR image. There are a number of different methods that are used to reconstruct a HDR image from its component images. The exact details of these are out of the scope of this thesis but the three methods explored in Chapter 5 are Debevec [95] reconstruction, Robertson [96] reconstruction, and the Mertens [97] method.

2.3.4 Colour Analysis

Colour in images, be that introduced through traditional Bayer filter, or through external illumination can be used to segment features in images based on spectral response. Colour is often represented in terms of a colour space, which defines the possible colours that a system can reproduce. Colour can also be represented by different models such as a combination of red, green, and blue (RGB), or a combination of hue, saturation, and value (HSV), for example. Colour information is another parameter under which we can examine images captured using the micro-camera. Features of interest can be extracted by filtering for a certain colour or colour range.

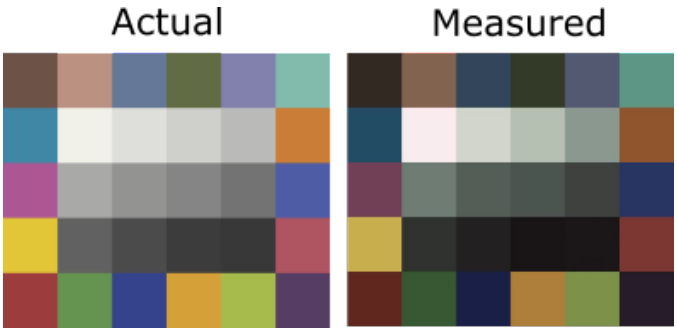

Figure 2.17. *Colour squares of a colour test target, with the actual RGB colour values of the target reconstructed digitally on the left (Actual), and the RGB colour values as captured by the NanEye camera sensor reconstructed digitally on the right (Measured).*

The International Commission on Illumination (CIE) provides some guidelines in determining colour accuracy. In this case, a ΔE 1976 value is calculated for each of the colour squares. Lower values imply a greater similarity between the colours. Figure 2.18 shows the ΔE value for each of the 30 colour squares on the target (Fig. 2.17). Numbering of squares is sequentially from the top left, to the bottom right, left to right, row by row. Typically values of ΔE below 50 can be considered more similar than not, and values in single digits steer towards only being perceptible

upon closer examination. However the exact nature of this relationship between perceptibility and ΔE depends on many factors, including use of standard illuminant, and of course the observer themselves. The colours reproduced are recognisable and distinct, yet muted. Under ideal lighting conditions this is expected to improve. Even in non-ideal conditions, which are more closely related to the final working conditions, the NanEye is able to reproduce colours in a recognisable manner.

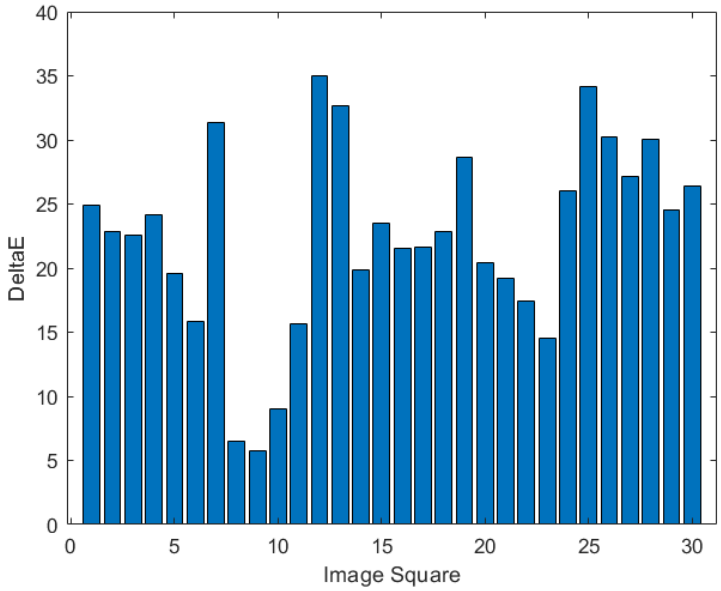

Figure 2.18. *ΔE calculated for each image square shown in Fig. 2.17. Squares numbered in ascending order from left to right, row by row.*

In the case of video data, an additional dimension of analysis presents itself, allowing the tracking of changes through time. Colour in an image may change as a result of oxygenation for example, or due to motion positioning the object closer to the sensor, resulting in higher pixel intensities. Photoplesthymography (PPG) is an optical technique that can detect physiological measurements such as heart and respiratory rate through variations in the image [98]. A Fourier Transform can be used to extract frequencies from the data returning the relevant parameters. This technique is used extensively in Paper **IV** where the video data from inside of a beating porcine heart is analysed.

The RGB colour space presents a high correlation between the image channels and while good for display is not optimal for colour image processing, whereas HSV, for example, separates colour information from intensity information [99]. HSV is often selected for its close similarity to human perception of colour.

2.4 Summary

The micro-camera offers a compact and cost effective imaging platform, that can be sensitive to different optical measurement modalities such as spectral and polarisation information. This, combined with the small size makes the sensors suitable for use in a range of biomedical applications, where the interaction of light and tissue results in some intensity profile across the imaging area of the camera. In this way an image of tissue and its features is formed. The image data can be manipulated in post processing steps to perform feature detection, identifying features such

as vessels or blobs. Images can be enhanced for contrast which may assist a human observer in analysing an image, and colour analysis can be performed. When video data is analysed, changes over time can also be tracked.

There are two primary manufacturers of the micro-cameras used in this work, *Omnivision* and *ams OSRAM*. These cameras are available with different lens solutions with different FOVs, and feature different pixel resolutions. Monochrome sensors are also available and may have benefits for such small sensors with limited pixel count and relatively poor light sensitivity. Lack of NIR cut off filters allows for NIR light to be used for illumination, which has a greater penetration depth in tissue. When integrating micro-cameras for medical applications, cost of the final devices will play an important role. The micro-cameras used in this work were purchased in small quantities, where the price per unit is approximately €100. A detailed cost analysis is out of scope for this work, however due to the scalability of CMOS technology, the price is expected to reduce significantly in a commercial mass production environment. Final costs depend on a variety of factors such as the other components needed for devices. The CMOS is unlikely to be the limiting factor when produced at scale. The author therefore expects prices to be commercially viable when integrating the sensors, along with illumination, into disposable devices for medical applications.

In summary, Chapter 2 has dealt with the fundamentals of biomedical optics and imaging and sensing in tissue. It has examined light tissue interactions, reflections, and polarisation. CMOS technology is discussed and the micro-cameras used in this work are introduced. Characterisation data is presented, and image manipulation and analysis techniques are reviewed. Assembly challenges and the integration of the sensors into systems is discussed in detail in the next chapter.

Chapter 3

Integration and Assembly

In this Chapter the clinical requirements of medical devices are discussed, and a detailed method for designing and assembling the systems used in this thesis is provided. Throughout the work conducted in this thesis the integration process underwent numerous design iterations and prototypes. Distilled here are the most successful of these and the learnings that developed due to this work. Assembly processes vary depending on the technology readiness level, scale, and budget. The processes discussed in this thesis relate to prototyping for lab based and small scale ex vivo experimental activity. A very low volume is required, and methods differ from large scale medical device ready assembly processes where sterilisation and ISO13485 requirements must be met. However, the fundamental consideration and designs are translatable to medical manufacturing. Some fundamental factors to consider such as numerical aperture of the imaging system, and flexibility are discussed. This chapter also introduces the reader to some of the imaging platforms used in this work, including physical systems, and control and image presentation.

3.1 Research Objective

The objective of the work is to demonstrate the research and development work undertaken to prototype integrated devices for the translation of the research. This includes integration capabilities and the development of a technology platform for the micro-camera which is the basis for the thesis. This platform integrates a micro-camera at the tip of various devices along with multi-spectral fibre illumination, automated readout, control, and image processing. Equally this technology can be applied to many other medical devices such as intra-surgical probes. This technology platform can then be adapted to a specific application.

3.2 Clinical Requirements

There are many challenges associated with effective translation of laboratory work to a clinical environment. Many are often unexpected and present themselves only when devices are used in close collaboration with patients, clinicians, and in an operating room. Unexpected problems arise, and iterative development is often a natural consequence [51]. These challenges can vary from the simple to the complex, and from the obvious to the obscure. From file format issues due to hospital workflow, which restrict the ability to obtain raw data; to clinicians' expectations differing from the researchers', along with language and terminology differences; to time restrictions imposed on work, in order to

uphold patient standard of care; or equipment simply being too large to fit into the small room that is used for a particular procedure; many different mechanisms affect how we must conduct our work. They often only come to light when a technology is being moved out of the laboratory and into a clinical setting.[1] As researchers, hoping to insert ourselves and our technology into the delicate ecosystem of a working hospital, it is important to be mindful of these differences and requirements. Fostering an effective relationship with clinical stakeholders allows for the development of technology which benefits all. So it becomes important to incorporate as many of the requirements, at as early a stage as possible, in the technology development process. Similarly, working in close collaboration with clinicians is essential when developing technology that is intended for clinical use. The sooner clinical partners are involved, the quicker feedback, and the more focused the outcome.

Work presented in this thesis has always been carried out in close collaboration with clinical partners. These were clinicians embedded in the research group, such as a cardiologist involved in the cardiovascular work; as well as external collaborators, such as the Surgical Oncology Group at the Netherlands Cancer Institute (NKI) in Amsterdam. Additionally, a 5 month pre-accelerator programme called Explorer was completed as part of the PhD work. This programme allowed for exploration of micro-camera technology through a commercial lens, and involved the interviewing of 14 clinicians across the island of Ireland, which shed a further light on requirements clinicians have for a medical product. Devices presented in this thesis are prototypes that explore the use cases of micro-camera technology in clinical settings; and in this way differ from a commercial product, the development of which comes with its own challenges [100]. However, engagement with various stakeholders at an early process can be beneficial to understand the relevance of the technology in a clinical setting [101].

From these conversations key parameters identified were patient outcome, ease of use, and real-time acquisition. The most important consideration is always patient care, and potential reduction of revisions was a key motivation for in Paper **II**. Familiarity[2] plays a large role in acceptance and adoption of new technology, as does simplicity of use [102]. The primary takeaway from the engagement with the independent clinicians about new imaging technology was that it should provide relevant data that is available on demand, when and where it is needed.

Time proves to be an essential consideration when designing prototype systems for clinical use. These may vary from time restrictions imposed by pathology departments who graciously allow time with patient tissue, to even more stringent time restrictions within the OR. A good example is the time restriction placed on *ex vivo* measurements conducted in Paper **II**, where the study protocol demanded that tissue samples were returned to pathology within approximately 40 minutes. This time frame includes travel time to and from pathology, time allotted for adjunct measurements such as radiology measurements, and time for the experiment. While we were lucky that the timeline was flexible, it was still important to develop systems and processes to support the requirement. Maintaining a good relationship with the stakeholders such as the pathologists proved an essential part of managing the *ex vivo* study, and quick return of the sample plays a key role. The complexity of the system is one of the factors influencing this time parameter, and a lot of work has gone in to producing systems which are convenient to use in terms of acquisition time, form factor, and by non-technical staff. One such example is the trolley system relevant to Paper **I** and **II** (Fig. 3.1) which is easy to manoeuvre, and contains everything necessary to run the experiment including data acquisition, illumination, powering, and sensor, in a compact form factor.

[1] While I was at the NKI, I came across an intriguing and somewhat unexpected requirement. The growing influence of computer processing in the medical field has brought about a need for effective cooling solutions for these devices when placed in the operating room. However, the use of conventional fans can disrupt the laminar airflow within the operating room, and can pose problems when a cart loaded with GPUs is brought in next to a patient for running cutting-edge machine learning algorithms, for instance.

Figure 3.1. *Example of imaging system mounted on a portable trolley as requested by clinical collaborators. The trolley includes powering, illumination, readout, and the measuring device and can easily be wheeled to location without being too obstructive. Data acquisition is also automated to save time.*

[2] Similarity to a certain product line already approved and used, does not only help convince regularity authorities but also clinical partners at an earlier stage of technology readiness.

An awareness of these requirements has informed all stages of the integration and assembly processes discussed in this chapter. The probes are designed to be simple to handle and use, and robust enough to withstand use in a hospital environment potentially by staff who are less familiar with the system and the technology. The systems are built to be disinfected, but at this stage not designed to withstand sterilisation procedures, since they are not used *in vivo*. Fibres and cabling is protected, light sources are built to be compact and portable, and the interfaces are designed with rapid data acquisition in mind. This approach ensures rapidity of measurements both for *ex vivo* tissue analysis and, of course, in an *in vivo* setting if the technology matures to this stage. Note also that backup systems should be readily available to allow for seamless replacement in case of damage to ensure clinical trials are not delayed and valuable specimens are not missed. Work in this thesis extends to TRL level 6 (i.e. prototype demonstration in specific environment) [103], and while adhering to strict medical device standards such as ISO13485 is not necessary, an awareness of their existence when considering next steps and *in vivo* trials is beneficial.

3.3 Chip-on-tip Systems

In order to build imaging systems with line of sight to *in vivo* use, the previously discussed micro-camera technologies must be integrated along with illumination and other optics into a platform that is suitable for the *ex vivo* studies. To do this a general methodology is followed, which is discussed in more detail in this Chapter and in Paper **V**.

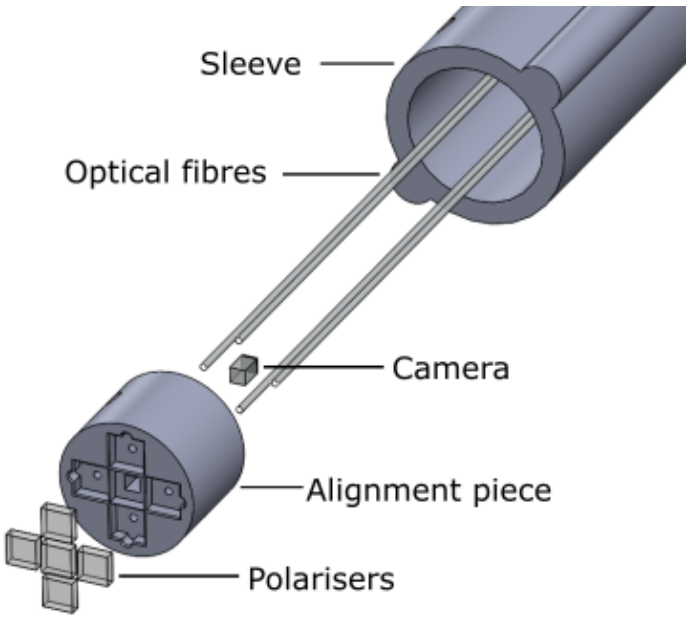

Figure 3.2. *Anatomy of a micro-camera on the tip system using a cross-polarised system as an example. Components, including optics (e.g. polarisers), image sensor, illumination/sensing fibres, are aligned and assembled using an alignment piece which can then be fitted into a sleeve.*

The design can be separated into two stages, the front end of the system consists of a small piece introduced here as the "distal alignment piece". This is where light delivery and sensing takes place. The remainder of the system serves to protect this front end, and to protect any cabling required for the system to work and deliver readout to the proximal end of the system and any readout electronics. A deconstructed

view of this is shown in Figure 3.2, where the optical components are assembled in the alignment piece, which can then be inserted into a sleeve. The sleeve can be rigid or flexible depending on application. All dimensions are also variable and application specific and detail are discussed in this Chapter.

3.4 Design Considerations

3.4.1 Alignment

[3] In this case "small" refers to sizes in the 100s of micrometers and generally smaller than 2 millimeters.

Working with small[3] parts necessitates additional considerations when it comes to the assembly and subsequent alignment. Due to the small form factor, custom solutions are often required. The components must be aligned in all directions. "Z-direction" alignment, that is along the direction of a catheter for example, was found to be among the most critical with misalignment causing intensity losses and light leakage, as well as potentially hazardous jagged edges or protruding fibres. Alignment along the X and Y directions is also important.

In order to align components at the distal end, the "distal alignment piece" is used. This piece serves a number of functions. First, it assists assembly of the components by allowing a step by step assembly process where parts can be inserted and secured in the piece before the piece is secured in its destination housing such as a catheter tube. Secondly, the piece assists in controlling distances between components. The piece should also provide optical isolation of components, and form a seal with the outer lumen once assembly is complete. The use of a distal alignment piece ensures consistency and reproducibility when multiple prototypes, or replacements, are required.

3.4.2 Light delivery and numerical aperture

The Numerical aperture (NA) of the imaging system will vary depending on the application space. The FOV of the camera is selected to suit the target application. Using the NanEye2D camera, the lower FOVs proved to have a sharper image with lower barrel distortion. Conveniently, these are also FOVs that were found to be suitable for imaging in small spaces, where a narrow area is examined by the clinician, and sharp images free from distortion are desirable. Therefore, the 90 degree FOV is selected for work where the interfacing medium between tissue and sensor is air. This is the case for the *Tissue Visualisation System* in Paper **I**, and the corresponding clinical work in Paper **II**. For work in a liquid field such as for work presented in supplementary Paper **IV**, there is a refractive index increase in the interfacing medium. This results in a narrowing of the FOV, and therefore a sensor with a higher FOV of 120° is selected. In water this FOV becomes approximately 90°.

When selecting illumination delivery methods for imaging probes, generating a suitable illumination profile is a priority. A suitable illumination profile aims to evenly illuminate the FOV of the camera sensor. The selected FOV of the sensor is therefore a key parameter to consider, as is the expected working distance of the final system. Illumination can be delivered using distally mounted LEDs or lasers or using optical fibres and a proximal source. Opting for fibre optic illumination allows for flexibility in what wavelengths to deliver, and alleviates heating and power concerns at the distal end by offloading the light generation to a dedicated proximal unit, discussed in Section 3.8.

Due to the relatively large FOVs of the image sensors when compared to available multimode fibre NAs, the default design choice is to maximise the NA of the illumination fibre. Figure 3.3 shows the effect of different commercially available fibre apertures, at a standard working

distance of 8.00 mm from the sample. A camera with an FOV of 90 degrees is selected, as this is the most common model used throughout this work. This is of course a rudimentary calculation that does not take into account the diameter of the fibre and treats it instead like a point source. However, it suffices to demonstrate the dramatic effect numerical aperture can have on illumination conditions.

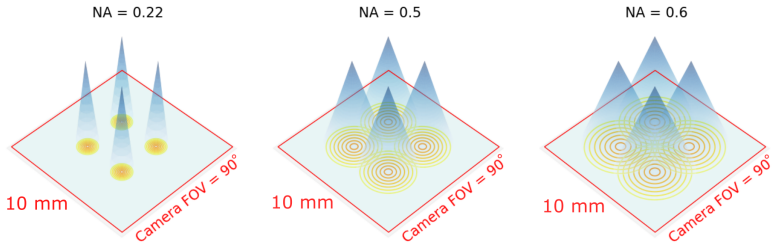

Figure 3.3. *Geometric simulation of fibres NAs and their effect on filling the field of view of a camera with 90° diagonal FOV.*

In Figure 3.3 the red box indicates the area imaged by the 90° FOV sensor at a working distance of 8.00 mm. This distance is selected as an optimal focus and good working distance when imaging tissue both *in vivo* and *ex vivo*. The fibre separation is selected to strike a balance between accommodating footprint requirements, and illuminating the FOV. In Figure 3.3 the blue light cones indicate light emitted from four fibres surrounding the central sensor, with the area illuminated at the working distance indicated in yellow. It is clear that FOV fill factor is drastically influenced by the NA. Problems arise at smaller footprint requirements, where high NA silica fibre is even less readily available. Note that when used in a liquid field the scattering due to the liquid particles appears to improve illumination profile. This is seen in Paper **IV** and Paper **V**.

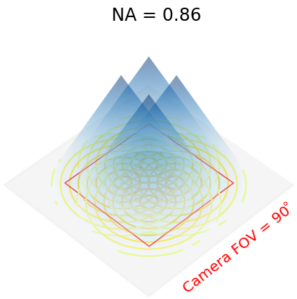

Figure 3.4. *Sample image showing the illumination using four fibre bundles with 0.86 NA for a 90° FOV camera at 8.00 mm. The red box shows the camera FOV with the area illuminated shown in yellow.*

The preferred illumination method, without adding additional lenses to the fibre tips, is with high NA fibre bundle illumination where a NA of 0.86 is commercially available (e.g. Schott fibre bundles). Figure 3.4 shows the drastic improvement a high NA fibre like this can make in illuminating the FOV, again at standard working distance of 8.0 mm from the sample. In many of the devices used in this thesis, however, due to supply issues a standard multi-mode fibre the largest readily available NA of 0.5 for glass fibre is selected. Silica fibre was selected at the beginning due to its availability and broad transmission range, with polymer fibre now the preferred illumination method especially in the visible spectrum. Polymer multi-mode fibre by default can achieve higher numerical apertures of 0.6, however runs into absorption problems in the NIR. It is however much more bend resistant, and achieves these higher NAs even at smaller OD than silica. With bundled fibres, the illumination and kink resistance could potentially be improved further.

3.4.3 Materials and tolerances

Much of the prototyping is conducted using 3D printing technology, which allows for rapid iterative prototyping and fast turn around time at a reasonable cost. CAD models are designed in house and 3D printing is often outsourced to third parties such as Protolabs. This achieves tight tolerances and allows access to unique materials. Material choice plays an important role in terms of stability of the components, and optical suitability. A number of different rapid prototyping processes were explored as part of this work, including 3D printing with micrometer resolution,

CNC milling of plastic parts, and direct metal laser sintering, with some examples shown in Figure 3.5. The final materials should have a good surface finish without burrs to allow for simple assembly. The dimensional tolerances should also be suitable for the small dimensional requirements of the prototypes. Parts need to be adjusted depending on the material and technology selected. The ABS material in Fig. 3.5 (a) has a larger minimum feature size compared to the Microfine™ material in Fig. 3.5 (c). When selecting a milling process such as in Fig. 3.5 (b), sharp corners are not possible and designs are adjusted to include machined rounded corners. The metal sintering process in Fig. 3.5 (d) proved inadequate for all dimensions due to instability and rough surface finish. Tolerances depend heavily on manufacturing technology, material, good design, and feature type. Parts are in general designed for tolerances as per the ISO2768-fine standard. That is, permissible linear deviations for ranges in nominal lengths 0.5 mm up to 3 mm are ± 50 μm. Better resolution is usually also achievable depending on the part. An investigation into smaller components such as those required for the 1.19 mm OD system described later in this chapter tightened the requirements to ± 5 μm due to footprint requirements which is achievable using speciality services (e.g. micro-milling provided by VU Brussels).

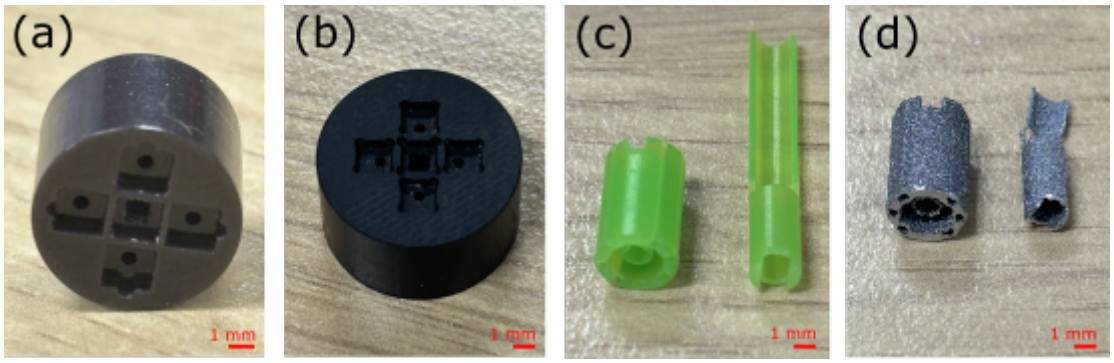

Figure 3.5. *Examples of distal alignment pieces manufactured using different materials and methods. (a) shows a black ABS 3D printed, (b) shows black ABS CNC milled. Both (a) and (b) are designed for a 10 mm diameter handheld distal alignment piece. Figure (c) shows Microfine Green™ material, and (d) shows direct metal laser sintering of AlSi10Mg, with both of these parts designed for a 5 mm diameter distal alignment piece. All pieces include through holes for camera sensor and fibres, and recesses for polarisers of 2 mm (a, b) and 0.5 mm (c, d).*

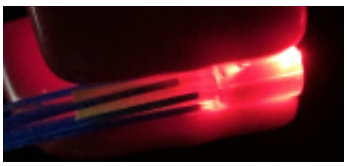

Figure 3.6. *700 nm light leaking through the Microfine Green™ material in the miniature polarimetry system.*

Components should be optically isolated by the distal alignment holders, and the camera sensor in particular must be suitably shielded across the VIS-NIR spectrum. Failure to adequately shield the sensor can result in light leakage and image artefacts. The camera assembly should isolate light leakage, however since optics are mounted in front of the sensor, light can still leak through the material and reflect back into the sensor. Protolabs Microfine Gray™ and Microfine Green™ materials are a good example of this. Both materials allow 3D printing of very small feature sizes. Microfine Gray™ is the preferred material due to its high opacity, and was used in the probes in Paper **I** and **II**. It achieved good optical isolation of the components, including through the thin separating walls in front of the polarising optics. Light artefacts were only a problem around the 940 nm spectral band (Fig. 3.27). Due to the material becoming unavailable, some later iterations of distal alignment holders had to employ the Microfine Green™ material instead. This material has significantly worse opacity than the gray material, and images presented significant light leaking artefacts (Fig. 3.6 and Fig. 3.7). Due to the gray material being unavailable and the under-performance of the green material, some parts were redesigned to be printed with a black ABS material. Due to its larger minimum feature size, this materials is not suitable for

the smallest dimensional requirements. The performance in the NIR is similar to the gray material, however Microfine Gray™ is still preferred.

Material choice proves an important consideration when 3D printing parts for optics. Materials are also important when choosing catheter lumen, as is the case in Paper **IV** and Paper **V**. This is discussed in more detail in Paper **V**. Materials for tubing should be selected depending on application, and often a trade-off between push-ability and flexibility must be made. More rigid materials tend to be more easily pushed, while more force must be applied to bend them. Material may also kink, or permanently deform in a location when bend too tightly. Fig. 3.8 shows an example of three different medical grade tubing materials and their ability to withstand tight bending. Two materials kink when bent tightly, with the third being more resistant to kinking requiring an even tighter bend radius before permanent deformation occurs. Kinking results in a permanent weakness in the deformed tubing, and as force is applied to the tubing, it tends to bend again in the kinked location resulting in a structural weakness. This in turn may make future use of the tubing, or navigation through pushing more difficult. The weakness is a problem in particular when the material struggles to recover to its original position, as it may get stuck.

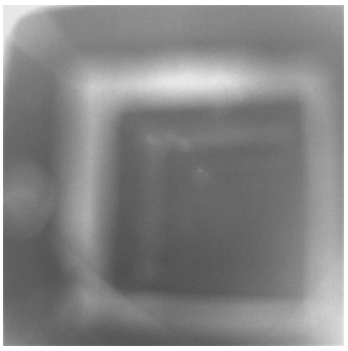

Figure 3.7. *Example of image artefacts due to light leaking through the material into the camera sensor.*

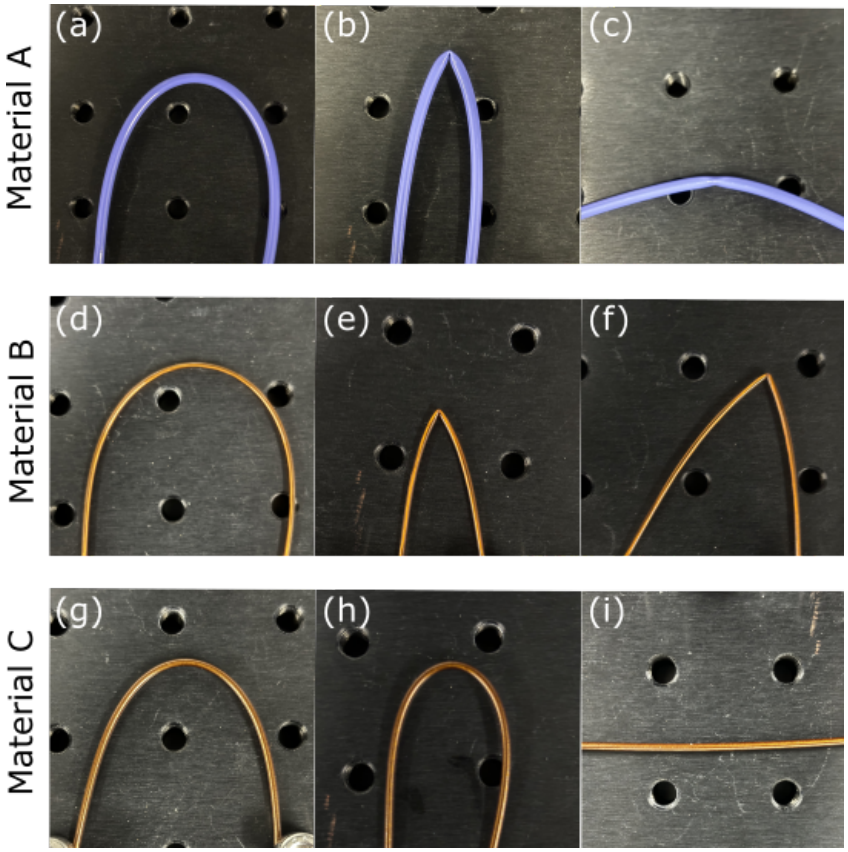

Figure 3.8. *Comparison of the bendability and kink resistance of three different tubing materials. Material A (a-c) is a Pebax® 72D material. Material B (d-f) is a simple polyimide tubing and Material C (g-i) a braid reinforced polyimide tubing. The materials demonstrate different levels of kink resistance. The materials are bent through varying radii and kinking is seen in (b) and (e). Material A and B show permanent damage at the sharp bend radii, in (c) and (f) respectively; with Material C recovering better (i) at this particular tight bend radius.*

Systems assembled as part of this thesis are not required to be de-

signed to withstand rigorous sterilisation processess (e.g. autoclave), due to either being laboratory prototypes, single use systems used in animal studies, or performing non-contact measurements of *ex vivo* specimens. The systems are designed to be disinfected, and they are built to be shielded from wear and tear, when used in a clinical environment. As a result fibres and wires are usually protected from any external elements using PVC tubing. This protects the components and makes cleaning them with wipes possible.

3.5 Assembly

Due to miniature footprint constraints, many of the distal end systems built as part of this thesis are of the millimetre scale, the smallest being 1.19 mm in outer lumen diameter. The individual components are of the order of 100s of μm, with a smallest feature size on many parts of the order of 10s of μm. The integration of components at this scale is challenging due to the size constraints. Prototype assembly is performed manually, almost always under a microscope. In general, components are fixed to each other using adhesives. These are selected for their bio-compatibility, material adhesion, and their curing properties. UV curing is often advantageous as components can be placed accurately before fixing, and the index matching properties of the cured adhesive are a benefit when working with optical components. The preferred UV curing adhesive, used extensively in this work, is Norland NOA68. It is classed as a USP Class IV bio-compatible adhesive with excellent adhesion between glass with glass, and glass with plastic. These adhesion properties work very well with the materials commonly used in this work. When UV curing is not an option, a fast curing cyanoacrylate glue (e.g. Loctite 495) is preferred. This type of glue cures in a few seconds, for quick fixing and had to be used when integrating polymer fibres as the high power UV curing system tended to melt the polymer. For end connectors and other parts of the system a two part epoxy that cures over a few minutes allows for adjustment of parts before curing and is often used to bond tubing to the system, and to help seal the system. Viscosity is an important consideration when selecting glue. A glue that is too liquid is not suitable as it will flow away from the target area.

The distal alignment piece is core to the assembly process, and is 3D printed (Examples are shown in Fig. 3.5). As previously discussed this piece enables alignment of all the components in the assembly relative to each other, and eases the assembly process. Different alignment pieces may include additional modifications that are application specific, and may include flush channels as in Paper **IV** and Paper **V**, or polarisers as in Papers **I**–**III**. All the alignment pieces feature through holes for the camera module, and holes or recesses for fibre illumination, into which the optical fibres are placed. The fibres are prepared before the assembly process. While it is not necessary to terminate the fibre to communication grade specifications, a good termination improves the quality of the illumination spot. Since the fibres sit flush with the front of devices, or in some cases even recessed back, polishing the tips after assembly is impossible. As a result silica fibres are cleaved before integration into a device. This cleaving is performed using a multimode fibre cleaver (Fujikura CT-105), and an example of an acceptable cleave for this application can be seen in Figure 3.9 where there is no chip in the core. POF is terminated using a sharp blade. Ideally the fibre coating and jacket should be stripped back as little as possible, as damage to the jacket can lead to light leaking out the end of the fibre. This stray light may result in some image artefacts, for example if it strikes the back of the image sensor. The ideal length is such that the jacket is in contact with the dis-

tal alignment piece. As long as the distal alignment piece has sufficient opacity at the desired wavelength, any stray light should be prevented from striking the sensor or otherwise disturbing image quality.

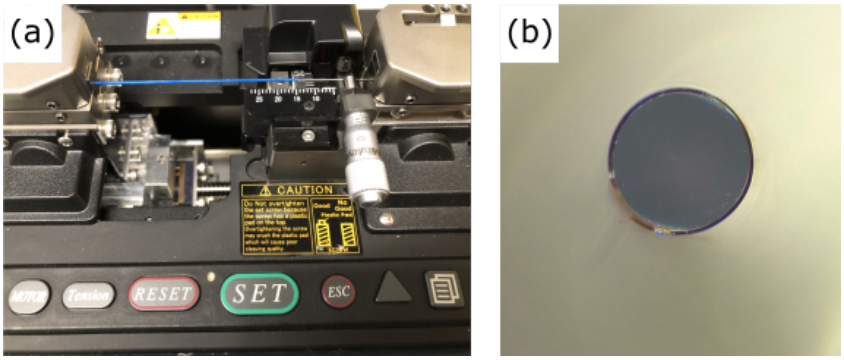

Figure 3.9. *Multimode fibre loaded into the Fujikura CT-105 cleaver (a), and cleaved fibre end (b). No damage is visible on the fibre surface, however there is slight separation of the cladding on the front edge of the fibre which was deemed acceptable for this purpose.*

Fibres are inserted into the distal alignment holder and aligned with the front face of the holder. In the case of polariser integration the fibres can be pushed up against the polarisers (Fig. 3.10). Otherwise a flat foot can be pushed against the front face temporarily to help align the fibres.

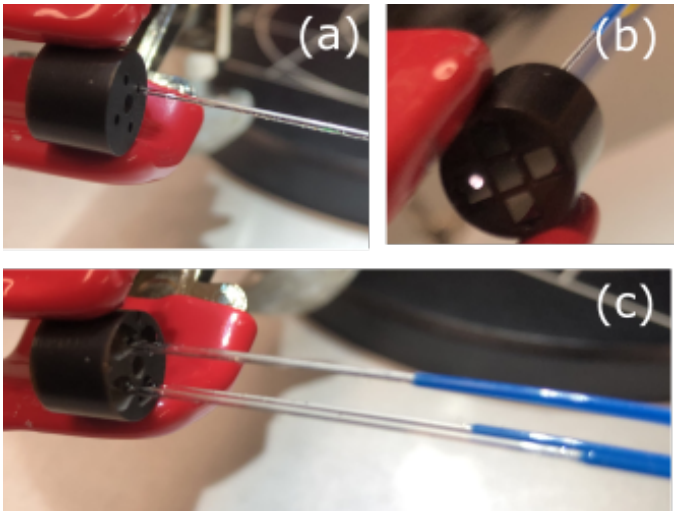

Figure 3.10. *Example assembly of multimode fibres glued into a distal alignment piece. In this case a 10 mm diameter distal alignment piece with polarisers is shown. Note the fibres are stripped back much further than advisable for illustrative purposes. The fibres are inserted into each of the designated holes individually (a) and checked for transmission of light (b). Fibres are glued into the back of the holder using a small amount of UV cure adhesive on the back of the holder. A small chamfered edge allows glue to flow in to the hole and attach to the fibre more easily.*

Fibres are terminated using a SMA connector on the proximal end, allowing for easy coupling into illumination systems. Fibres can be inserted into individual SMA connectors (Fig. 3.12), and can be either addressed individually, or collectively using a bifurcated fibre patch chord. Fibres can also be inserted into a single larger SMA connector and illuminated by butt-coupling a source patch chord and overfilling the apertures. The latter method allows for more straightforward termination using only

one SMA input. Fibres are inserted into the larger SMA ferrule, and UV adhesive is used to secure them in place and fill any gaps. The ferrule containing multiple fibres can be polished down using the normal polishing process. For appearance and protection purposes, heat shrink is used to cover seams, such are where the SMA connector connects to protective PVC tubing. Examples of this are shown in Figure 3.11.

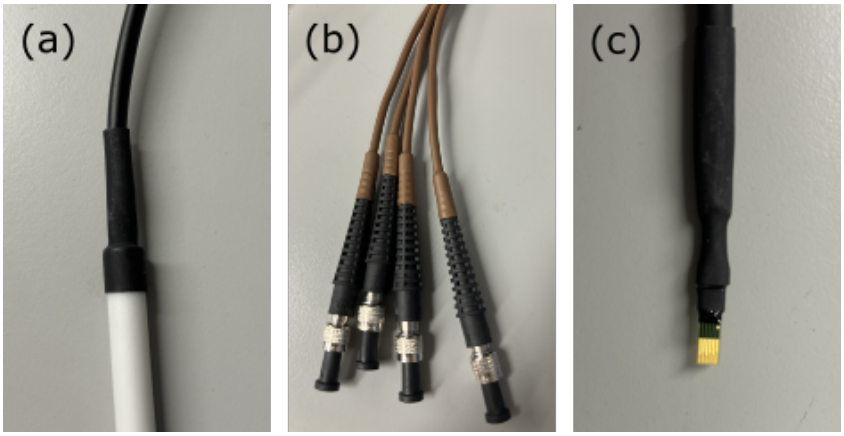

Figure 3.11. *Connections and seals are made using epoxy and shrink wrap where distal pieces connect to PVC tubing (a), SMA connectors connect to PVC tubing (b), or where the camera connector is terminated (c).*

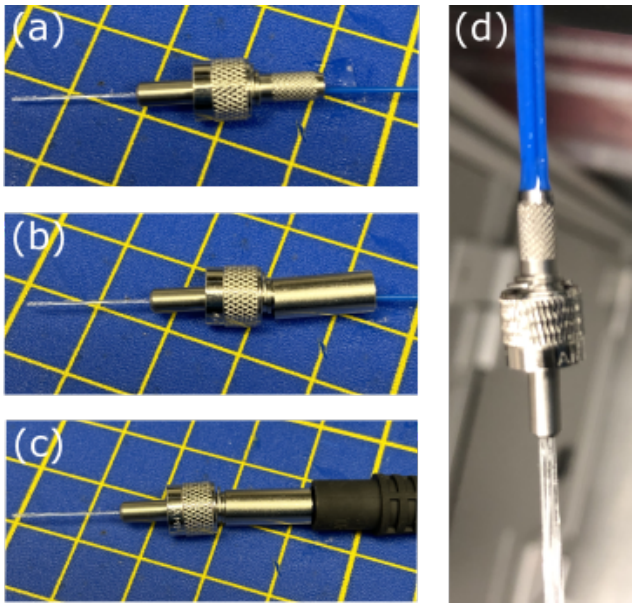

Figure 3.12. *Part of the SMA connector assembly process. The fibre is coated in UV cure adhesive (Norland NOA68) and inserted and glued into the SMA ferrule (a). The sleeve is attached to the ferrule using more adhesive (b). The flexible strain relief boot is pushed over the the sleeve (c), before the fibre is scribed using a ruby scribe leaving a small amount of fibre protruding from the front, and then the connector is polished. A similar procedure is used for combining multiple fibres into one larger SMA ferrule (d).*

The assembly process differs slightly from system to system. In order to showcase the general process, a probe designed for oral cavity examination is presented in this section. More specific integration techniques, such as polariser integration and very small scale integration will

be covered in subsequent sections. The oral probe presented is the second iteration of oral imaging probe, promising better image quality, illumination and robustness due to polymer optical fibres, stainless steel housing, and newer micro-camera sensor (NanEyeM).

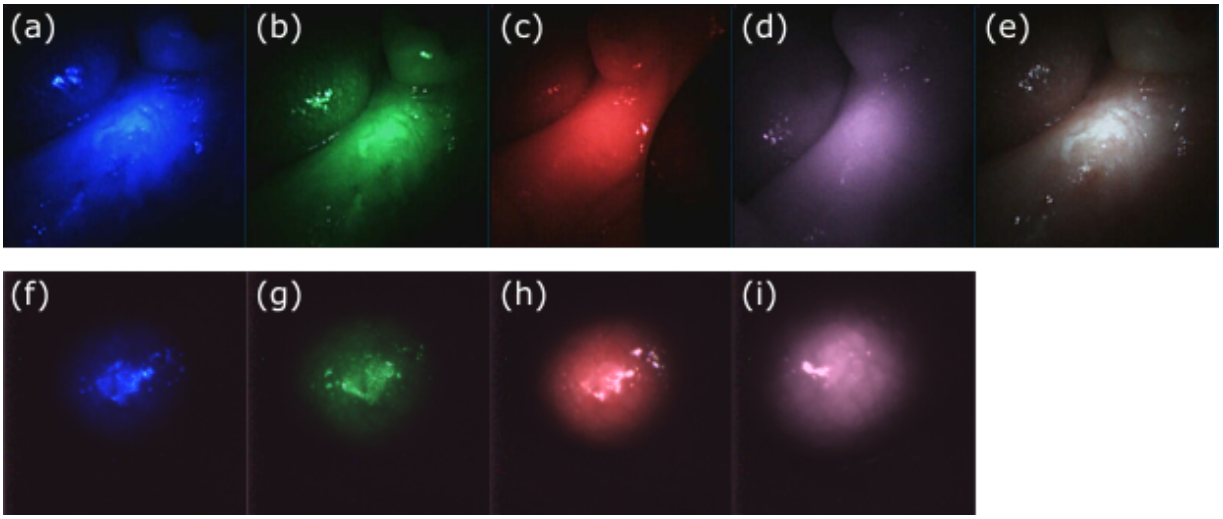

Figure 3.13. *Multi-spectral images using the new oral cavity examination system (a-e), and multi-spectral images captured using the old system (f-i).*

(i) First, fibres are cleaved for good termination and the components are layed out on a clean workbench.

(ii) Fibres and camera are passed through a PVC tubing and stainless steel housing to emerge on the distal end

(iii) Fibres are glued into the distal alignment piece using cyanoacrylate glue (as UV curing melts the polymer fibres). Alignment is performed under a microscope. A small amount of glue is placed on the distal alignment holder and the fibre pressed into the recess. The fibre is quickly adjusted using tweezers before being held in place to allow the glue to cure. More glue is placed around the length of the fibre in contact with the alignment holder to secure them in place.

(iv) The micro-camera is now inserted into the recess of the distal alignment holder. It is maneuvered into place using a wooden stick to ensure it is flush with the front of the holder. It can now be glued in place using cyanoacrylate glue, first by placing a small drop on the end to fix it in place and then by adding more glue to ensure adhesion.

(v) The distal alignment holder is press fit into the stainless steel housing and secured in place using adhesive which is inserted through the back of the tube. To achieve this the holder is pushed/pulled back into the stainless steel housing.

(vi) The PVC sheathing is secured to the stainless steel holder using adhesive and heat shrink.

(vii) The SMA connectors are assembled, and the flexible strain relief boot is connected to the PVC sheathing using a silicone sealant and heat shrink.

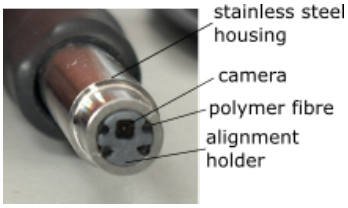

Figure 3.14. *Rigid oral cavity examination tool.*

The assembled device is shown in Figure 3.14. For further reading on design and assembly processes the reader is directed to Paper **V** where design iterations the assembly process of a catheter integrated cardiovascular imaging system is described.

3.6 Polariser Integration

Integration of polarisers into the system proved a necessary step for elimination of specular reflections to improve image quality, and for polarimetric measurements on a small scale. The polarisers are selected to be broadband across the VIS and NIR, and for high transmission, to obtain a clear image. In order to achieve the desired optical and dimensional specifications, glass polarisers are mechanically diced using a dicing saw for semiconductor applications. In the case of a handheld probe, used in Paper **I** and **II**, dimensions of 2 mm square are selected for the polarisers, allowing for more simple integration given a larger dimensional allowance. This system, consisting of large polarisers was also used as a proof of concept for the integration of polarisers into micro-camera imaging systems. For the miniature polarimetry system, presented in Paper **III**, the dimensional requirements of the polarisers further reduced to 500 μm, these can be seen mounted on the dicing tape in Figure 3.15. The saw blade used is itself approximately 200 μm in diameter as can be seen in the gaps between optics in Figure 3.15. The edges are slightly rough, and the occasional chip is observed in individual optics, but by and large, the active area in the centre which will sit on the circular fibre is undamaged. Polariser performance appears unaffected by the dicing process. The assembly process remains very similar to that of a system using larger polarisers as described in Figure 3.16.

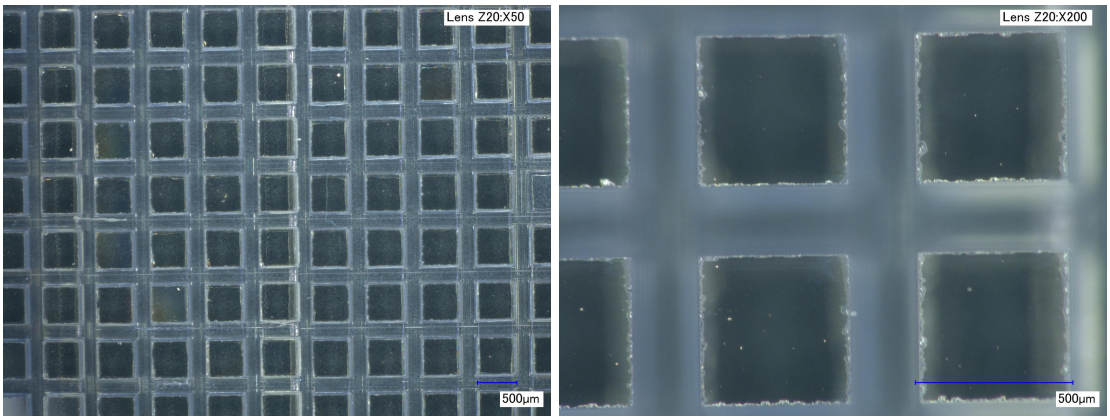

Figure 3.15. *3D microscope images of polarisers diced to 500 μm square.*

The integration of polarisers in the cross polarisation system used in Paper **I** and Paper **II** is described in Figure 3.16. The diced optics arrive on a medium tack dicing tape as seen in Figure 3.16 (a), from which they can be separated using a non-scratching instrument such as a wooden toothpick, and lifted off using a pair of fine tweezers. In the case of non-overcoat protected polarisers, the wire-grid side is placed face up on the dicing tape in order to prevent damage due to the adhesive. Protective overcoat polarisers are preferred, however. The polariser is placed into the corresponding 3D printed recess in Figures 3.16 (b-c). Next, the orientation of the polariser is verified using an externally mounted polarisers, as shown in Figure 3.16 (d). This verification process is repeated for each inserted polariser to ensure cross polarisation between the illu-

mination fibres and the central camera sensor. Once the polarisers are in place in their correct orientation, a small amount of UV cure optical adhesive (Norland NOA68) which has excellent glass-plastic adhesion, is applied to the edges of the polarisers. Care is taken to keep the FOV free from glue. This version of the probe includes small semicircular recesses on the illumination polarisers in order to make placement of glue more straightforward. Glue is placed using a sharpened wooden stick, which features a very sharp point for controlled placement and does not damage any of the optics. Figure 3.16 (e) shows placement of glue on the outer illumination polarisers, and Figure 3.16 (f) shows glue being placed on the corner of the internal camera polariser. After glue placement a UV lamp is used for curing as shown in Figure 3.16 (g), with the final prototype shown in Figure 3.16 (h). The illumination fibres and camera can now be pushed up against the polarisers on the inside of the alignment holder and secured in place, as previously described.

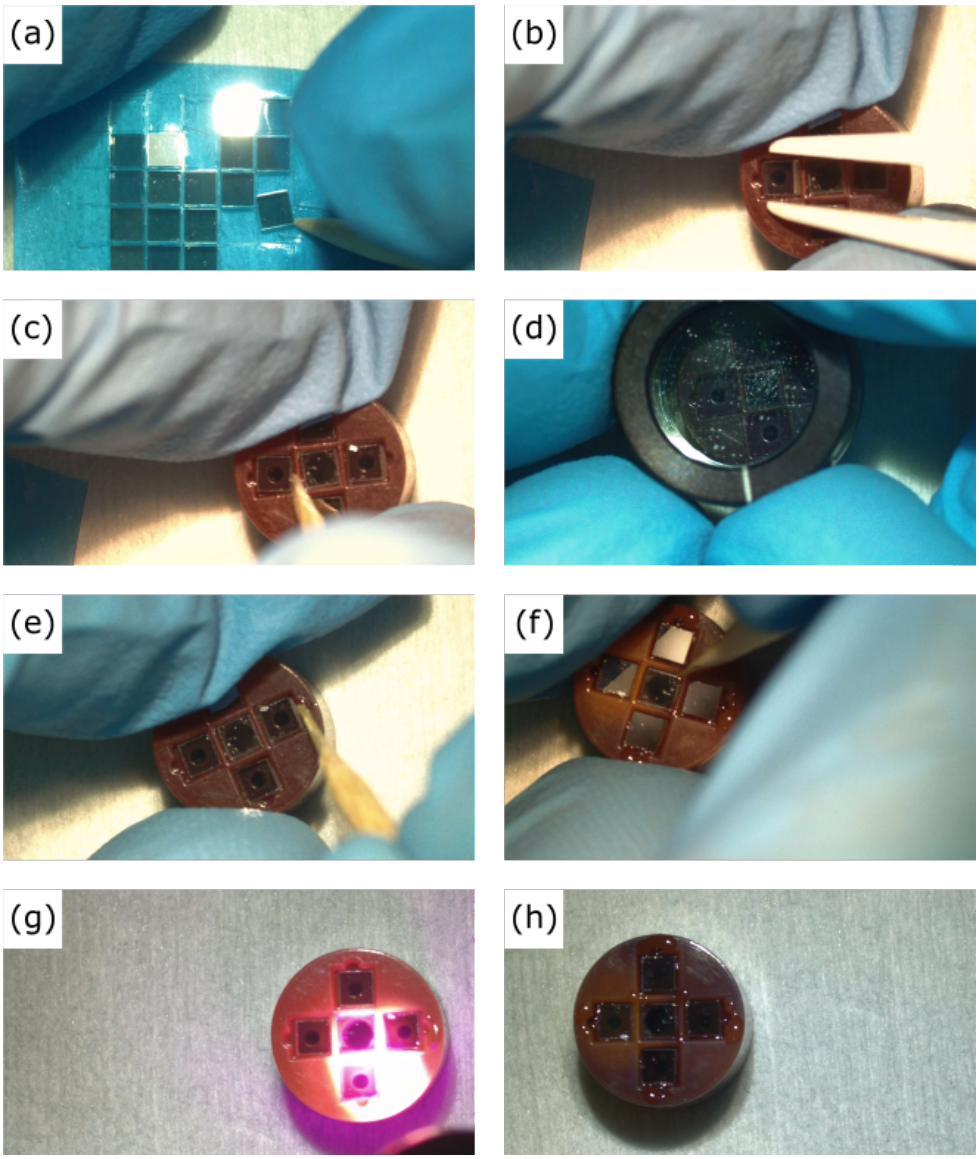

Figure 3.16. *Figures (a) - (h) show the assembly process of mounting polarisers into the handheld cross polarised probe.*

Note that an exploratory dicing run was able to achieve mechanical dicing of polarisers to dimensions as small as 300 μm, potentially allowing

for integration into a system at 3 Fr scale such as the one shown in Section 3.7.

3.7 Small Diameter Systems

The aforementioned design considerations and assembly processes provide the tools for assembly of very compact imaging systems for biomedical analysis. One such system is described more extensively in Paper **V**, where a NanEye2D camera was integrated into a catheter device alongside a flush channel, and illumination. This device was of the order of 7 French (Fr)[4] and navigated through a cardiac catheter to obtain images of the heart. In order to further push the boundaries of footprint, this section describes a system that approached the 3 Fr scale, which can navigate through tighter working channels, and deep into areas of the lung, for example. In order to achieve an imaging system at this scale, the smaller OVM6948 sensor was used along with a single 200 μm optical fibre that can deliver light *in situ*.

[4] 7 Fr is approx. 2.3 mm

Medical grade tubing (Nordson 141-0070) with an internal diameter of 1.04 mm and external diameter of 1.19 mm was selected as the carrier lumen for the on-the-tip camera sensor and illumination. This dimension approaches the 3 Fr catheter gauge, and can easily be inserted through the working channel of commercially available bronchoscopes.

The initially proposed design included a 3D printed alignment piece. A number of design iterations can be seen in Figure 3.17.

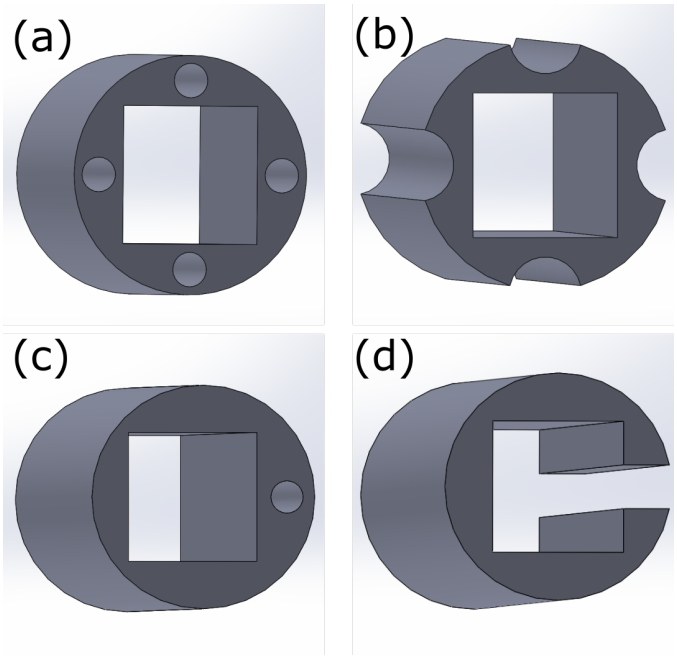

Figure 3.17. *Design iterations of the distal alignment system for the small footprint imaging probe with square hole for the camera sensor, and grooves or through holes for 1-4 fibres.*

Due to limitations with the available 3D printing processes, the scale of the proposed alignment system proved too small to be reliably manufactured. The minimum thickness of the Protolabs Microfine™material resulted in walls that were unstable. Even after design revisions, such as placing the fibres in grooves along the edges of the material, instead, the prototypes were mechanically unstable and failed quickly when handled. As a result, they proved an inadequate solution for alignment. Other

machining options were explored, including micro-molding, wire EDM and milling processes which could have achieved the dimensions while promising more structural integrity due to metal parts. The designs were amended for a milling process to include rounded recesses in the corners of the central camera hole, since this process is unable to manufacture 90° corners (Fig. 3.18). However, due to cost and time constraints the machining of the parts for this demonstrator was not feasible for this project. A manual alignment was performed instead to manufacture a proof of concept.

To perform this assembly, the OVM6948 module with attached cabling was threaded through the outer tubing (Nordson 141-0070) along with illumination fibre. This insertion into the tubing can be quite difficult, and to ease the process the camera is temporarily attached to a more rigid guiding wire which can be pushed through to the other side. Next, the assembly was mounted under a microscope, with the tubing at a slight angle. This allowed for vision into the tubing and allowed the camera module to rest on one side of the inner lumen. The camera was maneuvered into place by retracting it back into the tubing until it sat slightly protruding from the front. A small amount of UV cure-able adhesive was placed along side and corner of the camera module. Adhesive was placed using a piece of 100 μm glass fibre with which small spots of adhesive could be deposited manually. The adhesive remains a liquid until cured, which allows for final adjustment of the camera's position within the tubing. The camera was pushed back slightly using a non-scratching tool, until it aligned with the edge of the lumen after which it can be secured in place by exposing to UV radiation. The gaps between the camera and the inside lumen could now be carefully potted using adhesive and a similar iterative placement and curing procedure, while leaving room for the illumination fibre. The fibre is placed and aligned in a similar manner as the camera module, and the cleaved end fixed in place in plane with the camera lens. Care must be taken throughout the adhesive placement process to keep the adhesive off the camera sensor and the top of the fibre, and areas had to be wiped clean frequently using a lint free optical wipe due to placement errors incurred during the manual placement procedure. After securing both the illumination fibre and the camera module, the remaining gaps are potted using UV cure adhesive. The proximal end fibre connections are made and a final device is produced. The manual alignment, surface finish, is not perfect (Fig. 3.20), and optical isolation is less consistent using this method. This illustrates the advantage of a distal alignment piece as is described for small diameter systems in Paper **V**. Furthermore, using a more sophisticated alignment stage and glue placing machine will assist the assembly process dramatically. Nevertheless, the manual integration of a 650 μm camera module along with illumination fibre into a 1.19 mm OD medical tubing is achieved (Fig. 3.21).

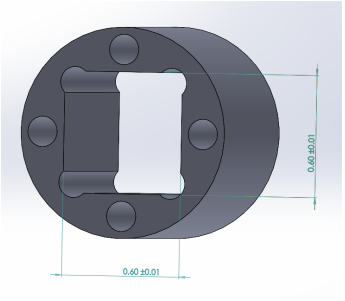

Figure 3.18. *Drawing showing the proposed distal alignment part for the small diameter system with the circular recesses at the four corners of the central holes to allow for machining using a milling process.*

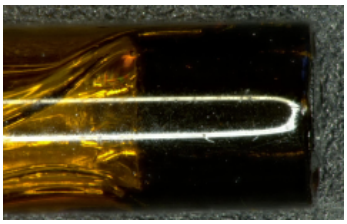

Figure 3.19. *Side view of the catheter probe with OD 1.19 mm. The polyimide catheter tubing is seen. No components protrude beyond the edge of the tubing. The black camera module is seen, and the glue encapsulation can be seen through the tubing, where the glue was allowed to flow past the camera module before curing.*

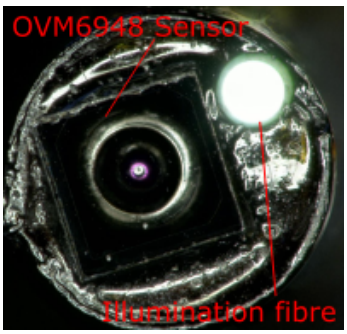

Figure 3.20. *Front view of the catheter probe with OD 1.19 mm showing the camera sensor and the illumination fibre with white light illumination on.*

Figure 3.21. *Tip of completed catheter probe with outer diameter of 1.19 mm shown to scale with human hand on the left. An angled side view is shown on the right with the sensor and illumination fibre indicated.*

The device is validated during an *ex vivo* laboratory experiment, more information in Chapter 4.

3.8 Back-end illumination

Optical fibre connectivity allows for flexibility and real-time control of the illumination delivered to the distal end of the systems. This illumination is delivered using custom built portable illumination systems that can provide either LED light, laser light, or a combination of both. The systems use a series of off the shelf diodes coupled through a series of dichroics into an optical fibre. Since the illumination wavelength can be switched rapidly, a near real-time colour reconstruction can be performed [104]. The laser source can be seen in Fig. 3.22 and the LED source in Fig. 3.23. The diodes and drivers are mounted on a custom designed breadboard that fits into a 200 mm x 300 mm x 96 mm housing (Thorlabs EC2030BR). Powering systems, as well as controls systems using NI-DAQs (National Instruments), are housed separately. The light from the diode is collimated and passed through the dichroics, after which it is focused into a single fibre. This allows any combination of wavelength and intensity, allowed by the selected diodes, to be coupled into a single output fibre. Coupling efficiency for LEDs is low, and 1 inch optics are selected as a reasonable trade off between cost and aperture size in order to maximise the light collected. This results in a power output of a few mW to tens of mW depending on size of the multimode fibre. These values are sufficient for illuminating the scene. More details on power characterisation can be found in Paper **VI**. By default, diodes are selected to be representative across the VIS-NIR spectrum, such that red, green, and blue (RGB), and at least two IR wavelengths can be output by the system. The RGB illumination allows for the reconstruction of white light whereas the infrared wavelengths are useful when probing deeper into tissue. Of course, the blueprint allows for customisation of the light source, and wavelength availability is dependant on the dichroics and diodes available. In this way, a cost-effective, compact, and versatile light source for biomedical applications is constructed. More information regarding the light source can be found in Paper **VI**. Both LED and laser illumination can similarly be coupled into the same fibre using this blueprint, should that be desirable.

Figure 3.22. *Internals of multi-wavelength laser source, turned on.*

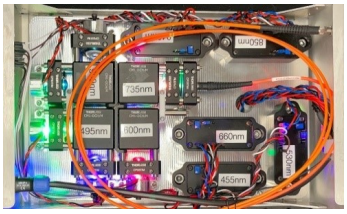

Figure 3.23. *Internals of the multi-LED Source, turned on.*

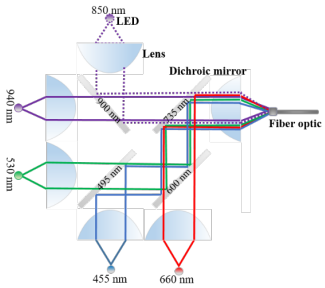

Figure 3.24. *Schematic drawing of the multi-LED Source.*

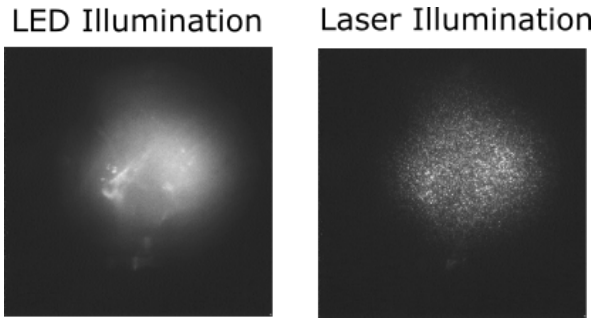

Figure 3.25. *Comparison of the same location of ex vivo kidney tissue using red LED and red Laser illumination captured using cross polarised monochrome NanEye2D sensor. Laser speckle is clearly visible in the right image but absent in the left.*

The coherent nature of the laser results in laser speckle when light reflects from the uneven tissue surface, interfering constructively and destructively. This effect can be useful in applications such as Laser Speckle Contrast Imaging (LSCI) which has been successfully performed

using a microcamera [105–107]. LSCI can detect blood perfusion [108], since the speckle pattern shifts with scatterer motion as can be seen in Fig. 3.25. However, laser speckle can also have a detrimental effect on image quality. One such example is shown in Figure 3.25 where biological tissue is illuminated using laser and LED illumination. Laser speckle is clearly visible, resulting in saturated pixels and uneven illumination pattern. As a result much of the images captured in this thesis are captured using LED illumination. Lasers may still be advantageous when specific absorbers are targeted and a narrow spectral width is desired, and it may be possible to reduce the effect of laser speckle when imaging with a camera by changing the coherence time mechanically - e.g. by means of rotating diffuser, or by vibrating the fibre [109]. Laser illumination also means much better coupling efficiency than LED illumination.

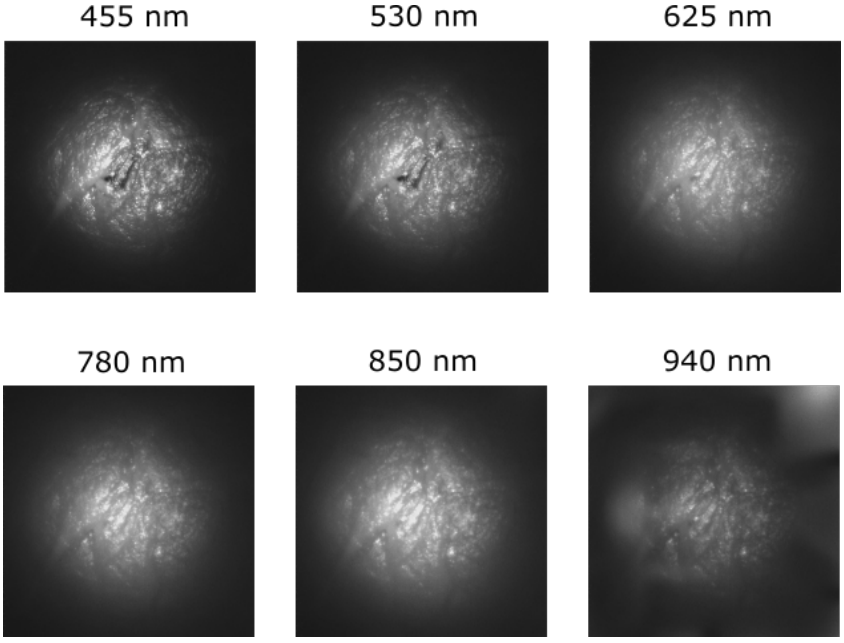

Figure 3.27. *Monochrome images of the same location of pork tissue captured using a monochrome NanEye2D sensor, using different wavelengths of LED illumination from the blue to the NIR.*

In Figure 3.27 images of pork tissue, acquired using a multispectral light source and a monochrome NanEye sensor are shown. The selected imaging location includes an embedded red coloured feature, which may have been a blood vessel or accumulation of blood. Interestingly, the multispectral images highlight the importance of wavelength choice when imaging biologicial features, with the contrast being most present in the blue wavelength band, followed by the green. The red and infrared bands do not show any contrast in the middle region and the feature is effectively invisible. This effect can be seen also in blood vessel detection, where green is often preferentially used as the colour providing greatest contrast [91]. This phenomenon was discussed and demonstrated in the Image Analysis section of Chapter 2 for vessel detection where the green channel was isolated and used for the Hessian matrix computation due to it offering the best contrast. In Figure 3.27 additional artefacts can be seen in the image at 940 nm. This is due to light leaking through the 3D print material and entering the camera sensor. It highlights again the importance of material choice and light isolation of the camera, as discussed in Chapter 3 Design Considerations.

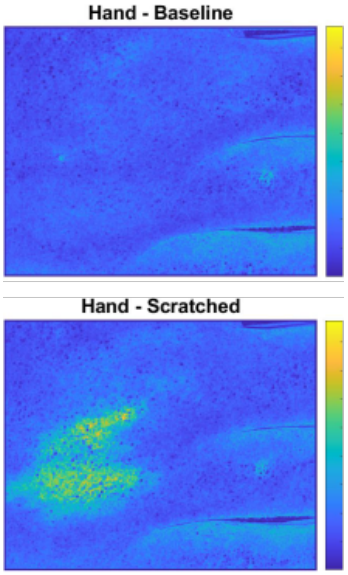

Figure 3.26. *Example of an image captured using benchtop LSCI system constructed as part of an undergraduate project, the co-supervision of which was conducted during this PhD. The image shows how LSCI can detect increased blood perfusion after agitating the back of the hand by scratching.*

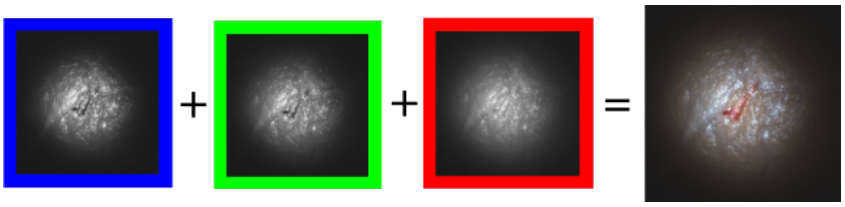

Figure 3.28. *RGB colour reconstruction from red, green, and blue sequentially illuminated images using a weighted linear recombination. A monochrome sensor is used.*

Multispectral illumination of a monochrome sensor allows for colour reconstruction as shown in Figure 3.28. In this case the blue, green, and red illuminated images are recombined into a single RGB image using a weighted linear recombination. The reconstruction code allows for the contribution of each channel to be adjusted, in this case until the image appears correct upon visual inspection by human observer, when compared to the original. This weighting process is one that could be easily automated. In the example in Figure 3.28, the recombination is performed to mimic an RGB image, however since the light sources allow for flexibility in wavelength, one or more of the "RGB" channels could be replaced with another wavelength, for example in the NIR. In certain cases, this could enable an enhancement in contrast. More detail on the LED source and its use for colour reconstruction with NIR capability can be found in Paper **VI**.

3.9 Image Acquisition

The goal is a system that can provide real-time, relevant, information to clinicians. This requires control and synchronisation of the camera, light sources, and other peripherals in combination with real-time image processing and analysis. The NanEye2D sensor readout is performed using a custom readout board, the *ac62kusb* board (BAPIS, Ergolding, Germany). This board is able to interface with LabView (National Instruments, Austin, Texas, USA) using a USB connection. Using custom LabView applications that are tailored to the application, images can be captured at video rate, and the light sources and other peripherals such as an optical switch, can be controlled within the same application. This allows for automation of the image acquisition. For HDR imaging the light intensity from the light source can be controlled and corresponding image stack can be captured on the click of one button. This HDR functionality is explored in Chapter 5. The optical switch used in Paper **I** was also controlled using custom Labview interface along with light source and camera. Automation such as this has allowed for a large time saving in the time-critical clinical applications the sensor has been used in. For the NanEyeM, readout options are currently being explored, with the best current solution being a wireless readout board provided by Kiehn Engineering Services GMBH (Oberflacht, Germany). However this board is limited by its inability to provide raw data readout at video rate due to the wireless interface. A USB option is being explored. The data can be captured and read out using a Python interface. Both boards for the NanEye camera range offer a compact form factor and could be integrated into a device handle, for example. The Omnivision sensors are controlled using their OVmed evaluation boards, which are slightly bulkier, and are limited in their usability due to the inability to automate the using Python or LabView. Other board options exist, however Omnivision proves difficult to engage with on a research level.

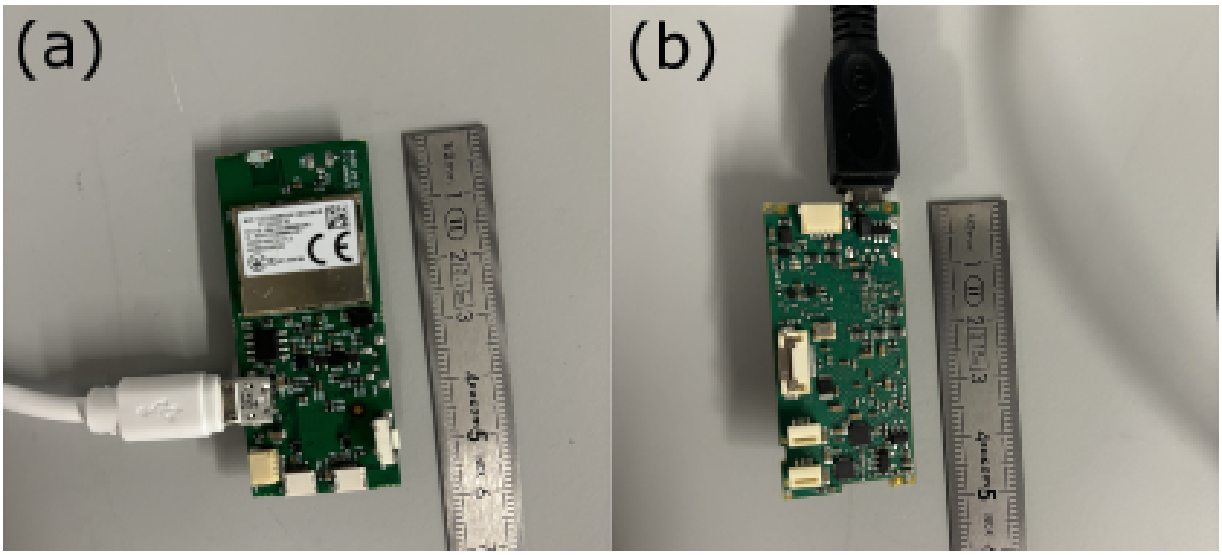

Figure 3.29. *Read-out boards for (a) NanEyeM, and (b) NanEye2D, with compact form factors.*

Keeping in mind portability and ease of use requirements, as well as the desire to run algorithms, including machine learning algorithms on real-time data, custom readout solutions using FPGAs have been explored in Paper **VII**. In this work vessel detection algorithms have been implemented on an FPGA platform. The platform allows for rapid, configurable, data analysis in a small footprint, and may be integrated in to the handle of a handheld device, for example. The ability to implement machine learning for image processing for biomedical images on an FPGA has already been demonstrated [110].

Chapter 4

Miniature *in-* and *ex vivo* Applications

*One of the primary motivations of using a micro-camera is capturing of diagnostically valuable images in clinical applications that require very small footprints. Their uses as adjunctive tools is discussed in terms of cardiovascular and pulmonary procedures, with the cardiovascular work found in Paper **IV** and Paper **V**. The clinical motivation in the cardiovascular application was to image and verify an ablation procedure by detecting colour changes in the tissue, and to provide images that can verify placement of a device. Data analysis demonstrates the ability to extract physiological parameters from in vivo video data. Small footprint devices allow for navigation in hard to reach places in the body, and provide data that is otherwise often unavailable. In this Chapter, systems with outer diameter (OD) footprints from 1.19 mm to 2.30 mm are presented. The small footprints allow for compatibility with existing devices such as guiding catheters and a commercial bronchoscope. The ability to use CIS in this context highlights the future potential of this technology in a biomedical context.*

4.1 Research Objective

The objective of this research phase, was to investigate the translation of micro-cameras in small footprint to real endoscopic applications. This is motivated by two clear clinical needs, namely the cardiovascular space and the peripheral lung clinical applications.

The aims and objectives for the cardiovascular work are well described in Paper **IV** and Paper **V**. In brief, as part of an industry funded project, a system is designed to be navigated into blood vessels and the heart. The objectives are twofold; firstly, to measure hypoxia *in vivo* in order to verify ablation and to extract physiological parameters *in situ*. Secondly, to provide images for surgical guidance to verify placement of devices such as a left atrial appendage occlusion device; and to verify the success of intravascular procedures. As such, a multi-modal system is proposed as in Paper **IV**.

The miniaturisation efforts conducted as part of this work, and as part of the wider IPIC2 project, led to the investigation of endoscopic imaging in the lung. Here the objective is to navigate peripherally further than possible with a traditional bronchoscope by pushing the miniaturisation research conducted in this work, while maintaining the ability to provide multi-spectral illumination via fibre optics. This is demonstrated on *ex vivo* tissue in a 3 Fr catheter.

4.2 *in vivo* Study for Intraluminal Cardiovascular Imaging

4.2.1 Intravascular imaging

Cardiovascular imaging is part of the current standard of care in the field. This imaging is performed externally using MRI, ultrasound, X-Ray, and CT for example; and intraluminally using IVUS and OCT. Both IVUS and OCT are well established techniques using ultrasound, and infrared interferometry respectively to reconstruct images inside of the vessels. Interventional examinations using IVUS and OCT include morphological examination of the structure of the vessels and neointima (scar tissue) assessment, plaque examination as well as detection of vulnerable plaques, and thrombus evaluation. The techniques also provide guidance during percutaneous coronary intervention, and can assist in assessment before and after device placement procedures such as stenting or the insertion of balloons [111–114]. Scanning fibre endoscopes (SFE) have also shown potential as angioscopes in the literature, but have not yet seen clinical translation. This technique uses a piezoelectric actuator to scan a single fibre in order to form an image [13]. It has been used with narrow band multispectral illumination to assess atherosclerosis in *ex vivo* samples [115], and has been shown to successfully image common procedures [116]. It may see use in the future in angioscopic imaging such as for neurological imaging and stroke assessment [14, 117]. Compared to micro-image sensors they require a scanning mechanism at the tip of the system in order to form an image.

In terms of CIS based technologies, the small diameter of the vessels places a harsh dimensional requirement on any imaging system. As a result, the technology has not seen percutaneous use, and instead imaging systems have been developed to access the heart in a transapical manner, through the thorax and puncturing the apex of the heart [44–46]. Micro-cameras, with their dimensional advantages, offer an opportunity for integration into catheter based imaging systems that may compete with the aforementioned trans-catheter technologies in terms of simplicity, versatility, and price.

All of these technologies are imaging the inside of the vessels or the heart to provide vision where there would otherwise be none. Fluoroscopic guidance fails to provide *in situ* images and requires exposure to radiation and is by nature 2 dimensional. Advancements in cardiovascular imaging, may have a profound impact on minimally invasive procedures in the future. Various procedures in interventional cardiology involve placing devices, such as pacemaker leads, stents, and valves. Imaging can be used to verify the correct placement of such devices. The imaging may be beneficial during minimally invasive valve repair interventions, such as Transcatheter Aortic Valve Implantation (TAVI), where a new valve is delivered through the blood vessels to a location in the heart, for example to treat stenosis of the valve. During pacemaker procedures, where leads are implanted in the heart, the correct placement of which can be verified using imaging techniques, reducing the reliance on fluoroscopy. The availability of imaging inside the body may have another diagnostic advantage. Endocarditis is a rapidly progressing condition which can arise as a complication associated with aforementioned device placements, arising in 0.5%-3% of patients within one year of the TAVI procedure alone [118]. Imaging techniques have been limited in their ability to diagnose the condition, especially early [119]. The ability to image and sense *in situ* may prove useful in verifying infection, and locating it, when non-invasive technologies fail to be conclusive. The micro-camera itself can provide multi-spectral contrast of chromophores that is not easily obtained using other technologies such as OCT. It also

provides the ability to record procedures and verify their success.

The cardiovascular study presented in this Chapter was motivated primarily by the clinical need to verify ablation procedures and device placement in an industry project. In order to solve vision problem inside of the body the micro-camera is selected. A complimentary DRS system aids in providing spectral resolution. In this Chapter and related publications Paper **IV** and Paper **V**, the feasibility of using a micro-camera based trans-catheter probe in endovascular examination is demonstrated on a porcine model. The cameras are integrated in a forward facing orientation for imaging ahead of the device, requiring no pull back, and allowing for the visualisation of the walls of the heart. This small scale integration challenge achieves angioscopic imaging during a cardiac catheterisation procedure using a small footprint CIS. Video data inside of the beating heart of the porcine animal is collected, making it possible to visualise procedures such as a trans-septal crossing. Some physiological parameters are extracted from the acquired video data, demonstrating the feasibility of using the camera as a diagnostic platform when assessing ablation, and oxygenation for example. The camera is also used to image an ablation study that is performed on the epicardium at the apex of the heart.

4.2.2 System and Navigation

The catheter system consists of a micro-camera, fibre optic illumination, and saline flush channel. The design and assembly are discussed in detail in Paper **V**. In brief, two fibres provide laser or LED illumination from a external light source. The saline flush channel can assist in clearing the blood field, and the micro-camera acquires images in a forward facing mode. These three systems are integrated into a catheter. The catheter is selected to account for kink resistance, and assembly is performed in a similar manner as discussed in Chapter 3 using a distal alignment piece. Platinum-iridium markers are included to allow fluoroscopic tracking of the device. The final footprint of the device is 2.30 mm OD.

The system was tested on separate occasions in a porcine and canine animal model. The canine model was used for initial validation of the imaging system intra-vascularly, while the porcine model is used to investigate the research objectives outlined above. The study protocol is described with in more detail in Paper **IV**. The micro-camera system is passed through a guiding catheter into the heart of the animal model during the study. Different locations in the heart are targeted, including the intra-atrial septum, the left atrium and the left ventricle. Performance characteristics of the intra-vascular imaging system, and ease and convenience to deliver to the various treatment sites was assessed. During the study in the porcine animal, an arterial occlusion is performed in order to reduce the oxygenation of the tissue being imaged, mimicking hypoxia. An RF ablation procedure is also performed on the epicardium and imaged using the camera system (Fig. 4.2). The porcine model was selected because of the anatomical and physiological similarities with the human heart and vascular system. Two adult animals were used in the study, which was conducted under approval of the protocol and ethics review board (Center for Cardiovascular Research and Development, American Heart of Poland Inc, TYN 2407-20). The canine trial was conducted with an industry project partner and was conducted at IMMR, Paris.

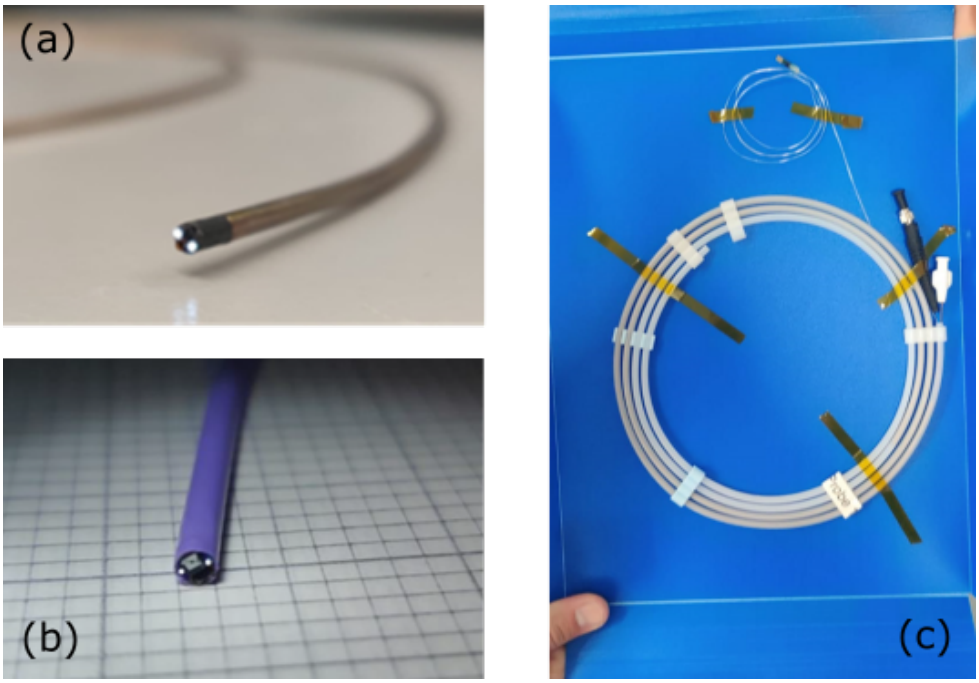

Figure 4.1. *Finished 2.30 mm OD devices with the first iteration using braided polyimide tubing in (a), the final iteration with the Pebax tubing in (b), and the device securely packaged in a protective sleeve with the proximal terminations for the fibre, camera connections, and flush visible in (c).*

Figure 4.2. *Image of the apex of the heart post RF ablation, with highly ablated regions displaying dark and charred, and a colour gradient seen in the image. Better image quality must be achieved for verification in a future study.*

When imaging in a blood filled environment some effort must be made to generate a clear image. In order to clear the FOV, a number of techniques were explored as part of the study, all requiring some form of saline flush. Aside from the integrated flush channel, the guiding catheter can assist in clearing the blood field by passing saline through it. A separate flushing catheter can also be introduced. The guiding catheter can be used as a seal to isolate an area to be imaged by gently holding it against the tissue. A balloon catheter can assist further in isolating a region inside of a vessel, for example, by obstructing the flow of blood and imaging through the clear balloon. The integrated flush channel is effective in cleaning the optics. In this way the camera is able to capture images in a variety of locations, including the beating heart (Fig. 4.3). Best quality images are achieved when the device is slightly recessed in the guiding catheter, and the catheter shields the device from additional blood flow after the field of view is flushed. It is important to note that it is not possible to flush saline continuously, and so video data in practice is captured in short bursts.

Illumination systems were changed in between the two animal studies, with LED illumination used in the canine study, and a multi-spectral laser system in the subsequent porcine study. The LED illumination appeared to provide a better image. It appeared that the Brownian motion of the liquid field reduced the effect of laser speckle, however image quality as a whole appeared worse to the human observer when using the laser illumination. The laser speckle, while not directly visible, still blurred the image compared to the white LED source. This, however, is a multivariable equation and more investigations must be conducted with the study conditions more closely controlled in order to draw conclusions.

For the intravascular portion of the study, the clinician navigates the device to locations under fluoroscopic guidance, through a guiding catheter. The device is introduced through the femoral artery and arrives in the right atrium of the heart. Here the wall of the right atrium is imaged, and a trans-septal crossing is performed. The device is now

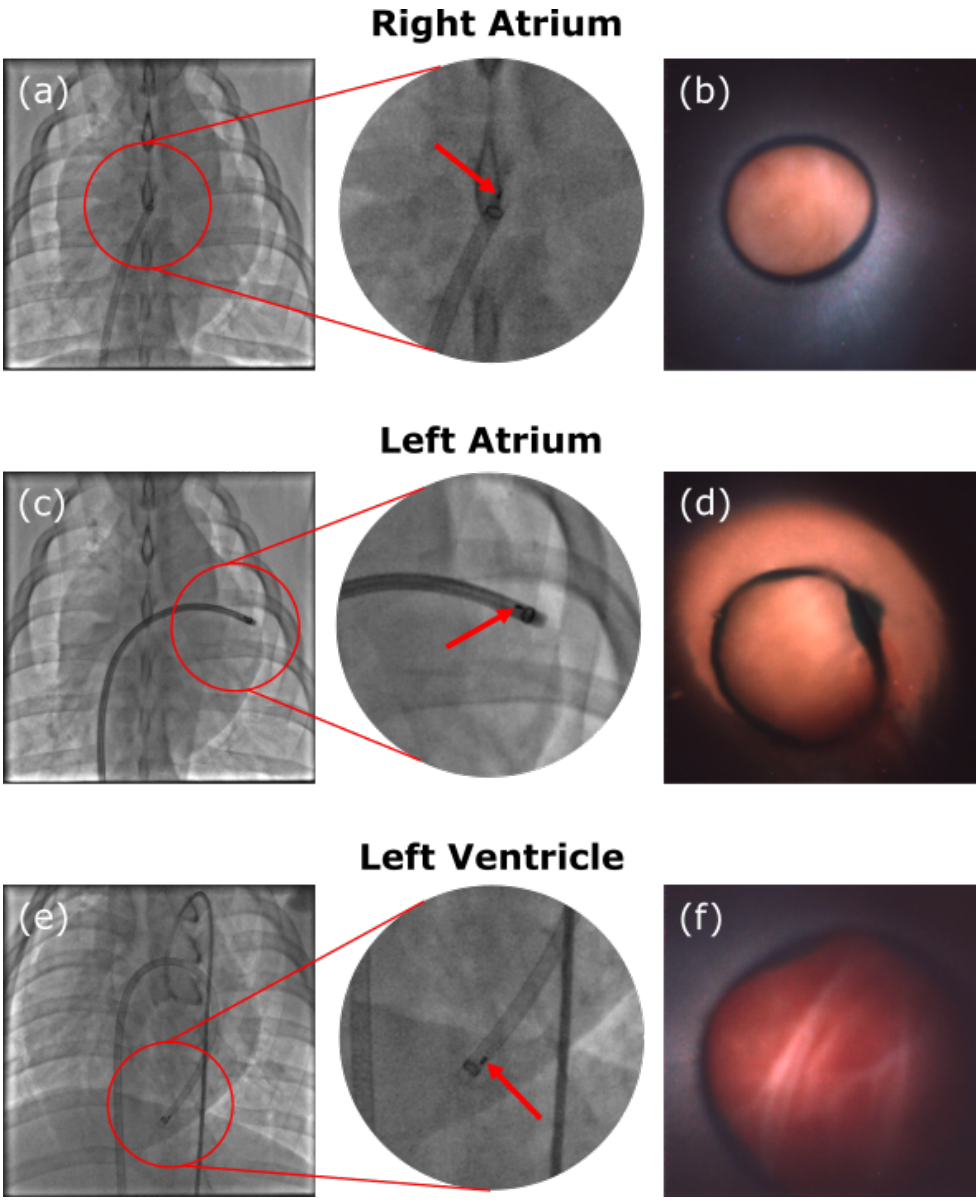

Figure 4.3. *Fluoroscopy images showing the guiding catheter and device at location, with corresponding camera images. The red arrow indicates platinum-iridium marker bands attached to the distal end of the device. A circular marker band at the tip of the guiding catheter is also visible. The device was navigated to the right atrium in (a) and images the intra-atrial septum (b). The device sits in the left atrium in (c) where an image of the endocardium in the left atrium is displayed in (d). Finally the device is located in the left ventricle with its position visible in (e) and an image of the endocardium of the apex of the heart can be seen in (f). In images (b), (d), and (f) the guiding catheter can be seen since the micro-camera has been retracted slightly within the catheter.*

passed through this trans-septal cross into the left atrium, where the wall can be imaged and the occlusion study is performed. Finally the device is navigated into the left ventricle and the apex of the heart is imaged. The entire video data consists of multiple minutes of continuously good video data. This is video footage where multiple minutes are captured with a cleared blood field, and the intrusion of blood into the guiding catheter is minimal. The cardiac tissue is clearly visible within a circular ROI bounded by the guiding catheter. When there is further blood intrusion, obscuring vision, it was cleared by flushing with additional saline ensuring good visibility.

DRS measurements were acquired using a separate probe, as part of this study, and results can be seen in Paper **IV**. While out of the scope of this thesis, this demonstrates the potential for integration of the micro-camera into a single system to enhance diagnostic capability by allowing for point measurements at the imaging location. This modality brings increased spectral contrast and offers enhanced sensitivity for analysing oxygen content in tissue.

4.2.3 Data Analysis

Video data acquired during the planned occlusion procedure to reduce oxygenation of the tissue, from inside of the left atrium is analysed. The video footage shows tissue in a circular region in the centre of the images, and the white inside of the guiding catheter around the edges. The camera can be navigated closer to the tissue or pulled back further, and multiple illumination wavelengths can be delivered such as NIR illumination to see deeper into the tissue (Fig. 4.4). The full video used in the data analysis is made available in the supplementary files of Paper **IV**.

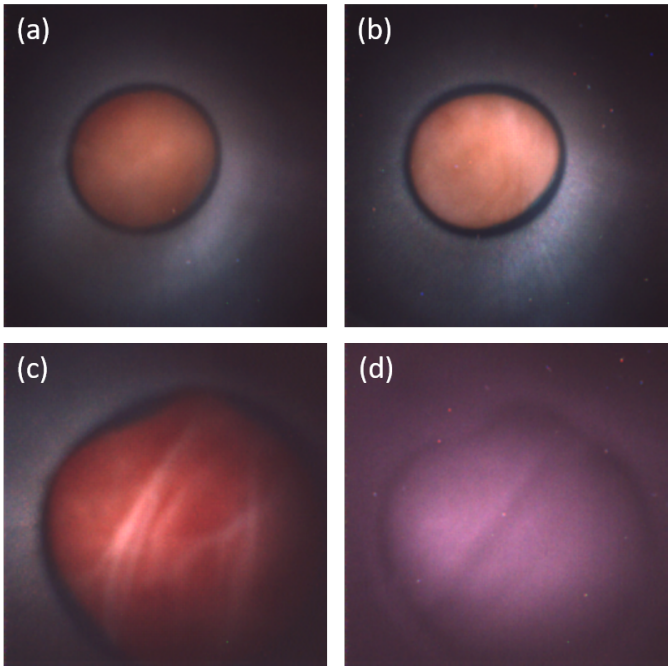

Figure 4.4. *Examples of images acquired in vivo in a porcine model. (a)-(b) Images of the septum. Images captured in the left ventricle under (c) visible and (d) NIR illumination.*

A section of the video with minimal blood intrusion is selected for analysis. During manoeuvring of the catheter and device the blood field often re-enters the flushed catheter. Depending on the positioning of the catheter, the blood field is more or less effectively cleared. The cleared

portions of the video data are used for further analysis. Stills from suitable segments of the video are shown in Figure 4.4. The video captured in the left atrium is used for analysis due to it being the most clear period of footage, and being captured during the periodic occlusion. A region of interest is selected to isolate the relevant pixels in the image, i.e. the pixels where tissue is visible. This ROI can be a square section that is manually selected in the centre of the imaging area, or can be circular and mapped to the boundaries of the guiding catheter in the image. In the latter case, a thresholding and dilating algorithm binarises the image and edge detection techniques detect the boundary of the region of interest. A number of other methods were also investigated, including calculating a centre of mass of the red area in the image (example in Fig. 4.5), using different edge detection techniques, and investigating different colour channels. The red channel is selected in this instance along with the aforementioned thresholding method. This is due to it performing the best on this given dataset. In a pilot study application such as this the data must be evaluated on a case by case basis. The red channel proved to provide the best contrast between the red cardiac tissue compared to the more white guiding catheter as seen in Fig. 4.4 (c). A large number of frames were analysed using the different methods and the fitting quality manually determined to find the optimal method in this case. Note that the optimal method is expected to depend greatly on the video data, and this method worked well in this particular case. A smaller circle is drawn concentrically with the detected edge, allowing for some space between the edge of the catheter and the pixels used for the analysis. A goodness measure was used to discard frames where the circle is not visible due to intrusion of blood into the FOV.

Data processing is performed firstly, to investigate the detectability of hypoxia during the occlusion by means of colour change observed by the camera[1]. This is performed to mimic a reduction in blood perfusion post ablation procedure. Secondly the extraction of physiological parameters is investigated using a PPG technique. The pixels in the ROI are extracted, and the frame is converted into the HSV colour space. This colour space is chosen due to its separate encoding of colour and intensity, and because it better matches human vision and is therefore used to approximate the experience of the clinicians and technicians during the trial.

Clinicians and technicians reported visually observing a colour change on the camera images during the occlusion procedure, however thus far the data analysis has failed to be able to conclusively verify this observation. As part of the data processing, multiple frames were binned and averaged together to reduce noise and movement artefacts. To attempt to track significant changes in colour during the occlusion, time traces of the pixel intensities were investigated at different frame bin sizes. A slight shift in the histograms of the colour values is seen pre and post occlusion and can be found in Figure 8 of Paper **IV**. However, no conclusive trend was seen in the processing. The camera should be more sensitive than the eye, however the experimental conditions and lack of accurate time stamping makes detection more difficult. A simple occlusion experiment is proposed for the future, where a limb is occluded and any resulting colour change tracked, in order to calibrate the analysis method in a more controlled setting.

In order to extract physiological parameter using the video feed in the heart, the PPG signal was analysed using both RGB and HSV colour spaces. The respiratory and heart rates showed better contrast when using HSV. The most effective analysis tool was a Fourier transform on each of the HSV channels. This allowed for the extraction of heart and respiratory rate of the animal at 98 and 12 bpm, respectively, and is shown in Figure 4.6. This plot represents the culmination of the analysis.

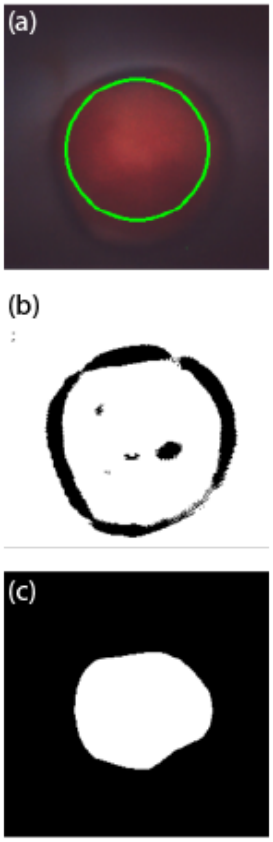

Figure 4.5. *Examples of two different approaches to find the ROI of the images. The detected ROI is overlayed in green on the corresponding RGB image (a). Image (b) shows a binary threshold performed on the red channel of the image to detect the catheter boundary. This edge can be used to construct a ROI. Image (c) shows a binary blob generated from the red area of the image, this blob's centre of mass can be used to construct a ROI.*

[1] The study was conducted remotely due to global health restrictions which placed considerable limitations on the study has a whole. The entire system had to be secured and shipped to the study location along with redundancies. Remote testing and dry runs were conducted. A lack of time stamping and correlation with video frames in part due to the remote nature of the study exacerbates the problem of conclusively showing a visible change. More repeated, and more clearly controlled studies are called for.

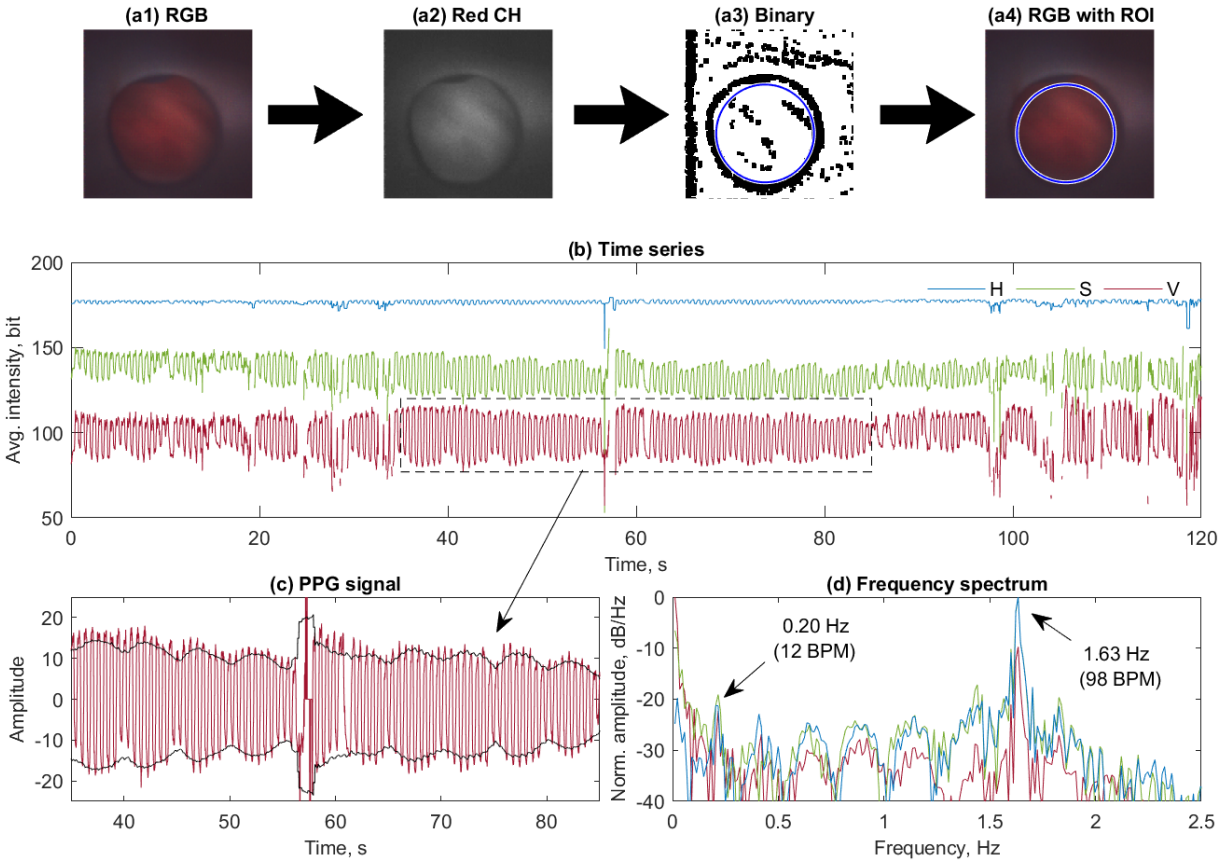

Figure 4.6. *Data analysis of video footage captured inside of the left atrium of the porcine animal. Images (a1)-(a4) show the circle fitting algorithm which detects the relevant tissue pixels, using the outer guiding catheter as a reference. The red channel (a2) is used and image is binarised using an edge-detection algorithm for detecting the boundary of the ROI. The boundary of the ROI is illustrated in the binary image (a3), and this results in the circular ROI (a4). This process is repeated for each frame. Frames where no circle is detected are discarded. Using this data a time series of each of the HSV channels is plotted (b) showing the variations in average intensity of the region in each frame. A section of the time series is selected for analysis (c), and the Fourier transform of each channel over this time segment revels features in frequency space (d). This shows a sharp peak at the heart-rate of the animal at 98 bpm and another peak at 12 bmp, the respiratory rate of the animal.*

4.3 Miniaturised Device for *ex vivo* Lung Imaging

4.3.1 Endoscopy in the Lung

In the lung, access to the peripheral regions is important in particular in the early diagnosis and treatment of lung cancer. Early diagnosis motivates the development of tools that can assess solitary nodules in the peripheral lung [120]. These are often detected using a CT scan, and must then be assessed further. The gold standard assessment remains biopsy followed by histopathological examination. The biopsy can take place percutaneously or endoscopically, and to improve the process, novel tools are being developed to access nodules in the outer branches of the bronchioles through the respiratory tract.

In order to access smaller airways and more peripheral regions, devices for accessing the airways are being miniaturised. In recent times many advances in peripheral lung endoscopy and tracking have also been made. These include the development of "ultrathin" bronchoscopes with 3.00 mm OD and 1.20 mm instrument channels with new navigational and tracking techniques [121]. Electromagnetic tracking can enhance navigation in the periphery [122]. Bronchoscopes are now available with OD of less than 3.00 mm. Many of these very miniature tools are adjunct, due to the small working channel diameter allowing only limited biopsy capability [123]. The devices do, however, allow for investigation of areas that are physically impossible to access through the airways otherwise. These areas would require percutaneous biopsy [124] to access. Developing miniature or "ultrathin" sensorised bronchoscopes and integrating some diagnostic capability in the future, may aid in diagnosis of these hard to reach and hard to biopsy nodules.

Robots such as the Johnson and Johnson Monarch™ and the Intuitive Ion[2] are also being developed to perform robotic assisted bronchoscopy in peripheral lung [125, 126]. These can help with navigation and stabilisation during procedures. Scanning fibre endoscopes are also among novel miniature technologies that have been investigated for pheripheral lung imaging. This technology is able to provide colour images inside 10th generation bronchioles due to the 1.60 mm footprint [17]. Similar to the cardiovascular equivalent of the technology, SFEs have not yet seen commercialisation in bronchoscopy.

[2] The Ion, for example, has a 3.50 mm OD.

In an effort to match the dimensions of the ultra-thin SFE, in this work a micro-camera is integrated into a 1.19 mm OD footprint along with illumination. This footprint is compatible with all commercial bronchoscope instrument channels, and is able to provide a colour image inside of the lung. The fibre illumination allows for multi-spectral and narrow band illumination, techniques which have been used successfully in larger endoscopes to enhance contrast and highlight vasculature, for example [127, 128]. The CMOS package is further miniaturisable, and work now continues on a revised design with plastic optical fibre and enhanced steerability and tracking. In the future, creating a multi-modal sensor, with fluorescence[3], DRS, and polarisation sensitivity are all avenues to be explored.

[3] The OV6948 and NanEye cameras were both tested for fluorescence sensitivity using PPIX in solution, however failed to conclusively detect any fluorescence. The experiment should be repeated and newer sensors from both suppliers included in the study. Any biophotonic imager that is developed should keep fluorescence sensitivity in mind.

4.3.2 Miniature Lung Endoscope

In this exploratory study, a miniature imaging system with OD 1.19 mm was validated in an *ex vivo* lung experiment. This empirical and preliminary *ex vivo* study is not featured in a standalone publication, however introduces interesting learnings and improvements for future integration of micro-cameras into small diameter lung endoscopes. An OV6948 sensor, the smallest commercially available, is used along with

a glass illumination fibre. Details on the integration can be found in Chapter 3 and Figure 3.21.

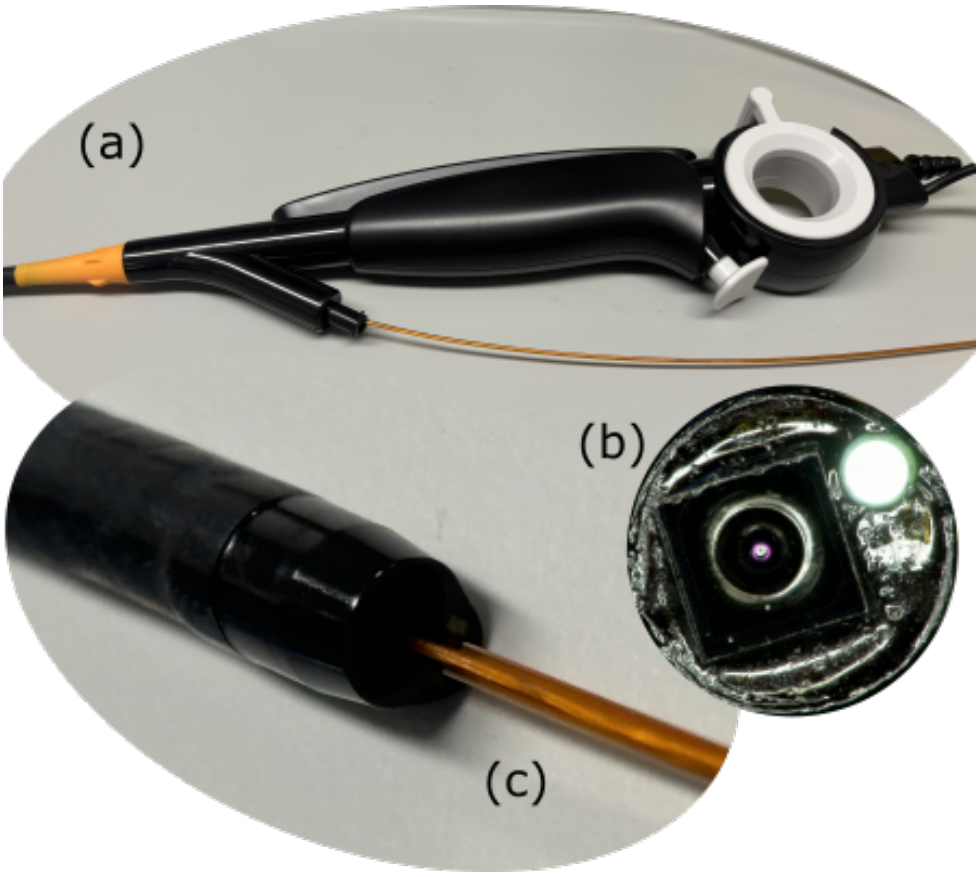

Figure 4.7. *1.19 mm OD system entering (a) and exiting (c) the 2.8 mm instrument channel of the Broncoflex® Vortex bronchoscope. The close up view of the tip of the device is shown in (b).*

The device inserted into a commercial bronchopscope is seen in Figure 4.7, where the small diameter system is inserted in through the instrument channel and emerges at the tip of the scope. To conduct the experiment, a sheep lung was obtained intact and fresh from the butcher. PVC tubing for inflation was secured in the trachea, and connected to a foot pump. A seal was maintained by physically constricting the airway around the tubing. Using the foot pump the lung was reinflated continuously, mimicking breathing. This expanded the airways and lobes of the lung allowing for devices to be inserted and navigated deeper into the lung. A commercially available bronchoscope, Broncoflex® Vortex (The Surgical Company, Amersfoort, Netherlands) was inserted into the trachea next to the intubation tube and navigated through the bronchi. The bronchoscope has an OD of 5.60 mm and a working channel with ID of 2.80 mm. Images from the scope are provided using a on-the-tip camera with FOV 87.5°. Once in position, the catheter camera probe could be inserted through the working channel of the bronchoscope. Due to its small size it was able to navigate further into the bronchi of the animal lung. This is seen clearly using the bronchoscope camera in the central column of Figure 4.8 where the miniature camera system is seen inserted further into small bronchi. Some images from the sensor are also seen in the same figure, showing branching paths of bronchi and bronchial wall. Not all images captured were of good quality, due to obstruction of the FOV or due to deterioration of the image quality over time as discussed in Chapter 2. The glass illumination fibre breaking due to strain also cre-

ated a complete reliance on the bronchoscope illumination. The sensor required wiping and reinsertion as liquid from inside of the lung obscured the lens, as in Fig. 4.9. The need for a cleaning strategy is clear, and an integrated flush channel as in the cardiovascular work may prove an important solution. Saline, or perhaps an air stream may then aid in cleaning the tool without requiring extraction.

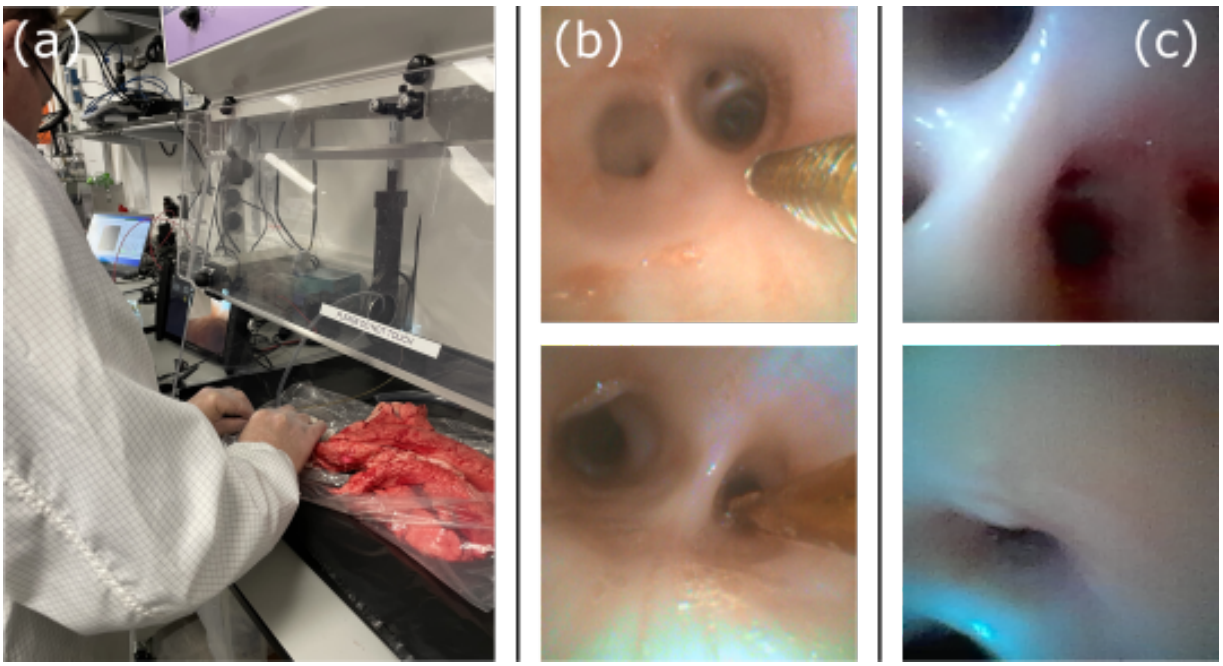

Figure 4.8. *Lung re-inflation performed in the lab with the ex vivo animal lung tissue seen on the leftmost image (a). The central column (b) shows images captured using the bronchoscope used in the procedure with the 1.19 mm catheter camera system protruding from the working channel. The rightmost column (c) shows images captured using the OVM6948 sensor integrated at the tip of the 1.19 mm diameter probe.*

Due to the harsh bending requirements and forces exerted on the tubing when pushed through the working channel of the bronchoscope, the glass fibre proved inadequate as an illumination fibre. It broke quickly towards the tip of the device resulting in light leaking through the break and not reaching the front of the device. Additionally, the low numerical aperture (NA) of the glass fibre made illumination difficult. The OVM6948 sensor has good low light sensitivity, and the bronchoscope illumination sufficed for the capture of test images as shown in Figure 4.8. However, for navigation deeper into the lung in future experiments, a new solution of polymer fibre is proposed. The polymer fibre has a much greater bend tolerance and can be obtained with a higher NA even at small diameters. Additionally, it may be possible to form lenses directly at the tip of these polymer fibres using a two-photon polymerisation process in order to modify the beam profile. This is an idea that is currently being explored. A future iteration of this device should also include steerability and potentially electromagnetic tracking in the tip. Steer-ability could be achieved using a common pull wire technique. This would allow for more autonomous navigation into the peripheral lung.

4.4 Discussion and Conclusion

Micro-cameras have demonstrated outstanding potential to be integrated into small diameter systems that can image correspondingly small diameter lumen in the body. The sensors have reached dimensions which allow them to compete with other technologies such as IVUS, OCT and SFE,

in both the cardiovascular and pulmonary space. The cameras are integrated into miniature endoscopes as presented in this work. The small footprint also enables other small footprint tools to be sensorised with a camera. The main output of the micro camera is an image, either monochrome or in colour, which is used in navigation and guidance at location *in vivo*. Sensing and diagnostics can also be performed using the image data.

In cardiovascular imaging, the micro camera's footprint allows it to be integrated into 3-6 Fr (1-2 mm diameter) catheter devices, which can be navigated to small blood vessels through a slightly larger guiding catheter. The footprint here is dependent primarily on the need for an integrated flush channel which can aid in clearing the field of view of the camera. The size of the camera is secondary, since sensors of 0.650 times 0.650 mm are available. The camera allows for imaging within the heart and vessels, a technique which can be useful for the verification of accurate device placement from valves, to stents, to pacemakers. Theoretically a camera can be integrated both forward facing and side facing, allowing for visualisation of sides of vessels, or heart walls and devices placed in front of the sensor. In this application we also demonstrate the diagnostic capability of the camera. Beyond visualisation and vision, the camera is able to collect physiological information, such as heart rate and respiratory rate from inside of the heart, in real time. Image processing also allows for highlighting of features such as blood vessels in the heart wall as seen in Figure 2.15. This may allow for the detection and assessment of micro-vasculature in plaques, for example, with the modification of the lens in front of the sensor to allow for high spatial resolution. In the future it is hoped to successfully detect tissue oxygenation *in vivo* with the camera to verify ablation using slight tissue oxygenation changes, and to measure tissue oxygen content *in situ*.

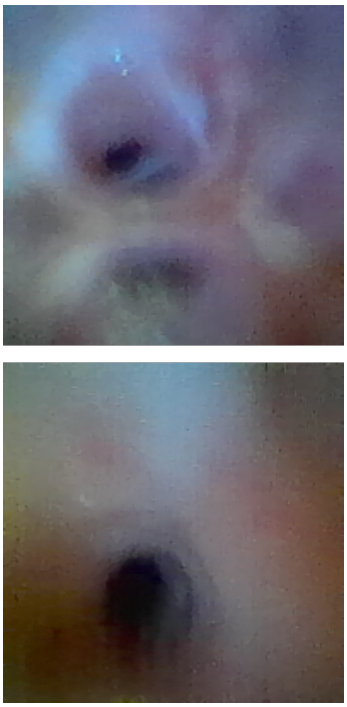

Figure 4.9. *Some additional images captured during the ex vivo lung experiments using the small diameter system showing decrease in image quality after secretions from the inside of the lung obscured the sensor lens.*

For the lung application, the footprint of the manufactured device was designed to be passed through the working channel of a traditional bronchoscope making it compatible with existing technologies. Whereas in the cardiovascular environment the guiding catheter solves the navigation problem. A navigation challenge has arisen in controlling the small diameter probe better in the lung application, since the goal is to navigate beyond the reach of current endoscopes. Bending was less of a problem in the cardiovascular application, since bend radii never exceeded those of the glass fibres. In the lung, manoeuvring with the articulating tip of the bronchoscope, and pushing the fibre through the instrument channel the glass fibre proved less effective. As a result, POF fibre should be considered for all applications where bend-ability is a concern. However, in the lung, overall, the integration of CMOS cameras is more straightforward, since clearing the blood field is not required. Cleaning is an issue, however, and the system may still benefit by the inclusion of a flush channel. The imaging system can be integrated into small footprints, with 1.19 mm demonstrated. Smaller dimensions are likely also possible and bounded mostly by sensor size and ability to delivery illumination. Steerability and tracking are also likely to be a big factor in the development of smaller and smaller imaging catheters in the pulmonary application space.

Micro-cameras have demonstrated the ability to image intravascularly, despite the difficulties associated with imaging in this space. The technique must now be developed further to compete with, or supplement established technologies such as IVUS and OCT. Cost and scalability advantages of CMOS may play an important role, as will the ability to produce a traditional camera image *in situ*. In the lung, feasibility of a ultra-thin CMOS bronchoscope is demonstrated, providing colour images in an *ex vivo* animal model. As mentioned previously in this thesis there has also been a push towards disposable devices in recent times, especially

in the respiratory area [35, 36], and the cost factor may come into play especially in this regard. The rapid development of CMOS technology is promising for the development of CIS technologies in medical applications. The development of biophotonic specific image sensors, such as the one developed as part of the overarching IPIC2 project funding this thesis, is soon to follow. Such sensors will be optimised for sensitivity to detect fluorescence and to enable low light imaging, and feature high frame-rate readout techniques. This thesis looks optimistically into the future and sees CIS growing in number in the miniature endoscope space.

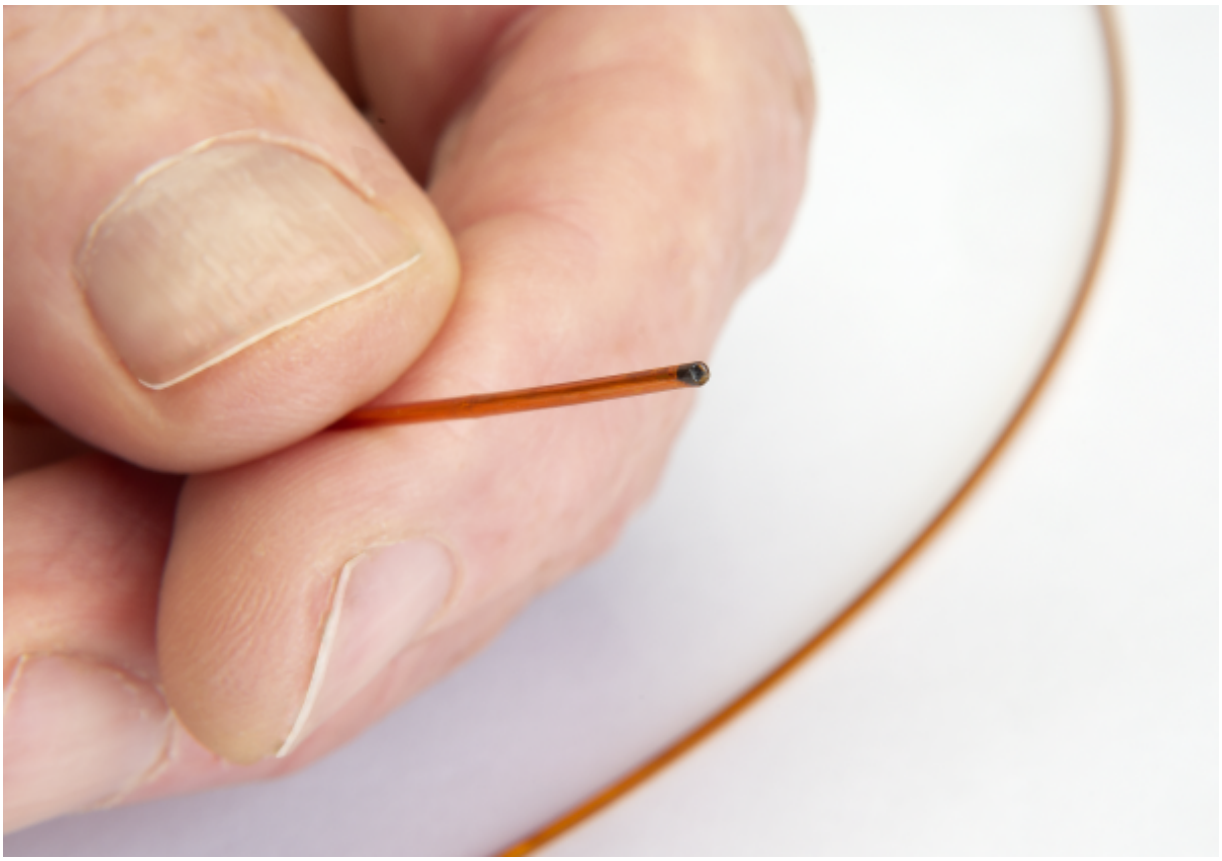

Figure 4.10. *Image of the previously described bronchoscope system held in hand.*

Chapter 5

Micro-cameras in Breast Conserving Surgery

*This Chapter primarily relates to Paper **I** and Paper **II** where micro-camera technology has been applied as a visualisation tool in breast conserving surgery of ductal carcinoma in situ. The work presented in the publications is summarised, and some background and additional work discussed. Paper **I** presents the system used to image tissue, and to overcome problems with specular reflections. Paper **II** presents the results of clinical measurements on ex vivo breast cancer samples. The two publications should be referred to for further and more in depth discussion of topics not covered in this Chapter.*

5.1 Research Objective

The objective of the work was to intra-surgically detect micro-calcifications up to 2 mm in the resection margin and on the lumpectomy. To do this a multi-spectral diffuse optical imaging technique for surgical guidance is proposed, and used to detect micro-calcifications. These areas of clinical interest can guide diagnostic tools such as diffuse reflectance spectroscopy (DRS) systems and provide periprocedural information on the success of a surgical resection, and in turn reduce revision rate and improve patient outcome.

5.2 Micro-calcifications and DCIS

Breast cancer is a leading cause of cancer mortality in women and is showing an increasing trend in disease burden [129, 130]. Breast conserving surgery, the primary treatment path [131], aims to remove the tumour with an adequate margin while removing the minimum amount of tissue[1].

Ductal carcinoma *in situ* (DCIS) is a precursor lesion of an invasive breast cancer, where malignant cells are still confined to the ducts and lobules of breast [133], and accounts for 20-30% of reported breast cancers [134, 135]. DCIS lesions are often non-palpable, presenting in scattered groups, making it difficult to distinguish them from surrounding tissue. Guidelines dictate that tumour resection margins in DCIS are small, with guidelines varying from no tumour cells on the surface, to none within 2 mm [136]. A margin of 2 mm is now thought to minimise the recurrence risk in DCIS treated with breast conserving excision and radiotherapy [137]. This number forms a requirement for system sensitivity, with any novel detection method needing to have sensitivity within this margin. A

Figure 5.1. *Slice of lumpectomy specimen from breast conserving surgery.*

[1] Beyond the oncological considerations, cosmetics also play an important role in breast conserving surgery [132].

tumour-positive resection margin is a major factor for recurrence and may require a revision [138–140]. Histopatholigical assessment of the margins remains the gold standard, with tools to assist the lengthy process being developed [141]. This histopathological step can not be performed during a procedure, and a positive margin therefore means return of the patient to the operating theatre and a significant burden on both patient and healthcare system. There is a need for intra-operative imaging solutions in breast cancer surgery both to localise the lesion and to help determine the resection margins [26], since effective surgical resection of difficult to distinguish lesions requires image guidance [142].

Micro-calcifications are deposits of calcium oxalate or calcium phosphate that form in the lobules and ducts of the breast. Micro-calcifications are often present in the mammography in DCIS cases with only a small number of patients, as low as 7% in some studies, presenting with a mammographic mass that is not associated with micro-calcifications [142–144]. These micro-calcifications can be an indicator of non palpable lesions [145], however not all micro-calcifications are associated with malignancy. Composition, size, morphology, and distribution all play a role in differentiation of calcifications. The Breast Imaging Reporting and Data System (BI-RADS) considers both presence and distribution of micro-calcifications for this reason [146]. This visualisation of micro-calcification for diagnostic purposes is currently performed exclusively using x-ray mammographic imaging in clinical practice (Fig. 5.2). Micro-calcifications may prove to be a useful marker during intra-operative imaging as well. In this thesis, the first imaging system which is able to detect micro-calcifications in tissue mid procedure is described. The micro-camera can provide a real-time, magnified perspective of the surgical field. Assessment of the margins intra-operatively allows for excision of additional tissue during the procedure, if required. This may reduce the burden on the patient and the healthcare system, by reducing the number of revisions.

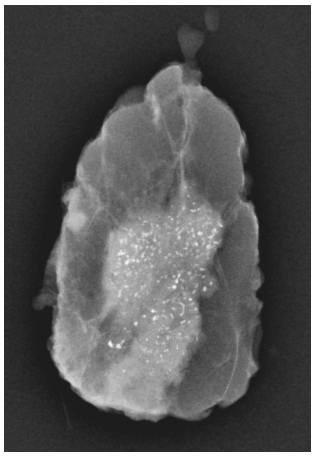

Figure 5.2. *Small clustered micro-calcifications present on the x-ray of a lumpectomy slice.*

5.3 Handheld Tissue Visualisation System

The micro-camera was selected as a tool due to its ability to rapidly image an area, which can help identify areas of interest where micro-calcifications are present. Such a system may be combined with other measurement modalities in the future to target areas of clinical interest. Techniques such as DRS point measurements [24, 147, 148], Raman spectroscopy [149], and hyper-spectral imaging [23, 150], have, for example, demonstrated promise in differentiating malignant and healthy breast tissue including in the detection of micro-calcification. These techniques could be easily incorporated with a miniature imaging system in the future.

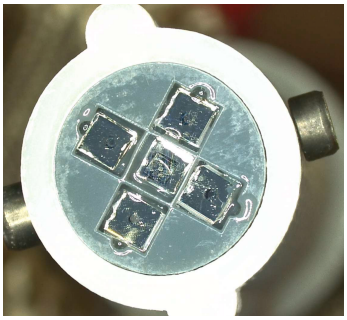

Figure 5.3. *Close up of polarisers mounted in the tip of the probe.*

The system is designed to be handheld, in a pen-like probe. The camera is mounted distally and illumination fibres allow for delivery of multi-spectral illumination, as previously discussed in Chapter 3 of this thesis. The dimensional requirements for this iteration of the study were such that system had to fit comfortably into a hand, in a 12 mm maximum OD. The system is able to be further miniaturised with the ideal footprint for a handheld tool of 8 mm OD determined after discussion with clinical collaborators. The camera and fibres can of course be integrated into much smaller footprints, as demonstrated elsewhere in this thesis, and therefore allow integration with other tools and technologies. The system underwent a number of iterations throughout the course of the study, with the first handheld probes employing no specular reflection reducing techniques, and initial light sources requiring the manual switching of optical fibres over the course of the experiment. The sec-

ond iteration of the system is described in Paper **I**. The handheld probe received a small redesign to incorporate specular reflection techniques by allowing the fibres to be individually addressed. A second handheld probe with cross polariser integration was also constructed. The light source was also updated to the system described in Paper **VI**. The system was updated a third time, with a software update, to allow for the rapid acquisition of images with varying illumination intensities. This enabled HDR imaging of the tissue, which was explored to alleviate the non-uniformity of pixel intensity across the sensor. This is a function of both the lens and the Gaussian-like non-uniform, illumination pattern, as previously discussed.

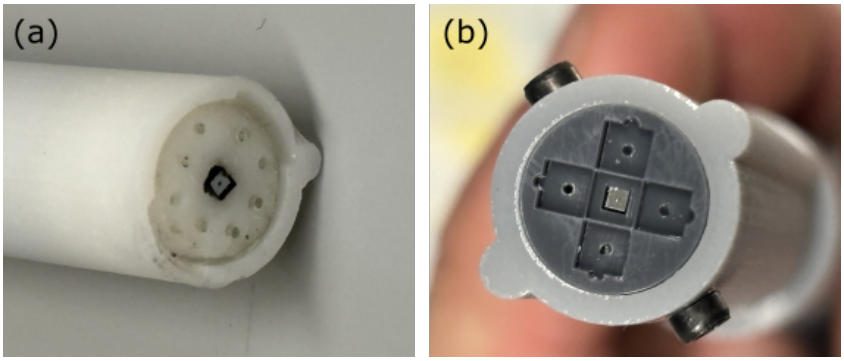

Figure 5.4. *Iterations of the handheld system. In (a) the first probe design is shown, with no specular reflection reduction and 8 illumination fibres. In (b) the probe has been redesigned to be more robust, and to include polariser mounts at the tip. The number of fibres was reduced from 8 to 4.*

A micro-camera and NIR illumination are able to detect features at a depth of up to 2 mm, as validated on tissue mimicking phantoms (Fig. 5.5). In order to mimic micro-calcifications, hydroxyapatite particles are embedded in a tissue mimicking phantom. The phantom is multilayered, and thin layers can be added on top of the base layer to mimic depth. Figure 5.6 shows the relationship between depth and illumination wavelength using a multi-layer phantom using a cross-polarised system. The system is used in Paper **II** to image excised breast tissue in order to detect micro-calcifications.

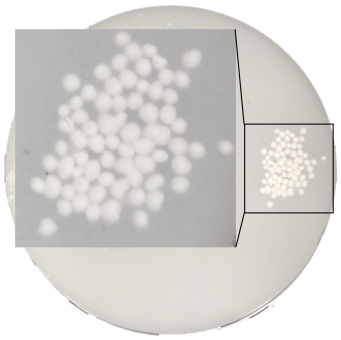

Figure 5.5. *Phantom with hydroxyapatite features embedded.*

5.4 Specular Reflections

Specular reflections were encountered early on as a potential hurdle in identifying micro-calcifications in tissue images, as they obscured much of the underlying information, and have a lot of similarity with micro-calcifications. Two methods were investigated to overcome tissue specular reflections in small form factor micro-camera systems.

5.4.1 Multi-flash

The multi-flash technique uses multiple (n) illumination positions which illuminate the scene sequentially from different angles. The camera captures an image for each of the illumination positions, k. In this case four illumination fibres concentrically arranged around the central sensor are used to illuminate the scene, i.e. $n = 4$. As long as the positional difference causes a shift in the direct reflections from the scene the specular reflections can be detected algorithmically and filtered out using the Feris et al. algorithm [151, 152]. The intensity gradient, G_k, of each image,

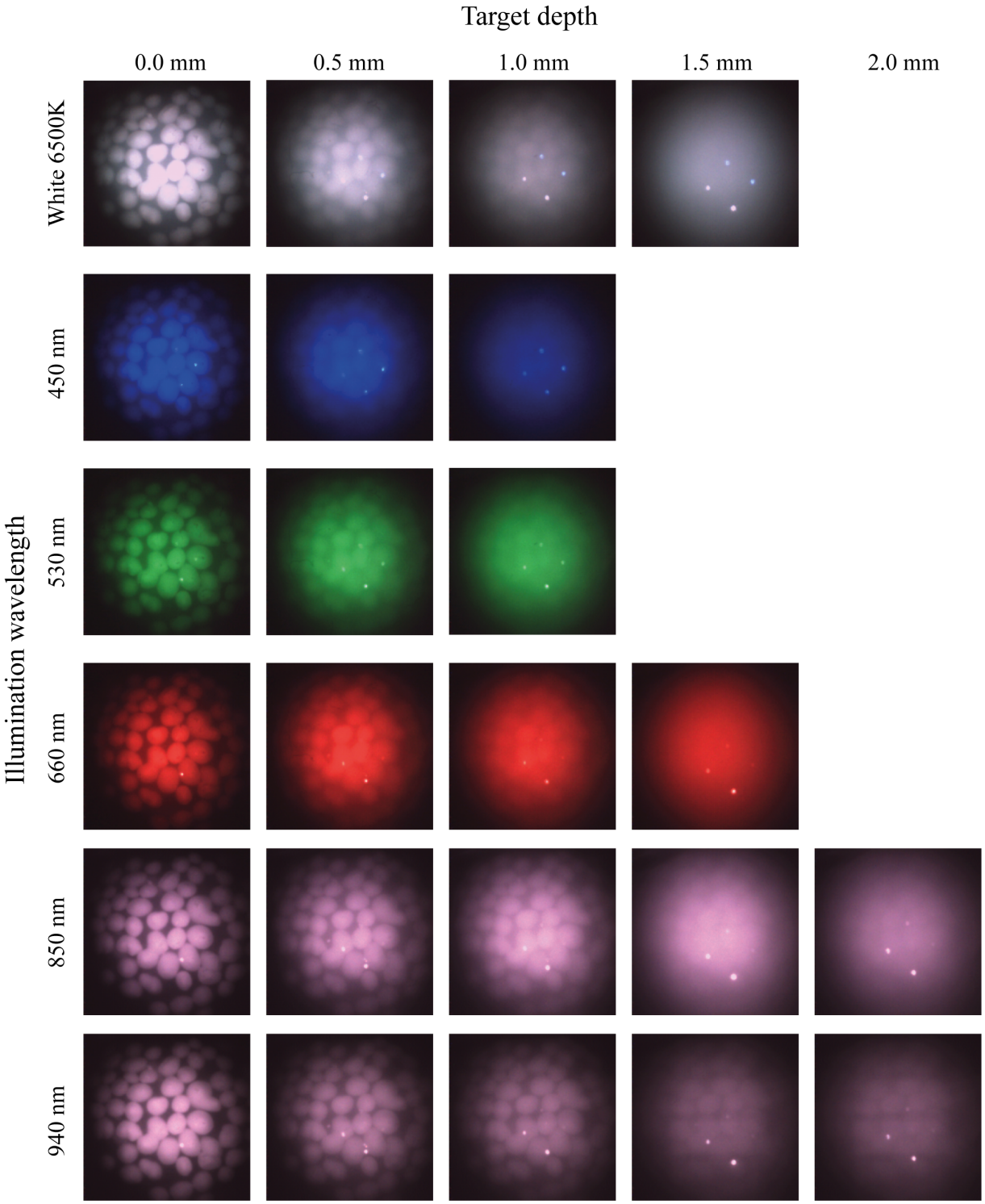

Figure 5.6. *Phantom depth measurements hydroxyapatite features using the cross-polarised system. Similar verification was performed for the multi-flash and is discussed more extensively in Paper* ***I****.*

I_k, is calculated.

$$G_k = \nabla I_k \tag{5.1}$$

The median of these gradients is calculated, and used to minimise $|\nabla I - G_{median}|$ when reconstructing the image I. A Poisson based gradient image reconstruction results in the specular reflection reduced image [153–155].

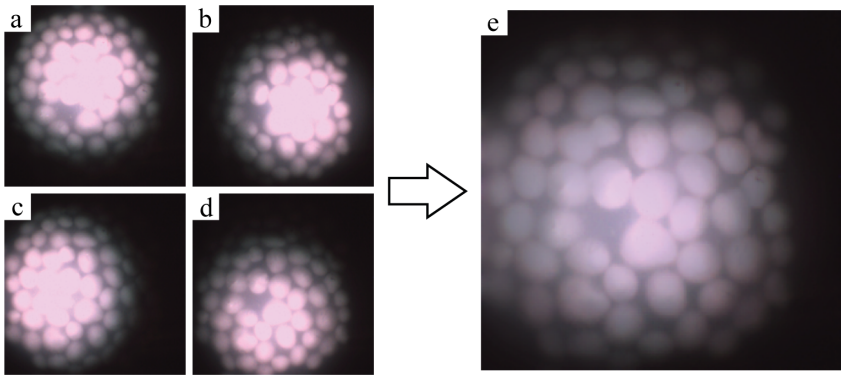

Figure 5.7. *Removal of specular reflections on phantom using multi-flash. Four images (a) - (d) of the same locations but with shifted illumination sources are captured. The post-processed specular reflection reduced image is shown in (e).*

In practice the switching of illumination sources is performed using an optical switch system (Leoni mol 1 × 4) which is intermediary to the light source. The system is capable of acquiring multi-flash images within 0.20 s. Fig. 5.7 shows the technique working on a tissue mimicking phantom under white light illumination. The bright specular reflections in images (a) - (d) obscure the boundaries of the underlying features, which are revealed in image (e) after processing. The technique has also been validated on tissue with an example seen in Fig. 5.8. However due to the requirement to hold the probe still for an, albeit short (less than a second), period of time, the technique was discarded in favour of cross-polarisation.

5.4.2 Cross-polarisation

As discussed in Chapter 2, direct reflections are polarisation maintaining. As a result, using crossed polarisers across source and detector can filter out these direct reflections. Using this method, a cross-polarised probe can effectively filter out specular reflections in breast tissue. This technique works due to the fundamental properties of light and reflection, and requires no post-processing. Being a real-time technique, it works when scanning the probe across tissue. Fig. 5.8 shows the removal of specular reflections on breast tissue using the multi-flash and cross-polarised techniques.

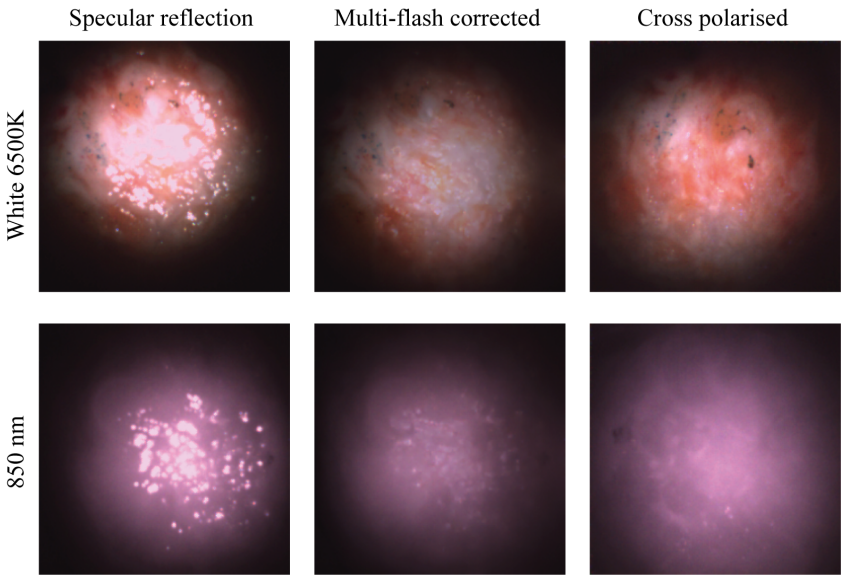

Figure 5.8. *Removal of specular reflections on excised human breast tissue, a comparison of the multi-flash and cross-polarised techniques. The first column shows specular reflections on breast tissue when illuminated using a single source. The central column shows the output of the multi-flash technique. The rightmost column shows the cross polarised probe reducing specular reflections. Locations are imaged using white light and NIR 850 nm illumination. No micro-calcifications are present in the images selected for this comparison.*

The cross polarised system allows for imaging of the tissue with minimal specular reflections, with the added benefit that the scene is more uniformly illuminated since all four illumination fibres are active at the same time. However, due to practical limitations of the polarisers, the specular reflection reduction using cross-polarisation is not perfect and residual reflections are sometimes still seen (Fig. 5.9). These are wavelength-dependent and particularly prominent in the blue wavelength range, due to the performance of the polarisers seen in Fig. 5.10. The contrast ratio of the polarisers used reduces by a factor of six from 700 nm to 450 nm. This explains the prevalence of blue specular reflections in images. There is also an angular dependence which affects the performance of the polarisers.

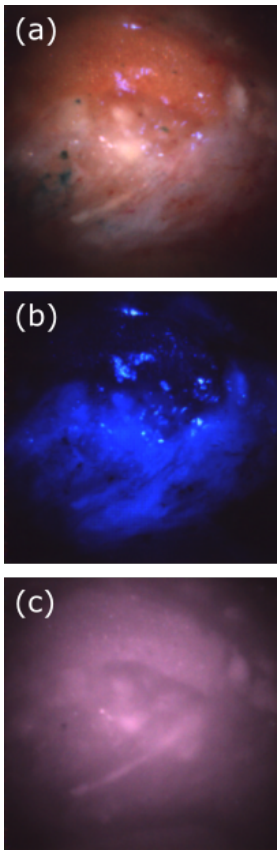

Figure 5.9. *Residual specular reflections in white light illumination (a), the blue (b), and the 850 nm NIR (c) due to polariser performance*

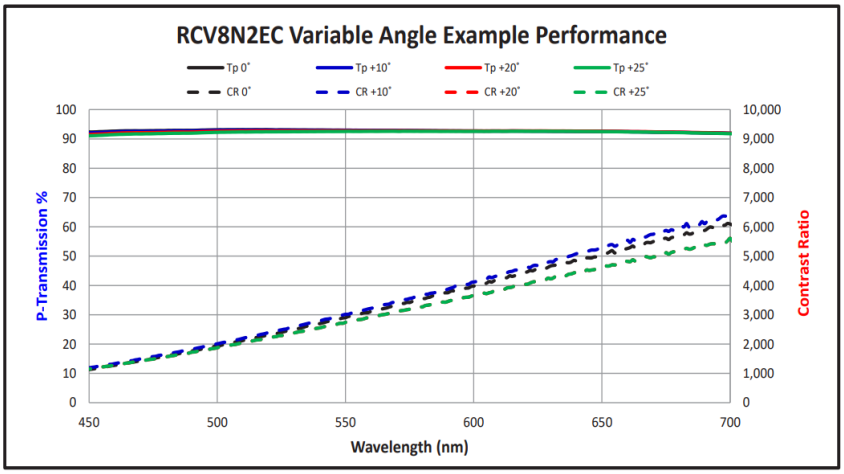

Figure 5.10. *Spectral response in the visible spectrum of the Moxtek RCV8N2EC polarisers used, reproduced from manufacturer data-sheet [156]. Solid lines show transmission, the dotted lines show contrast ratio.*

5.5 Measurement Protocol

Data was acquired in a collaborative study with the Netherlands Cancer Institute (NKI). This study was approved by the Institutional Review Board (IRB) of the NKI-AVL and registered with number IRBm20-086. Data was acquired in concordance with the IRB guidelines of the NKI-AVL, in accordance with Dutch guidelines and legislation, to ensure compliance with Article 82 of the European Medical Device Regulation [157]. Over the course of the study, slices from over 25 patients were imaged using the different systems. Acquisition of data followed the following protocol, for which a time-frame of approximately 40 minutes is allotted. This time frame is dictated by the pathologists in charge of the patient samples, and can vary. It may also vary depending on the time of day of the measurement. Good time management is achieved through a robust and well rehearsed measurement protocol, as well as automation in data acquisition[2]. To be included in the study patients had to be over 18 years of age and present micro-calcifications in a pre-operative mammography. Post operation the lumpectomy slices were screened for presence of micro-calcifications using x-ray in order to be selected. The workflow is conducted as follows.

(i) Identify potential patient on OR schedule, and inform pathology of intent to measure sample.

(ii) Receive a call from pathology informing of sample readiness.

(iii) Collect the sliced sample and bring to radiology for x-ray.

(iv) Return samples to pathology and select relevant slices containing micro-calcifications.

(v) Transport slices to the OR *ex vivo* sample study room.

(vi) Conduct measurements as per protocol.

(vii) Return the samples to pathology.

[2] The process requires coordination and support from various departments within the Netherlands Cancer Institute, for which we are very grateful.

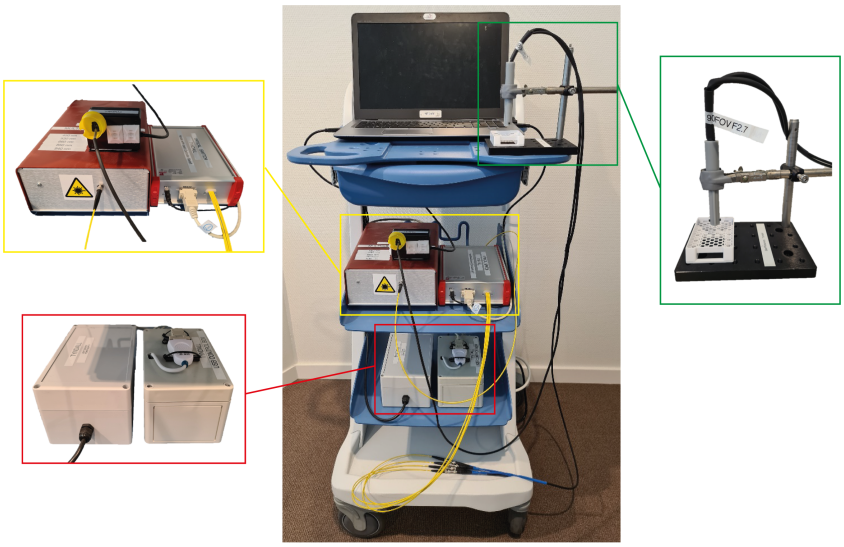

Figure 5.11. *Entire clinical trolley with light source and optical switch (yellow), power supply and data acquisition box (red), and camera probe with sample holder (green).*

The excised tumour is sliced during the pathology process. The slices themselves vary in area, depending on the size of the excised tissue. Initially the slice thickness was not controlled. Later, the pathologists were asked to slice to 4 mm in thickness, however slice thickness was still inconsistent, and accurate thickness control should be considered in future iterations of the study. The x-ray images show micro-calcifications, and are used to select slices for the study as well as for validation of measurement locations. See examples of the slices and x-rays in Fig. 5.12. The selected samples are transported to the study room, where the measurements are conducted as per the data acquisition protocol below.

(i) Place the sample on to the sample dish, and place the dish under the point projection mapping system (PPMS) [158].

(ii) Based on the x-ray data, morph the x-ray to fit the slice, and select areas of interest containing micro-calcifications, as well as negative controls.

(iii) Capture a colour image using the PPMS, with and without the projected light dots.

(iv) Place the handheld micro-camera tissue visualisation system above the projected points at a fixed distance of 8 mm.

(v) Acquire multi-spectral data of the selected area, using the automated illumination and image acquisition systems.

The data acquisition protocol ensures that all required data is captured to allow for the co-location and validation of measurement sites. Note that it is advantageous to perform these measurements in darkness to ensure there is precise control of illumination[3]. In order to track measurement locations, and map them to the x-ray images, a point projection mapping system [158] is used. This mapping system can perform an affine transformation on the x-ray image to overlay it with the sample placed under its image sensor. Points of interest are selected by the user and light dots are projected onto the sample. The probe is then placed over the projected light dot. The location imaged on the slice can subsequently be co-located with the x-ray image as discussed in the next section. Due to hospital workflow, the x-rays are stored as a DICOM file which are scrubbed of patient data, converted to bitmap format, and the dimensional parameters extracted for further processing. The images captured using the other systems are free from patient data, with each patient assigned a number depending on their position in the measurement order, and the tissue slices numbered by the pathologist. The measurement protocol, data handling and data analysis had to be performed in such a way as to ensure that the rights, safety, dignity and well-being of subjects is protected [157].

[3] The micro-cameras used has poor low light sensitivity, requiring an external light source in order to image successfully. Ambient light was found to have little to no impact on the acquired images. Nevertheless performing the measurement in the dark eliminated a potential variable.

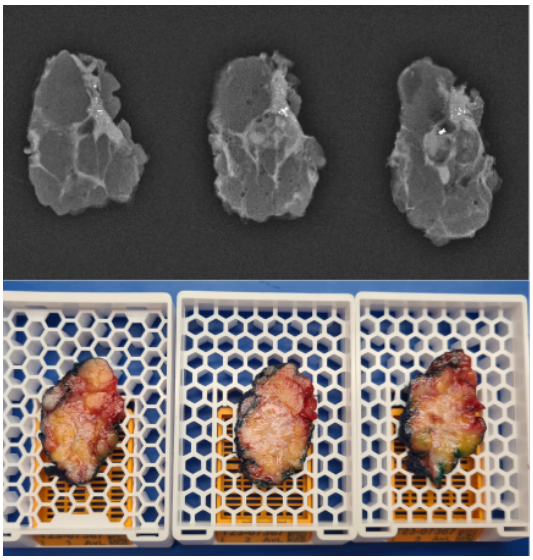

Figure 5.12. *Slices of tissue with the x-ray on top and the slices as measured on the bottom. The slice deformation and morphological difference due to compression during the x-ray is evident.*

Figure 5.13. *Patient 14 Slice 6 shows micro-calcifications at the boundary of the image after co-location. Calcifications shifted to the edge of the image due to sub-optimal probe placement and morphology changes.*

Out of the 25 total patients, a final cohort of 12 patients were measured between March 2022 and June 2023. This cohort used the most up to date cross-polarised system, and is used for analysis in Paper **II**. Only patients measured using this most recent iteration of the system are included to ensure uniform experimental conditions.

5.6 Clinical Validation

To validate the detection of micro-calcifications using the micro-camera tissue visualisation system, the imaged locations are co-located with the x-ray images. A multi-part co-location had to be employed due to constraints in the data acquisition protocol. The co-location maps x-ray imaged locations of the micro-calcifications to the locations imaged using the micro-camera system. The workflow of this co-location is shown in Fig. 5.15.

Since the samples are x-rayed using the same system used for mammographies, the process compresses the tissue slices resulting in slight deformation. The aforementioned PPMS corrects for in-plane deformations using an affine transformation, and can map the x-ray to the RGB image of the slice. However the micro-camera image must be co-located with the x-ray also, and in this case a 3-dimensional deformation must be taken into account. Manual placement of the handheld probe above the light spot projected on the tissue resulted in slight positional variations from location to location. As a result the projected light dot does not always correspond exactly with the measurement location. The short working distance of the probe means that even a small shift in the angular position of the probe can mean the desired location is missed (e.g. Fig. 5.13). The probe orientation also changed from measurement to measurement, and so a rotation correction must be employed. The uneven tissue surface, including roll off at the edges of the tissue, created additional morphological variations. The challenge therefore is to map the 2-dimensional x-ray image to the 2-dimensional projection of 3-dimensional tissue image that is projected onto the image sensor. In order to co-locate two images, matching features must be manually selected on both images. Micro-calcifications, even if visible, should not

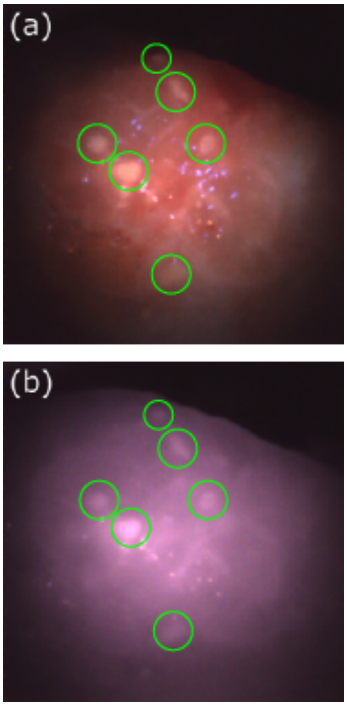

Figure 5.14. *Patient 18 Slice 12 in (a) standard RGB and (b) 850 nm NIR illumination shows excellent micro-calcification features both in the VIS and NIR indicated by green circles. Calcifications are present close to the surface.*

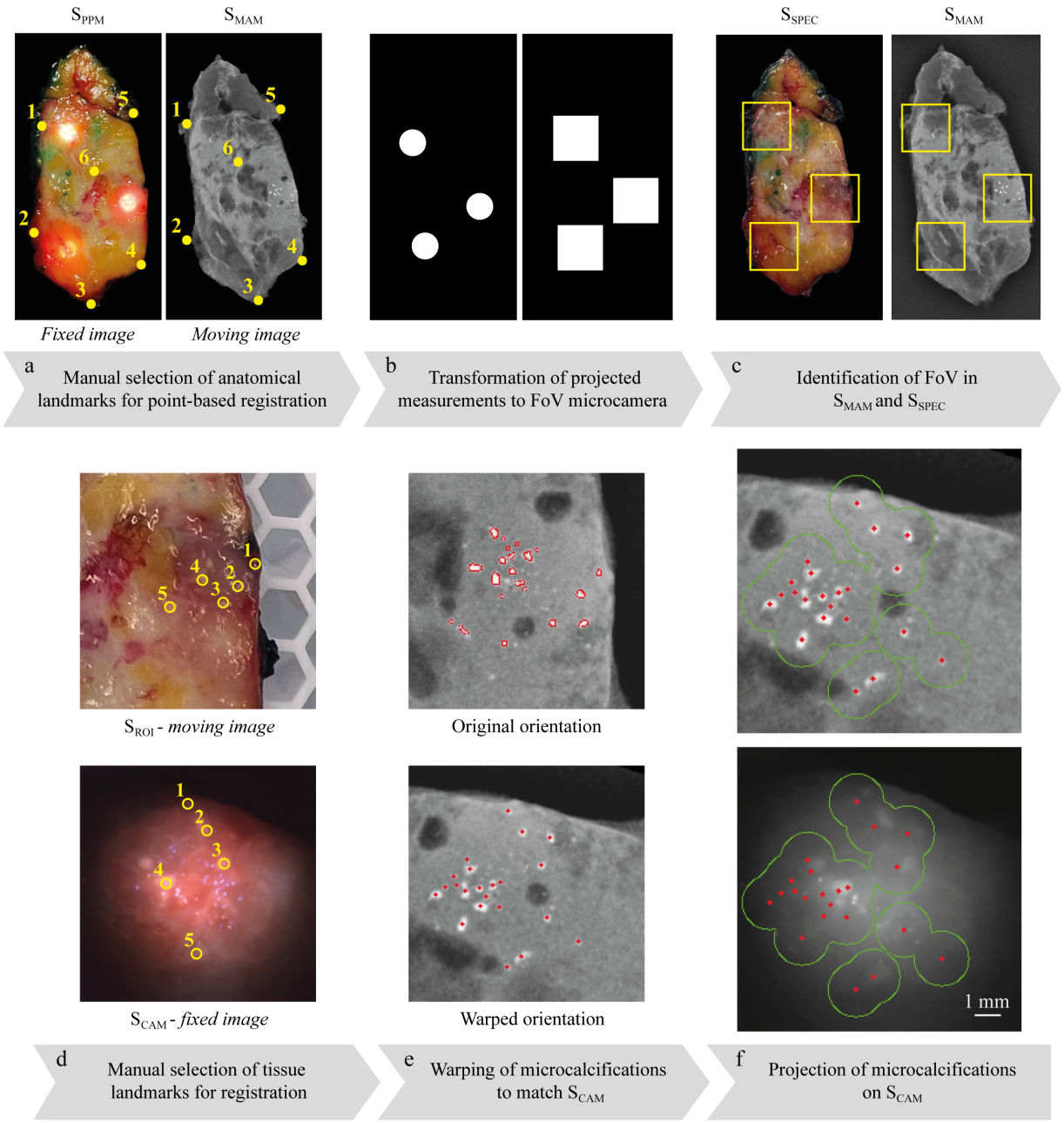

Figure 5.15. *Workflow of the co-registration method for identification of micro-calcifications in the S_{CAM} images. (a) The point-based image registration is performed by manually selecting corresponding anatomical landmarks in S_{PPM} and S_{MAM}. (b) Binary image of the projected measurement locations were transformed to squares to match the field of view (FOV) of the optical probe. (c) The measurement locations are overlaid on the S_{PPM} and S_{MAM}, generating the exact counterpart of the S_{CAM} image. (d) S_{ROI} and S_{CAM} co-located based on landmarks on both images. (e) Based on the co-location in step 4, S_{MAM} is warped to match S_{CAM}, thereby providing a new orientation of the micro-calcifications. (f) Lastly, the micro-calcifications from S_{MAM} are projected on S_{CAM} with a circle representing an error of 1mm in all directions.*

be selected as matching features to not bias the co-location. For all of the aforementioned reasons a homo-graphic perspective transform is employed to achieve the co-location of the micro-camera image.

The simplest method of feature selection is to select surface features on the colour images and use these to transform or warp one of the two images. Point selection is performed using a custom built Python script, which presents both images to the clinician side-by-side, and requires the user to manually select corresponding point features in each image. In general, the more points are selected the better the co-location will be, with distribution of the points across the image also having an impact. It was found that between 15-20 points sufficed in most cases for a good co-location. Surface features such as colour variations due to staining, fat and other tissue features, and edges of the slice, proved to be useful markers for co-location (Fig. 5.16).

The objective is to co-locate the x-ray, with the micro-camera image. First the x-ray is co-located with a high quality camera image of the slice by selecting points on both images. This step overlays the x-ray and the high quality image of the slice and is performed using the PPMS. This high quality camera image is in turn co-located with the colour image captured using the micro-camera. The precise location captured using the micro-camera on the slice is now known. Since the colour micro-camera image and NIR micro-camera image are co-incident in space, the NIR image can be co-located with the x-ray ground truth. Since the micro-camera image is the image that is presented to the clinician, it is used as the static image. The x-ray location is therefore the moving image, and is warped to overlay with the micro-camera image. Now, by performing simple binary thresholding the locations of the micro-calcification captured by the x-ray can be superimposed on the micro-camera image. Similarly the contours can be extracted and the shapes of the calcifications superimposed on the micro-camera image[4].

Not all micro-calcifications are detected using the micro-camera. Since relative to slice thickness the x-ray imaging depth is effectively infinite, it captures all micro-calcifications present in the slice. This is not the case for VIS and NIR imaging techniques, the depth of which is limited in this case to approximately 2 mm or less. This is a partial explanation for non detection of micro-calcifications - they may simply be buried too deep in the tissue. This was the motivation for attempting to control slice thickness. The slice thickness was not fully under experimental control, and while later requests were made to keep slice thickness to 4 mm, it still varied from sample to sample. A slice thickness of 4 mm would allow for imaging of both sides of the tissue and a better estimation of how many micro-calcifications are detected using the system. However, this was not feasible for this iteration of the study and will have be conducted in a follow on. Additionally, when features are at greater depth we expect some blurring as the diffuse light scatters in the length of tissue it traverses. As such, multiple small calcifications that are distinct in the x-ray may blend into a larger calcification in the micro-camera image. Finally, the imaging method may simply be missing the contrast that allows for detection with confidence. This is especially apparent at the boundaries of the images, where the illumination and distortion problems of the senors have a greater effect.

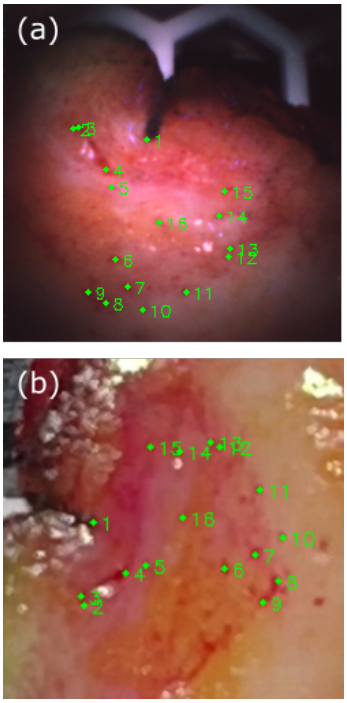

Figure 5.16. *Examples of points selected for co-location in (a) colour micro-camera image, and (b) cropped colour PPMS image.*

[4] A number of different methods were explored to achieve this warping, some performing better than others. A random sampling "RANSAC" and least squares method proved most successful. The RANSAC method is selected for most of the points. Other methods tested where a least medians method and PROSAC.

5.7 Feature Detection

While the detection of calcifications has been demonstrated empirically, the automated detection of the same may prove valuable in a system to automatically highlight areas of interest in tissue for further analysis. The approach for detection was to use image processing techniques discussed

earlier in the thesis in order to detect the blob-like structures of micro-calcifications. When analysing an image with known micro-calcifications, such as from Patient 18 Slice 12, where calcifications are clearly visible, using a surface plot, the structure of the calcifications can be clearly identified. The calcification presents as a bright blob like structure with a positive slope on the intensity map. In contrast, specular reflections, some of which remain present in the image, generally feature a much smaller and sharper peak than the micro-calcifications, with a relatively steep slope.

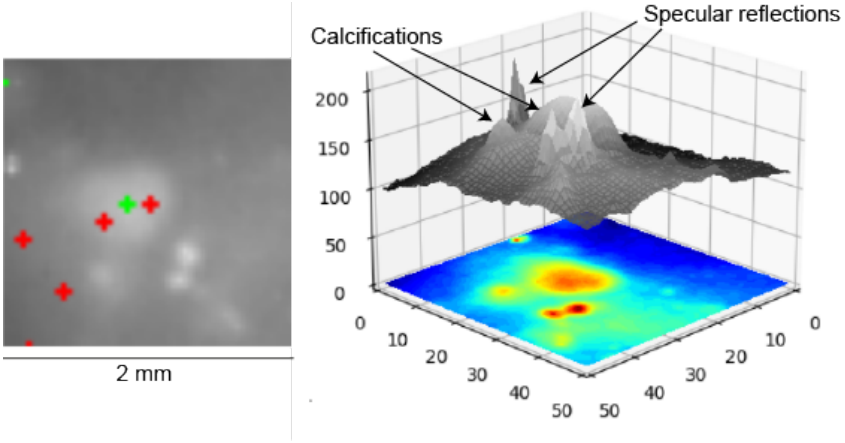

Figure 5.17. *Zoomed in view of a 50x50 pixel region under NIR illumination, containing a micro-calcification and specular reflections and corresponding surface plot and heat map. Specular reflections present as a sharper peak whereas the micro-calcification is much broader. Green dots indicate micro-calcifications detected, and red dots mammography co-registered locations of micro-calcifications.*

These blob-like structures can be detected using a LOG method. The method is a multi-scale method that can detect blobs of various sizes as the scale is changed throughout the computation [159]. By selecting a scale threshold blobs of different sizes can be filtered out. Assuming that all specular reflections present as small sharp peaks (Fig. 5.17), they can, in this way, be separated from other blob like features in the image[5]. This method eliminates any blob-like features below a certain dimension, however, and is not only limited to specular reflections. For presentation, any locations below the threshold chosen can be filtered out by blurring with a median filter in that area (Fig. 5.18). This removes the sharp intensity peak and results in a smoothed area, where intensities more closely match the surroundings of the peak.

The automated detection can be used to plot the locations of predicted micro-calcifications on the image alongside the locations of the mammographically detected calcifications after co-registration, as in Fig. 5.19. There is a small discrepancy in the positions after the warp, and not all micro-calcifications are seen. Additionally the automated detection over-predicts some locations as micro-calcifications.

[5] Note that image artefacts, such as residual specular reflections in this case, are not a phenomenon that only occurs with this micro-camera based imaging method. They also occur on x-ray film cassettes, for example, where they similarly interfere with micro-calcification detection.

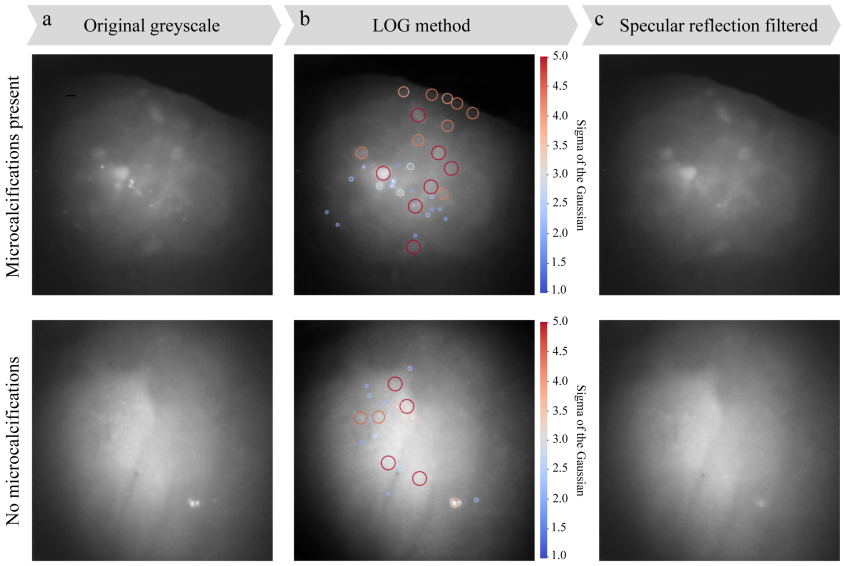

Figure 5.18. *Grayscaled 850 nm NIR image of two locations on slices of lumpectomy specimens. The images are post-processed using the LOG algorithm, and features below a certain size are removed using a median blur to reduce the residual specular reflections on the image.*

Other methods of feature detection were also explored, such as a Fourier domain based method showcased in Figure 5.20. This method uses high frequency filters to isolate sharp peaks in the image. The 2D Fourier transform of the image is computed. A filter of different sizes can now be applied to the image, and in this way peaks are identified. Figure 5.20 shows these Fourier transforms ((a)-(c)) and filtered images using different high pass filters ((d)-(i)). When the filter is set to a higher threshold such as in ((d)-(g)), In the later images such as (h) and (i) only the very sharp peaks remain. In this way a bandpass filter can selectively filter out features of different sizes, and exclude miniature artefacts such as specular reflections. The technique was not included in the publications, as the LOG method proved sufficient. However, it may be explored further in the future.

Machine learning methods may also be useful in identifying microcalcifications, however due to the requirement of larger training datasets [160] and the relatively small number of test images available after this exploratory study, the use of machine learning was not explored at this stage. Images can be further manipulated for presentation using HDR Imaging and contrast enhancement. Different methods of HDR image reconstruction were explored as part of this project. While the Debevec [95] and Robertson [96] reconstructions help to solve some of the darkening at the edge of the scene, the Mertens [97] image was deemed the most successful due to the best perceived preservation of contrast between features in the image.

In order to create the HDR image, the light source's illumination intensity was adjusted. This resulted in 25 images of varying intensities for each illumination colour. Not all images were necessary to reconstruct a HDR image, with 5 being sufficient. Images with low illumination intensity, medium illumination intensity, and high illumination intensity were chosen. Their relative intensities were fed into the algorithm as pseudo exposure times, in order for the HDR image to be generated. A colour map is then applied to return the images to an approximate colour. Upon presentation of the images to the clinicians, the HDR approach in

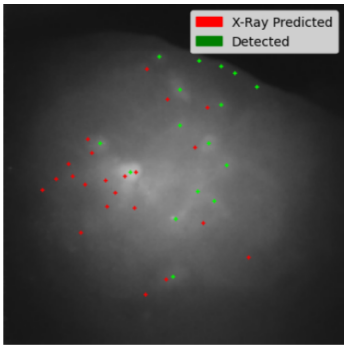

Figure 5.19. *Predicted locations vs detected locations for Patient 18 Slice 12. The green dots show the LOG detected microcalcifications after thresholding to remove small features. The red dots show the positions of microcalcifications on the mammography. The images are overlayed using the previously described co-location workflow. Currently there is no direct pairing of points performed and this should be seen as a qualitative result. More work needs to be done in relation to controlling slice thickness, determining sensitivity of the system, and optimising automated detection.*

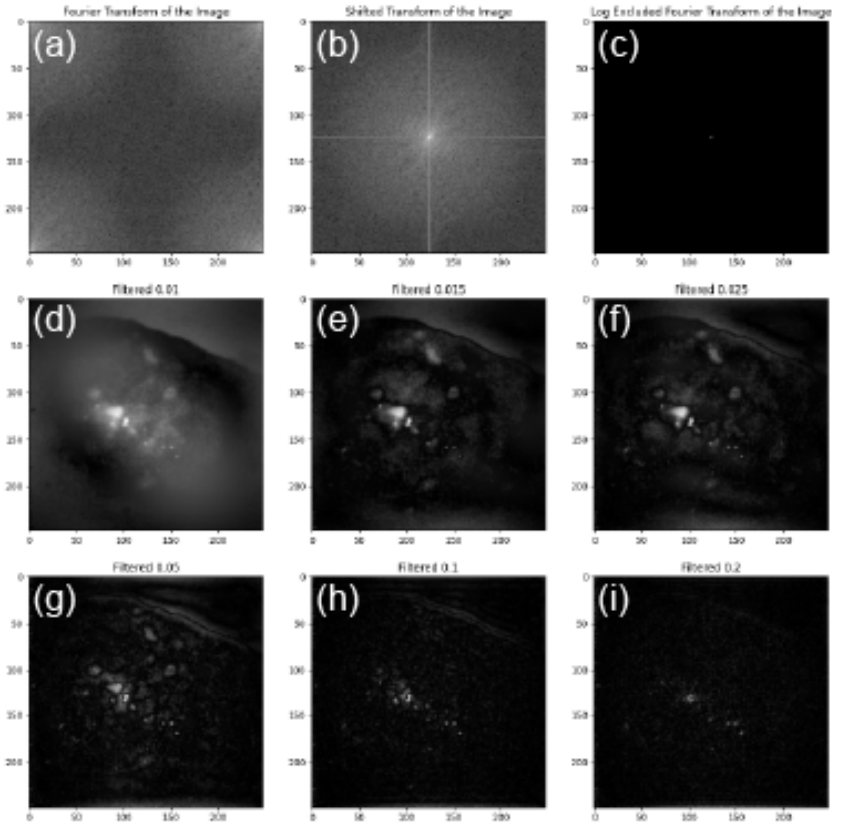

Figure 5.20. *Images showing the effect of Fourier high pass filtering the Patient 18 Slice 12 image. The first row, (a)-(c) shows various representations of the Fourier transform of the image. Images (d)-(i) show the result of high pass filtering with different thresholds set.*

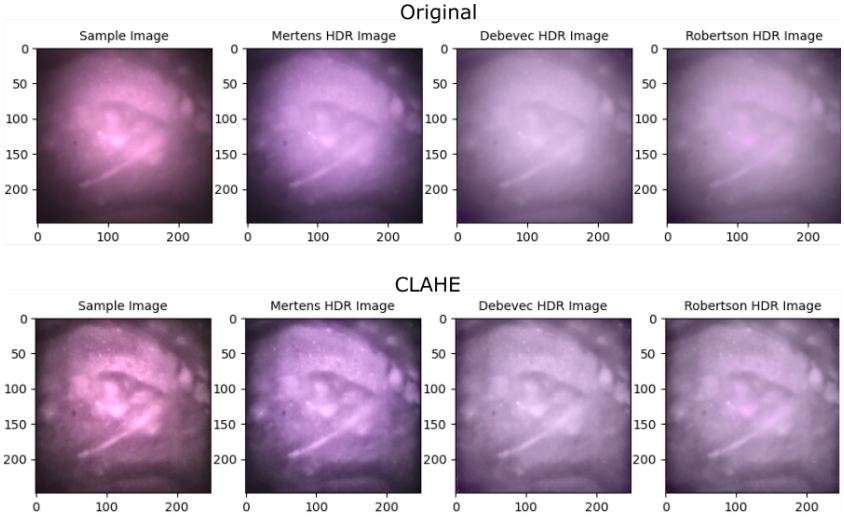

Figure 5.21. *A comparison of HDR methods, with and without CLAHE. Dark areas reduced by employing HDR imaging. Some contrast is lost with Debevec and Robertson methods. CLAHE enhancement has a big impact on the contrast of the images, with and without any HDR methods employed. A false colour map is applied to the images to return them to the original colour.*

this case was not deemed to be necessary, however the CLAHE contrast enhancement was appreciated since it gave a demonstrable increase in

visual contrast. The micro-camera images performed best when micro-calcifications were present in the well-illuminated centre of the image, where HDR did not have a major effect on the visibility of the calcifications. However contrast enhancement allowed for structural features to be picked out more clearly by visual examination and is therefore included in the results. The HDR method shows promise in brightening the edges of the image however, and in this way, overcoming some of the limitations of illumination profile, camera sensor distortion and sensitivity roll off. It remains a useful technique that may play a role in future micro-camera work.

Images of 22 specimens collected from 12 patients with the updated system were analysed in the aforementioned manner. This included 8 patients for which HDR data was collected. The goal of the feature analysis and image processing is both to identify relevant features and improve displayed image quality for evaluation.

5.8 Results

Micro-calcifications have for the first time been successfully detected using a handheld imaging system using VIS and NIR illumination in *ex vivo* human breast tissue. This was verified post co-location using independent clinical and technical reviewers. NIR illumination proved most successful in detecting calcifications. The micro-camera allows for excellent magnification of a region and NIR illumination gives penetration depth while maintaining reasonable contrast. Locations of micro-calcifications have been verified using a co-registration method and x-ray ground truth.

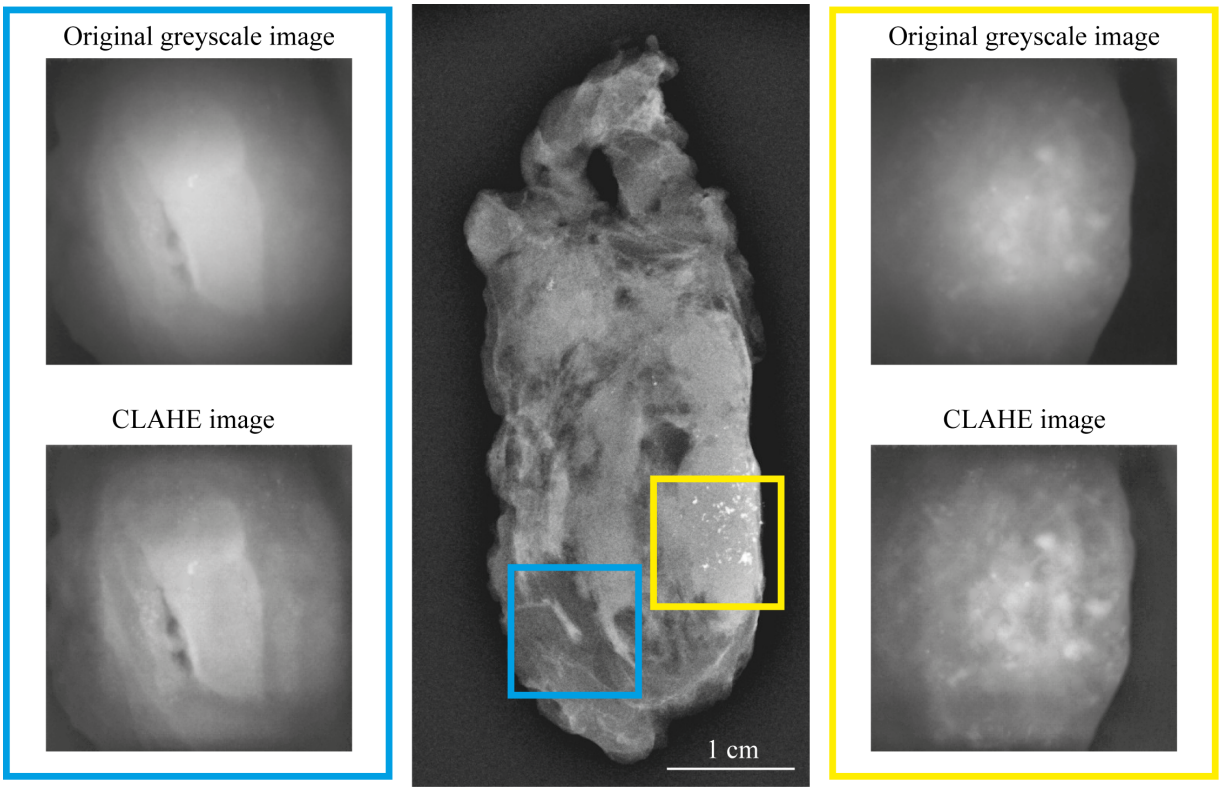

Figure 5.22. *Image of detection of micro-calcifications and corresponding location on the mammography. The yellow box represents the measurement with micro-calcifications, whereas the blue box is a negative control.*

Slices were analysed for the presence of micro-calcifications and compared with a negative control. There tends to be a surface change to the image in the presence of micro-calcifications, which can be enhanced for

the human observer using a CLAHE algorithm (Fig. 5.22). This image in Figure 5.22 shows an x-ray of a tissue slice in the centre. A negative control area is indicated in blue, and the corresponding images are presented in the blue box to the left of the x-ray. The image presents a clear and homogenous diffuse image of tissue with little to no structure showing. A residual specular reflection is seen in the centre of the image as a solitary feature. The area containing micro-calcifications is indicated with the yellow box with corresponding camera images shown to the right. Here the image shows structural changes where micro-calcifications are present. Different distributions of micro-calcifications were imaged during the study. Large clusters of calcifications, in this case deemed clinically most relevant, showed a definite structural change on the tissue images. The negative control areas on the slices contained no micro-calcifications in the x-ray analysis. Any bright areas in these images were due to specular reflections, and were isolated occurrences and therefore easily identified and distinguished from the field of less-sharp intensity peaks that a cluster of calcifications presents as.

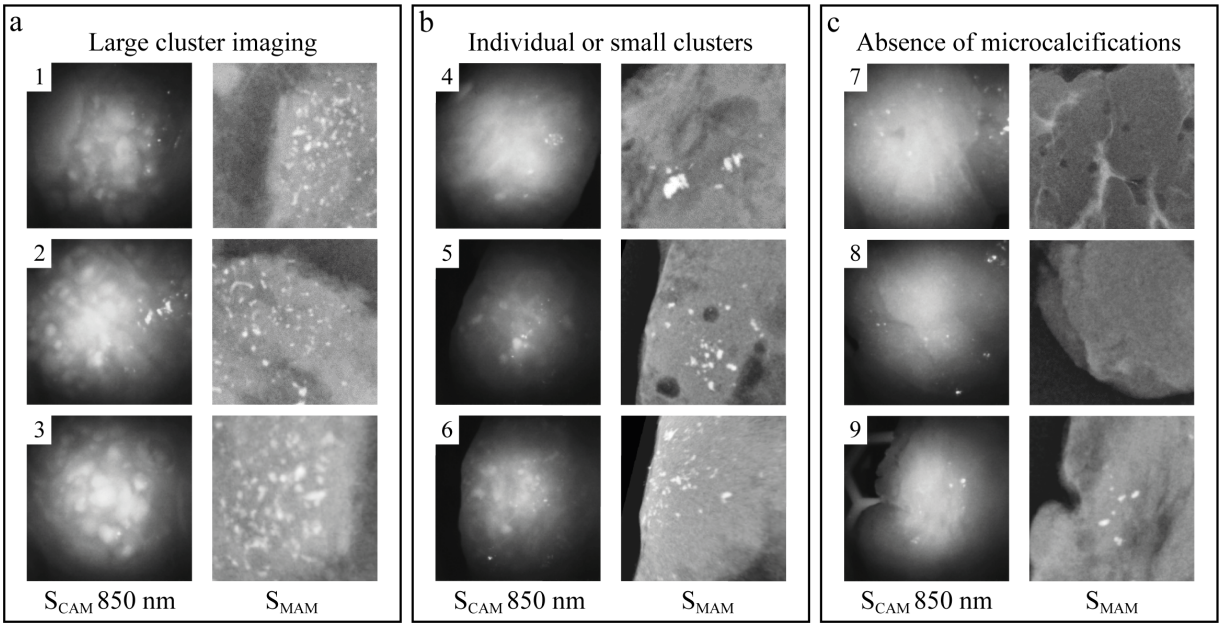

Figure 5.23. *Nine micro-camera images S_{CAM}, of various micro-calcification distributions, accompanied with the corresponding mammography, S_{MAM}. (a) Large clusters of micro-calcifications within both S_{MAM} and S_{CAM}. (b) Small groups of clustered micro-calcifications, and (c) absence of micro-calcifications in S_{CAM} images due to absence of micro-calcifications in the mammography (examples 7 and 8), or suspected distribution at depth more than 2 mm (example 9). Note that these images have not been post-processed to remove residual specular reflections.*

Fig. 5.23 shows a selection of images captured during the study, featuring different clusters of micro-calcifications. In any areas with positive micro-calcifications these may present either in larger clusters covering the entire image, or in smaller clusters of individual or few calcifications. Both cases are imaged using the system in Fig. 5.23 (a) and (b), respectively. Imaging of large clusters in particular (Fig. 5.23 (a)) shows a very clear difference to an area with absence of micro-calcifications in the image. Absence of micro-calcifications in the captured micro-camera images, as in Fig. 5.23 images 7-9, may be because there are no calcifications present in the sample (Image 7 and 8), or because the calcifications are not detected using the system (Image 9). Failure to detect a micro-calcification may be due to them being buried too deep, being too small, or being obscured by a residual specular reflection or some other diffuse feature in the tissue. As previously discussed, much work has been

done to post-process the images to mitigate the effects of residual reflections. Calcifications that are buried in the slice at a depth below the 2 mm detection threshold of the optical imaging system are unlikely to be detected. Calcifications below the resolution of the imaging system as discussed in Chapter 2 will not be individually resolvable. Variation in size of calcifications may be due to depth or size, and can not be differentiated without an absolute depth measure. These limitations in particular, account for many of the discrepancies between calcifications present on the x-ray images and those detectable using the camera in Fig. 5.23.

To verify presence of calcifications, the obtained images were independently scored by two clinicians and two technicians. Further details and analysis can be found in Paper **II**.

5.9 Outlook

It is important to note that the value of this micro-calcification detection method is seen in its ability to rapidly provide information on sites that may be of clinical interest. It allows for wide field imaging and scanning over a tissue surface, inside or outside of the surgical cavity. This, however, is not a comprehensive diagnostic tool. DCIS is not always accompanied by micro-calcifications and the visualisation of calcifications alone is insufficient as an aid for clinical decision making. DRS in particular has been effectively used to discern malignant and benign tissue in DCIS [24, 148]. Further development of the technology would see the image sensor embedded next to a more diagnostically focused tool, such as a DRS probe. This could be integrated easily into the existing system by adding two additional fibres to the probe. The idea then is to scan tissue using the camera, and when regions of interest are identified, perform an additional measurement which determines the pathological state of the tissue more accurately. The micro-calcification is therefore a guide star, and the imaging system a supplementary system, to the diagnostic tool. This must be kept in mind when developing future iterations of the system. A number of improvements are recommended for future iterations.

Improvement to the cross polarisation, including selection of polarisers with a higher contrast ratio, in particular in the blue wavelengths would improve the performance of specular reflection reduction. It would also enable further multi-spectral investigations. It should be noted that while specular reflections do detract from the underlying information due to their dependence on illumination angle and surface geometry, they can be easily identified by a user in a live video simply by moving the probe. The specular reflections will move and the underlying information can be revealed by changing the position of the device slightly. A specular reflection reducing technique, such as the two presented here, mainly has value when analysing static images, and in removing the distracting specular reflections altogether when quickly scanning tissue. Dicing these polarisers to smaller dimensions, as has been demonstrated elsewhere in this thesis, can lead to the integration into a smaller footprint. This in turn allows for integration with other measuring modalities. A final system size of 8.00 mm OD has been suggested by clinicians, however other dimensions are easily achievable.

A revised system should be constructed in order to be more easily sterilisable, perhaps even with an autoclave to enable *in vivo* studies. Such a design consists of a machined stainless steel housing, and some form of cover class fitted on the front of the sensor to protect the cameras and polarisers from the environment, and enable more easy wiping of the imaging area during the procedure. Likely this system needs to be man-

ufactured with a prototyping partner who has the ability to manufacture to the requisite medical standards.

Analysis of the slices using a micro-CT would allow for a better understanding of the depth of micro-calcifications, and the resulting sensitivity to micro-calcifications on the micro-camera images. It would also allow for a more in-depth investigation of wavelength and detection depth. Further characterisation in this regard should be performed. To date, the sensitivity of the camera when imaging blob-like features at depth has only been measured using tissue mimicking phantoms in Paper **I**, and not been investigated in real tissue. More work needs to be done to measure the depth sensitivity in the clinical setting on real tissue. This will also further inform sensitivity and specificity measurements of micro-calcification detection and is expected to improve the same.

Automated detection of micro-calcifications from image data has been demonstrated using two different techniques. In the future, detecting clusters of calcifications, different patterns, and calcification size may help make clinically relevant decisions. For the moment image processing is effective in filtering out residual specular reflections to improve image quality. Along with image contrast enhancement, these will aid clinical decision making by providing an informed image to a clinicians for rapid and easy assessment.

The feasibility of the micro-camera to detect micro-calcifications on real excised breast tissue is demonstrated. This is the first investigation into the real time analysis of micro-calcifications in breast tissue. It promises a potentially novel technique that can aid a surgery where tight margins are required, and revision surgery is currently a frequent occurrence.

It is important to note that DCIS does not always progress to an invasive carcinoma, and in recent years treatment in the Netherlands has trended towards less extensive interventions to avoid over-treatment of patients [161]. During the course of this study, the standard of care in the treatment of DCIS in the Netherlands changed. As a result, DCIS is operated on less frequently, and the interest in micro-calcification detection has diminished. This also led to a significant decrease in suitable patients. Despite this, micro-calcifications remain of clinical relevance in the diagnosis of breast cancers. Study of intra-operative surgical visualisation tools in breast conserving surgery is an exciting, and developing field, and micro-calcifications are anticipated to continue to play an important role in the future. Imaging technologies will likely also see continued development in minimally invasive techniques, and CMOS will play an important role in providing vision to surgical tools in the future.

Chapter 6

Miniaturised Polarisation Imaging

*This Chapter introduces a polarisation resolved system that uses the micro-camera as a platform. The work is the natural continuation of the miniaturisation of both camera systems and polarisers as discussed previously in the thesis with the intention to provide additional contrast to imaging. The prototype system constructed is able to achieve flexible polarisation-resolved imaging at a 5.00 mm OD by including both a polarisation state generator and analyser in the tip of the system. In this way the polarisation properties of the fibres need not be known, and bending losses or changes to the polarisation state need not be considered. A benchtop system is also constructed, and measurements are taken on optical elements and on human breast tissue. The relevant publication is Paper **III**.*

6.1 Research Objective

This research is developed as a follow on from the breast conserving surgery work presented in Chapter 5. Initially the aim was to develop a complimentary benchtop system to examine the excised bulk tissue, and to enhance contrast with polarisation techniques. The hypothesis was that collagen tissue breakdown would be detectable through shifts in polarisation. The dicing of polarising optics led to the investigation of flexible polarimetry systems.

The objective of this work is therefore to develop miniature and flexible polarisation resolved systems with line of sight to tissue imaging, and to investigate multi-spectral polarisation resolved imaging.

6.2 Introduction

With the integration of polarisers into miniature chip-on-tip systems as discussed previously in this thesis, the logical next step was to use the technology for polarisation-resolved measurements. This led to an exploratory study investigating the efficacy of constructing a polarisation resolved chip-on-tip system with current micro-camera technology and previously used components. Using polarisation for imaging in this way, provides another dimension of analysis for chip-on-tip systems.

Polarised light as an analysis tool has seen cross-disciplinary applications. For example in industry, for material classification [162], food science [163], and for tissue analysis in biomedical optics [164]. In general, changes in tissue structure may contribute to changes in linear retardance, especially where there is a change from aligned tissue structures to

disorganised structures. In particular in the progression of cancer, structural changes can be a sign of malignancy. Uncontrolled cellular proliferation is one of the primary features progression of the disease [165], and changes in collagen organisation another major factor [166]. Both of these have an effect on the polarisation parameters and therefore are detectable by changes in the Mueller matrix of the tissue [80, 165, 166].

Polarised light has been used to visualise superficial tissue such as skin where birefringent collagen strongly randomises incident polarisation [167, 168]. Superficially back-scattered light is distinguished from the diffuse component in the analysis. Beyond superficial applications, it sees applications in microscopy [169] and the analysis of thin slices of tissue, and there is a push towards bulk tissue imaging and to develop *in vivo* uses of the technique [170]. Polarisation imaging has been successfully used on thin tissue slices to distinguish malignant and healthy tissue [171] and has been used on breast tissue slices to guide a mass spectrometer probe using wide-field imaging [172]. Moving towards bulk tissue and *in vivo* uses, polarisation has been used to characterise the ablation of 4 mm thick myocardium tissue, where depolarisation changes are likely due to changes in scattering and changes in tissue anisotropy [173]. Polarisation imaging has also been used to image cervical tissue *in vivo* using a polarisation resolved colposcope detecting changes in collagen as an indicator for precancerous tissue [174]. In the brain, reflection mode imaging of fiber tracts in thick slices of healthy brain tissue has been demonstrated [175].

Figure 6.1. *A torque coil used to accurately transfer rotation over a distance. The coil consists of multiple layers of flat or round wires.*

Bulk tissue provides the additional challenges of increased depolarisation, reliance on back-scattered light, and a thicker tissue volume each layer which may interact differently with polarised light [75]. Despite these challenges polarimetric contrast is seen in bulk tissue and is an interesting technology for translation into clinical use. Imaging of bulk tissue, in reflection mode is of particular interest in a clinical setting, with recent advances paving the way for clinical translation [80]. In order to be translated to *in vivo* clinical use, polarisation-resolved sensing must be integrated into surgical tools. For *in vivo* applications, acquisition time reaching real-time speeds is an important factor, and motion artefacts should be minimised. The concept of measuring reduced Mueller matrices to speed up this acquisition time is being explored [176].

Rigid laparoscopic systems based on fibre laparoscopes, have been developed and are capable of resolving a 3x3 [177] or 4x4 Mueller matrix [15] using rotating sheathings and a proximally mounted CCD camera. A narrow band imaging rigid endoscope capable of increasing contrast of vessel detection in porcine tissue has also been developed [178]. What these systems collectively lack is flexibility. A flexible fibre based system has been presented [179]. This system uses optical fibres and distally mounted polarisers to illuminate and sense. Flexibility introduces additional characterisation requirements due to the detection fibres bending, which may influence polarisation of light. Such fibre-based systems provide point measurements only. Flexible polarisation-resolved wide-field imaging systems have been discussed in the literature, either to image with a cross polarised CCD mounted at the tip [180], or using a CMOS sensor and elaborate mechanical actuation at the tip to create an endoscope with 13.5 mm OD capable of capuring a 3×3 Mueller matrix [181].

Recently, pixel arrays with embedded polarisers, such as the Sony IMX250MZR sensor have become available. These sensors capture four different states of linear polarisation using embedded polarising features above each pixel. Technologies which are capable of full Mueller matrix measurements on chip including circular polarisation states, using metasurfaces, have also been developed [182, 183]. Such technologies promise faster acquisition times with fewer moving parts, and may prove ideal for

flexible endoscopic use, however further miniaturisation is required. In this work, a mixed approach, using distally polarised illumination light, and a micro-camera with rotating polarisation element is presented as a first step towards wide field polarisation resolved imaging in a compact flexible footprint of 5.00 mm OD. This means both PSA and PSG are mounted at the tip of the device, which allows for a flexible integration and enables polarisation resolved imaging in difficult to navigate areas. The micro-camera has the additional benefit of offering a potentially cost-effective solution due to the CMOS technology.

6.3 Methods

As described in Chapter 2 capturing the Mueller matrix of a sample requires a polarisation state generator and analyser. These are constructed using polarisers and waveplates, and described in more detail in the system specific sections of Chapter 6. Due to simpler systems, in this feasibility and range finding study, a reduced Mueller matrix using only linearly polarising optics is often captured. In order to capture the reduced 3x3 Mueller matrix of a sample, 9 images of different input and output polarisation states are taken. These are usually captured at 0, 45, and 90 degree orientations for PSA and PSG. Optics that have a known effect on the polarisation state of light prove convenient test targets. These include linear polarisers, retarders, and diffusers. In this study, linear polarisers are selected as a test element in order to conduct tests on the system. These are placed on a tissue mimicing phantom, the same used in Chapter 5. Scattering values similar to human tissue and used to mimic the expected depolarisation of human tissue. Data is analysed using the polaranalyser Python package [184].

6.4 Benchtop Imaging System

To investigate polarisation imaging, a benchtop imaging system (Fig. 6.2) was constructed to compliment and validate the polarisation measurements captured using the miniature system in the future. Initially the benchtop polarimetry system was proposed as an tool to compliment margin assessment on the bulk lumpectomy mid-procedure, during breast conserving surgery procedures (Ch. 5). This concept evolved into a range finding and validation system for a flexible miniature endoscope. The system uses the FLIR Blackfly polarised camera (BFS-U3-51S5P-C) which has a polarised Sony IMX250MZR sensor. Illumination is supplied from a multi-spectral source through a liquid light guide which is collimated using an aspheric lens. The illumination path is aligned at an angle to the detection path to further reduce specular reflections in the non-cross polarised measurement states. Polarisers (Meadowlark VFM-100-NIR) and quarter waveplates (Meadowlark AQM-100S) are aligned with the illumination and detection path in order to generated polarisation images. These polarising optics are specifically selected to operate across a broad wavelength range between 400 nm - 1100 nm to enable multi-spectral investigations. Initially a 3x3 Mueller matrix was captured, in order to compare with the 3x3 images captured using the micro-camera. Rotation is achieved using manual rotation mounts. The system can produce full 4x4 Mueller matrix images with the inclusion of automated rotation and waveplates. This requires better alignment of the optics relative to each other, and a cage system set up with automated rotating elements is proposed as a future step.

Figure 6.2. *Benchtop system with polarised monochrome camera sensor, and illumination arm angled w.r.t the detection arm. A liquid light guide can couple into the illumination lens sytem for a collimated spot. Polariser in front of the illumination lens system allows for control of incident polarisation.*

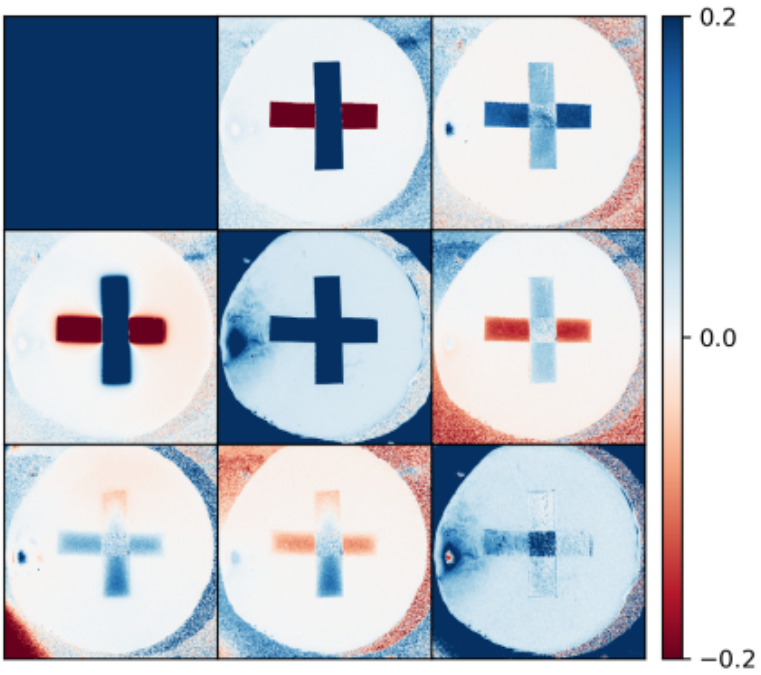

Figure 6.3. *Mueller matrix of two linear plastic polarisers that are placed orthogonally to each other on a tissue mimicking phantom, normalised with respect to the m_{00} component.*

The system was first tested on polarising optics placed on a tissue mimicking phantom as in Figure 6.3. Two linear polarisers generate a diattenuating signal that is picked up in the Mueller matrix, with orthogonally aligned linear polariseration having an opposite sign. This result is later compared to similar optics captured using a micro-camera sensor instead, in Figure 6.9. Calibration and characterisation of the system must be performed as a next step in order to obtain quantitative results.

Since access to tissue was readily available during the study in Chapter 5, some multi-spectral data was captured of breast tissue slices under the same ethical approval. Figure 6.4 shows one of the slices imaged under four different illumination wavelengths. The use of on chip polarisation allows for a single image to be captured which is demosaiced during analysis. In total, four different slices were imaged using multi-spectral illumination, in this way. As discussed in Chapter 5 the slices all contain excised tumour tissue.

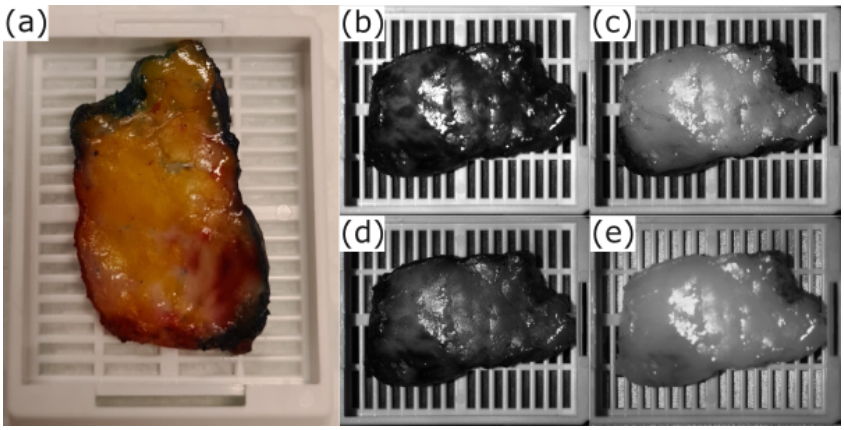

Figure 6.4. *Images captured using the benchtop polarimetry system of excised human breast tissue in NKI. A colour camera image is shown for reference in (a). Different illumination wavelengths are used: 450 nm (b), 660 nm (c), 530 nm (d), and 850 nm (e). The images in (b)-(e) are captured using the polarised sensor, and all polarisation states are still encoded in each image. A demosaicing algorithm must be employed to separate the channels for further processing.*

An example of the processed data is seen in Figure 6.5, where the red illumination wavelength is chosen for analysis. It is clear that the thick tissue is, as expected, primarily depolarising with the strongest signal along the diagonal of the matrix. This is a typical example of the tissue analysed and the multi-spectral aspect will be further explored in a continuation of this work. In the future, it is hoped that such a benchtop system can be used more extensively on *ex vivo* samples, in conjunction with histopathological examination, in order to validate a flexible polarised endoscope on real tissue samples in the clinic.

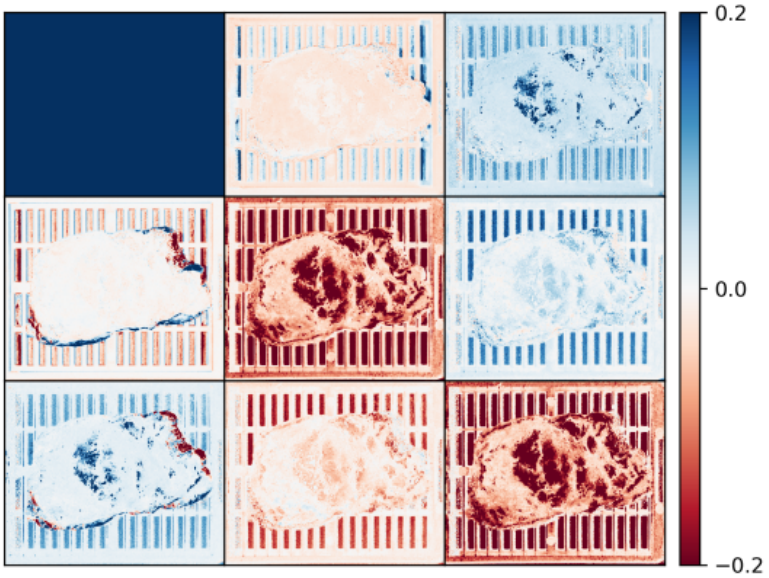

Figure 6.5. *Normalised Mueller matrix of the slice of breast tissue imaged using 660 nm LED illumination.*

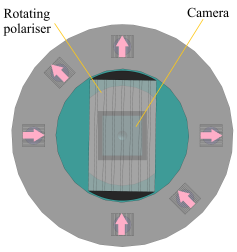

Figure 6.6. *Schematic front view. Polariser orientations are indicated using the pink arrows, the camera can be seen in the centre with the PSA polariser mounted in front of it on the inner sheath.*

6.5 Miniaturisation

In order to develop a flexible system in a compact form factor that is capable of polarisation-resolved imaging, a micro-camera is mounted at the tip of a short distal alignment holder. This holder is theoretically limited in length only by its ability to hold the optics and the camera. However, it is designed to be longer for the initial prototypes for stability. The primary part of the holder, is 7.00 mm in length, with the internal rotating sheath featuring an elongated tail to be mounted to a torque coil which can provide rotation. The camera sensor is fixed within the outer holder, and an inner sheath is able to rotate freely between 0 and 90 degrees around the camera. This rotation can be controlled proximally using a torque coil (Asahi Intecc). The Design can be seen in Figures 6.6 and 6.7 revealing the polariser orientation and the inner rotating sheath, respectively. Since the part is allowed to only rotate freely between 0 and 90 degrees, the camera connector does not necessarily need to be passed through the torque coil, and can instead be passed through a dedicated slot in the back of the rotating piece. This is only of importance in the context of the prototype, since disconnecting the connector from the camera leads is tedious and inefficient without specialised equipment. The integration into a flexible catheter is also shown in Figure 6.7.

Illumination fibres are terminated individually, and pairs of fibres with the same polarisation output at the front of the device are activated together in order to generate polarised illumination. Currently this switching of fibres is performed manually, however it can be automated easily with the use of an optical switch, and bifurcated fibre connectors.

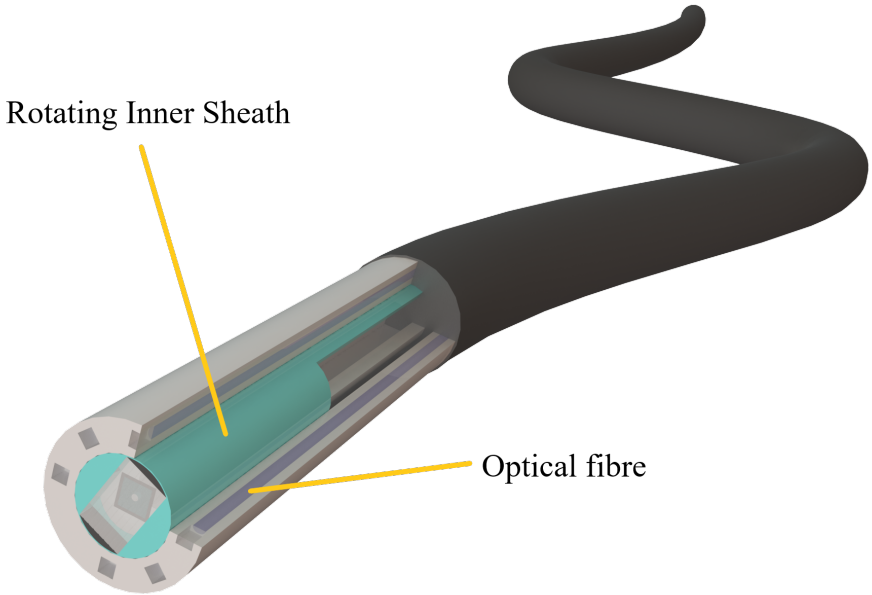

Figure 6.7. *The outer shell is part of a core component (indicated grey) which also connects to the camera housing in the center. The inner sheath (indicated cyan) is allowed to rotate freely within a limited range of motion from 0 to 90 degrees within this core component.*

For prototyping, the polarisers (Edmund Optics 12-649) are diced to 500 μm square and inserted into the recesses of the 3D print. The polarisers are orientated at 0, 45, and 90 degrees with respect to the zero axis of the probe as shown in Figure 6.6. A larger polariser is affixed

in front of the camera on the rotating sheath, and the camera is glued in place. A close up view captured using a 3D microscope is shown in Figure 6.8. There is a small gap visible between inner sheathing and outer sheathing which is fixed as tolerances are tightened in later print runs. The same applies for the slight tilt in camera position, this is a tolerance error that is resolved in new print runs. Due to the poor performance of the material as shown later in this section, the production of devices was temporarily paused.

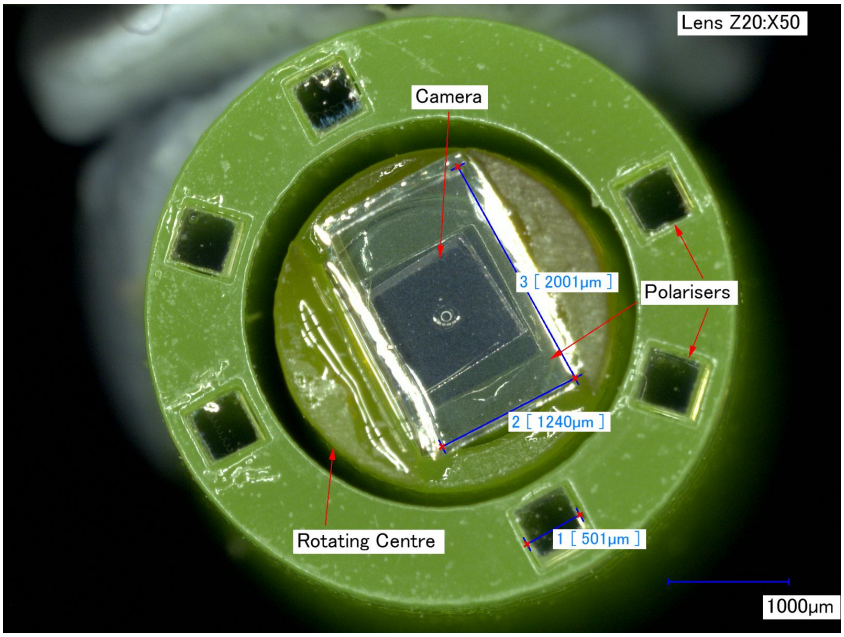

Figure 6.8. *Image of the 3D printed holder with integrated polarisers concentric around the camera, and the rotating centre piece with larger linear polariser.*

6.6 Results

The first polarisation-resolved images captured using a micro-camera (Fig. 6.9) were captured using an external benchtop illumination system through a polariser acting as PSG, and a polariser rotating in front of the micro-camera acting as PSA. Images of polarisers sitting orthogonal to each other, on a tissue-mimicking phantom were captured, with polarisation orientations of 0, 45, and 90 degrees for both PSA and PSG. In total nine images are captured in order to calculate the Mueller matrix. The illumination profile in this experimental set up is not ideal and while the illumination intensity of the source remains constant across the acquisition, there is an intensity gradient present across the image. Additionally some sort of shadow is introduced in images in the middle show which distorts the measurement. The image can be cropped to a region where this shadow is not present. For demonstrating feasibility this configuration was deemed adequate. The image in Figure 6.9 shows the first Mueller matrix images captured using a micro-camera sensor. The crossed polarisers show a strong diattenuating signal as expected. Comparing the results for the bench top system with the larger FLIR camera above in Figure 6.3 we observe the same diametric signal for the orthogonal polarisers as before.

Migrating to the miniaturised system, as in Figure 6.8, images of various optics arranged in the field of view were captured in Figure 6.10. A diametric diattenuating signal is again seen with the polarisers.

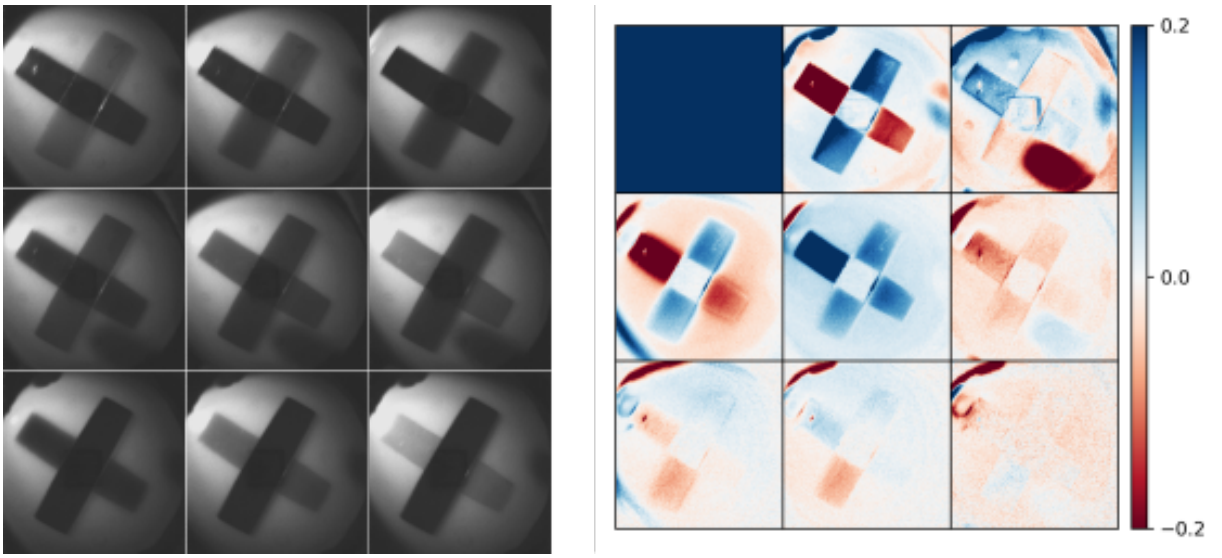

Figure 6.9. *First polarisation measurements captured using a micro-camera in the laboratory. Two linear plastic polarisers are placed orthogonally to each other on a tissue mimicking phantom. The left image shows the 9 input images. The right image shows a normalised 3x3 Mueller matrix.*

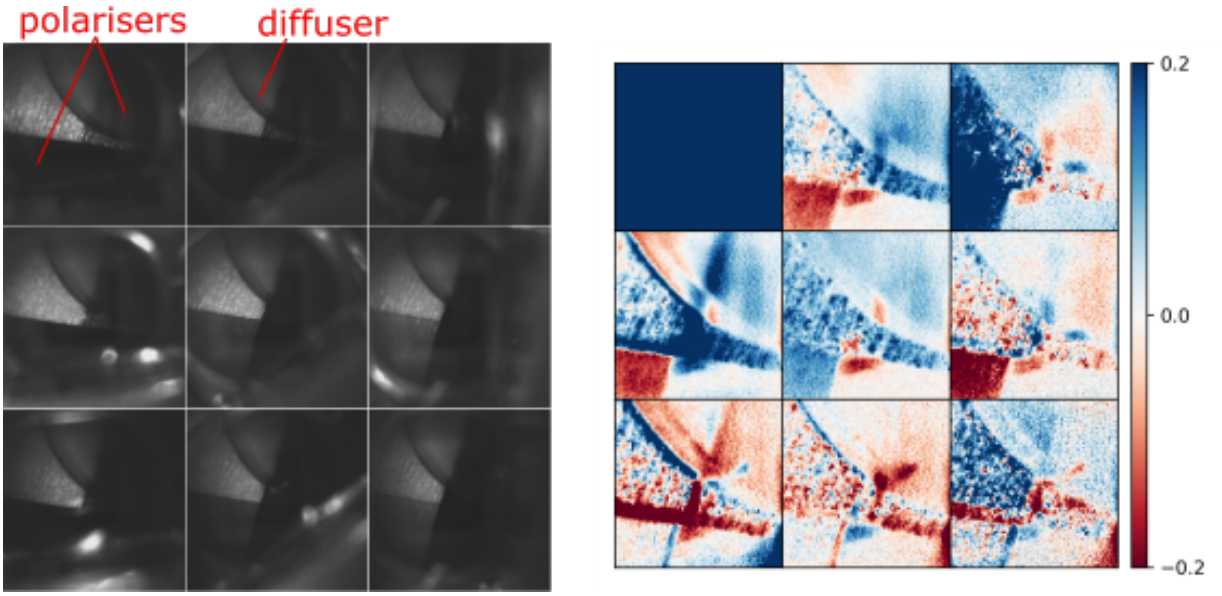

Figure 6.10. *Polarisation measurements captured using the miniature micro-camera polarimetry system. Different optics are arranged in the FOV of the system, with a linear polariser in the bottom left and orthogonal polariser along the right side, and a diffuser in the top right. The left image shows the 9 input images. The right image shows a normalised 3x3 Mueller matrix.*

The image as a whole is significantly noisier than previous images. Light leakage through the material proved a significant problem in obtaining images of suitable quality. This is discussed in more detail in Chapter 3. Isolating the camera better optically may help to mitigate the problem somewhat, however due to the need of an optic placed in front of the sensor, there are reflections that enter the camera sensor from the front. Intensity mismatch between the fibres is a secondary problem to the light leaking. Once the light leakage problem is addressed the system needs to be calibrated to account for the polarisation properties

of the optics and the shifting illumination profile.

Images of *ex vivo* animal tissue were also captured using the miniaturised system but yielded no significant results. The system requires redesign to resolve existing issues and then adequate calibration. Following this, further analysis techniques such as decomposition [77] can be performed.

6.7 Discussion and Future Work

The feasibility study presented in this Chapter has been successful in building the first flexible and miniature chip-on-tip prototype capable of polarisation resolved imaging. The systems needs to be developed further and can benefit from a number of improvements.

Improvements to the benchtop system include automated measurements and a decrease in the overall acquisition time. While at the NKI, the intention was to collect data on a number of tissue specimen. However long acquisition time meant that this was not possible, as the core projects related to the tissue samples had to take priority. With motorised rotation and synchronisation between light source and PSA/PSG it is expected that multi-spectral data can be acquired within the space of a minute. This initial design of the system also proved challenging to align. Waveplates were included in the first iteration of the system, but the magnetic mounting used proved difficult to align with the illumination and detection paths. Additionally the insertion and removal of the waveplate changed the FOV of the camera as well as illumination intensity slightly, and highlighted the need for adequate calibration. The next iteration of the system should, however, be capable of 4x4 Mueller matrix imaging. The proposal is therefore to mount all optics and rotation stages in line using a Thorlabs cage system type set up. This will drastically improve alignment of the parts, and along with automation will enable adequate calibration of the system.

The constructed flexible miniature prototype succeeded in demonstrating the feasibility of using micro-cameras in chip-on-tip polarimetry systems. The system opens the door for more extensive exploration of polarimetry with micro-image sensors at small scale. The aforementioned problems with light leakage are expected to be overcome with material updates. Material choice and machining processes are discussed in more detail in Chapter 3. Reconstruction of the system using stainless steel machined distal alignment pieces may be the most effective way to deal with stray light. However other plastics have previously shown adequate performance. The primary requirement in that case is high enough machining tolerances to allow for the manufacturing of small parts of the order of hundreds of micrometers to a few millimeters, while adhering to the ISO2768-fine standard discussed in Chapter 3. Friction between rotating element and outer sheath need to be considered and investigated. A mechanism for determining the exact position of the frontal piece may be beneficial for calibration. Currently a back-end motor control is used for positioning.

A rigorous characterisation and calibration protocol [185–187] must be followed in order to validate polarisation results and draw conclusions from the data. This must be combined ideally with some ground truth measurement, i.e. a histopathology step. Then further data analysis and matrix decomposition can be investigated. This also enables further investigation into the value of multi-spectral imaging combined with polarimetry. Multi-spectral illumination adds the additional dimension of chromophore contrast. Calibration is required so that a comparison between the wavelengths can be made. While differences in intensities are seen between the different illumination wavelengths in the Mueller ma-

trices of the acquired data, with a higher signal apparent in the blue and green compared to red and NIR wavelengths, the system needs to undergo proper calibration and repeat of the experiment in order to be able to draw conclusions.

Due to time constraints, in particular related to closing out other projects discussed in this thesis and finishing the PhD, not all of these improvements were able to be completed. The investigation in flexible miniature polarisation resolved imaging has therefore just begun.

Future studies may focus on targeting a specific disease state, in a location where it makes sense for a flexibile device to be used. In this case acquisition time for the relevant polarisation states should be reduced to near real time. This is especially true for an *in vivo* tool. A benchtop system that images excised samples for example, has some more leeway regarding acquisition time. There are a number of potential locations where polarimetry may be particularly interesting. In the investigation of Barrett's oesophagus and screening for disease progression, there is a change in the epithelium [21]. In patients who present with the condition, endoscopic surveillance is already routine and polarisation may provide additional contrast helpful in the screening process. In the bowel, and the investigation of inflammatory bowel disease (IBD), for example, changes in collagen may provide sufficient contrast in the polarisation regime [75, 188]. Contrast enhancement between healthy and cancerous areas of colon has also been shown [189]. This again is a space where endoscopy is a routine procedure and a polarisation enabled system may fit in well with the clinical workflow. The integration of polarisation resolved imaging could be combined with the cardiovascular work presented in Chapter 4 in another potential avenue of exploration [173, 190]. Here the extreme miniaturisation of a system to 2.30 mm is interesting for intra-vascular use, for example to monitor tissue post infarction [190, 191].

With the advent of on-chip polarisation, the miniaturisation of these technologies is the obvious next step towards *in vivo* endoscopic use of polarimetry. This removes the need for delicate moving parts, while maintaining the flexibility that a distal end device offers. It allows for detection of all necessary polarisation states at once, resulting in a dramatic decrease in acquisition time. The above presented design could be simplified and footprint reduced in this way. The need for the rotating element would be removed. The fibre illumination is kept the same with the addition of some lensing to improve the illumination profile. This could potentially turn around a polarisation-resolved system that is ready for use in the clinic. The meta-surface technology [182, 183] can be retroactively applied onto an image sensor, and does not necessarily need to be integrated with the production process. Existing sensors used in endoscopes, or even micro-cameras could be sensitised provided the bare die is available. At the very small scale, in applications such as the cardiovascular system, limited resolution sensors may still benefit from a mechanical approach at the tip in order to maximise spatial resolution.

The development of flexible polarisation resolved imaging tools enables research into the practical applications of bulk tissue imaging for a variety of biomedical applications. The system presented in this work is a proof of concept to demonstrate the potential of chip-on-tip polarisation resolved systems, which the author of this thesis expects to become more and more prevalent in the coming years. This promises exciting innovations in the clinical translation of polarimetry measurements.

Chapter 7

Conclusion

This thesis has investigated biomedical imaging using miniature CMOS image sensors and provides important contributions to development of chip-on-tip systems for clinical imaging. The investigation has focused on commercially available micro image sensors and their applications as adjunct tools during medical procedures. In this way they can provide additional useful vision information to a clinician, and have the ability to compliment a procedure or other diagnostic tools. CMOS technology promises to be a cost effective solution for wide-field imaging that will see much future development. In this thesis, micro-camera technology has for the first time been used in a variety of novel clinically relevant use-cases.

In order to achieve the integration of the micro-cameras into systems that are ready for such tissue imaging, a comprehensive design and integration strategy has been discussed in Chapter 3. As part of this, various important capabilities have been demonstrated. The efficacy of 3D printing for prototype development was shown, and materials as well as tolerances were discussed. The capability to dice and integrate polarisers and other small optics was demonstrated. Using these, the ability to remove specular reflections and maximise the limited resolution of the sensors was shown. Image processing tools capabilities are also demonstrated. Chip-on-tip systems down to 3 Fr scale were assembled. These investigations have driven the development of a micro-camera technology platform. This is a flexible platform that integrates an imaging sensor on the tip with multi-spectral illumination through optical fibres, and includes custom compact proximal-end illumination units, read-out, control, and image processing systems. The work in Chapter 3 focused on designing and building these multi-spectral imaging systems that were used in the biomedical applications discussed later in the thesis. This technology platform was subsequently applied to different clinical applications. The footprint of the systems and specific requirements naturally varied depending on the application. For some of these applications such as those discussed in Chapter 4 very small footprint systems between 1.19 mm and 2.30 mm were required. For others, such as those in Chapter 5, a handheld device was sufficient. The small size of the sensor also allows for integration with other tools.

In the cardiovascular space, for example, intra-vascular interventions through cardiac catheterisation are well established. The placement of devices through a guiding catheter is a major part of these interventions. In Chapter 4 verification of device placement and of successful ablation was a major motivating factor for the investigation. By developing a catheter compatible imaging system along with integrated saline flush, a micro-camera device was successfully navigated into a porcine animal's beating heart. Here video data of the intra-atrial septum, the left atrium,

and the left ventricle was captured. In order to mimic ablation, hypoxia was induced through an atrial occlusion procedure. While the study was not yet conclusive in its ability to detect hypoxia using colour changes in the video data, analysis was able to extract the heart and respiratory rate *in situ*. Additionally an ablation procedure was performed on the apex of the heart, the imaging of which displayed a colour gradient between healthy and ablated tissue. These results have shown promise for future intravascular imaging using the micro-camera platform. Here the devices can have an adjunct impact on established procedures, providing visual and diagnostic information. The imaging study was also conducted alongside a catheter based DRS system for combination of the two modalities in the future. In this way the camera can also provide navigation for another diagnostic tool. In the lung, a miniature micro-camera platform was shown to be able to navigate further than a traditional bronchoscope, with the study informing the reader on important considerations regarding maneuverability and flexibility of systems. Further development of imaging in the peripheral lung is an interesting line of sight goal.

There are also interesting applications as adjunct handheld tools in surgical applications, as the cameras can be integrated alongside other surgical or diagnostic tools. Ductal carcinoma *in situ* is a precursor lesion to breast cancer where very tight resection margins are observed. The development of tools to help identify positive resection margins intra-operatively was therefore of great clinical interest. One of the potential indicators of malignancy is presence and distribution of micro-calcifications in the tissue. These are traditionally imaged and observed only via mammography. In Chapter 5 the detection of micro-calcifications was shown using traditional imaging on excised breast tissue, for the first time. A handheld imaging tool was developed in collaboration with clinical partners in a cancer hospital. The tool was cross-polarised to remove specular reflections. Lumpectomy slices from 25 patients with DCIS who presented with micro-calcifications in the mammography were imaged using multi-spectral imaging over the course of a study. A rigorous co-location algorithm was developed to validate the results, and image processing techniques were employed to automate detection. Future studies promise further development of the technology and integration with well researched DRS tools for example. The camera can guide point measurement devices through wide-field imaging.

A major advantage of camera imaging is this wide-field contrast that can be achieved. This contrast can be achieved through multi-spectral imaging due to chromosome contrast in the tissue. Contrast can also be created by utilising polarising optics, and capturing the polarisation information of the imaged sample. The capability to integrate polarising optics into small scale integrations as demonstrated in Chapter 3 directly enables the development of miniature and flexible polarisation resolved chip-on-tip imaging tools such as those presented in Chapter 6. In this Chapter, a feasibility study is conducted to investigate the potential of polarisation sensitive imaging using the platform. A micro-camera is integrated alongside diced polarisers into a system that is able to capture 3x3 Mueller matrix images. A benchtop imaging system acts as a validation system and is also used on multi-spectral polarisation resolved imaging of *ex vivo* breast cancer tissue. Feasibility is demonstrated, and the study has informed future improvements and development.

In summary, a micro-camera based miniature imaging platform was presented as an adjunctive clinical tool. Challenges surrounding integration and imaging are overcome. The platform was used successfully in a variety of clinical applications, including *in vivo* imaging in animal studies, and *ex vivo* imaging in a surgical oncology study. Enhancing the imaging capabilities of the camera through image processing, multi-

spectral imaging, and polarisation was demonstrated. The micro-camera promises to be a flexible and effective imaging system that has shown potential to compliment and have a positive impact on medical procedures.

Comments on the Papers

I **Microcamera Visualisation System to Overcome Specular Reflections for Tissue Imaging**
This paper presents two solutions to overcome specular reflections compatible with micro-camera based systems that are designed to visualise biological tissue. The multi-flash technique uses multiple fibres as shifting illumination points to algorithmically filter out specular reflections. The cross polarised method uses orthogonal polarisers across the illumination and detection paths to reduce direct reflections. Both methods proved effective in reducing specular reflections and are further miniaturisable.

I contributed substantially in all aspects of the work, including the planning, design, fabrication, data acquisition and analysis. I also wrote the manuscript.

II **Real-time peri-operative microcalcification detection in superficial breast tissues**
A micro-camera tissue visualisation system is used to detect micro-calcifications in ex-vivo human breast tissue, for the first time. The system is co-registered with x-ray ground truth images, and is able to detect micro-calcifications while removing specular reflection artefacts from images. NIR illumination proved most effective, probing tissue at depth. The detection of micro-calcifications can help locate areas of clinical interest in DCIS surgery and shows promise for integration with other diagnostic tools in the future.

In this joint first authored paper, I was responsible for building the system as well as liaising with clinical collaborators. I contributed in the data acquisition. I performed the data analysis, developed the co-registration algorithm and the image processing, and assisted in the writing of the manuscript.

III **Towards a flexible polarimetric camera-on-tip miniature endoscope for 3×3 Mueller matrix measurements of biological tissue**

In this conference paper, a flexible polarimetry probe designed to capture a partial 3x3 Mueller matrix, with a 5 mm outer diameter is presented. The system uses a micro-camera to act as apolarisation state analyser, and a rotating linear polariser mounted in front of the camera to detect polarisation states. Optical fibres provide illumination, and distally mounted polarisers in front of the fibres act as polarisation state generators.

I ideated the project, developed the concept and co-ordinated the execution. I also contributed significantly to the mechanical design, built the system, performed the measurements, and wrote the manuscript.

IV **Camera-on-tip Angioscope for in-vivo Cardiovascular Diagnostics and Surgical Guidance**

This paper presents a micro-camera and a DRS catheter system to image and sense in the vascular system and the heart. The catheter probe is passed through a guiding catheter into the porcine heart, where video data of the septum, left atrium, and left ventricle is captured. Beyond image guidance, this video data is used to extract physiological information such as respiratory rate and heart rate. The DRS signal is used to differentiate between oxygenated and de-oxygenated tissue during an occlusion.

I contributed to the data analysis and validation, contributed in characterisation measurements of the cameras, and contributed in writing a large portion of the manuscript.

V **Design and assembly of miniature diagnostic catheter imaging systems based on an angioscope study**

The integration of very small components for pre-clinical trial ready prototypes is a challenging. In this paper the design considerations of small footprint imaging systems and the assembly processes are discussed. The bulk of this discussion is based on a novel micro-camera angioscope that successfully navigated into the porcine heart in an animal study, with other smaller footprint devices also discussed.

I contributed to the integration of micro-cameras in very small footprints, was involved in the characterisation measurements of the cameras, and made a substantial contribution to the preparation of the manuscript.

VI **Open-source compact and customisable multi-LED platform for biophotonics applications**

The delivery of light is key to biophotonic applications. A compact light source that fits into a shoe-box sized box is developed. The light source is modular, and with simple exchanging of LEDs and dichroics the available wavelengths of illumination can be controlled. Multiple LEDs are coupled into a single fibre, and can be turned on and off individually, allowing for a combination of LED wavelengths should this be required by the application. This allows for illumination of a variety of systems in a clinical environment. The designs, software, and paper will all be made open source to enable the community to easily replicate and use the compact light source.

I was involved in the construction of the light sources, building one of the first iterations myself, and assisted heavily in the characterisation work. I also provided minor contributions to the writing of the manuscript.

VII **Multi-spectral in-vivo FPGA-based surgical imaging**

Real time in-vivo image analysis is a major requirement in clinical imaging. In addition, more and more image processing and machine learning techniques are applied to acquired images. In this paper, we demonstrate the potential of an FPGA to process data from micro-camera clinical images. An FPGA implementation of a vessel detection algorithm is presented. The re-configurable and application specific nature, in combination with the compactness of the FPGA platform promises to deliver compact, and rapid image processing which can sit close to the imager.

I was involved in developing the concept, providing the algorithms including initial code, and helping with the motivation of the work.

Reflection and Perspectives

As I approach the culmination of my doctoral journey, I find it fitting to reflect on the breadth of challenges and experiences that permeated my time as a doctoral student. I want to reflect not only on the wealth of experience I gained working on what forms the bulk of the thesis, which has been adequately covered in the previous pages, but on the experience as a doctoral student as a whole.

During my time as a PhD student I was faced with a wide range of interesting challenges. I developed a passion for hands-on practical work in the lab, designing and assembling systems under excellent mentorship. I gained a broad knowledge spanning electronics, optics, packaging, and medicine through my involvement in the IPIC2 project and the interdisciplinary collaborations and meetings. Being embedded in such a large and varied group as Biophotonics@Tyndall and involved in such an interdisciplinary project, I was exposed to a variety of different technologies and techniques. I was lucky to be able to interact with clinicians, electronic engineers, and physicists, and learn a little about a lot from all of those interactions. I was able to develop my own work, using miniature image sensors to build systems that were used in clinical studies. Beyond an in-depth understanding of micro-camera technology, breast conserving surgeries, and potential endoscopic applications of the technology, the PhD allowed me to develop a broad foundational knowledge. Through activities in the group I gained an understanding of the wider biophotonics field, from acousto-optics, to upconverting nanoparticles, to spectroscopy, which I hope to use as a springboard for ideas in future projects. Towards the end of my PhD work I discovered the field of polarisation imaging and polarimetry. As I think is often the case, I wish I had discovered this sooner along the journey. It is work which I believe to have lot of potential in clinical translation, and I hope I can explore in more depth in the future. Due to both the research and university modules completed, I received technical training in CAD software, prototyping and assembly, clean-room lithography, and statistics. I developed my ability to structure experiments, and analyse data. It was an educational experience that I will cherish and draw on forever.

I was fortunate enough to enjoy a close working relationship with clinical partners at the Netherlands Cancer Institute, which proved to be one of the most rewarding interactions during this PhD. The collaboration allowed me to work on a fascinating and novel translational project, in close collaboration with clinicians. It also afforded me the opportunity to spend a two month secondment in the hospital in Amsterdam. During this time I was able to close out a three year project on imaging micro-calcifications. I was also able to visit the operating theatre and observe a number of surgeries, including open, laparoscopic, and robotic procedures. I gained the opportunity to experience the “bio” aspect of my work, from the clinical side, and am incredibly grateful for the oppor-

tunity to work with, and in, such an environment alongside both medical and technical staff. Miraculously, I managed to avoid fainting. Since this eye opening experience, I am even more convinced of the importance of immersing yourself in the clinical side of the work. This has certainly been a defining moment of my time as a student and researcher, and cemented my passion for working on projects with direct line of sight to clinical impact and translation. This experience has left a significant and lasting impact on me that I hope will stand to me in my future career.

I also gained huge personal development through professional and leadership activities, that were adjacent to the research. I was involved in the professional societies of SPIE and OPTICA, and spent 3 years on their student chapter committee in Tyndall, as president and vice-president. During this time I saw the chapter grow and inspire myself and many other student members. My involvement has afforded me fantastic networking opportunities both with my peers locally, and with the wider OPTICA and SPIE community abroad. I gained experience in conference organisation, first through my involvement in the IONS2020 conference which we hosted virtually in 2021. Later in 2023, through a connection made at IONS when I co-organised the 31st Plastic Optical Fibre conference hosted locally in Cork. Here we developed an interdisciplinary programme to expand the scope of the conference, to explore the applications of polymer fibres in a variety of disciplines, including, and most interesting to me, in the medical space. Through a postgraduate module, I developed my passion for science communication. I led the relaunch the university's in-house student-led science communication journal, The Boolean. I built a team, developed, and ensured the longevity of the journal in the future. This has seen me invited to give presentations and talks during a number of university postgraduate modules to relay my experience about science communication and open access publishing.

A postgraduate certificate in innovation, commercialisation, and entrepreneurship was completed in conjunction with the PhD with the degree formally award in 2023. This saw the completion of 30 ECTS credits worth of business modules, including IP law, business planning, and marketing. The Explorer programme, a commercial pre-accelerator programme, saw me further develop these learnings through their practical application as I investigated the commercial potential of the work undertaken in my PhD. I was put out of my comfort zone, writing the first ever legal essay of my life, and learning to speak to strangers about technology and how it may solve problems they face in their everyday line of work. It is a skill I hope to develop further in the future, where I hope to speak to more clinicians and identify problems and develop technology to solve those problems. The biggest take-away was how receptive, open, and helpful people can be when asked for a few minutes of their time. This is a lesson I can leverage not only when investigating commercial success in the future, but also when asking for help, and developing networks.

Despite a global health crisis impacting a large portion of my PhD, I got the opportunity to travel, attend and present at conferences and summer schools. This included a fantastic conference at ECBO 2023, and included the huge laser exhibition and trade show. A trip to Photonics Ireland 2023 was where I received a much overdue formal introduction to Irish Photonics research and was able to present my work to peers in Ireland. I was also selected to attend the 2023 OPTICA Student Leadership Experience, and the FiO+LS conference, where 100 international photonics students were brought together for workshops around science

communication, networking, leadership, and careers. I also had the opportunity to attend the fantastic Biophotonics Summer School 2022, where I developed a deeper understanding of the biophotonics field as a whole, and had the pleasure of interacting with biophotonics researchers of all different career stages, both formally and informally. Through my newly developed networks, conference attendance, and my attendance at the summer school, I have been able to meet and interact with leading researchers in my field. I learned to speak to different audiences, lay and technical. I learned to connect with peers and colleagues, and the importance of the same. These experiences have seen me develop many soft skills and is something I won't soon forget.

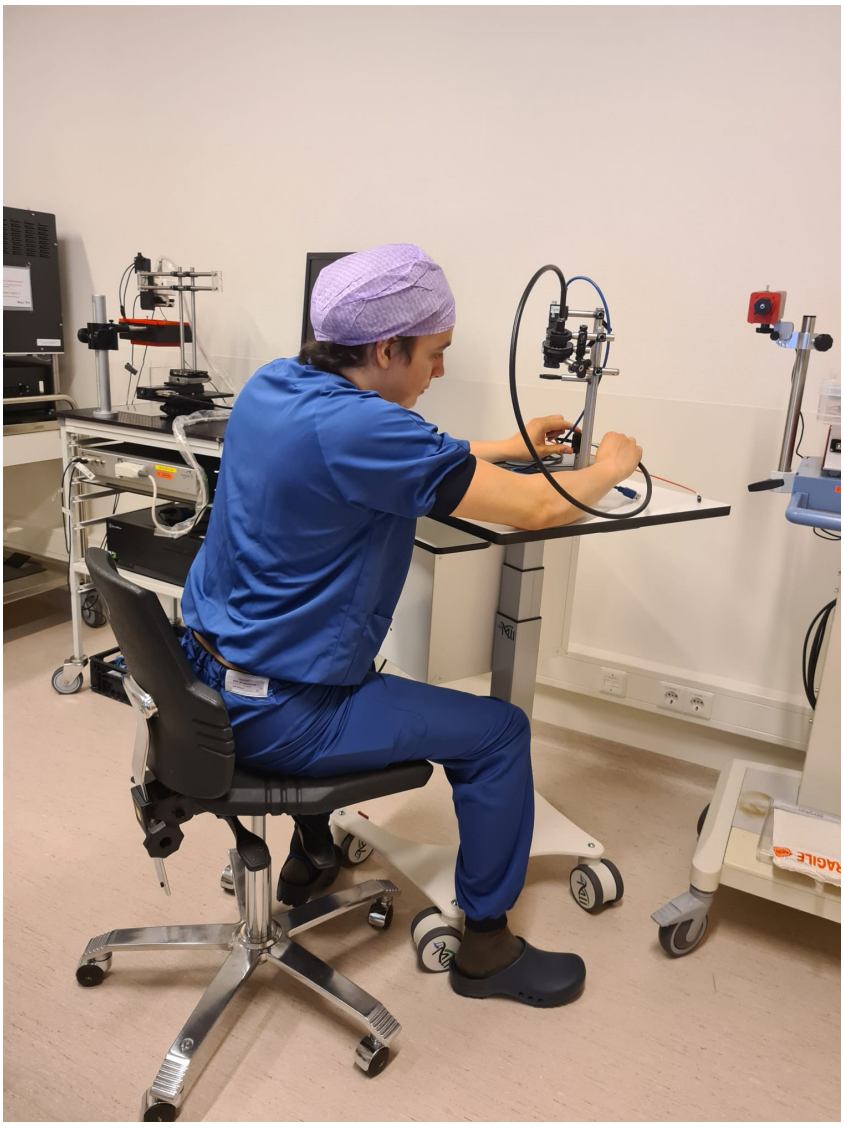

Figure 1. *Working in the OR lab in the Netherlands Cancer Institute, taking measurements on samples using the benchtop polarimetry system described earlier.*

References

[1] Brian W Pogue. Perspective on the optics of medical imaging. *Journal of Biomedical Optics*, 28(12):121208–121208, 2023.

[2] Laura Marcu, Stephen A Boppart, Mark R Hutchinson, Jürgen Popp, and Brian C Wilson. Biophotonics: the big picture. *Journal of biomedical optics*, 23(2):021103–021103, 2018.

[3] James G Fujimoto, Wolfgang Drexler, Joel S Schuman, and Christoph K Hitzenberger. Optical coherence tomography (oct) in ophthalmology: introduction. *Optics express*, 17(5):3978–3979, 2009.

[4] Pablo Artal. Wearable adaptive optics for visual applications. In *Digital Optical Technologies 2023*, volume 12624, page 1262405. SPIE, 2023.

[5] Melissa C Skala, Kristin M Riching, Annette Gendron-Fitzpatrick, Jens Eickhoff, Kevin W Eliceiri, John G White, and Nirmala Ramanujam. In vivo multiphoton microscopy of nadh and fad redox states, fluorescence lifetimes, and cellular morphology in precancerous epithelia. *Proceedings of the National Academy of Sciences*, 104(49):19494–19499, 2007.

[6] Yinghua Sun, Jennifer Phipps, Daniel S Elson, Heather Stoy, Steven Tinling, Jeremy Meier, Brian Poirier, Frank S Chuang, D Gregory Farwell, and Laura Marcu. Fluorescence lifetime imaging microscopy: in vivo application to diagnosis of oral carcinoma. *Optics letters*, 34(13):2081–2083, 2009.

[7] Rupsa Datta, Tiffany M Heaster, Joe T Sharick, Amani A Gillette, and Melissa C Skala. Fluorescence lifetime imaging microscopy: fundamentals and advances in instrumentation, analysis, and applications. *Journal of biomedical optics*, 25(7):071203–071203, 2020.

[8] Kevin K Tremper. Pulse oximetry. *Chest*, 95(4):713–715, 1989.

[9] Konstantin Grygoryev, Huihui Lu, Celina L Li, Alexander V Zhdanov, Ray Burke, and Stefan Andersson-Engels. Multi-spectral clinical prototype for fluorophore detection. *Frontiers in Physics*, 9:724962, 2021.

[10] Haiyan Xie, Zhiyuan Xie, Monirehalsadat Mousavi, Niels Bendsoe, Mikkel Brydegaard, Johan Axelsson, and Stefan Andersson-Engels. Design and validation of a fiber optic point probe instrument for therapy guidance and monitoring. *Journal of biomedical optics*, 19 (7):071408–071408, 2014.

[11] Marcelo Saito Nogueira, Siddra Maryam, Michael Amissah, Huihui Lu, Noel Lynch, Shane Killeen, Micheal O'Riordain, and Stefan Andersson-Engels. Evaluation of wavelength ranges and tissue

depth probed by diffuse reflectance spectroscopy for colorectal cancer detection. *Scientific reports*, 11(1):798, 2021.

[12] LL De Boer, BG Molenkamp, TM Bydlon, BHW Hendriks, J Wesseling, HJCM Sterenborg, and TJM Ruers. Fat/water ratios measured with diffuse reflectance spectroscopy to detect breast tumor boundaries. *Breast cancer research and treatment*, 152:509–518, 2015.

[13] Eric J Seibel, Richard S Johnston, and C David Melville. A full-color scanning fiber endoscope. In *Optical fibers and sensors for medical diagnostics and treatment applications VI*, volume 6083, pages 9–16. SPIE, 2006.

[14] Luis E Savastano and Eric J Seibel. Scanning fiber angioscopy: a multimodal intravascular imaging platform for carotid atherosclerosis. *Neurosurgery*, 64(CN Suppl 1):188, 2017.

[15] Ji Qi and Daniel S Elson. A high definition mueller polarimetric endoscope for tissue characterisation. *Scientific reports*, 6(1):25953, 2016.

[16] Timothy D Soper, Michael P Porter, and Eric J Seibel. Surface mosaics of the bladder reconstructed from endoscopic video for automated surveillance. *IEEE Transactions on Biomedical Engineering*, 59(6):1670–1680, 2012.

[17] Timothy D Soper, David R Haynor, Robb W Glenny, and Eric J Seibel. In vivo validation of a hybrid tracking system for navigation of an ultrathin bronchoscope within peripheral airways. *IEEE Transactions on Biomedical Engineering*, 57(3):736–745, 2009.

[18] Ricky Cordova, Kelli Kiekens, Susan Burrell, William Drake, Zaynah Kmeid, Photini Rice, Andrew Rocha, Sebastian Diaz, Shigehiro Yamada, Michael Yozwiak, et al. Sub-millimeter endoscope demonstrates feasibility of in vivo reflectance imaging, fluorescence imaging, and cell collection in the fallopian tubes. *Journal of biomedical optics*, 26(7):076001–076001, 2021.

[19] Marco Lai, Stefan D van der Stel, Harald C Groen, Mark van Gastel, Koert FD Kuhlmann, Theo JM Ruers, and Benno HW Hendriks. Imaging ppg for in vivo human tissue perfusion assessment during surgery. *Journal of Imaging*, 8(4):94, 2022.

[20] Stefan D van der Stel, Marco Lai, Harald C Groen, Mark Witteveen, Koert FD Kuhlmann, Brechtje A Grotenhuis, Niels FM Kok, Mark van Gastel, Benno HW Hendriks, and Theo JM Ruers. Imaging photoplethysmography for noninvasive anastomotic perfusion assessment in intestinal surgery. *Journal of surgical research*, 283:705–712, 2023.

[21] Anouk L Post, Albert J de Groof, Xu U Zhang, Anne-Fré Swager, Kiki N Fockens, Roos E Pouw, Bas LAM Weusten, Dirk J Faber, Daniel M de Bruin, Jacques JGHM Bergman, et al. Toward improved endoscopic surveillance with multidiameter single fiber reflectance spectroscopy in patients with barrett's esophagus. *Journal of biophotonics*, 14(4):e202000351, 2021.

[22] Muhammad Khalid Khan Niazi, Anil V Parwani, and Metin N Gurcan. Digital pathology and artificial intelligence. *The Lancet Oncology*, 20(5):e253–e261, 2019.

[23] Esther Kho, Lisanne L de Boer, Koen K Van de Vijver, Frederieke van Duijnhoven, Marie-Jeanne TFD Vrancken Peeters, Henricus JCM Sterenborg, and Theo JM Ruers. Hyperspectral imaging for resection margin assessment during cancer surgery. *Clinical cancer research*, 25(12):3572–3580, 2019.

[24] Lisanne L de Boer, Esther Kho, Koen K Van de Vijver, Marie-Jeanne TFD Vranken Peeters, Frederieke van Duijnhoven, Benno HW Hendriks, Henricus JCM Sterenborg, and Theo JM Ruers. Optical tissue measurements of invasive carcinoma and ductal carcinoma in situ for surgical guidance. *Breast cancer research*, 23(1):1–15, 2021.

[25] Natan T Shaked, Stephen A Boppart, Lihong V Wang, and Jürgen Popp. Label-free biomedical optical imaging. *Nature Photonics*, pages 1–11, 2023.

[26] Stephen A Boppart, J Quincy Brown, Camile S Farah, Esther Kho, Laura Marcu, Christobel M Saunders, and Henricus JCM Sterenborg. Label-free optical imaging technologies for rapid translation and use during intraoperative surgical and tumor margin assessment. *Journal of biomedical optics*, 23(2):021104–021104, 2018.

[27] Banghe Zhu, Farouc A Jaffer, Vasilis Ntziachristos, and Ralph Weissleder. Development of a near infrared fluorescence catheter: operating characteristics and feasibility for atherosclerotic plaque detection. *Journal of Physics D: Applied Physics*, 38(15):2701, 2005.

[28] Rachel Georgel, Konstantin Grygoryev, Simon Sorensen, Huihui Lu, Stefan Andersson-Engels, Ray Burke, and Daniel O'Hare. Silicon photomultiplier—a high dynamic range, high sensitivity sensor for bio-photonics applications. *Biosensors*, 12(10):793, 2022.

[29] Ray Fontaine. The evolution of pixel structures for consumer-grade image sensors. *IEEE Transactions on semiconductor manufacturing*, 26(1):11–16, 2013.

[30] Konstantin Grygoryev, Katarzyna Komolibus, Jacqueline Gunther, Gerard Nunan, Kevin Manley, Stefan Andersson-Engels, and Ray Burke. Cranial perforation using an optically-enhanced surgical drill. *IEEE Transactions on Biomedical Engineering*, 67(12):3474–3482, 2020.

[31] Huihui Lu, Konstantin Grygoryev, Niamh Bermingham, Michael Jansen, Michael O'Sullivan, Gerard Nunan, Kevin Buckley, Kevin Manley, Ray Burke, and Stefan Andersson-Engels. Combined autofluorescence and diffuse reflectance for brain tumour surgical guidance: initial ex vivo study results. *Biomedical Optics Express*, 12 (4):2432–2446, 2021.

[32] Jürgen Popp, Dennis Matthews, Alfredo Martinez-Coll, Thomas Mayerhöfer, and Brian C Wilson. Challenges in translation: models to promote translation. *Journal of Biomedical Optics*, 23(2): 021101–021101, 2018.

[33] Martin Wäny, Stephan Voltz, Fabio Gaspar, Lei Chen, and AWAIBA Lda Madeira Tecnopolo. Ultrasmall digital image sensor for endoscopic applications. In *Proc. Int. Image Sensor Workshop*, pages 1–3, 2009.

[34] S Schlegel, B Blase, D Brüggemann, F Bühs, R Dreyer, M Kelp, H Lehr, and S Oginski. Endoscope with flexible tip and chip-on-the-tip camera. In *World Congress on Medical Physics and Biomedical Engineering May 26-31, 2012, Beijing, China*, pages 2111–2114. Springer, 2013.

[35] Cori L Ofstead, Krystina M Hopkins, Matthew J Binnicker, and Gregory A Poland. Potential impact of contaminated bronchoscopes on novel coronavirus disease (covid-19) patients. *Infection Control & Hospital Epidemiology*, 41(7):862–864, 2020.

[36] Momen M Wahidi, Carla Lamb, Septimiu Murgu, Ali Musani, Samira Shojaee, Ashutosh Sachdeva, Fabien Maldonado, Kamran Mahmood, Matthew Kinsey, Sonali Sethi, et al. American association for bronchology and interventional pulmonology (aabip) statement on the use of bronchoscopy and respiratory specimen collection in patients with suspected or confirmed covid-19 infection. *Journal of bronchology & interventional pulmonology*, 27(4): e52–e54, 2020.

[37] Gregor Matz, Bernhard Messerschmidt, Werner Göbel, Severin Filser, Christian S Betz, Matthias Kirsch, Ortrud Uckermann, Marcel Kunze, Sven Flämig, André Ehrhardt, et al. Chip-on-the-tip compact flexible endoscopic epifluorescence video-microscope for in-vivo imaging in medicine and biomedical research. *Biomedical optics express*, 8(7):3329–3342, 2017.

[38] Lueder Alexander Kahrs, Theodore R McRackan, and Robert F Labadie. Intracochlear visualization: comparing established and novel endoscopy techniques. *Otology & Neurotology*, 32(9):1590–1595, 2011.

[39] Joshua Gafford, Michael Freeman, Loris Fichera, Jack Noble, Robert Labadie, and Robert J Webster. Eyes in ears: a miniature steerable digital endoscope for trans-nasal diagnosis of middle ear disease. *Annals of biomedical engineering*, 49:219–232, 2021.

[40] Brennan L Moeller, Brian W Herrmann, and Mark E Rentschler. A novel articulating chip–on–tip endoscope for dynamic middle ear surgical visualization. *IEEE Transactions on Biomedical Engineering*, 2023.

[41] Xianming Ye, John-John Cabibihan, and W Jong Yoon. Design and verification of a flexible device for steering a tethered capsule endoscope in the stomach. In *2017 14th International Conference on Ubiquitous Robots and Ambient Intelligence (URAI)*, pages 550–555. IEEE, 2017.

[42] Gills Fai, Sarah Ostlie, Michael Greminger, Roy Cho, and H Erhan Dincer. Tool for transbronchial biopsies of peripheral lung nodules. In *Frontiers in Biomedical Devices*, volume 41037, page V001T06A006. American Society of Mechanical Engineers, 2019.

[43] Maximilian Eisel, Frank Strittmatter, Stephan Ströbl, Christian Freymüller, Thomas Pongratz, and Ronald Sroka. Comparative investigation of reusable and single–use flexible endoscopes for urological interventions. *Scientific Reports*, 10(1):5701, 2020.

[44] Muralidhar Padala, Jorge H Jimenez, Ajit P Yoganathan, Albert Chin, and Vinod H Thourani. Transapical beating heart cardioscopy technique for off-pump visualization of heart valves. *The Journal of thoracic and cardiovascular surgery*, 144(1):231–234, 2012.

[45] Georgios Fagogenis, Margherita Mencattelli, Zurab Machaidze, Benoit Rosa, Karl Price, F Wu, V Weixler, Mossab Saeed, John E Mayer, and Pierre E Dupont. Autonomous robotic intracardiac catheter navigation using haptic vision. *Science robotics*, 4(29), 2019.

[46] Amal Alotaibi, Ghannam Al-Dossari, and Patrick T Roughneen. Cardioscope: A new innovation for visualization of intracardiac pathology. *Structural Heart*, 3:27, 2019.

[47] Christopher J Payne, Gauthier Gras, Michael Hughes, Dinesh Nathwani, and Guang-Zhong Yang. A hand-held flexible mechatronic device for arthroscopy. In *2015 IEEE/RSJ International Conference on Intelligent Robots and Systems (IROS)*, pages 817–823. IEEE, 2015.

[48] Han-Chao Chang and Wen-Yu Chiu. A single-pore knee arthroscopy system for injured athletes. In *2018 IEEE International Conference on Applied System Invention (ICASI)*, pages 1086–1087. IEEE, 2018.

[49] Benjamin Gorissen, Michael De Volder, and Dominiek Reynaerts. Chip-on-tip endoscope incorporating a soft robotic pneumatic bending microactuator. *Biomedical microdevices*, 20:1–7, 2018.

[50] Masaaki Nakayama, Chieko Hamada, Keitaro Yokoyama, Yudo Tanno, Nanae Matsuo, Junichiro Nakata, Yoshio Ishibashi, Atsushi Okuzawa, Kazuhiro Sakamoto, Tamaki Nara, et al. A disposable, ultra-fine endoscope for non-invasive, close examination of the intraluminal surface of the peritoneal dialysis catheter and peritoneal cavity. *Scientific reports*, 10(1):17565, 2020.

[51] Andrew D Rocha, William K Drake, Photini F Rice, Dilara J Long, Hasina Shir, Ryan HM Walton, Mary N Reed, Dominique Galvez, Taliah Gorman, John M Heusinkveld, et al. Iterative prototyping based on lessons learned from the falloposcope in vivo pilot study experience. *Journal of Biomedical Optics*, 28(12):121206–121206, 2023.

[52] Steven L Jacques and Brian W Pogue. Tutorial on diffuse light transport. *Journal of biomedical optics*, 13(4):041302–041302, 2008.

[53] Ashley J Welch, Martin JC Van Gemert, et al. *Optical-thermal response of laser-irradiated tissue*, volume 2. Springer, 2011.

[54] Thomas J Dougherty, Charles J Gomer, Barbara W Henderson, Giulio Jori, David Kessel, Mladen Korbelik, Johan Moan, and Qian Peng. Photodynamic therapy. *Journal of National Cancer Institute*, 90(12):889–905, 1998.

[55] Patrizia Agostinis, Kristian Berg, Keith A Cengel, Thomas H Foster, Albert W Girotti, Sandra O Gollnick, Stephen M Hahn, Michael R Hamblin, Asta Juzeniene, David Kessel, et al. Photodynamic therapy of cancer: an update. *CA: A Cancer Journal for Clinicians*, 61(4):250–281, 2011.

[56] William L Epstein, Kimie Fukuyama, and John H Epstein. Early effects of ultraviolet light on dna synthesis in human skin in vivo. *Archives of Dermatology*, 100(1):84–89, 1969.

[57] Fred A Mettler. Medical effects and risks of exposure to ionising radiation. *Journal of Radiological Protection*, 32(1):N9, 2012.

[58] Andreas H Hielscher, Judith R Mourant, and Irving J Bigio. Influence of particle size and concentration on the diffuse backscattering of polarized light from tissue phantoms and biological cell suspensions. *Applied optics*, 36(1):125–135, 1997.

[59] Matthew H Smith, Paul D Burke, Arthur Lompado, Elizabeth A Tanner, and Lloyd W Hillman. Mueller matrix imaging polarimetry in dermatology. In *Biomedical Diagnostic, Guidance, and Surgical-Assist Systems II*, volume 3911, pages 210–216. SPIE, 2000.

[60] Jungrae Chung, Woonggyu Jung, Marie J Hammer-Wilson, Petra Wilder-Smith, and Zhongping Chen. Use of polar decomposition for the diagnosis of oral precancer. *Applied optics*, 46(15):3038–3045, 2007.

[61] RMP Doornbos, Roland Lang, MC Aalders, FW Cross, and HJCM Sterenborg. The determination of in vivo human tissue optical properties and absolute chromophore concentrations using spatially resolved steady-state diffuse reflectance spectroscopy. *Physics in Medicine & Biology*, 44(4):967, 1999.

[62] Can T Xu, Qiuqiang Zhan, Haichun Liu, Gabriel Somesfalean, Jun Qian, Sailing He, and Stefan Andersson-Engels. Upconverting nanoparticles for pre-clinical diffuse optical imaging, microscopy and sensing: Current trends and future challenges. *Laser & Photonics Reviews*, 7(5):663–697, 2013.

[63] Laura Marcu. Fluorescence lifetime techniques in medical applications. *Annals of biomedical engineering*, 40:304–331, 2012.

[64] Isaac Pence and Anita Mahadevan-Jansen. Clinical instrumentation and applications of raman spectroscopy. *Chemical Society Reviews*, 45(7):1958–1979, 2016.

[65] Steven L Jacques. Optical properties of biological tissues: a review. *Physics in Medicine & Biology*, 58(11):R37, 2013.

[66] Ralph Weissleder. A clearer vision for in vivo imaging. *Nature biotechnology*, 19(4):316–317, 2001.

[67] Caroline Boudoux. *Fundamentals of biomedical optics*. Blurb, 2017.

[68] E. Hecht. *Optics*. Pearson education. Addison-Wesley, 2002. ISBN 9780321188786. URL https://books.google.ie/books?id=T3ofAQAAMAAJ.

[69] Craig F Bohren and Donald R Huffman. *Absorption and scattering of light by small particles*. John Wiley & Sons, 2008.

[70] Grant R Fowles. *Introduction to modern optics*. Courier Corporation, 1989.

[71] Andrew M Smith, Michael C Mancini, and Shuming Nie. Second window for in vivo imaging. *Nature nanotechnology*, 4(11):710–711, 2009.

[72] Laura A Sordillo, Sebastião Pratavieira, Yang Pu, Kaliris Salas-Ramirez, Lingyan Shi, Lin Zhang, Yury Budansky, and RR Alfano. Third therapeutic spectral window for deep tissue imaging. In *Optical Biopsy XII*, volume 8940, pages 128–134. SPIE, 2014.

[73] Shree K Nayar, Xi-Sheng Fang, and Terrance Boult. Separation of reflection components using color and polarization. *International Journal of Computer Vision*, 21(3):163–186, 1997.

[74] William T Doyle. Scattering approach to fresnel's equations and brewster's law. *American Journal of Physics*, 53(5):463–468, 1985.

[75] Jessica C Ramella-Roman and Tatiana Novikova. *Polarized Light in Biomedical Imaging and Sensing: Clinical and Preclinical Applications*. Springer Nature, 2022.

[76] MK Swami, S Manhas, P Buddhiwant, N Ghosh, A Uppal, and PK Gupta. Polar decomposition of 3× 3 mueller matrix: a tool for quantitative tissue polarimetry. *Optics express*, 14(20):9324–9337, 2006.

[77] Shih-Yau Lu and Russell A Chipman. Interpretation of mueller matrices based on polar decomposition. *Journal of the Optical Society of America A*, 13(5):1106–1113, 1996.

[78] Shih-Yau Lu and Russell A Chipman. Mueller matrices and the degree of polarization. *Optics communications*, 146(1-6):11–14, 1998.

[79] KM Yoo and RR Alfano. Time resolved depolarization of multiple backscattered light from random media. *Physics letters A*, 142 (8-9):531–536, 1989.

[80] Ji Qi and Daniel S Elson. Mueller polarimetric imaging for surgical and diagnostic applications: a review. *Journal of biophotonics*, 10 (8):950–982, 2017.

[81] Wanrong Gao. Changes of polarization of light beams on propagation through tissue. *Optics Communications*, 260(2):749–754, 2006.

[82] Ahmet T Erdogan, Tarek Al Abbas, Neil Finlayson, Charlotte Hopkinson, Istvan Gyongy, Oscar Almer, Neale AW Dutton, and Robert K Henderson. A high dynamic range 128× 120 3-d stacked cmos spad image sensor soc for fluorescence microendoscopy. *IEEE Journal of Solid-State Circuits*, 57(6):1649–1660, 2022.

[83] Andrew B Matheson, Ahmet T Erdogan, Charlotte Hopkinson, Sam Borrowman, Gary J Loake, Michael G Tanner, and Robert K Henderson. Handheld wide-field fluorescence lifetime imaging system based on a distally mounted spad array. *Optics Express*, 31 (14):22766–22775, 2023.

[84] WM Lee and SH Yun. Adaptive aberration correction of grin lenses for confocal endomicroscopy. *Optics letters*, 36(23):4608–4610, 2011.

[85] Dominique Galvez, Zhihan Hong, Andrew D Rocha, John M Heusinkveld, Piaoran Ye, Rongguang Liang, and Jennifer K Barton. Characterizing close-focus lenses for microendoscopy. *Journal of Optical Microsystems*, 3(1):011003–011003, 2023.

[86] Nicholas Hollows, Gregory; James. Resolution. [retrieved 18 June 2024], https://www.edmundoptics.eu/knowledge-center/application-notes/imaging/resolution/.

[87] Glenn D Boreman. *Modulation transfer function in optical and electro-optical systems*, volume 4. SPIE press Bellingham, Washington, 2001.

[88] John Canny. A computational approach to edge detection. *IEEE Transactions on pattern analysis and machine intelligence*, (6):679–698, 1986.

[89] Alejandro F Frangi, Wiro J Niessen, Koen L Vincken, and Max A Viergever. Multiscale vessel enhancement filtering. In *Medical Image Computing and Computer-Assisted Intervention—MICCAI'98: First International Conference Cambridge, MA, USA, October 11–13, 1998 Proceedings 1*, pages 130–137. Springer, 1998.

[90] Cristian Lorenz, I-C Carlsen, Thorsten M Buzug, Carola Fassnacht, and Jürgen Weese. Multi-scale line segmentation with automatic estimation of width, contrast and tangential direction in 2d and 3d medical images. In *International Conference on Computer Vision, Virtual Reality, and Robotics in Medicine*, pages 233–242. Springer, 1997.

[91] A Elbalaoui, M Fakir, K Taifi, and A Merbouha. Automatic detection of blood vessel in retinal images. In *2016 13th International Conference on Computer Graphics, Imaging and Visualization (CGiV)*, pages 324–332. IEEE, 2016.

[92] Karl Krissian, Grégoire Malandain, Nicholas Ayache, Régis Vaillant, and Yves Trousset. Model-based detection of tubular structures in 3d images. *Computer vision and image understanding*, 80 (2):130–171, 2000.

[93] Marcin Rudzki. Vessel detection method based on eigenvalues of the hessian matrix and its applicability to airway tree segmentation. In *Proceedings of the 11th International PhD Workshop OWD*, pages 100–105, 2009.

[94] Stephen M Pizer, E Philip Amburn, John D Austin, Robert Cromartie, Ari Geselowitz, Trey Greer, Bart ter Haar Romeny, John B Zimmerman, and Karel Zuiderveld. Adaptive histogram equalization and its variations. *Computer vision, graphics, and image processing*, 39(3):355–368, 1987.

[95] Paul E Debevec and Jitendra Malik. Recovering high dynamic range radiance maps from photographs. In *Seminal Graphics Papers: Pushing the Boundaries, Volume 2*, pages 643–652. 2023.

[96] Mark A Robertson, Sean Borman, and Robert L Stevenson. Dynamic range improvement through multiple exposures. In *Proceedings 1999 international conference on image processing (Cat. 99CH36348)*, volume 3, pages 159–163. IEEE, 1999.

[97] Tom Mertens, Jan Kautz, and Frank Van Reeth. Exposure fusion. In *15th Pacific Conference on Computer Graphics and Applications (PG'07)*, pages 382–390. IEEE, 2007.

[98] John Allen. Photoplethysmography and its application in clinical physiological measurement. *Physiological measurement*, 28(3):R1, 2007.

[99] Heng-Da Cheng, X_ H_ Jiang, Ying Sun, and Jingli Wang. Color image segmentation: advances and prospects. *Pattern recognition*, 34(12):2259–2281, 2001.

[100] Brian C Wilson, Michael Jermyn, and Frederic Leblond. Challenges and opportunities in clinical translation of biomedical optical spectroscopy and imaging. *Journal of biomedical optics*, 23(3): 030901–030901, 2018.

[101] Daniel M Beswick, Arjun Kaushik, Dylan Beinart, Sarah McGarry, Ming Khoon Yew, Brendan F Kennedy, and Peter Luke Santa Maria. Biomedical device innovation methodology: applications in

biophotonics. *Journal of Biomedical Optics*, 23(2):021102–021102, 2018.

[102] Courtney Celian, Veronica Swanson, Maahi Shah, Caitlin Newman, Bridget Fowler-King, Sarah Gallik, Kaitlin Reilly, David J Reinkensmeyer, James Patton, and Miriam R Rafferty. A day in the life: a qualitative study of clinical decision-making and uptake of neurorehabilitation technology. *Journal of neuroengineering and rehabilitation*, 18(1):1–12, 2021.

[103] John C Mankins et al. Technology readiness levels. *White Paper, April*, 6(1995):1995, 1995.

[104] Zhan-Yu Chen, Ankur Gogoi, Shao-Yu Lee, Yuan Tsai-Lin, Po-Wei Yi, Ming-Kuan Lu, Chih-Cheng Hsieh, JinChang Ren, Stephen Marshall, and Fu-Jen Kao. Coherent narrow-band light source for miniature endoscopes. *IEEE Journal of Selected Topics in Quantum Electronics*, 25(1):1–7, 2018.

[105] Caitlin Regan, Sean M White, Bruce Y Yang, Thair Takesh, Jessica Ho, Cherie Wink, Petra Wilder-Smith, and Bernard Choi. Design and evaluation of a miniature laser speckle imaging device to assess gingival health. *Journal of biomedical optics*, 21(10):104002–104002, 2016.

[106] Amrit S Lotay and John M Girkin. Towards a portable laser speckle based device to evaluate the level of atrophy in tissue. In *Design and Quality for Biomedical Technologies XII*, volume 10870, pages 29–40. SPIE, 2019.

[107] Lukas Markwalder, Rodney Gush, Faisel Khan, Colin E Murdoch, and Nikola Krstajic. In vivo laser speckle contrast imaging of microvascular blood perfusion using a miniaturized chip-on-tip camera. *Laser Speckle Contrast Imaging of Microvascular Blood Perfusion Using a Miniaturized Chip-on-Tip Camera*, 2023.

[108] David Briers, Donald D Duncan, Evan Hirst, Sean J Kirkpatrick, Marcus Larsson, Wiendelt Steenbergen, Tomas Stromberg, and Oliver B Thompson. Laser speckle contrast imaging: theoretical and practical limitations. *Journal of biomedical optics*, 18(6): 066018–066018, 2013.

[109] Toshiaki Iwai and Toshimitsu Asakura. Speckle reduction in coherent information processing. *Proceedings of the IEEE*, 84(5): 765–781, 1996.

[110] Majed Alsharari, Son T Mai, Romain Garnier, Carlos Reaño, and Roger Woods. An intelligent image processing system for enhancing blood vessel segmentation on low-power soc. In *International Conference on Embedded Computer Systems*, pages 123–138. Springer, 2023.

[111] Teruyoshi Kume and Shiro Uemura. Current clinical applications of coronary optical coherence tomography. *Cardiovascular intervention and therapeutics*, 33:1–10, 2018.

[112] Shinjo Sonoda, Kiyoshi Hibi, Hiroyuki Okura, Kenichi Fujii, Yasuhiro Honda, and Yoshio Kobayashi. Current clinical use of intravascular ultrasound imaging to guide percutaneous coronary interventions. *Cardiovascular intervention and therapeutics*, 35:30–36, 2020.

[113] Hector M Garcia-Garcia, Marco A Costa, and Patrick W Serruys. Imaging of coronary atherosclerosis: intravascular ultrasound. *European heart journal*, 31(20):2456–2469, 2010.

[114] Takashi Kubo, Takashi Akasaka, Junya Shite, Takahiko Suzuki, Shiro Uemura, Bo Yu, Ken Kozuma, Hironori Kitabata, Toshiro Shinke, Maoto Habara, et al. Oct compared with ivus in a coronary lesion assessment: the opus-class study. *JACC: Cardiovascular Imaging*, 6(10):1095–1104, 2013.

[115] Luis E Savastano, Quan Zhou, Arlene Smith, Karla Vega, Carlos Murga-Zamalloa, David Gordon, Jon McHugh, Lili Zhao, Michael M Wang, Aditya Pandey, et al. Multimodal laser-based angioscopy for structural, chemical and biological imaging of atherosclerosis. *Nature Biomedical Engineering*, 1(2):0023, 2017.

[116] Patrick Z McVeigh, Raphael Sacho, Robert A Weersink, Vitor M Pereira, Walter Kucharczyk, Eric J Seibel, Brian C Wilson, and Timo Krings. High-resolution angioscopic imaging during endovascular neurosurgery. *Neurosurgery*, 75(2):171, 2014.

[117] Patrick Z McVeigh, Tony Moloney, Brian C Wilson, and Mark Wheatcroft. High-resolution scanning fiber angioscopy as an adjuvant to fluoroscopy during endovascular interventions. *Journal of Endovascular Therapy*, 25(5):617–623, 2018.

[118] TJ Cahill, Mao Chen, Kentaro Hayashida, Azeem Latib, Thomas Modine, Nicolo Piazza, S Redwood, L Søndergaard, and Bernard D Prendergast. Transcatheter aortic valve implantation: current status and future perspectives. *European heart journal*, 39(28):2625–2634, 2018.

[119] Abass Alavi, Babak Saboury, and Sandip Basu. Imaging the infected heart. *Science Translational Medicine*, 3(99):99fs3–99fs3, 2011.

[120] International Early Lung Cancer Action Program Investigators. Survival of patients with stage i lung cancer detected on ct screening. *New England Journal of Medicine*, 355(17):1763–1771, 2006.

[121] Kashif Ali Khan, Pietro Nardelli, Alex Jaeger, Conor O'Shea, Padraig Cantillon-Murphy, and Marcus P Kennedy. Navigational bronchoscopy for early lung cancer: a road to therapy. *Advances in therapy*, 33:580–596, 2016.

[122] Herman A Jaeger, Pietro Nardelli, Conor O'shea, Josef Tugwell, Kashif A Khan, Timothy Power, Michael O'shea, Marcus P Kennedy, and Pádraig Cantillon-Murphy. Automated catheter navigation with electromagnetic image guidance. *IEEE Transactions on Biomedical Engineering*, 64(8):1972–1979, 2017.

[123] David Fielding and Masahide Oki. Technologies for targeting the peripheral pulmonary nodule including robotics. *Respirology*, 25 (9):914–923, 2020.

[124] Hongxia Zhang, Yang Guang, Wen He, Linggang Cheng, Tengfei Yu, Yu Tang, Haiman Song, Xin Liu, and Yukang Zhang. Ultrasound-guided percutaneous needle biopsy skill for peripheral lung lesions and complications prevention. *Journal of Thoracic Disease*, 12(7):3697, 2020.

[125] Abhinav Agrawal, D Kyle Hogarth, and Septimiu Murgu. Robotic bronchoscopy for pulmonary lesions: a review of existing technologies and clinical data. *Journal of thoracic disease*, 12(6):3279, 2020.

[126] Abhishek Kumar, Jose D Caceres, Siddharthan Vaithilingam, Gurshan Sandhu, and Nikhil K Meena. Robotic bronchoscopy for peripheral pulmonary lesion biopsy: Evidence-based review of the two platforms. *Diagnostics*, 11(8):1479, 2021.

[127] Helmut Neumann, Mitsuhiro Fujishiro, C Mel Wilcox, and Klaus Mönkemüller. Present and future perspectives of virtual chromoendoscopy with i-scan and optical enhancement technology. *Digestive Endoscopy*, 26:43–51, 2014.

[128] Partha Pal, Aniruddha Pratap Singh, Navya D Kanuri, and Rupa Banerjee. Electronic chromo-endoscopy: technical details and a clinical perspective. *Translational Gastroenterology and Hepatology*, 7, 2022.

[129] Junjie Huang, Paul SF Chan, Veeleah Lok, Xiao Chen, Hanyue Ding, Yinzi Jin, Jinqiu Yuan, Xiang-qian Lao, Zhi-Jie Zheng, and Martin CS Wong. Global incidence and mortality of breast cancer: a trend analysis. *Aging (Albany NY)*, 13(4):5748, 2021.

[130] Nasrindokht Azamjah, Yasaman Soltan-Zadeh, and Farid Zayeri. Global trend of breast cancer mortality rate: a 25-year study. *Asian Pacific journal of cancer prevention: APJCP*, 20(7):2015, 2019.

[131] Fátima Cardoso, S Kyriakides, S Ohno, F Penault-Llorca, P Poortmans, IT Rubio, S Zackrisson, and E Senkus. Early breast cancer: Esmo clinical practice guidelines for diagnosis, treatment and follow-up. *Annals of oncology*, 30(8):1194–1220, 2019.

[132] KS Asgeirsson, T Rasheed, SJ McCulley, and RD Macmillan. Oncological and cosmetic outcomes of oncoplastic breast conserving surgery. *European Journal of Surgical Oncology (EJSO)*, 31(8): 817–823, 2005.

[133] Anita Bane et al. Ductal carcinoma in situ: what the pathologist needs to know and why. *International Journal of Breast Cancer*, 2013, 2013.

[134] Gaiane M Rauch, Brian P Hobbs, Henry M Kuerer, Marion E Scoggins, Ana P Benveniste, Young Mi Park, Abigail S Caudle, Patricia S Fox, Benjamin D Smith, Beatriz E Adrada, et al. Microcalcifications in 1657 patients with pure ductal carcinoma in situ of the breast: correlation with clinical, histopathologic, biologic features, and local recurrence. *Annals of surgical oncology*, 23:482–489, 2016.

[135] Virginia L Ernster, Rachel Ballard-Barbash, William E Barlow, Yingye Zheng, Donald L Weaver, Gary Cutter, Bonnie C Yankaskas, Robert Rosenberg, Patricia A Carney, Karla Kerlikowske, et al. Detection of ductal carcinoma in situ in women undergoing screening mammography. *Journal of the National Cancer Institute*, 94(20):1546–1554, 2002.

[136] Susan G Brouwer de Koning, Marie-Jeanne TFD Vrancken Peeters, Katarzyna Jóźwiak, Patrick A Bhairosing, and Theo JM Ruers. Tumor resection margin definitions in breast-conserving surgery: systematic review and meta-analysis of the current literature. *Clinical breast cancer*, 18(4):e595–e600, 2018.

[137] Monica Morrow, Kimberly J Van Zee, Lawrence J Solin, Nehmat Houssami, Mariana Chavez-MacGregor, Jay R Harris, Janet Horton, Shelley Hwang, Peggy L Johnson, M Luke Marinovich, et al. Society of surgical oncology–american society for radiation

oncology–american society of clinical oncology consensus guideline on margins for breast-conserving surgery with whole-breast irradiation in ductal carcinoma in situ. *Practical radiation oncology*, 6 (5):287–295, 2016.

[138] Adri C Voogd, Maja Nielsen, Johannes L Peterse, Mogens Blichert-Toft, Harry Bartelink, Marie Overgaard, Geertjan van Tienhoven, Knud West Andersen, Richard J Sylvester, Joop A van Dongen, et al. Differences in risk factors for local and distant recurrence after breast-conserving therapy or mastectomy for stage i and ii breast cancer: pooled results of two large european randomized trials. *Journal of clinical oncology*, 19(6):1688–1697, 2001.

[139] Funda Meric, Nadeem Q Mirza, Georges Vlastos, Thomas A Buchholz, Henry M Kuerer, Gildy V Babiera, S Eva Singletary, Merrick I Ross, Frederick C Ames, Barry W Feig, et al. Positive surgical margins and ipsilateral breast tumor recurrence predict disease-specific survival after breast-conserving therapy. *Cancer: Interdisciplinary International Journal of the American Cancer Society*, 97(4):926–933, 2003.

[140] Michael S Toss, Sarah E Pinder, Andrew R Green, Jeremy Thomas, David AL Morgan, John FR Robertson, Ian O Ellis, and Emad A Rakha. Breast conservation in ductal carcinoma in situ (dcis): what defines optimal margins? *Histopathology*, 70(5):681–692, 2017.

[141] Riries Rulaningtyas, Agoes Santika Hyperastuty, and Anny Setijo Rahaju. Histopathology grading identification of breast cancer based on texture classification using glcm and neural network method. In *Journal of Physics: Conference Series*, volume 1120, page 012050. IOP Publishing, 2018.

[142] David P Winchester, Jan M Jeske, and Robert A Goldschmidt. The diagnosis and management of ductal carcinoma in-situ of the breast. *CA: A Cancer Journal for Clinicians*, 50(3):184–200, 2000.

[143] Béatrice Barreau, Isabelle de Mascarel, Caroline Feuga, Gaétan MacGrogan, Marie-Hélène Dilhuydy, Véronique Picot, Jean-Marie Dilhuydy, Christine Tunon de Lara, Emmanuel Bussières, and I Schreer. Mammography of ductal carcinoma in situ of the breast: review of 909 cases with radiographic–pathologic correlations. *European Journal of Radiology*, 54(1):55–61, 2005.

[144] Solveig Hofvind, Barbro F Iversen, Liv Eriksen, Bodil M Styr, Kjell Kjellevold, and Kathinka D Kurz. Mammographic morphology and distribution of calcifications in ductal carcinoma in situ diagnosed in organized screening. *Acta radiologica*, 52(5):481–487, 2011.

[145] Tanu Sharma, James A Radosevich, Geeta Pachori, and Chandi C Mandal. A molecular view of pathological microcalcification in breast cancer. *Journal of Mammary Gland Biology and Neoplasia*, 21:25–40, 2016.

[146] Carl J D'Orsi. *Breast Imaging Reporting and Data System: breast imaging atlas: mammography, breast ultrasound, breast MR imaging*. ACR, American College of Radiology, 2003.

[147] Lisanne L De Boer, Torre M Bydlon, Frederieke Van Duijnhoven, Marie-Jeanne TFD Vranken Peeters, Claudette E Loo, Gonneke AO Winter-Warnars, Joyce Sanders, Henricus JCM Sterenborg, Benno HW Hendriks, and Theo JM Ruers. Towards

the use of diffuse reflectance spectroscopy for real-time in vivo detection of breast cancer during surgery. *Journal of translational medicine*, 16:1–14, 2018.

[148] Lisanne L De Boer, Benno HW Hendriks, Frederieke Van Duijnhoven, Marie-Jeanne TFD Vrancken Peeters-Baas, Koen Van de Vijver, Claudette E Loo, Katarzyna Jóźwiak, Henricus JCM Sterenborg, and Theo JM Ruers. Using drs during breast conserving surgery: identifying robust optical parameters and influence of inter-patient variation. *Biomedical optics express*, 7(12):5188–5200, 2016.

[149] Renzo Vanna, Carlo Morasso, Beatrice Marcinnò, Francesca Piccotti, Emanuele Torti, Davide Altamura, Sara Albasini, Manuela Agozzino, Laura Villani, Luca Sorrentino, et al. Raman spectroscopy reveals that biochemical composition of breast microcalcifications correlates with histopathologic features. *Cancer research*, 80(8):1762–1772, 2020.

[150] Esther Kho, Behdad Dashtbozorg, Lisanne L De Boer, Koen K Van de Vijver, Henricus JCM Sterenborg, and Theo JM Ruers. Broadband hyperspectral imaging for breast tumor detection using spectral and spatial information. *Biomedical optics express*, 10(9): 4496–4515, 2019.

[151] Rogerio Feris, Ramesh Raskar, Kar-Han Tan, and Matthew Turk. Specular reflection reduction with multi-flash imaging. In *Proceedings. 17th Brazilian symposium on computer graphics and image processing*, pages 316–321. IEEE, 2004.

[152] Rogerio Feris, Ramesh Raskar, Kar-Han Tan, and Matthew Turk. Specular highlights detection and reduction with multi-flash photography. *Journal of the Brazilian Computer Society*, 12:35–42, 2006.

[153] Amit Agrawal, Ramesh Raskar, Shree K Nayar, and Yuanzhen Li. Removing photography artifacts using gradient projection and flash-exposure sampling. In *ACM SIGGRAPH 2005 Papers*, pages 828–835. 2005.

[154] William H Press, Saul A Teukolsky, William T Vetterling, and Brian P Flannery. *Numerical recipes in C*. Cambridge university press Cambridge, 1992.

[155] Amit Agrawal. Code a: Matlab code for poisson image reconstruction from image gradients. (2004) [retrieved 24 May 2022], https://web.media.mit.edu/~raskar/photo/code.pdf.

[156] Moxtek. Visible light polarizers ppl, pfu rcv series datasheet. [retrieved 24 February 2024], https://moxtek.com/wp-content/uploads/OPT-DATA-1004-PPL-PFU-and-RCV-Series.pdf.

[157] Regulation (eu) 2017/745 of the european parliament and of the council of 5 april 2017 on medical devices, amending directive 2001/83/ec, regulation (ec) no 178/2002 and regulation (ec) no 1223/2009 and repealing council directives 90/385/eec and 93/42/eec (text with eea relevance.), May 2017.

[158] Lianne Feenstra, Stefan D van der Stel, Marcos Da Silva Guimaraes, Behdad Dashtbozorg, and Theo JM Ruers. Point projection mapping system for tracking, registering, labeling, and validating optical tissue measurements. *Journal of Imaging*, 10(2):37, 2024.

[159] Tony Lindeberg. Detecting salient blob-like image structures and their scales with a scale-space primal sketch: A method for focus-of-attention. *International Journal of Computer Vision*, 11(3):283–318, 1993.

[160] Marc D Kohli, Ronald M Summers, and J Raymond Geis. Medical image data and datasets in the era of machine learning—whitepaper from the 2016 c-mimi meeting dataset session. *Journal of digital imaging*, 30:392–399, 2017.

[161] Jacky D Luiten, Ernest JT Luiten, Maurice JC van der Sangen, Willem Vreuls, Lucien EM Duijm, Vivianne CG Tjan-Heijnen, and Adri C Voogd. Patterns of treatment and outcome of ductal carcinoma in situ in the netherlands. *Breast Cancer Research and Treatment*, 187:245–254, 2021.

[162] Shoji Tominaga and Akira Kimachi. Polarization imaging for material classification. *Optical Engineering*, 47(12):123201–123201, 2008.

[163] Jagdish Tewari, Ranjana Mehrotra, and Joseph Irudayaraj. Direct near infrared analysis of sugar cane clear juice using a fibre-optic transmittance probe. *Journal of near infrared spectroscopy*, 11(5): 351–356, 2003.

[164] Chao He, Honghui He, Jintao Chang, Binguo Chen, Hui Ma, and Martin J Booth. Polarisation optics for biomedical and clinical applications: a review. *Light: Science & Applications*, 10(1):194, 2021.

[165] Vadim Backman, Rajan Gurjar, Kamran Badizadegan, Irving Itzkan, Ramachandra R Dasari, Lev T Perelman, and Michael S Feld. Polarized light scattering spectroscopy for quantitative measurement of epithelial cellular structures in situ. *IEEE Journal of Selected Topics in Quantum Electronics*, 5(4):1019–1026, 1999.

[166] Dizem Arifler, Ina Pavlova, Ann Gillenwater, and Rebecca Richards-Kortum. Light scattering from collagen fiber networks: micro-optical properties of normal and neoplastic stroma. *Biophysical journal*, 92(9):3260–3274, 2007.

[167] Steven L Jacques, Jessica R Roman, and Ken Lee. Imaging superficial tissues with polarized light. *Lasers in Surgery and Medicine: The Official Journal of the American Society for Laser Medicine and Surgery*, 26(2):119–129, 2000.

[168] Steven L Jacques, Jessica C Ramella-Roman, and Ken Lee. Imaging skin pathology with polarized light. *Journal of biomedical optics*, 7(3):329–340, 2002.

[169] Ilyas Saytashev, Sudipta Saha, Joseph Chue-Sang, Pedro Lopez, Megan Laughrey, and Jessica C Ramella-Roman. Self validating mueller matrix micro–mesoscope (sammm) for the characterization of biological media. *Optics Letters*, 45(8):2168–2171, 2020.

[170] Sanaz Alali and Alex Vitkin. Polarized light imaging in biomedicine: emerging mueller matrix methodologies for bulk tissue assessment. *Journal of biomedical optics*, 20(6):061104–061104, 2015.

[171] Prashant Shukla and Asima Pradhan. Mueller decomposition images for cervical tissue: Potential for discriminating normal and dysplastic states. *Optics express*, 17(3):1600–1609, 2009.

[172] Alessandra Tata, Adam Gribble, Manuela Ventura, Milan Ganguly, Emma Bluemke, Howard J Ginsberg, David A Jaffray, Demian R Ifa, Alex Vitkin, and Arash Zarrine-Afsar. Wide-field tissue polarimetry allows efficient localized mass spectrometry imaging of biological tissues. *Chemical science*, 7(3):2162–2169, 2016.

[173] Iftikhar Ahmad, Adam Gribble, Masroor Ikram, Mihaela Pop, and Alex Vitkin. Polarimetric assessment of healthy and radiofrequency ablated porcine myocardial tissue. *Journal of Biophotonics*, 9(7): 750–759, 2016.

[174] Jérémy Vizet, Jean Rehbinder, Stanislas Deby, Stéphane Roussel, André Nazac, Ranya Soufan, Catherine Genestie, Christine Haie-Meder, Hervé Fernandez, François Moreau, et al. In vivo imaging of uterine cervix with a mueller polarimetric colposcope. *Scientific reports*, 7(1):2471, 2017.

[175] Philippe Schucht, Hee Ryung Lee, Hachem Mohammed Mezouar, Ekkehard Hewer, Andreas Raabe, Michael Murek, Irena Zubak, Johannes Goldberg, Enikö Kövari, Angelo Pierangelo, et al. Visualization of white matter fiber tracts of brain tissue sections with wide-field imaging mueller polarimetry. *IEEE transactions on medical imaging*, 39(12):4376–4382, 2020.

[176] Tatiana Novikova and Jessica C Ramella-Roman. Is a complete mueller matrix necessary in biomedical imaging? *Optics Letters*, 47(21):5549–5552, 2022.

[177] Ji Qi, Menglong Ye, Mohan Singh, Neil T Clancy, and Daniel S Elson. Narrow band 3× 3 mueller polarimetric endoscopy. *Biomedical optics express*, 4(11):2433–2449, 2013.

[178] Neil T Clancy, Shobhit Arya, Ji Qi, Danail Stoyanov, George B Hanna, and Daniel S Elson. Polarised stereo endoscope and narrowband detection for minimal access surgery. *Biomedical optics express*, 5(12):4108–4117, 2014.

[179] Sarah Forward, Adam Gribble, Sanaz Alali, Andras A Lindenmaier, and I Alex Vitkin. Flexible polarimetric probe for 3× 3 mueller matrix measurements of biological tissue. *Scientific Reports*, 7(1):11958, 2017.

[180] Nadhi Thekkek, Mark C Pierce, Michelle H Lee, Alexandros D Polydorides, Raja M Flores, Sharmila Anandasabapathy, and Rebecca R Richards-Kortum. Modular video endoscopy for in vivo cross-polarized and vital-dye fluorescence imaging of Barrett's-associated neoplasia. *Journal of biomedical optics*, 18(2):026007–026007, 2013.

[181] Yifan Fu, Zhiwen Huang, Honghui He, Hui Ma, and Jian Wu. Flexible 3x3 mueller matrix endoscope prototype for cancer detection. *IEEE Transactions on Instrumentation and Measurement*, 67(7): 1700–1712, 2018.

[182] Jiawei Zuo, Jing Bai, Shinhyuk Choi, Ali Basiri, Xiahui Chen, Chao Wang, and Yu Yao. Chip-integrated metasurface full-stokes polarimetric imaging sensor. *Light: Science & Applications*, 12(1):218, 2023.

[183] Jiawei Zuo, Ashutosh Bangalore Aravinda Babu, Mo Tian, Dongyao Wang, Zengyu Ceng, Kolappan Chidambaranathan, Jing Bai, Shinhyuk Choi, Hossain Mansur Resalat Faruque, Smitha S Swain, et al. Metasurface-based mueller matrix microscope. *Advanced Functional Materials*, page 2405412, 2023.

[184] Maeda Ryota. Polanalyser v1.2.0. https://github.com/elerac/polanalyser, 2022.

[185] Eric Compain, Stéphane Poirier, and Bernard Drevillon. General and self-consistent method for the calibration of polarization modulators, polarimeters, and mueller-matrix ellipsometers. *Applied optics*, 38(16):3490–3502, 1999.

[186] RMA Azzam and Ali G Lopez. Accurate calibration of the four-detector photopolarimeter with imperfect polarizing optical elements. *Journal of the Optical Society of America A*, 6(10):1513–1521, 1989.

[187] RMA Azzam, E Masetti, IM Elminyawi, and FG Grosz. Construction, calibration, and testing of a four-detector photopolarimeter. *Review of scientific instruments*, 59(1):84–88, 1988.

[188] Robert H Riddell, Harvey Goldman, David F Ransohoff, Henry D Appelman, Cecilia M Fenoglio, Rodger C Haggitt, Christer Ahren, Pelayo Correa, Stanley R Hamilton, and Basil C Morson. Dysplasia in inflammatory bowel disease: standardized classification with provisional clinical applications. *Human pathology*, 14(11):931–968, 1983.

[189] Tatiana Novikova, Angelo Pierangelo, Sandeep Manhas, Abdelali Benali, Pierre Validire, Brice Gayet, and Antonello De Martino. The origins of polarimetric image contrast between healthy and cancerous human colon tissue. *Applied Physics Letters*, 102(24), 2013.

[190] Michael FG Wood, Nirmalya Ghosh, Marika A Wallenburg, Shu-Hong Li, Richard D Weisel, Brian C Wilson, Ren-Ke Li, and I Alex Vitkin. Polarization birefringence measurements for characterizing the myocardium, including healthy, infarcted, and stem-cell-regenerated tissues. *Journal of Biomedical Optics*, 15(4):047009–047009, 2010.

[191] Peter Whittaker, Derek R Boughner, and RA Kloner. Analysis of healing after myocardial infarction using polarized light microscopy. *The American journal of pathology*, 134(4):879, 1989.

Papers

Paper I

Microcamera Visualisation System to Overcome Specular Reflections for Tissue Imaging

Niemitz, Lorenzo and van der Stel, Stefan D and Sørensen, Simon and Messina, Walter and Venkata Sekar, Sanathana Konugolu and Sterenborg, Henricus JCM and Andersson-Engels, Stefan and Ruers, Theo JM and Burke, Ray.

Micromachines **14(5)**, 1062– (2023).

micromachines

MDPI

Article

Microcamera Visualisation System to Overcome Specular Reflections for Tissue Imaging

Lorenzo Niemitz [1,*], Stefan D. van der Stel [2,3], Simon Sorensen [1], Walter Messina [1], Sanathana Konugolu Venkata Sekar [1,4], Henricus J. C. M. Sterenborg [2], Stefan Andersson-Engels [1,4,5], Theo J. M. Ruers [2,3] and Ray Burke [1]

[1] Biophotonics @ Tyndall, IPIC, Tyndall National Institute, University College Cork, T12 R5CP Cork, Ireland
[2] Netherlands Cancer Institute–Antoni van Leeuwenhoek, 1066 CX Amsterdam, The Netherlands; h.j.sterenborg@amsterdamumc.nl (H.J.C.M.S.)
[3] Group Nanobiophysics, Faculty TNW, Twente University, 7522 NB Enschede, The Netherlands
[4] BioPixS Ltd.–Biophotonics Standards, IPIC, Lee Maltings Complex, Dyke Parade, T12 R5CP Cork, Ireland
[5] Department of Physics, University College Cork, T12 K8AF Cork, Ireland
* Correspondence: lorenzo.niemitz@tyndall.ie

Abstract: In vivo tissue imaging is an essential tool for medical diagnosis, surgical guidance, and treatment. However, specular reflections caused by glossy tissue surfaces can significantly degrade image quality and hinder the accuracy of imaging systems. In this work, we further the miniaturisation of specular reflection reduction techniques using micro cameras, which have the potential to act as intra-operative supportive tools for clinicians. In order to remove these specular reflections, two small form factor camera probes, handheld at 10 mm footprint and miniaturisable to 2.3 mm, are developed using different modalities, with line-of-sight to further miniaturisation. (1) The sample is illuminated via multi-flash technique from four different positions, causing a shift in reflections which are then filtered out in a post-processing image reconstruction step. (2) The cross-polarisation technique integrates orthogonal polarisers onto the tip of the illumination fibres and camera, respectively, to filter out the polarisation maintaining reflections. These form part of a portable imaging system that is capable of rapid image acquisition using different illumination wavelengths, and employs techniques that lend themselves well to further footprint reduction. We demonstrate the efficacy of the proposed system with validating experiments on tissue-mimicking phantoms with high surface reflection, as well as on excised human breast tissue. We show that both methods can provide clear and detailed images of tissue structures along with the effective removal of distortion or artefacts caused by specular reflections. Our results suggest that the proposed system can improve the image quality of miniature in vivo tissue imaging systems and reveal underlying feature information at depth, for both human and machine observers, leading to better diagnosis and treatment outcomes.

Keywords: micro cameras; imaging; specular reflection; surgical guidance; endoscopy; multi-flash; cross polarisation

check for updates

Citation: Niemitz, L.; van der Stel, S.D.; Sorensen, S.; Messina, W.; Venkata Sekar, S.K.; Sterenborg, H.J.C.M.; Andersson-Engels, S.; Ruers, T.J.M.; Burke, R. Microcamera Visualisation System to Overcome Specular Reflections for Tissue Imaging. *Micromachines* **2023**, *14*, 1062. https://doi.org/10.3390/mi14051062

Academic Editor: Antonella Battisti

Received: 24 March 2023
Revised: 9 May 2023
Accepted: 15 May 2023
Published: 17 May 2023

Copyright: © 2023 by the authors. Licensee MDPI, Basel, Switzerland. This article is an open access article distributed under the terms and conditions of the Creative Commons Attribution (CC BY) license (https://creativecommons.org/licenses/by/4.0/).

1. Introduction

In a clinical setting, bio-photonic techniques play a role as complementary methods which can increase the breadth of diagnostic options, with quick turnaround spot testing that can aid clinical decisions. Gathering data for evidence-informed decisions, in particular in a fast-paced medical environment, can be in competition with acquisition time and the volume of potential data available. Therefore, evidence should be rapidly available when and where it is needed and be relevant to the task performed [1,2]. In vivo diagnostic imaging methods such as diffuse optical imaging [3,4], diffuse reflectance spectroscopy [5–8], fluorescence imaging [6,9], optical coherence tomography [10] and in vivo microscopy [11] are undergoing continual development as medical diagnostic techniques. Applications range across medical disciplines, from screening, to tumour margin detection and surgical

guidance, and many techniques have been adapted into medical devices seeing real-world use. In order to fit into the clinical workflow, these technologies are now being integrated into handheld or endoscope-based imaging probes, paving the way for their introduction into clinical settings. Such integrated sensorised probes are usually either fibre- [12–14] or camera-based [15,16]. For example, camera-based hyperspectral imaging probe, as well as camera-based surgical pen type fluorescence probes for diagnosing tumour status, are actively being researched. Currently, different imaging probes are being investigated for usability in tumor imaging [17] and fluorescence-guided surgery [5]. Breast cancer monitoring is an example where handheld probes have suggested use cases [18]. The development of sub-mm sized micro cameras, such as the AMS NanEye device, offers a promising platform for small-footprint medical imaging and work to develop applications is ongoing [19,20]. The main advantage of placing a camera on the tip of an endoscopic probe is in providing flexibility for the user. Such a device can aid and complement decision making by potentially acting as the sensor while also providing a guidance image.

Due to variations in camera-light sensitivity and frequent operation in dark environments in the body, medical imaging probes require external illumination. The ability to deliver various wavelengths to the target, for targeting specific bio-markers, controlling penetration depth, and multi- and hyper-spectral imaging applications are of interest for tissue imaging. Illumination is often provided by means of distally mounted LEDs, or in the case of this paper using optical fibres. The use of a point source for illumination causes specular reflections. These reflections are direct reflections from the surface and preserve the polarisation of the illumination source. The glossy and smooth tissue surface and clinical lighting environment give rise to large specular reflections, which can obstruct vision particularly in the most popular feature analysis domain, that of colour [21].

Because of the necessity to provide clear data to clinicians and image-processing algorithms, the image should be free from undesirable artefacts. Additionally, a pixel saturated by specular reflection obscures the information available in that area, and underlying features that may be of interest become unavailable for viewing. Image-processing algorithms in particular may produce errors in algorithms that segment and detect shapes [22]. Therefore, minimising or eliminating the effects of specular reflections should be a priority for image-based probes. There exist a number of techniques to remove specular reflections [23], that are either software or hardware based. One such multiple-image-based approach uses multiple illumination points to shift the specular reflections in subsequent images of a scene. This allows for a mixed software- and hardware-based approach which eliminates overlapping and partially overlapping reflections [24,25]. This multi-flash approach collects more light and does not require expensive filters. A purely hardware-based approach employs linear polarisers in an orthogonal, or crossed, arrangement, to remove specular reflections. This is a well-known technique that has seen wide commercial adoption in professional photography and eye wear. It has also seen use in the removal of corrupting glare from hyperspectral images [26] and been shown to have application in medical tissue images [4,12]. The deterioration of polarisation state occurs rapidly in tissue due to multi-scattering events. Orthogonal polarisation imaging exploits the fact that direct reflections as well as single scattering events maintain polarisation [27]. However, as light propagates through tissue and enough scattering events take place the polarisation state is subsequently lost. The rate of loss is dependent on the polarisation state of the incident light. The background theory and further details on de-polarisation of light in tissue is well described in the literature [28–32]. By linearly polarising the incoming light, while detecting with an orthogonal polariser, the diffusely reflected component of the light can effectively be filtered.

The objective of this work is to study these aspects of diagnostic potential to guide developments that can provide the clinician with tools for rapid imaging and decision making, with line of sight to diagnostics, by developing a microcamera-based platform that is capable of overcoming the challenges of specular reflections. There has not been any clear study to determine which of these two techniques is better for tissue imaging to reduce

specular reflection. The importance of specular reflection removal to fully image subsurface structures in optical diagnostic imaging, and the depth dependence of this imaging has not been studied. Furthermore, miniaturisation of both techniques to this scale has not been demonstrated previously. In this work, we present miniaturised multi-flash and cross-polarised systems using micro cameras. They integrate well into clinically relevant handheld probes, while allowing for miniaturisation to 2.3 mm endoscopic probes which can navigate into peripheral spaces in the body.

The scope for miniaturisation is desirable, as well as the possibility to extend device capability into other domains aside from traditional imaging, such as sensing. This refers to the delivery of multiple wavelengths and fibre connectivity to enable multi-modality. In this paper, the groundwork for a clinical imaging system is presented. Two imaging probes with fundamentally different specular reflection removal techniques are presented in the context of clinical tissue images. Images of phantoms and tissue are acquired, and both specular-reflection removal methods are demonstrated to effectively preserve information from pixels that have been saturated by specular reflection. An analysis of imaging depth vs. illumination wavelength for different techniques is performed. A light source capable of custom variable illumination is used for illumination and a control code ensures rapid data acquisition. The ability to image using microcameras through diced polarisers is demonstrated.

2. Materials and Methods

2.1. Multi-Flash Illumination Micro-Imager Probe

A schematic of the experimental imaging probe is shown in Figure 1. A 1.0 × 1.0 mm^2 AMS NanEYE RGB micro-camera, with a field-of-view (FOV) of 90° and F# 2.7, is integrated into a 3D-printed handheld imaging probe. Additionally, four 0.5 NA, 400 µm core diameter illumination fibres (Thorlabs FP400ERT) are positioned concentrically around the camera, at a distance of 2.4 mm, to provide uniform illumination with the intention of maximising the illuminated FOV of the camera sensor from each fibre position. The handheld probes are designed for a larger diameter of 10 mm for simple handling during the experimental phase. This arrangement also allows for further miniaturisation, which is discussed later. The illumination fibres are separated to ensure overlap between the emitted light cones, both for maximising illumination power in the case of all four fibres being used for illumination and ensuring that the multi-flash algorithm functions correctly by shifting the light cone with subsequent flashes.

The optical fibres allow light to be delivered to the sample from four slightly offset illumination locations. A shift in specular surface reflections can thereby be induced which can later be low-pass filtered during post-processing eliminating the more intense surface reflections. A one-to-four optical switch (Leoni mol 1 × 4) allows for quick switching between illumination fibres, minimising effects of movement by allowing for acquisition times of under half a second limited by the synchronisation with the frame grabber. The system is controlled using a LabView (National Instruments, Austin, Texas) based control software. Multiflash images were analysed using a multiflash algorithm [24,25] and reconstructed using a MATLAB v2021a (Mathworks, Natick, MA, USA) code and Poisson image reconstruction based on a sine transform [33–35]. The small shift in the location of the specular reflections was used to eliminate the reflections from the image. The choice of fibre to illuminate allows additional flexibility in illumination wavelength selection.

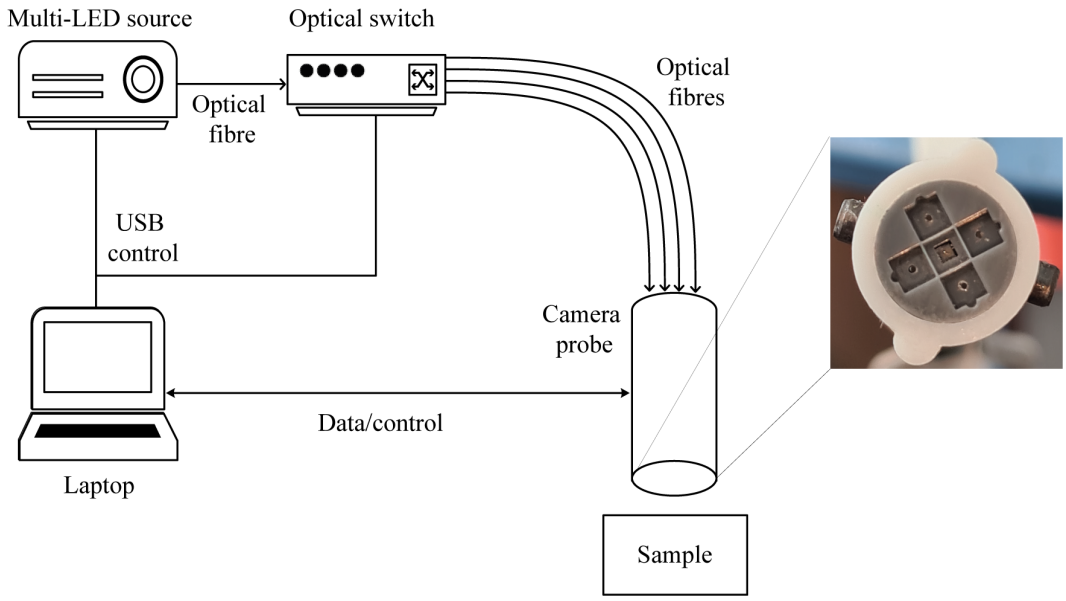

Figure 1. Schematic diagram of the experimental arrangement for the multi-flash measurements and close-up view of the multi-flash probe showing central camera sensor and concentrically arranged illumination fibres.

2.2. Orthogonal-Polarisation Micro-Imager Probe

The cross-polarised version of the probe incorporates the same physical design as the multi-flash probe. High-quality, glass substrate, linear polarisers, selected for high transmission and contrast across the visible and near-infrared (NIR), with average transmission in the visible of 90% and up and a contrast ratio of 1500 at 650 nm (MoxTek RCV8N2EC) were mechanically diced to 2.0 mm square and mounted in front of the camera sensor and the optical fibres. The orientation of the polarisers was such that orthogonal polarisation was achieved between the camera and each illuminating fibre. The polarisers were cut using a mechanical silicon wafer dicing machine, and their size was chosen to be the maximal permissible size given the desired probe dimensions. The dicing saw was used to partially cut through the glass, and the small components could then be separated from the bulk by carefully cracking them off. We have since achieved a dice of 0.50 × 0.50 mm enabling further miniaturisation.

The experimental set up along with a close-up view of the tip of the probe, showing the UV-glued polarisers are shown in Figure 2 above. In this probe, illumination is delivered through each of the four fibres simultaneously. Therefore, the optical switch is not required when utilising this set up. The use of four fibres simultaneously also allowed for a good illumination profile, which, given adequate light intensity and coupling on the back-end, overcomes some of the losses due to the polarisers.

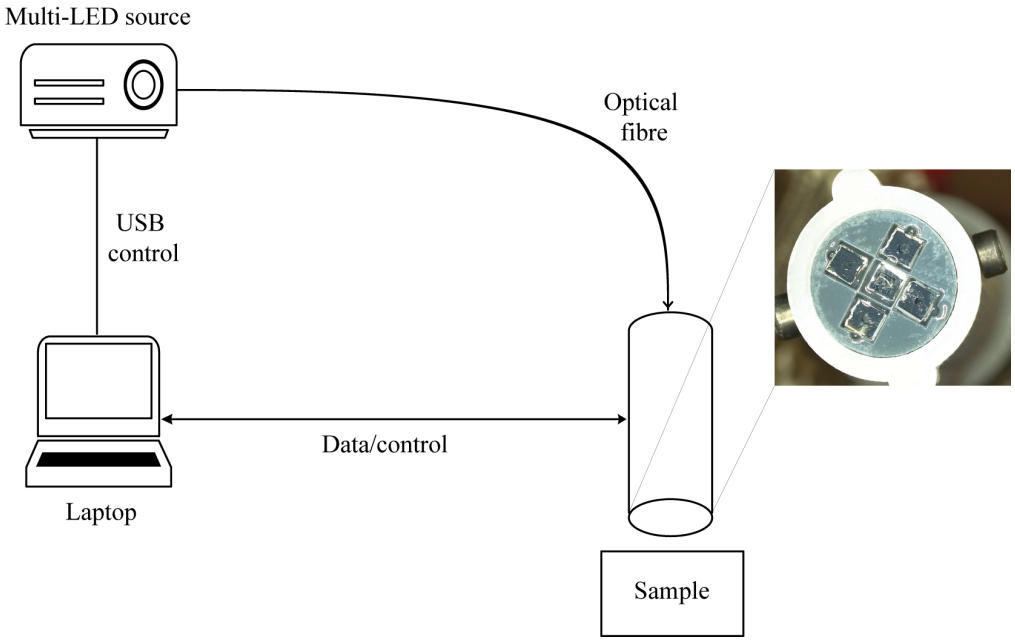

Figure 2. Schematic diagram of the experimental arrangement for the cross-polarisation measurement and close-up view of the polariser probe showing central camera sensor and concentrically arranged illumination fibres, each with a small diced glass polariser mounted in front. The polarisers on the camera and image fibres, respectively, are positioned orthogonally to one another.

2.3. Light Source and Portable Set Up

Illumination was delivered using a custom-built, portable, fibre-coupled multi-LED light source, designed and built in house. This work will be published separately. The source is capable of illuminating with five different wavelengths from 400 nm to 940 nm. Wavelengths were selected to allow for the reconstruction of white light using a combination of red (660 nm—Thorlabs M660D2), green (540 nm—Thorlabs M530D3), and blue (450 nm—Thorlabs M450D3) wavelengths. Moreover, two NIR wavelengths were selected to provide deeper penetration depth in tissue. These were at 850 nm (Thorlabs M850D2) and 940 nm (Thorlabs M940D2). The LEDs are coupled into a single optical fibre using an arrangement of dichroic mirrors. This results in a fibre-coupled source which can be used plug and play style with either of the two aforementioned measurement configurations. The wavelengths choices are adaptable and can be adjusted depending on application.

The entire apparatus is mounted on a movable trolley as shown in Figure 3. This allows the system to be portable and easily transported between the laboratory and operating theatre. The probes can be swapped by simply plugging them in to the LED source. The probes themselves can be used freehand or mounted in a fixed position above a sample. The laptop allows for near real-time data acquisition and control, with the camera data being parsed through a custom-made readout board (BAP Image Systems, Ergolding, Germany) which interfaces with LabView.

This portable trolley set up provides a portable system. The probe can be used handheld when desired, and a system such as this has a form factor which is acceptable in a clinical setting. When capturing images for validation the sample is placed in the sample holder and the probe fixed at a set distance of 8.0 mm above the sample to ensure the field of view remains fixed for consecutive acquisitions.

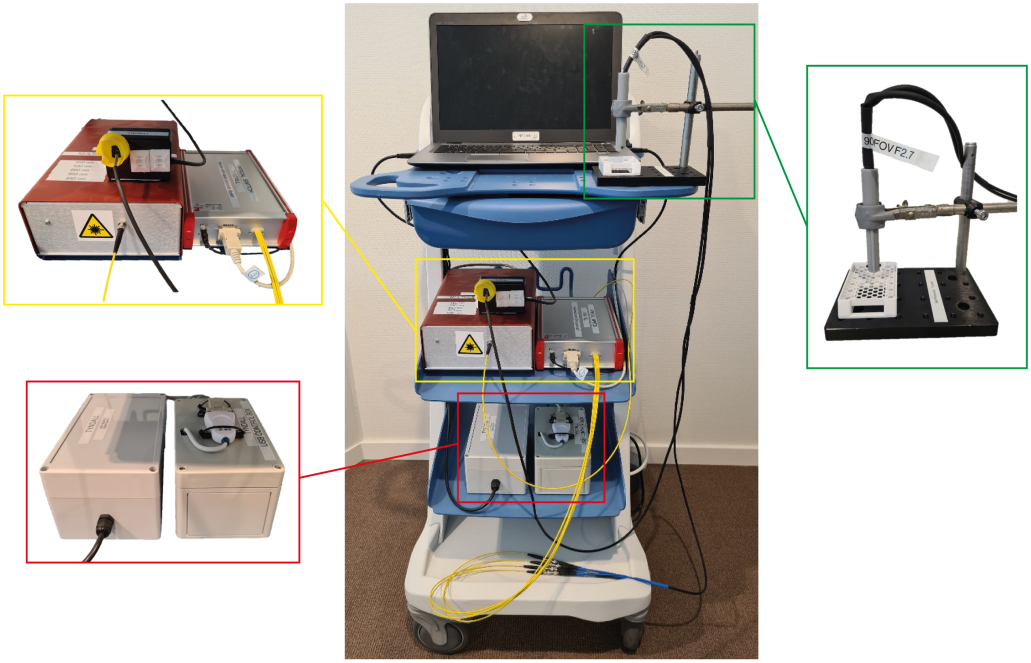

Figure 3. Entire clinical trolley with light source and optical switch (yellow), power supply and data acquisition box (red), and camera probe with sample holder (green).

2.4. Ex Vivo Validation

Tissue Mimicking Phantoms

The primary goal was to verify the specular-reflection-removal techniques on a highly reflecting standard. Tissue-mimicking phantoms (BioPixS0020 by BioPixS, Cork, Ireland), with well-defined scattering and absorption values to match the optical properties of human tissue, were used to verify functionality of both probes. The phantoms, seen in Figure 4 consist of a base phantom and a number of top layer phantoms. These can be combined together to create range of multilayer phantoms with different top layer thickness while the air gap in eliminated due to the phantom design to avoid optical boundary effects. Well defined layers of depth 0.50 mm, 1.0 mm, and 2.0 mm, allowed also for a verification of feature detection at different imaging depths with both probes. This is of particular interest when using near infrared illumination which has a deeper penetration depth. The phantoms present a glossy surface and contain embedded features of hydroxyapatite of 1 mm diameter. The phantoms therefore allow a deliberate challenging of specular reflections, presenting even more significant surface reflections than what can be expected from real biological tissue. They allow for repeatability and unlike tissue samples do not dry out. The hydroxyapatite particles were used to mimic a feature of interest to a clinician, who may be looking to detect abnormalities embedded in tissue. Hydroxyapatite is similar to human hard tissue and a suitable analogue to mimic the imaging of cardiovascular plaque, for example, while the phantom is not directly analogous to a human organ and imaging phantoms in a controlled environment does not translate directly to live observation in a human or animal, the phantom does provide optical properties that mimic the light transport through the tissue. Therefore, it is suitable when investigating the ability to resolve sub-surface features after specular reflection removal.

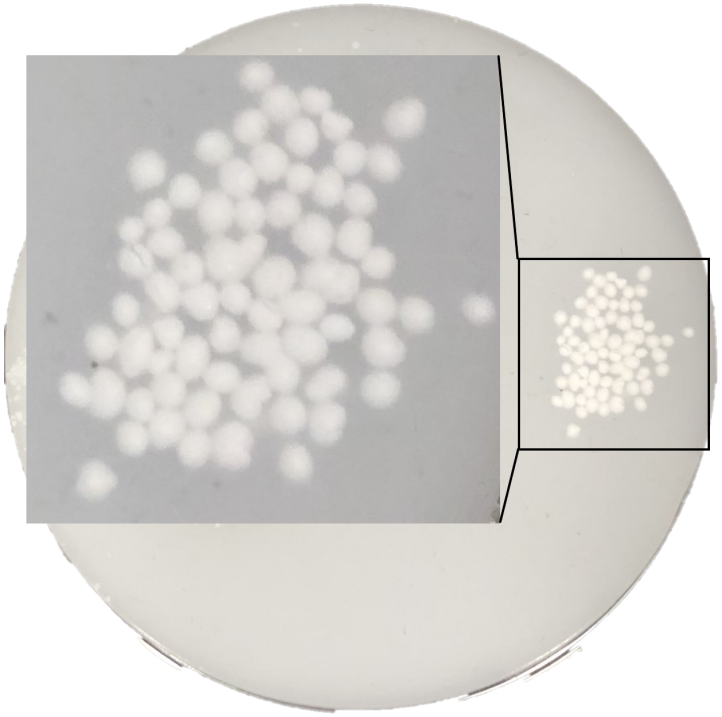

Figure 4. Image of base layer of the tissue-mimicking phantom developed for this study, with a close-up view of the 1.0 mm features imaged in this work.

2.5. Ex Vivo Human Tissue Imaging

To validate this system on tissue, images of breast slices after breast conserving surgery were acquired. The glossy surface of breast specimens were used to test the capacities of the system on human tissue. Images of excised human breast tissue were acquired using the aforementioned probes as part of a post-operative pathological workflow. An image of the clinical set up used to image the excised tissue samples is shown later in the text. The tissue samples were imaged using both the multi-flash capable probe as well as the polariser probe. Regions of interest on the tissue samples were selected, and subsequently imaged.

3. Results

3.1. Ex Vivo Validation: Phantom Images

The performance of the multi-flash algorithm as well as cross-polarisation imaging was validated in the laboratory before introduction of the devices into a clinical settings. Images of phantoms captured using both probes are presented in this section using different illumination wavelengths and phantom depths. The reconstruction algorithm for the multi-flash method was also validated.

Figure 5 shows an example of the multi-flash system's image outputs. Each illumination fibre sequentially illuminates the sample, in this case a bare tissue phantom. The four images that are generated can be seen in Figure 5a–d where it is clear that the illumination pattern changes as the scene is illuminated from slightly different positions. The specular reflections present themselves as very bright areas in the center of the illuminated area, where the detector saturates and the hydroxyapetite features are not discernible. The specular reflection shift can also be seen in each of the four images where the saturated region is observed in a different location of the sample. Figure 5e shows the reconstructed output

of those four images. The bright saturation due to direct surface reflections is filtered out and the margins of the features are visible once again. The reconstruction error of this method was examined by feeding four identical images into the reconstruction algorithm and analysing the differences. This error in the reconstruction was found to be of the order of 10^{-10}.

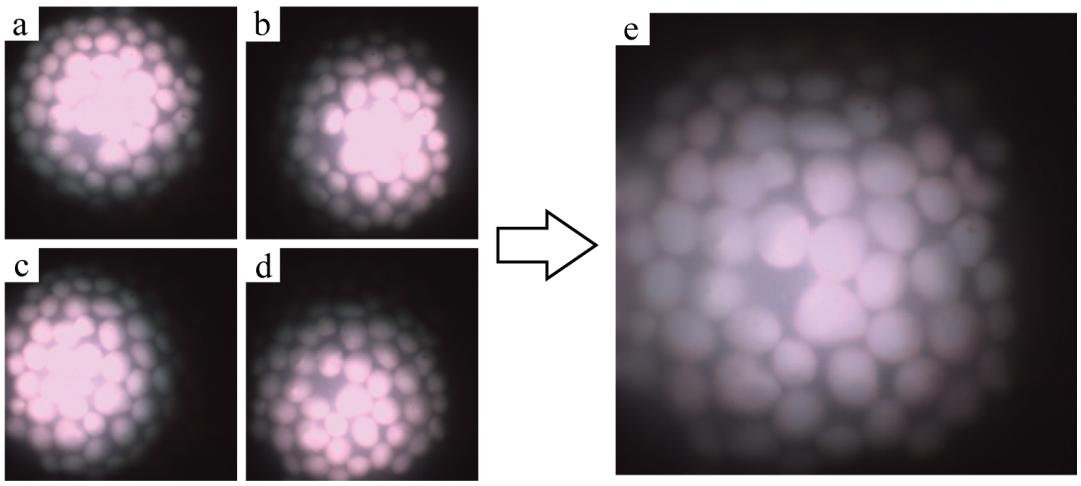

Figure 5. Images displaying four separately illuminated white light images of the same site on the phantom from different illumination locations (**a**–**d**) and the reconstructed output of the multi-flash specular reflection reduction algorithm (**e**).

To further explore the reconstruction in terms of wavelength and depth, multi-flash images are presented in Figure 6 below, where the features embedded in the multi-layer phantom are imaged at different imaging depths and using wavelengths from the blue to the NIR. The probes were fixed 8 mm above the sample, and images were captured at a range of imaging intensities, with the best ones for inspection being selected. A similar procedure takes place in clinical situations when examining tissue samples, where the clinician will adjust the system settings until an adequate image is generated.

The first row of images displays images under white light illumination that have not been corrected for specular reflections. Very strong surface reflections saturate the pixels and the margins of the features are no longer distinguishable. The second row of white-light-illuminated images shows the traditional guidance image (illuminated using white light) corrected for specular reflections using the multi-flash post-processing approach, and the hydroxyapatite crystal features can now be clearly distinguished. In the following rows, multi-flash corrected images are shown for the other illumination wavelenghts used. The measurement depth is varied using the multi-layer phantom by adding the corresponding layer on top of the bare tissue phantom. It is observed that as the thickness of the phantom above the feature increases the features become less discernible. The longer wavelengths can be seen to penetrate deeper into the tissue mimicking phantom and features are more clearly seen. Note that the illumination intensity is selected such that the features are the most visible to a human observer, hence the apparent decrease in brightness under the 660 nm illumination as the depth increases. Higher intensity illumination here over-saturated the image, making it impossible to discern features especially when the light is already highly scattered. Increasing wavelengths clearly allows for observation of features at greater depth. The 940 nm illumination allows features under 2.0 mm of phantom layers to be resolved, although there is some blurring observed at this depth due to scattering. In all cases, surface reflections are effectively removed from the image, revealing underlying information.

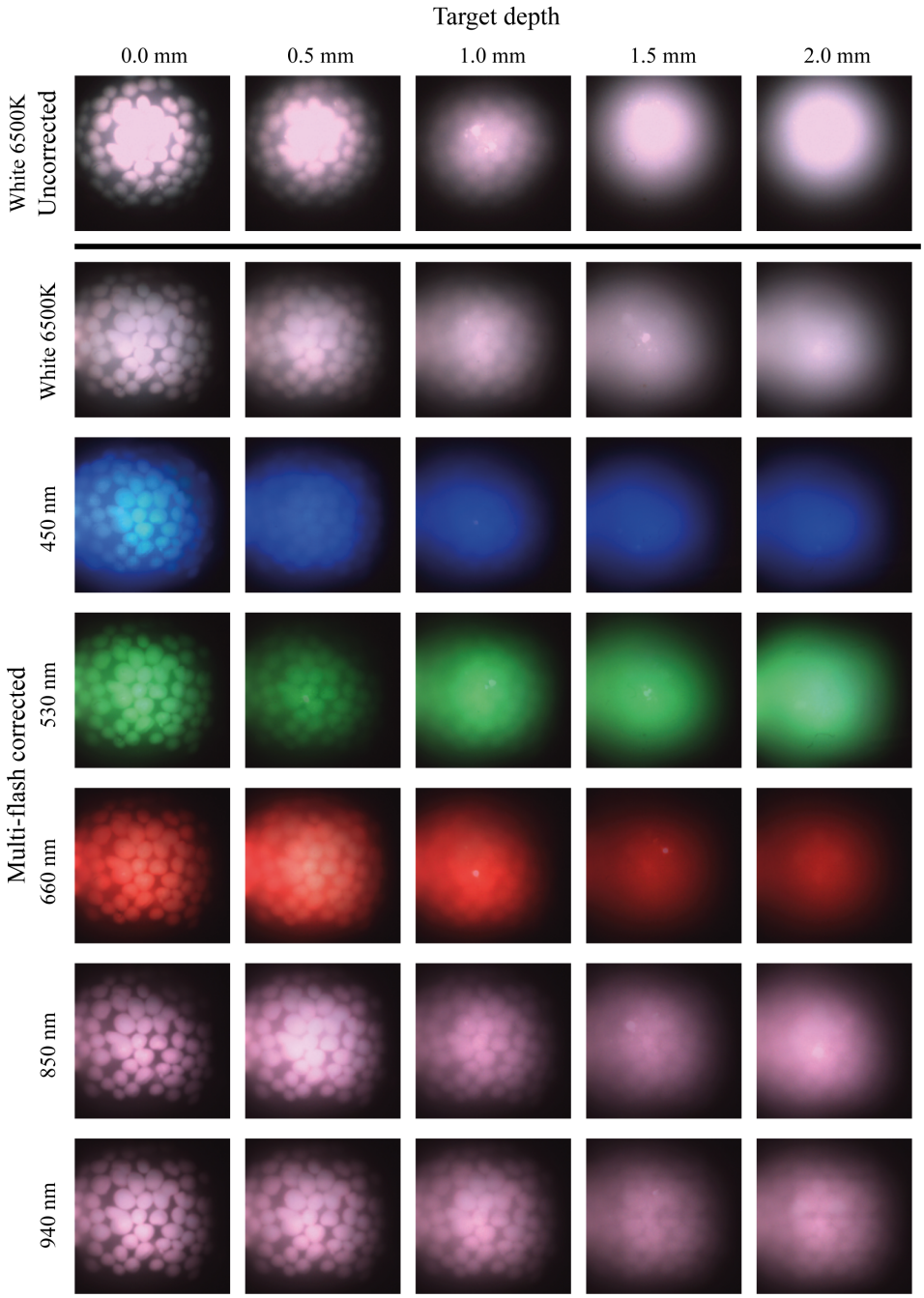

Figure 6. Uncorrected images of tissue-mimicking phantoms with embedded features shown under white illumination in the first row. Reconstructed multi-flash images of tissue-mimicking phantoms at different imaging depths and different illumination wavelengths shown below.

The same measurement procedure was repeated for the cross-polarised imaging probe in Figure 7. Similar to the multi-flash probe, the longer wavelengths penetrate deeper

into the phantom. A comparison of the 940 nm wavelength suggests the ability to resolve features slightly better than the multi-flash probe at this NIR wavelength. Additionally, the boundaries of the features appear more well defined under all illumination wavelengths. The fibre reflections can be seen in the images captured using the cross-polarised probe and will be discussed later. These always appear at the same location.

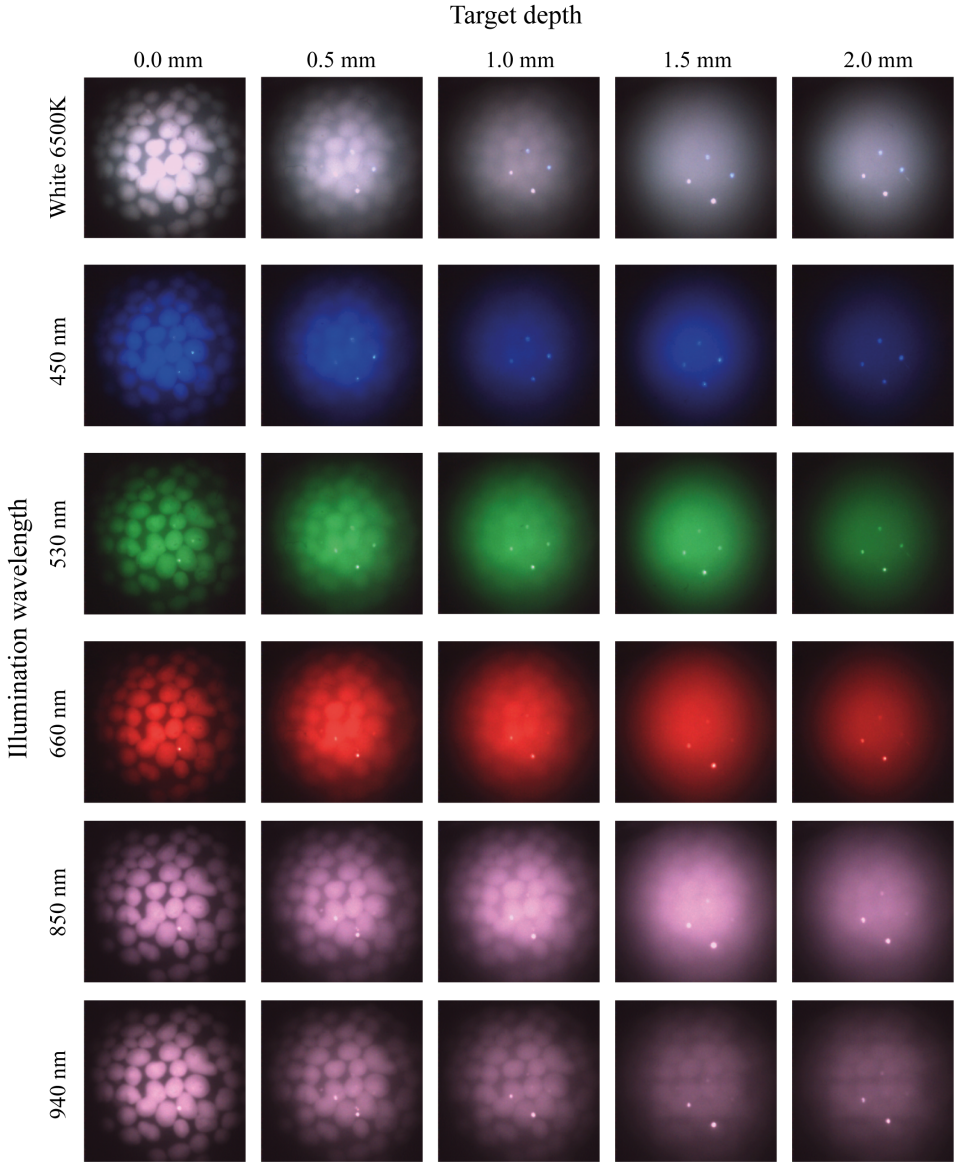

Figure 7. Cross-polarised images of tissue-mimicking phantoms at different imaging depths and different illumination wavelengths. Note the four bright spots that are visible on most of the images are direct reflections from the four illumination fibres. The surface of the phantom is very flat and reflective and the polarisers fail to filter out these brightest spots.

3.2. Ex Vivo Human Tissue Imaging

To demonstrate the clinical value of the proposed solutions, excised human breast tissue was imaged. Figure 8 shows a comparison between a camera image with single fibre illumination, the reconstructed multi-flash image, and the cross-polarised image, respectively. It is an example of a typical clinical imaging target. Both the multi-flash reconstruction as well as the cross-polarisation effectively eliminate the specular component of the reflected light. In both cases, only the diffuse component remains providing a blemish free image that presents the information of the surface and underlying features.

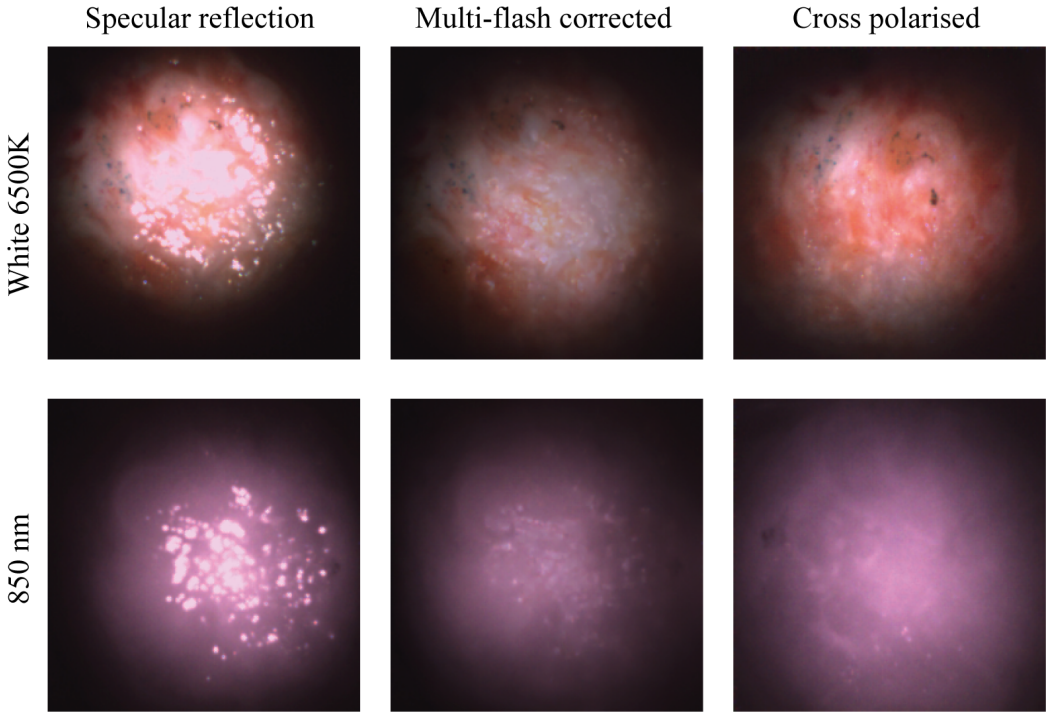

Figure 8. Humanbreast tissue images showing single fibre illumination with no polarisation (**Left**), reconstructed image after multi-flash post processing (**Middle**), and cross-polarisation imaging (**Right**).

The same location is imaged using white light and NIR illumination. In the white image, a set of grey blue dots can be seen in the top left quadrant of the image. Specular reflection is clearly seen in the first set of images where the sample is only illuminated without any specular reduction method using a single fibre source. Here, the glossy tissue surface is obscuring the view of the underlying morphology of the tissue. In the next two sets of images it is clear that both the multi-flash corrected image and the cross-polarised image have effectively removed the specular reflection and revealed previously obscured underlying information. Under both illumination types, white and NIR, the cross polarised image appears brighter here due to the intensity choice in the multi-flash image that returns the best result. A balance is struck between illumination intensity and output image quality, in particular in the algorithmic specular reflection removal approach. Both methods show excellent image quality and colour reproduction. This has been validated with many measurements on human tissue beyond the selection selection shown here, with further publications to follow.

4. Discussion

The results of cross-polarised imaging, as well as multi-flash imaging, using micro-cameras, of phantom test targets and human tissue demonstrate two effective methods for removing surface reflections. The orthogonal polariser imager rejects the polarisation maintaining direct reflections, from the glossy tissue surfaces. Imaging into the tissue by collecting only multiple-scattered light is thereby achieved. Similarly, the multi-flash imaging probe shifts the specular reflections as illumination strikes the surface from different positions. These shifts in specular reflections can be filtered out and the image below can be reconstructed. Important to note is that the two methods fundamentally interrogate different physical properteries of reflected light. The multi-flash approach effectively samples all polarisation states, whereas the polarimetry approach only samples multiple-scattered light. This should be considered when choosing a technique, while the polarisers provide a solution that is free from post processing, it is limited by the dimensional constraints of the dicing process and the specifications of the polarisers. This in turn bounds the minimum dimensions of any potential device. An alternative option may be to deposit or grow polarisers directly onto fibre tips and sensor to drive the footprint down further. For the multi-flash approach, the dimensions are bounded by the requirement to have four illuminating fibres, and the illumination cone overlap condition, as well as the illumination profile in combination with the camera. From a clinical compliance standpoint, the images from the polariser-based solution are more desirable. For real-time imaging and intraoperative scanning across tissue, the cross-polarisation probe is preferred as there is no requirement to keep the probe and tissue static during image acquisition. Currently the multi-flash approach can acquire images in approximately 0.20 s with the synchronisation of image acquisition with the optical switch being the made bottleneck. With a faster camera and a synched rapidly switching optical switch, however, these limitations could be mitigated in the future.

Illumination pattern is important so that the FOV of the camera is fully illuminated. Illuminating with four fibres simultaneously, provides a more even illumination pattern that covers a greater area of the FOV of the camera. More illumination intensity is easily provided using the illumination system. By using more powerful light sources, any intensity problems should be eliminated entirely. Fibre selection is ideally large diameter and high numerical aperture, however this can be supplemented with lens design. Important in all cases is illuminating much of the FOV as possible and therefore the cameras are selected with a low FOV to allow for a maximum illuminated area. Additionally the lower FOV micro cameras were selected due to the reduced barrel distortion observed on the graded-index lens camera cube package. This becomes more challenging when reducing footprint and trade-offs in illuminated area and illumination pattern must be made with cost. For multi-flash imaging, correct overlap of the light cones is an additional consideration so that as much area as possible is illuminated by each fibre position, ensuring that any areas with specular reflections have a shift in reflection.

Micro cameras typically provide good magnification, and the FOV in these images is of the order of 10.0 mm. This is a positive aspect, given sufficient spatial resolution and pixel count, when looking for small features in tissue. However, it can become a negative when scanning a larger region of tissue is necessary. One of the main limitations of micro camera endoscopy systems is the number of available pixels. In colour cameras, only a fraction of the pixels are active in each spectral band. This becomes more of a problem when using the pixels not just for guidance but for diagnostic measurement. Using a monochrome camera can help resolve this, as now all pixels are sensitive to a broadband visible and NIR illumination. This, in turn, increases the spatial resolution of our sensor for each of the colour bands. These colour bands can then be delivered sequentially using the aforementioned illumination system, or if desired laser illumination [36], again limited by motion of the probe or tissue in relation to acquisition time.

The ex vivo results obtained using this system demonstrates the efficacy of both specular reflection removal approaches when imaging human tissue. Figure 8 shows effective elimination of specular reflections in both modalities, with the features on the tissue surface now discernible. Figures 6 and 7 present depth measurements of embedded features in multi-layer phantoms. In Figure 7, the cross polarised system fails to eliminate all of the specular reflections, as bright hot spots can be seen in almost all the images but in particular the white and NIR illuminated images. These are reflections from the illuminating fibres, which are not fully eliminated due to the limitations in the polarisation system. A number of possible effects should be considered. The first is that of the performance limitations of the polarisers leading to not all the incident and collected light being completely cross polarised. The second effect is likely an angular effect where when using a large NA camera objective, different pixels will be looking at the surface under different angles. The polarisation of the specular reflection from the surface will be parallel to the surface everywhere. Hence, depending on the location on the surface, the specular reflection reaching the camera will have a slightly different angle with the polarisation filter in the camera for each pixel. On average these align to be zero, but there will be a range of angles where transmission is non-zero. This likely reduces the overall performance of the system however in the case of the hotspots remaining in the same location the contribution is primarily that of contrast in the polarisers. The diffuse reflection is an order of magnitude lower than the specular reflection from the surface, and as a result hotpots form in certain locations. A slight angular shift in the probe positioning, i.e., the probe is not aligned perfectly perpendicular with the surface of the phantom may play an additional role. When compared with specular reflection uncorrected images, such as images in Figures 5a–d and 8 however, a drastic improvement is seen. The final use case of such probes remains the clinic where conditions are never ideal. The images in Figure 8 remain indicative of the value of these techniques in particular when used on biological tissue.

Due to tissue optical properties, in the visible to NIR range, tissue can be interrogated at greater depth with increasing wavelength. From the phantom images it is clear that there is an increase in imaging depth with an increase in wavelength, as was expected. Figures 6 and 7 demonstrate an ability to image into tissue at depth in particular when using NIR wavelengths. These effects are significant and this paper recommends the inclusion of NIR modalities into micro camera endoscopy systems. In many cases features of interest present themselves not just in plane with the surface. The human body often presents complicated morphology, and therefore there exists a clinical requirement to image at some depth, or detect embedded features. The removal of specular reflections improves image quality and enables real-time feature detection algorithms to detect these in the future. Flexibility in illumination wavelength is additionally beneficial for these systems, to interrogate different colour bands, and to allow the combination of wavelengths to enhance contrast. This gives clinicians tools to view a scene in the way that best suits the particular use case. Quick scanning with white light illumination allows for viewing of surface features and morphology assessment. Switching to more specific wavelengths, such as the NIR to probe at depth, when features or structured of interest present beneath the surface, or the blue to examine surface features. Wavelength flexibility also enables viewing of particular bio-markers sensitive to certain wavelengths. This can also be extended to additional imaging modalities such as diffuse reflectance spectroscopy applications. The techniques presented in this paper are adaptable to systems of all sizes, including traditional chromoendoscopy systems, and specular reflection removal improves image quality independent of system. It is of particular importance when miniaturising systems using micro cameras, where the magnification is quite high and the field of view and pixel count relatively low, and any artefacts in the image have a high impact on image quality.

This system lays the groundwork to provide clinicians with diffuse images, where acquisition is quick and simple, and the input wavelengths can be carefully controlled.

A platform is presented that is adaptable to 3–7 Fr applications using the fibre illumination and micro camera. Examples where this system can provide an addition to the current workflow including in tissue-conserving surgeries to ensure that the resections margins are tumour-free, as a tool in peripheral lung applications to ensure image quality, or as a tool in imaging of vulnerable plaque in cardiovascular medicine. However, such a probe should include multiple modalities to provide an enhanced image that goes beyond simple image guidance. It would also vary in dimensions depending on the use case. Future work should therefore include adapting the probe into a multi modal system that is capable of diffuse reflectance spectroscopy as well as image guidance, with the ability to co-locate features detected with different modalities. Work is also being carried out on integrating image processing with high dynamic range and multi spectral imaging to highlight areas of interest for the clinician.

As medicine takes more and more steps towards minimally invasive approaches, it is expected that the demand for such techniques will increase. Rapid acquisition and real-time feedback for clinical use will become a standard. The techniques demonstrated in this paper are not uncommon in larger dimensions, e.g., in professional photography; however, the challenge lies in the development of small footprint systems that can find their place in a clinical environment. For clinical applications, a generalized probe for use in clinical settings has not yet been introduced. For example, imaging probes would be valuable in outward clinics in providing general practitioners or dermatologists detailed visualization of small skin abnormalities, resulting in more accurate diagnosis and treatment. Additionally, imaging probes can be extensions for surgeons in assessing tumours or lesions during surgical procedures. To optimize clinical use, direct and non-invasive assessment with real-time feedback is essential. Moreover, the probe and system should be easy to use, in order to minimize the need for technical assistance. This paper has miniaturised such a system into a 10.0 mm handheld portable footprint. The techniques presented lend themselves to being further miniaturised, with ongoing work moving towards a footprint of 2.3 mm as shown in Figure 9. At this footprint, the device will lend itself to use in the working channel of many endoscopes, for navigation deeper into peripheral lung space, for example. Camera technology is expected to continue to evolve. In the medical technology field especially the gold standard is a guidance image in situ, and so we expect further footprint reductions, and micro cameras to be used more frequently in areas previously inaccessible for imaging. For their effective use, systems must be miniaturisable to fit the small form factor the micro camera allows. Clinical relevance can also not be neglected. Portability, handheld nature, and image and information quality must all be taken into consideration. Micro cameras then open doors to miniaturising benchtop systems and providing information from areas where it was previously unavailable. Work is also ongoing to develop robust sterilizable systems suitable for use in operating theatres.

Future work will involve optimising this technology to meet clinical needs in particular clinical applications, providing valuable information to clinicians which was previously unavailable. This includes further miniaturisation if necessary, in combination with image processing and feature recognition software to improve output images, and inclusion of diffuse reflectance imaging modes. The current system is built to support these modalities. Consideration should also be given to improving image quality by using monochrome cameras instead of RGB cameras, and further exploration of sequential illumination is necessary. Most importantly, all of this work should be performed with the clinical requirements in mind. This means in close collaboration with clinicians, with the systems being used in a clinical environment.

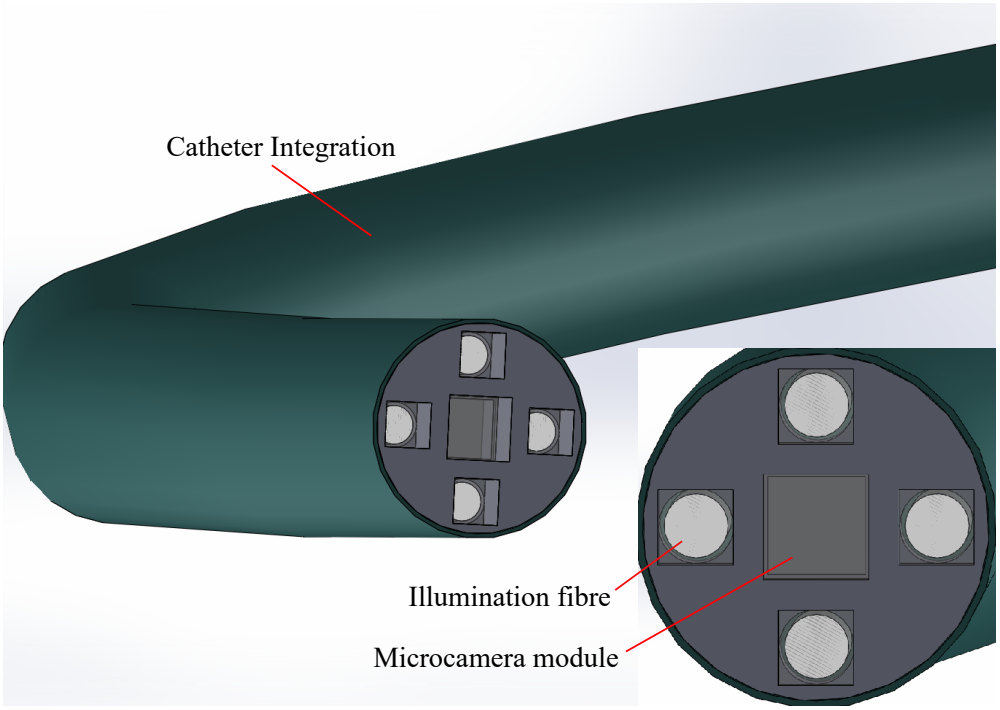

Figure 9. Schematic representation of the miniaturisation possibilities for the two implemented specular-reflection-reduction methods. In this case, a smaller camera sensor OV6948 will be utilised with 0.50 mm and 0.70 mm polarisers integrated in front of the sensor and the 0.40 mm illumination fibres.

5. Conclusions

Surface reflections are often undesirable and make it difficult to determine with certainty whether a feature is present in the image or not, complicating the determination of sub-surface tissue structures. This can cause erroneous results in human and machine analysis, and is not desirable in clinical care, where quick representation of important data is critical. In this paper, two handheld systems of the same footprint, capable of producing specular-reflection-reduced images of tissue using two different techniques, have been presented. These probes use micro-camera technology, which provides a flexible imaging platform and represents an emerging technology in surgical settings. The design is handheld and portable to easily fit into clinical workflow, as well as miniaturisable. To remove undesirable specular reflections two techniques are implemented. One, the integration of cross-polarisation using diced high-quality polarisers, and two, multi-flash imaging to shift reflections and filter them out algorithmically, in a post processing step. The use of these techniques enables the generation of images that are free from undesirable surface reflections. Both techniques achieve the goal of removing surface reflections on various targets including resected breast specimens, returning more suitable images for visual inspection. Advantages and disadvantages of both methods are discussed. Phantom verification shows the ability to image features at a depth of up to 2.0 mm with both techniques when using NIR illumination. The polarisers show clearer edges of the features upon visual inspection, although require more illumination power due to their attenuation. Both techniques are further miniaturisable, the multi-flash technique requiring four illumination sources to be integrated, bounding the minimum dimensions, and these sources need to be switched on sequentially.

The multi-flash approach therefore also requires the camera probe to be stationary for a fraction of a second, whereas the polarised probe is a solution that works independent of motion. The miniaturisation of the cross-polarised approach is dimensionally bounded by the size of the polarisation. In the clinical environment, the cross-polarised approach is currently preferred. In conclusion, two approaches to specular-reflection removal for endoscopy are presented. A balance must be struck between miniaturisation, acquisition time, interaction with other system modalities, and application, while design decisions for endoscopic applications are application-specific to a high degree. It is shown that specular reflection problems must be considered, and flexibility in illumination wavelengths including in the NIR is recommended. Both options presented show promise for use in a micro-camera platform for examining tissue.

Author Contributions: Conceptualization, H.J.C.M.S., L.N., R.B., S.A.-E. and S.S.; methodology, H.J.C.M.S., L.N., S.A.-E., S.S. and R.B.; software, L.N. and S.S.; validation, L.N. and S.D.v.d.S.; investigation, L.N. and S.D.v.d.S.; resources, L.N., S.S., S.K.V.S. and W.M.; data curation, L.N., S.S. and S.D.v.d.S.; writing—original draft preparation, L.N.; writing—review and editing, all authors have contributed; visualization, L.N. and S.D.v.d.S.; supervision, H.J.C.M.S., R.B., S.A.-E., S.S. and T.J.M.R.; project administration, H.J.C.M.S., R.B., S.A.-E. and T.J.M.R.; funding acquisition, R.B., S.A.-E. and T.J.M.R. All authors have read and agreed to the published version of the manuscript.

Funding: This research was funded by Science Foundation Ireland Grant SFI-12/RC/2276_P2 and SFI-15/RP/2828.

Informed Consent Statement: The patient specimen was acquired in accordance with the IRB guidelines of the AVL-NKI. According to Dutch guidelines and local ethics committee, informed consent was not required by the patient.

Data Availability Statement: Data underlying the phantom results presented in this paper are being made publicly available, and will be accessible at DOI:10.5281/zenodo.7709437. Tissue images are available from the authors upon reasonable request.

Acknowledgments: The authors would like to thank Paul Tassie for their help with the polariser dicing.

Conflicts of Interest: Sanathana Konugolu Venkata Sekar and Stefan Andersson-Engels are shareholders of BioPixS Ltd. with interest in tissue optical phantoms.

Abbreviations

The following abbreviations are used in this manuscript:

NIR	Near Infrared
FOV	Field-of-view

References

1. Tierney, W.M. Improving clinical decisions and outcomes with information: A review. *Int. J. Med Inform.* **2001**, *62*, 1–9. [CrossRef] [PubMed]
2. Bate, L.; Hutchinson, A.; Underhill, J.; Maskrey, N. How clinical decisions are made. *Br. J. Clin. Pharmacol.* **2012**, *74*, 614–620. [CrossRef] [PubMed]
3. Gibson, A.; Dehghani, H. Diffuse optical imaging. *Philos. Trans. R. Soc. A: Math. Phys. Eng. Sci.* **2009**, *367*, 3055–3072. [CrossRef] [PubMed]
4. Jung, B.; Choi, B.; Durkin, A.J.; Kelly, K.M.; Nelson, J.S. Characterization of port wine stain skin erythema and melanin content using cross-polarized diffuse reflectance imaging. *Lasers Surg. Med.* **2004**, *34*, 174–181. [CrossRef]
5. Stewart, H.L.; Birch, D.J. Fluorescence Guided Surgery. *Methods Appl. Fluoresc.* **2021**, *9*, 042002. [CrossRef]
6. Keller, M.D.; Majumder, S.K.; Kelley, M.C.; Meszoely, I.M.; Boulos, F.I.; Olivares, G.M.; Mahadevan-Jansen, A. Autofluorescence and diffuse reflectance spectroscopy and spectral imaging for breast surgical margin analysis. *Lasers Surg. Med.* **2010**, *42*, 15–23. [CrossRef]
7. Boer, L.L.D.; Bydlon, T.M.; Duijnhoven, F.V.; Peeters, M.J.T.V.; Loo, C.E.; Winter-Warnars, G.A.; Sanders, J.; Sterenborg, H.J.; Hendriks, B.H.; Ruers, T.J. Towards the use of diffuse reflectance spectroscopy for real-time in vivo detection of breast cancer during surgery. *J. Transl. Med.* **2018**, *16*, 1–14. [CrossRef]

8. Gkouzionis, I.; Nazarian, S.; Anandakumar, A.; Darzi, A.; Patel, N.; Peters, C.; Elson, D.S. Using Diffuse Reflectance Spectroscopy Probe Tracking to Identify Non-tumour and Tumour Tissue in Upper Gastrointestinal Specimens. In Proceedings of the European Conferences on Biomedical Optics 2021 (ECBO), Munich, Germany, 20–24 June 2021.
9. Lin, D.; Qiu, S.; Huang, W.; Pan, J.; Xu, Z.; Chen, R.; Feng, S.; Chen, G.; Li, Y.; Short, M.; et al. Autofluorescence and white light imaging-guided endoscopic Raman and diffuse reflectance spectroscopy for in vivo nasopharyngeal cancer detection. *J. Biophotonics* **2018**, *11*, e201700251. [CrossRef]
10. Gora, M.J.; Suter, M.J.; Tearney, G.J.; Boppart, A.; Bouma, B.E.; Brezinski, M.E.; Weissman, N.J.; Southern, J.F.; Fujimoto, J.G.; Rollins, A.M.; et al. Endoscopic optical coherence tomography: Technologies and clinical applications [Invited]. *Biomed. Opt. Express* **2017**, *8*, 2405–2444. [CrossRef]
11. Bishop, K.W.; Maitland, K.C.; Rajadhyaksha, M.; Liu, J.T.C. In vivo microscopy as an adjunctive tool to guide detection, diagnosis, and treatment. *J. Biomed. Optics* **2022**, *27*, 040601. [CrossRef]
12. Clancy, N.T.; Arya, S.; Qi, J.; Stoyanov, D.; Hanna, G.B.; Elson, D.S.; Henricson, J.; Anderson, C.; Leahy, M.J.; Nilsson, G.E.; et al. Polarised stereo endoscope and narrowband detection for minimal access surgery. *Biomed. Opt. Express* **2014**, *5*, 4108–4117. [CrossRef]
13. Nakayama, M.; Hamada, C.; Yokoyama, K.; Tanno, Y.; Matsuo, N.; Nakata, J.; Ishibashi, Y.; Okuzawa, A.; Sakamoto, K.; Nara, T.; et al. A disposable, ultra-fine endoscope for non-invasive, close examination of the intraluminal surface of the peritoneal dialysis catheter and peritoneal cavity. *Sci. Rep.* **2020**, *10*, 1–6. [CrossRef]
14. Lee, C.M.; Engelbrecht, C.J.; Soper, T.D.; Helmchen, F.; Seibel, E.J. Scanning fiber endoscopy with highly flexible, 1 mm catheterscopes for wide-field, full-color imaging. *J. Biophotonics* **2010**, *3*, 385–407. [CrossRef]
15. Modir, N.; Shahedi, M.; Dormer, J.D.; Fei, B. Development of a real-time spectral imaging system using in-site micro-LED-based illumination and high-speed micro-camera for endoscopic applications. *Proc. SPIE Int. Soc. Opt. Eng.* **2021**, *11654*, 37–44. [CrossRef]
16. Yoon, K.; Kim, K.; Lee, S. A Surgical Pen-Type Probe Design for Real-Time Optical Diagnosis of Tumor Status Using 5-Aminolevulinic Acid. *Diagnostics* **2021**, *11*, 1014. [CrossRef]
17. Martelli, C.; Dico, A.L.; Diceglie, C.; Lucignani, G.; Ottobrini, L. Optical imaging probes in oncology. *Oncotarget* **2016**, *7*, 48753. [CrossRef]
18. Jayachandran, B.; Ge, J.; Regalado, S.; Godavarty, A. Design and development of a hand-held optical probe toward fluorescence diagnostic imaging. *J. Biomed. Opt.* **2007**, *12*, 054014. [CrossRef]
19. Ascensão, B.; Santos, P.; Dias, M. Distance Measurement System for Medical Applications Based on the NanEye Stereo Camera. In Proceedings of the 2018 International Conference on Biomedical Engineering Applications, ICBEA 2018—Proceedings, Funchal, Portugal, 9–12 July 2018. [CrossRef]
20. Lotay, A.S.; Girkin, J.M. Towards a portable laser speckle based device to evaluate the level of atrophy in tissue. In *Design and Quality for Biomedical Technologies XII*; SPIE: San Francisco, CA, USA, 2019; Volume 10870, pp. 29–40. [CrossRef]
21. Bouget, D.; Allan, M.; Stoyanov, D.; Jannin, P. Vision-based and marker-less surgical tool detection and tracking: A review of the literature. *Med. Image Anal.* **2017**, *35*, 633–654. [CrossRef]
22. Nayar, S.K.; Fang, X.S.; Boult, T. Separation of Reflection Components Using Color and Polarization. *Int. J. Comput. Vis.* **1997**, *21*, 163–186. [CrossRef]
23. Artusi, A.; Banterle, F.; Chetverikov, D. A survey of specularity removal methods. *Comput. Graph. Forum* **2011**, *30*, 2208–2230. [CrossRef]
24. Feris, R.; Raskar, R.; Tan, K.H.; Turk, M. Specular reflection reduction with multi-flash imaging. In Proceedings of the 17th Brazilian Symposium on Computer Graphics and Image Processing, Curitiba, Brazil, 20–20 October 2004; pp. 316–321. [CrossRef]
25. Feris, R.; Raskar, R.; Tan, K.H.; Turk, M. Specular highlights detection and reduction with multi-flash photography. *J. Braz. Comput. Soc.* **2006**, *12*, 35–42. [CrossRef]
26. Nguyen-Do-Trong, N.; Keresztes, J.C.; Ketelaere, B.D.; Saeys, W. Cross-polarised VNIR hyperspectral reflectance imaging system for agrifood products. *Biosyst. Eng.* **2016**, *151*, 152–157. [CrossRef]
27. Groner, W.; Winkelman, J.W.; Harris, A.G.; Ince, C.; Bouma, G.J.; Messmer, K.; Nadeau, R.G. Orthogonal polarization spectral imaging: A new method for study of the microcirculation. *Nat. Med.* **1999**, *5*, 1209–1212. [CrossRef] [PubMed]
28. MacKintosh, F.C.; Zhu, J.X.; Pine, D.J.; Weitz, D.A. Polarization memory of multiply scattered light. *Phys. Rev. B* **1989**, *40*, 9342. [CrossRef] [PubMed]
29. Gandjbakhche, A.H.; Schmitt, J.M.; Bonner, R.F. Use of polarized light to discriminate short-path photons in a multiply scattering medium. *Appl. Opt.* **1992**, *31*, 6535–6546. [CrossRef]
30. Gao, W. Changes of polarization of light beams on propagation through tissue. *Opt. Commun.* **2006**, *260*, 749–754. [CrossRef]
31. Gao, W. Mueller matrix decomposition methods for tissue polarization tomography. *Opt. Lasers Eng.* **2021**, *147*, 106735. [CrossRef]
32. Chang, Y.; Gao, W. Interpreting and quantifying depolarization properties of tissue with differential polarization parameters. *Waves Random Complex Media* **2022**. [CrossRef]
33. Agrawal, A.; Raskar, R.; Nayar, S.K.; Li, Y. Removing photography artifacts using gradient projection and flash-exposure sampling. In Proceedings of the Special Interest Group on Computer Graphics and Interactive Techniques Conference, Los Angeles, CA, USA, 31 July–4 August 2005; pp. 828–835.

34. Press, W.H.; Teukolsky, S.A.; Vetterling, W.T.; Flannery, B.P. *Numerical Recipes in C*; Cambridge University Press: Cambridge, UK, 1992.
35. Agrawal, A. Code A: Matlab Code for Poisson Image Reconstruction from Image Gradients. 2004. Available online: https://web.media.mit.edu/~raskar/photo/code.pdf (accessed on 24 May 2022).
36. Chen, Z.Y.; Gogoi, A.; Lee, S.Y.; Tsai-Lin, Y.; Yi, P.W.; Lu, M.K.; Hsieh, C.C.; Ren, J.C.; Marshall, S.; Kao, F.J. Coherent Narrow-Band Light Source for Miniature Endoscopes. *IEEE J. Sel. Top. Quantum Electron.* **2019**, *25*, 7100707. [CrossRef]

Disclaimer/Publisher's Note: The statements, opinions and data contained in all publications are solely those of the individual author(s) and contributor(s) and not of MDPI and/or the editor(s). MDPI and/or the editor(s) disclaim responsibility for any injury to people or property resulting from any ideas, methods, instructions or products referred to in the content.

Paper II

Real-time peri-operative microcalcification detection in superficial breast tissues

van der Stel, Stefan D and Niemitz, Lorenzo, and Sørensen, Simon and Feenstra, Lianne and Sterenborg, Henricus JCM and Andersson-Engels, Stefan and Ruers, Theo JM and Burke, Ray.

Submitted to Translational Medicine Communications **-**, under review (submitted: Sep 2023).

Real-time peri-operative microcalcification detection in superficial breast tissues

S.D. van der Stel[1,2†]*, L. Niemitz[3†], S. Sorensen[3], L. Feenstra[1,2], S. Andersson-Engels[3,4,5], H.J.C.M Sterenborg[2,6], T.J.M. Ruers[1,2], R. Burke[3]

[1]Group Nanobiophysics, Faculty TNW, Twente University, Enschede, the Netherlands

[2]Netherlands Cancer Institute-Antoni van Leeuwenhoek, Department of Surgery, Amsterdam, the Netherlands

[3]Biophotonics Tyndall, IPIC, Tyndall National Institute, University College Cork, Cork, Ireland

[4]BioPixS Ltd.–Biophotonics Standards, IPIC, Lee Maltings Complex, Dyke Parade, T12 R5CP Cork, Ireland

[5]Department of Physics, University College Cork, T12 K8AF Cork, Ireland

[6]Department of Biomedical Engineering and Physics, Amsterdam University Medical Center, Amsterdam, The Netherlands

[†]These authors contributed equally to this work

Corresponding author:

S.vd.stel@nki.nl

One-sentence summary:

A novel cross-polarized camera-on-tip surgical tool for non-invasive and real-time detection of microcalcifications in superficial breast tissues.

Abstract

Surgical management of ductal carcinoma *in situ* (DCIS) involving suspicious morphology and orientation of microcalcifications stands as one of the primary treatment options. However, the absence of real-time technical assistance in the form of a intraoperative surgical tool for detection of microcalcifications in the resection margins presents a grand challenge. Consequently, the dependency on postoperative histopathological evaluations, as the current standard of care causes substantial time delays for patient and clinician, and may lead to additional surgery and revision.

In the context of breast conserving surgery, *ex-vivo* imaging of excised breast tissues slices from 12 patients was conducted. Employing a cross-polarized microcamera setup with multiple wavelengths and magnification up to 50 µm, tissue visualization in-depth using diffuse optical imaging (DOI) up to 2 mm was achieved, providing real-time feedback during acquisition. Mammography images were used for accurate correlations, allowing for microcalcification identification in the microcamera images.

Detection efficacy of microcalcifications within microcamera images was notably influenced by both calcification clustering and distribution depth within the tissue. Calcifications within the 2 mm range were detected through their distinct optical manifestations in relation to the adjacent tissues. Moreover, distinct optical characteristics of microcalcifications were observed when compared to surrounding soft breast tissues. Four independent reviewers, two medical and two technical, achieved an average sensitivity of 77.8%, specificity of 80.0%, and overall accuracy of 79.0%.

This study demonstrates an integrated microcamera in an surgical tool, and novel cross-polarized setup for non-invasive and real-time detection of microcalcifications in superficial breast tissues. By focusing on the context of the region of interest (superficial 2 mm), the current approach provides both promising results as well as considerable anticipation for future studies and applications.

Introduction

Since the introduction of breast cancer screening programs, and the implementation of the Breast Imaging Reporting and Data System (BI-RADS), breast cancer is often detected at early or premalignant stages *(1)*. In case of suspicious tissue alternations in screening mammography, additional in-hospital diagnostic examinations are required *(2)*. For example, 22.070 women from the preventive breast cancer screening program in the Netherlands were referred to the hospital for additional examination in 2018 *(3)*. A common reason for referral is the presence of suspicious microcalcifications on mammography, in many cases without a visible tumor. Moreover, of all referrals in 2018, 34.7% of patients were referred for additional examination solely due to presence of microcalcifications *(3)*.

Microcalcifications are deposits of calcium in the lobular system of the breast and can be a sign of a (pre) malignant lesion called ductal carcinoma *in situ* (DCIS) *(4)*. DCIS is the precursor lesion of an invasive carcinoma (IC) of the breast and is characterized by isolated proliferation of malignant cells in the ductolobular system of the breast *(5)*. DCIS accounts for 20-30% of all breast cancer diagnosis *(6)*, and a key characteristic is that microcalcifications are present in 60-90% of DCIS lesions *(7, 8)*. Despite being a common finding in breast mammography in preventive screening programs, not all calcifications are related to DCIS. Hence, radiologists differentiate between benign and malignant calcifications based on size, morphological appearances and distribution *(9)*. Malignant calcifications are small, mostly located intraductal, display fine linear, branching and pleomorphic morphological characteristics and are distribution linear or segmentally, whereas benign calcifications are larger in size and distributed diffusely within the lobuli *(10)*.

In current treatment guidelines of breast cancer, surgery preceded by neoadjuvant chemo-radiotherapy remains the best option to ensure complete removal of all malignant tissue *(11)*. However, DCIS is usually presented as scattered islands of malignant cells and not as a solid mass, making it increasingly difficult to distinguish from the surrounding healthy tissue in the surgical setting, resulting in up to 30% tumor-positive resection margins after postoperative histopathological examination *(12)*. Residual tumor cells in the resection margins are a major prognostic factor for local tumor recurrence in breast conserving surgery (BCS) and are more prevalent after DCIS-indicated surgeries compared to IC of the breast *(13)*.

Currently, the gold standard for resection margin assessment is histopathological evaluation by a pathologist *(14)*. However, this procedure can take up to multiple days, delaying the final conclusion. To overcome this gap, multiple optical imaging techniques are being explored for resection margin assessment and tumor tissue differentiation. In the past, diffuse reflectance spectroscopy (DRS) *(15–17)*, hyperspectral

imaging (HSI) *(18, 19)* and Raman spectroscopy *(20)* showed promising results for characterizing tumor and healthy breast tissue. Despite showing the great potential in identifying solid tumors, characterizing smaller islands of DCIS with the aforementioned techniques remains challenging *(16)*. In recent years, the biology and physiology of microcalcifications have become a popular research topic, leading to a better understanding of their origin and involvement in breast cancer *(4, 20, 21)*. So far, however, little research has been reported into intraoperative visualization of microcalcifications.

Microcameras have increasingly popular tools in the surgical workflow, facilitating real-time visualization and precision through minimally invasive access points *(22, 23)*. In particular, a microcamera can offer clinicians enhanced visualization of superficial tissues, by providing magnified perspectives of the surgical field. In BCS, the integration of microcameras holds particular promise by offering real-time assessment of the resection plane for presence of tumor or microcalcifications in case of DCIS. The main advantage here is that assessment of resection planes intraoperatively, provides the opportunity to excise additional tissue in the same surgical setting if indicated.

Recently, we presented a new cross-polarized microcamera setup, utilizing diffuse optical imaging (DOI) at multiple wavelengths to visualize the superficial 2 mm, magnified up to 50 µm, within an experimental setup *(24)*. By offering enhanced visualization of the superficial 2 mm of the resection plane, this technique holds promise to aid surgeons in achieving accurate resection planes, while preserving as much healthy tissue as possible in the process, ultimately leading to improved cosmetic outcomes. Here we present the first *ex-vivo* results in patients that underwent BCS (n = 12) using an optical cross-polarized microcamera system. The main aim of this study is to assess the feasibility in detecting microcalcifications in the superficial layers of excised breast tissue.

Methods

Study population

Between March 2022 and June 2023, 12 patients were included in the Netherlands Cancer institute – Antoni van Leeuwenhoek hospital (NKI-AVL) that underwent BCS. Inclusion criteria were >18 years and microcalcifications present in preoperative mammography. This study was approved by the Institutional Review Board (IRB) of the NKI-AVL and registered with number IRBm20-086. Data was acquired in concordance with the IRB guidelines of the NKI-AVL.

Cross-polarized microcamera setup

The DOI microcamera setup and subsequent technical features are described in detail in our previous work *(24)*. In short, the setup consisted of a handheld probe containing four optical fibers and a 1.0 x 1.0 mm camera with cross-polarizers to attenuate surface reflections (Figure 1). Images with a field of view (FoV) of 1.0 x 1.0 cm and magnification up to 50 µm were generated of the region of interest. The optical fibers were connected to a multi-LED source containing five independent LEDs in the visible and near-infrared range: blue (450 nm), green (530 nm), red (660 nm) and near-infrared (850 and 940 nm). Each LED can be switched on and off independently, allowing for five multispectral images per measurement location. In addition, RGB images can be reconstructed by combining the red, green and blue images. The most favorable wavelengths for microcalcification visualization were found to be in the near infra-red (NIR), however the visible wavelengths proved important for image guidance and co-location. The camera and LEDs were controlled with a custom-build user interface programmed in LabVIEW (LabVIEW National Instruments, Austin, Texas).

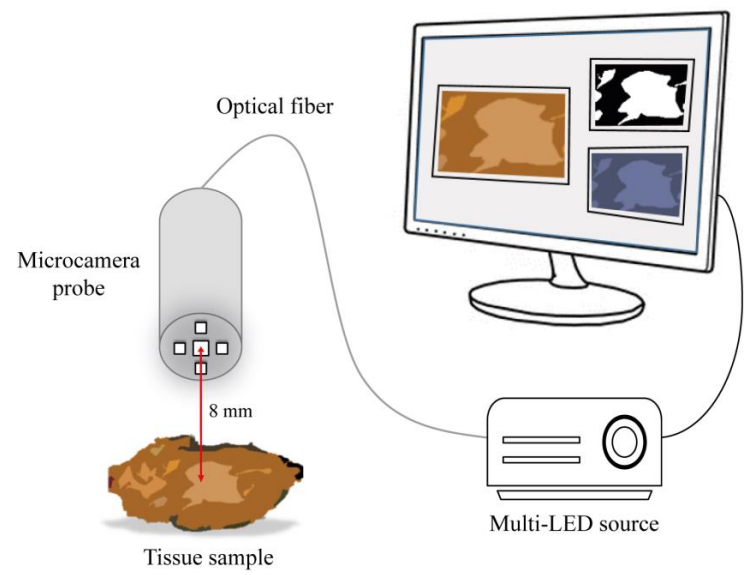

Figure 1. *Microcamera endoscopy setup. The microcamera probe consists of a central camera sensor and four concentrically arranged illumination fibers, each with diced glass polarizers placed orthogonally to the fibers. The probe is placed at a fixed distance of 8mm from the tissue sample to achieve a field of view of 1.0 x 1.0 cm with upwards to 50 µm magnification. The multi-LED source provides the light used for illuminating the tissue. During acquisition, real-time images in color, greyscale and infrared are shown on the screen.*

Study protocol

Immediately after surgery, the resected specimen was brought to the department of Pathology. According to standard pathology protocol, resection margins were inked, for the assessment of resection margins. When frozen, the specimen was gross-sectioned in slices with a thickness between 2 and 5 mm and placed on an A4 plastic sheet. Next, the slices were brought to the department of Radiology where a slice mammography (X-Ray) was taken of all slices. After examination of the slice mammography, one or two slices with microcalcifications were selected for optical imaging. Each selected slice was placed in a macrocasette.

Measurement protocol

First, the aimed measurement locations, regions of interest (ROIs), were identified in the mammography slice images (S_{MAM}). The slice was placed under a Point Projection and Mapping (PPM) system *(25)*. A top-view image from the breast tissue slice (S_{SPEC}) was acquired from which 2–5 measurement locations were selected manually. The selected measurement locations were then projected as light dots on the specimen, and a new top-view image was acquired in order to track the measurement locations (S_{PPM}). Measurement locations were selected in areas containing calcifications, and areas without. The handheld probe was placed at a fixed distance of 8 mm from the tissue for optimal focus. The center of the probe was carefully placed over the center of the projected measurement locations. Acquisitions were made by switching through the aforementioned LEDs of different wavelengths. Of each measurement location, high-dynamic range (HDR) images were generated, resulting in 20-40 images for each wavelength per measurement location ($S_{MicroCam}$). Afterwards, the slice(s) were returned to the department of Pathology and processed according to standard protocol.

Data visualization

The illumination fibers and camera are cross polarized to filter out specular surface reflections. However, under certain conditions some specular reflections remain due to the limited contrast ratio and angular performance of the polarizers. These reflections are present in the form of small bright peaks in the image. Using the Laplacian of Gaussian method, blob-like features in the image can be identified. Such features include both specular reflections as well as other larger blob-like features in the image. The method is a multi-scale method, using a varying sigma of the Gaussian convolution to detect features of differing sizes. Subsequently, features below a threshold of 400 µm in size are excluded. This feature size is based on the size of microcalcifications, which can be as low as 300 µm, but mostly exceeds 400 µm *(26)*. In order to present a filtered image to the clinician, the locations of these excluded features can be median blurred to remove the sharp specular reflection peaks. The results of this process can be seen in Figure 2. Figure 2a

show two raw greyscale images of different locations in S_{SPEC}, with and without microcalcifications present, respectively. Figure 2b shows the output of the blob detection algorithm, with different colors indicating different sigma values and therefore different sizes of features. Figure 2c show the corrected images. It is important to note that this visual correction can be beneficial when excluding features with certain criteria in a static measurement set up, however the impact of specular reflections is reduced when using the system to actively scan tissue. Specular reflections are easily identified in this case due to their movement with probe movement, whereas features in the tissue will remain in the image. Image visualization for a human observer can be further improved by employing a contrast limited adaptive histogram equalization (CLAHE) algorithm.

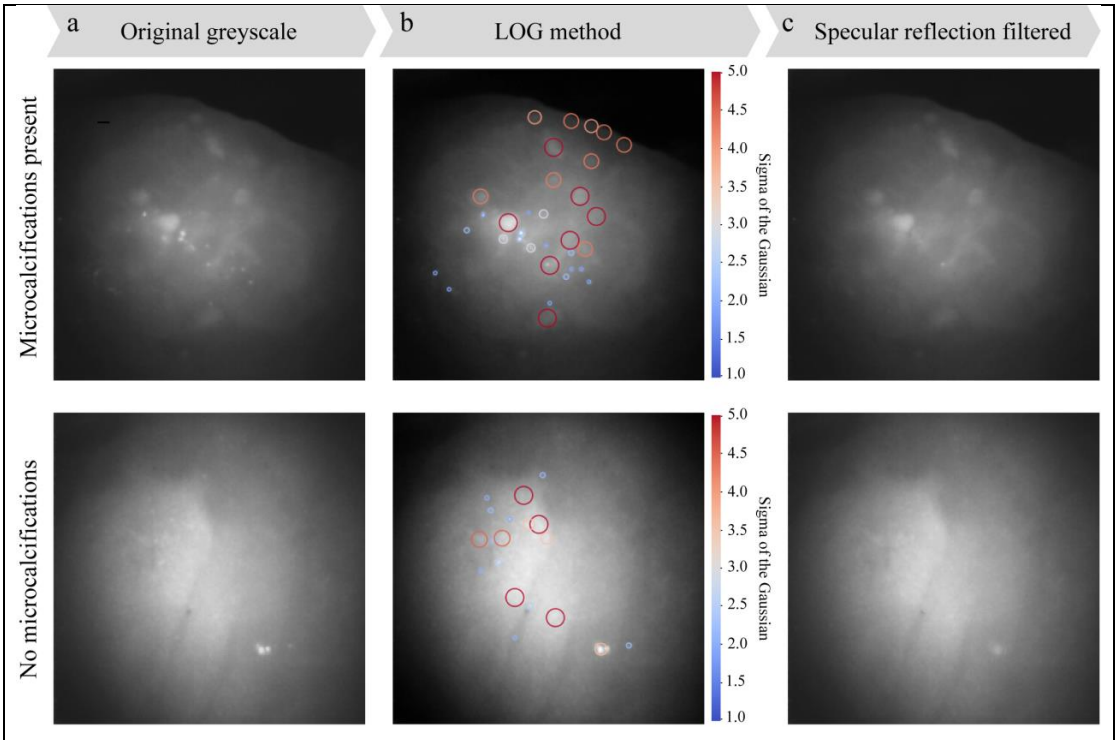

Figure 2. *Method for filtering specular reflections from $S_{MicroCam}$ images. (a) Original greyscale images. (b) Blob-like features are detected in the image and blobs under a certain size are filtered out using a median filtering technique. (c) specular reflection filtered images are generated.*

Data analysis

For identification of microcalcifications in the $S_{MicroCam}$ images, multiple registration steps were performed (Figure 3). A top-view image of the S_{PPM} was acquired as described in detail in previous study from our institute *(25)*. Since there is limited deformation between S_{MAM} and S_{PPM} a point-based registration was performed, by selecting 6-8 corresponding anatomical landmarks in both images. Since the S_{SPEC} are squashed during the mammography, the S_{PPM} was chosen as the fixed image (Figure 3a). Next, a binary image of the projected measurement locations was created by selecting the center point. The projected measurement points (circle with a true diameter of 0.5 cm) were transformed to match the FoV of the camera (square of 1.0 x 1.0 cm) (Figure 3b). The binary FoV image, was then overlaid with S_{SPEC} and S_{MAM}. As a result, the exact measurement locations were identified in S_{MAM} (Figure 3c).

The second registration involved the exact overlay of $S_{MicroCam}$ and S_{ROI}. For this, 15 and 20 corresponding anatomical landmarks were manually selected, after which S_{ROI} was transformed to fit $S_{MicroCam}$ (Figure 3d). Simultaneously, microcalcifications were identified and transformed to fit the orientation of $S_{MicroCam}$ (Figure 3e). Lastly, circles with a radius of 1 mm are drawn around the microcalcification in S_{MAM} and overlaid on the 850 nm $S_{MicroCam}$ (Figure 3f). Ultimately, four independent reviewers, two with medical knowledge and two with technical expertise, were asked to evaluate all $S_{MicroCam}$ images. They had to score the images on the presence of microcalcifications, and performance scores were computed (sensitivity, specificity, accuracy and F-score).

Statistical analysis

Statistical analysis was performed using IBM SPSS statistics v27 (SPSS Inc., United States) and Matlab (R2021b, the Mathworks Inc, Massachusetts). Quantitative data are presented as means and standard deviations, whereas qualitative data is presented as numbers and percentages.

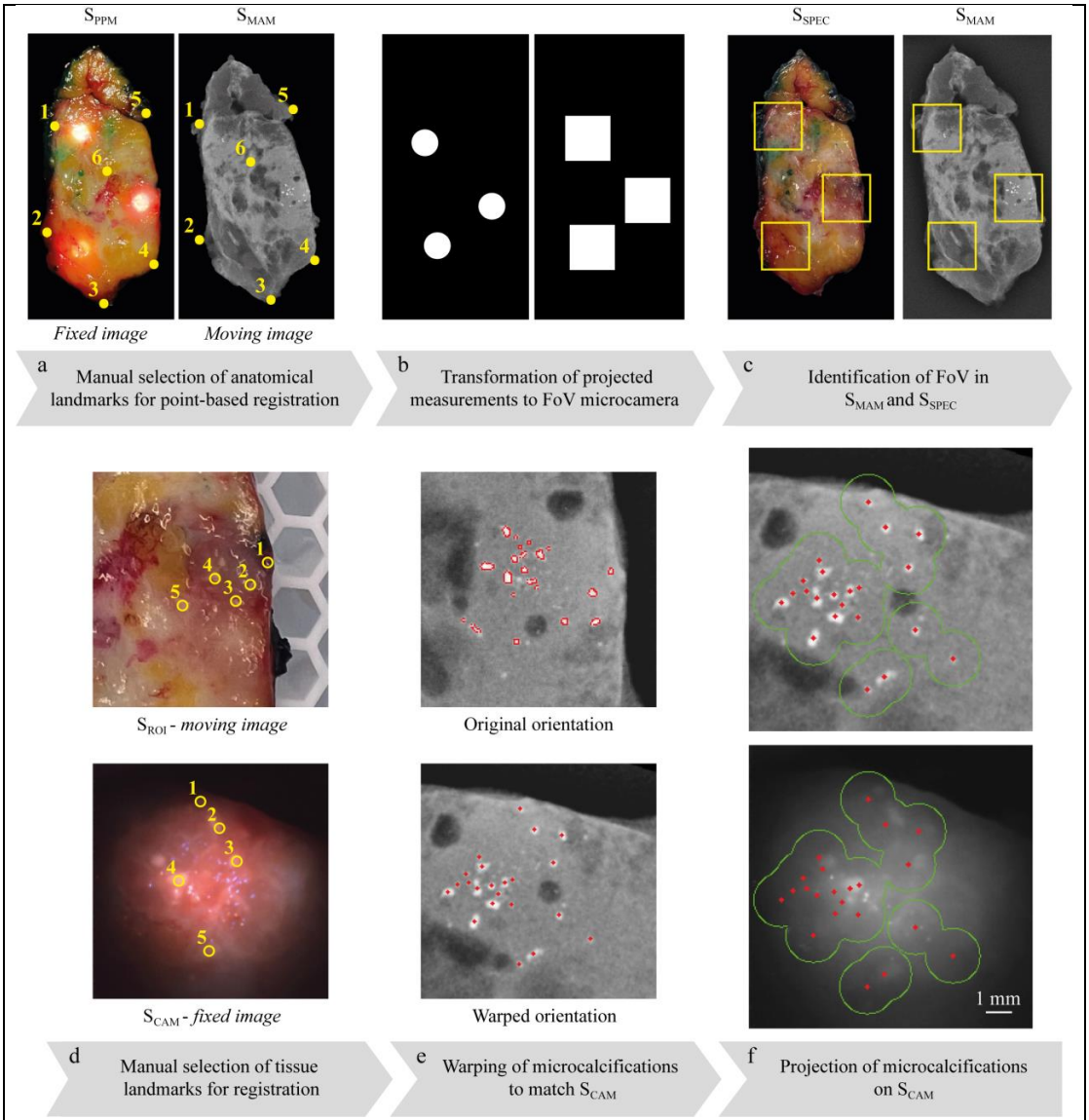

Figure 3. *Workflow of the co-registration method for identification of microcalcifications in the* S_{MicroCam} *images. (a) The point-based image registration is performed by manually selecting corresponding anatomical landmarks in* S_{PPM} *and* S_{MAM}*.. (b) Binary image of the projected measurement locations were transformed to squares too match the field of view (FoV) of the optical probe. (c) The measurement locations are overlaid on the* S_{PPM} *and* S_{MAM}*, generating the exact counterpart of the* S_{MicroCam} *image. (d)* S_{ROI} *and* S_{MicroCam} *co-located based on landmarks on both images. (e) Based on the co-location in step 4,* S_{MAM} *is warped to match* S_{MicroCam}*, thereby providing a new orientation of the microcalcifications. (f) Lastly, the microcalcifications from* S_{MAM} *are projected on* S_{MicroCam} *with a circle representing an error of 1mm in all directions.*

Results

12 patients, providing 22 tissue slices, were included in this study – baseline characteristics are shown in table 1. In total 64 measurements were performed on locations with microcalcifications (35.9%) and without microcalcifications (64.1%). The majority of the patients underwent surgery as a result of DCIS (83.4%). The diameter of clustered microcalcifications were on average 30 mm and could be as large as 71 mm.

***Table 1**: patient demographics*

	N	
Total patients	12	
Total WLE slices	22	
Measurement locations with microcalcifications	23	35.9 %
Measurement locations without microcalcifications	41	64.1 %
Gender		
Female	12	100 %
Age, *median (range)*	55	52–62
Tumor type		
DCIS grade 1	1	8.3 %
DCIS grade 2	2	16.6 %
DCIS grade 3	7	58.3 %
Lobular carcinoma in situ	1	8.3 %
Invasive carcinoma in situ	1	8.3 %
Diameter of clustered microcalcifications, *mm, mean (range)*	30	5–71
Area of microcalcifications, mm^2, *mean (range)*	22	1–143

Ex-vivo study

Each measurement location was assessed on the presence of microcalcifications in the $S_{MicroCam}$ image and the corresponding S_{MAM} image, which was considered as ground truth. For every $S_{MicroCam}$ image, CLAHE images were generated for improved feature differentiation. A typical example is shown in figure 4. When microcalcifications were present in the $S_{MicroCam}$ images, they appeared highly reflective compared to the surrounding breast tissues (yellow box). When no microcalcifications were present, these features would be absent (blue box).

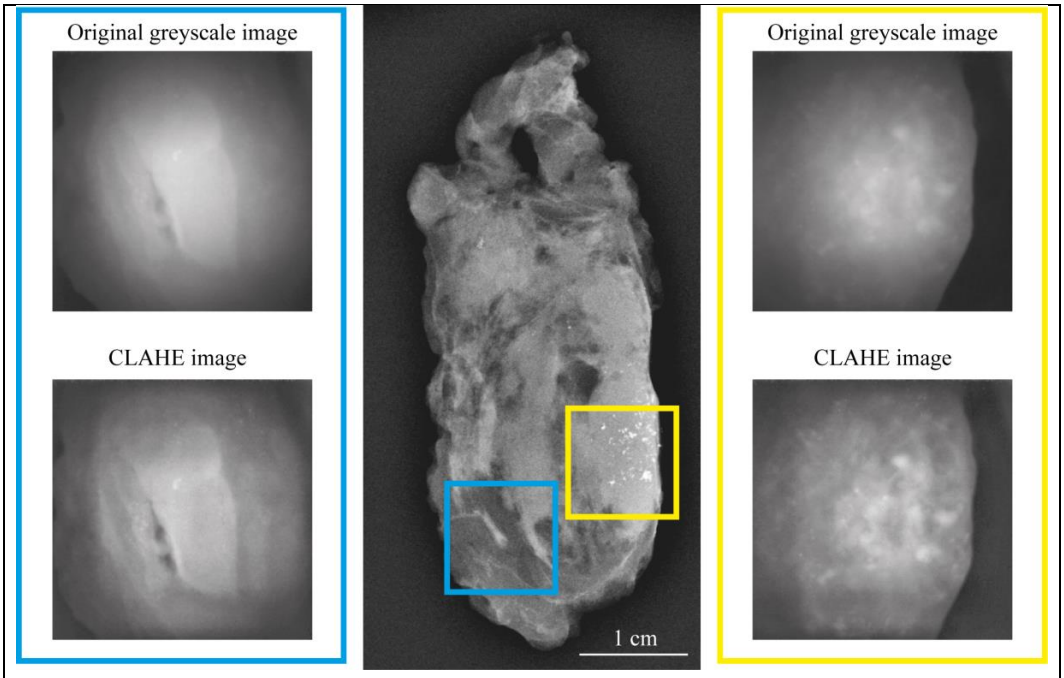

Figure 4. *S_{MAM} with corresponding greyscale $S_{MicroCam}$ images of near infrared light at 850nm. The yellow box represents the measurement with microcalcifications, whereas the blue box is considered a negative control.*

The detectability of microcalcifications with the FoV of the microcamera was notably affected by the situated distribution and depth of the microcalcifications. Notably, microcalcifications situated within 2 mm of the tissue surface could be identified as bright features (Figure 5a). However, in many cases microcalcifications were distributed throughout the complete tissue slice, leading to detection of only a fraction of the calcifications. (Figure 5b). In negative control tissue slices, no features resembling microcalcifications were detected (Figure 5c). Even so, microcalcifications that were situated below the imaging depth of 2 mm were not detected, while being observed in the control mammography (example 9).

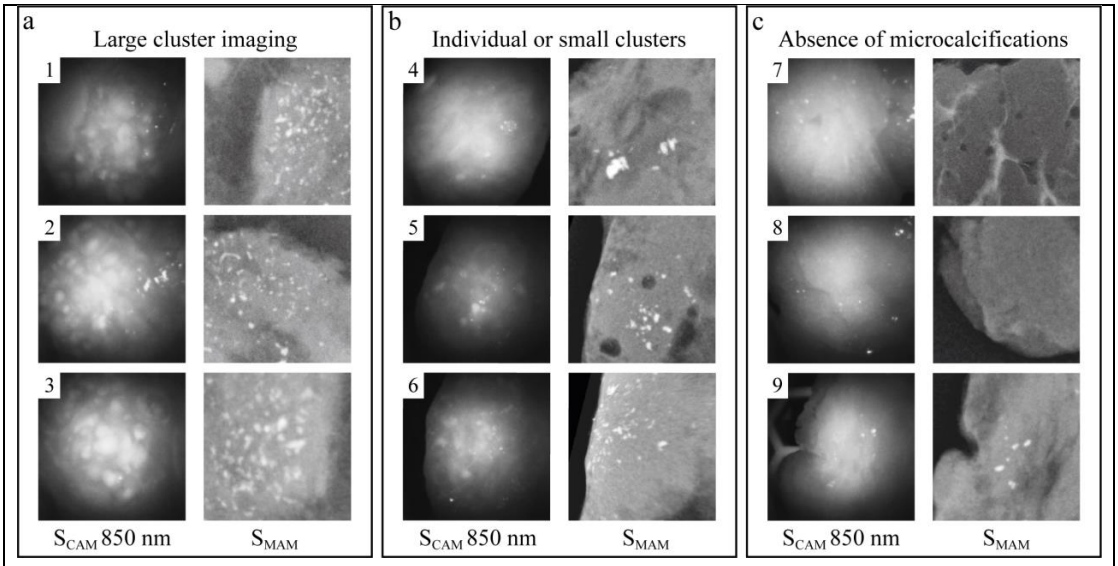

***Figure 5**. Nine examples of $S_{MicroCam}$ images of various microcalcification distributions, accompanied with the corresponding S_{MAM}. (a) Large clusters of microcalcifications within both S_{MAM} and $S_{MicroCam}$. (b) Small groups of clustered microcalcifications,, and (c) absence of microcalcifications in $S_{MicroCam}$ images due to absence of microcalcifications in the mammography (examples 7 and 8), or suspected distribution at depth more than 2 mm (example 9).*

Four independent reviewers were asked to evaluate all $S_{MicroCam}$ images. They were tasked with the binary assessment of microcalcifications within the provided images, as shown in Table 2. Their collective analysis yielded an average sensitivity of 77.8% and specificity of 80.0%, resulting in an overall accuracy of 79.0%. The calculated F-score stood at 73.8%.

Table 2. Independent reviewer assessment scores

	Sensitivity (%)	**Specificity (%)**	**Accuracy (%)**	**F-score (%)**
Reviewer 1 (clinician)	73.9	87.8	82.8	75.6
Reviewer 2 (clinician)	79.2	84.2	82.3	77.6
Reviewer 3 (technician)	78.2	77.5	76.6	70.6
Reviewer 4 (technician)	80.0	70.3	74.2	71.4
Average	**77.8**	**80.0**	**79.0**	**73.8**

Discussion

The present study demonstrates the first results of a cross-polarized DOI microcamera imaging setup for detecting microcalcification in the superficial 2 mm of breast tissue. Measurements were performed on *ex vivo* breast specimens containing microcalcifications of varying sizes and distributions. Regions of interest of 1.0 cm^2 were imaged, providing highly detailed features with a magnification up to 50 µm. These images were registered to the corresponding areas in the S_{MAM} with an in-house developed registration method for identification of microcalcifications in $S_{MicroCam}$ images (Figure 3). The final images were independently scored by two medical specialists and two technical specialists, achieving an overall sensitivity of 77.8%, specificity of 80.0% and accuracy of 79.0%.

Up to 30% of all excised DCIS lesions result in tumor-positive resection margins after histopathology *(6)*, and currently there is no objective imaging technique available for real-time intraoperative assessment of the resection margin. Moreover, DCIS is well known for containing microcalcifications in 60-90% of cases, which are being formed and deposited at the invasive border of the lesion *(4, 7, 8)*, making them an interesting target for resection margin assessment. The golden standard for resection margin assessment remains histopathology, however this can take up to several days. Over the last years, new innovations in the operating theatres allow for scanning of the entire breast lump directly after excision *(27)*, having the potential of providing direct feedback to the surgeon. However, these techniques are not able to visualize the resection plane that remains in the breast after excision of the tumor.

One prominent advantage of the proposed DOI microcamera setup is the possibility for real-time assessment of tissue structures during imaging and scanning large portions of tissue in a short amount of time. The current setup allows for fast switching between visualization of tissue structures on and below the tissue surface. Moreover, a microcamera setup presents a highly favorable approach for assessing the resection plane within the breast cavity post tumor excision. The compact and easily maneuverable nature of the microcamera probe, together with the real-time and high-resolution visualization capabilities enables meticulous evaluation of the cavity. This holds significance not only in visualizing calcifications but also in evaluating residual tumor burden. The small footprint of the camera allows for simple integration with other sensing modalities, and addition of a camera sensor on to existing surgical tools if desired.

The microcamera system utilizes cross-polarization, as described in detail in our recent work *(24)*. However, due to limitations in the contrast ratio of the polarizers not all specular reflections were removed. A trade-off was made between contrast ratio and transmission across a wide wavelength range when selecting polarizers for this work. Nonetheless, this is a technical challenge, and not a theoretical limit to

the proposed microcamera technique. With high contrast polarizers at select wavelengths the removal of specular reflections could be improved further. Specular reflection reduction by cross-polarization is important when improving the overall image quality of such a small sensor, examining a small area of interest. It is important to note that these small remaining specular reflections are easily distinguished from features of interest, since they will change with different viewing positions and angles when moving the camera during a tissue scan. When showing static images, post processing can be employed to remove the remainder of the specular artifacts. In the present study, the remaining specular reflections were identified and eliminated during post-processing, improving the quality of $S_{MicroCam}$ images and visualization of microcalcifications. Hence, from this study it can be concluded that specular reflections occurring at the tissue surface can obfuscate the microcalcifications that reside inside the tissue, limiting the performance metrics. By effectively eliminating the surface reflections, either with improved cross-polarizing filters or by post-processing, performance metrics will increase.

In the current study, an overall sensitivity of 77.8% was achieved in detecting microcalcifications in $S_{MicroCam}$ images. At first glance, this sensitivity might appear relatively modest. However, in reality the thickness of the tissue slices (3-5 mm), and the fact that microcalcifications can be spread throughout the entire slice, might exceeds the penetration depth of the used wavelengths (2 mm). When calcifications were present in the superficial 2 mm of the tissue slice, in almost all cases they were visible in the $S_{MicroCam}$ images. However, when the calcifications were located deeper than 2 mm, they could not be seen, explaining the modest sensitivity. While this may sound as a limitation of the presented setup, the superficial 2 mm are considered clinically relevant for assessing resection margins after surgical resection of the tumor *(28)*. Hence, identification of calcifications in the superficial 2 mm would provide the clinician with information regarding the possibility of residual tumor cells in the resection margin.

It is important to note that the described technique is only tested on the visualization of microcalcifications. However, due to the fact that DCIS is not accompanied by microcalcifications in 10-40% of cases, visualization of solely microcalcifications in the resection margins is likely insufficient to aid in decision making in the clinical setting. Therefore, the current approach should be tested in combination with a supplementary technique, such as DRS, or any other technique able to differentiate between breast tissue and tumor tissue with a high sensitivity. In recent studies, DRS was able to detect DCIS and IC with high accuracies, potentially aiding in surgical guidance intra and postoperative *(16, 29)*. As such, the combination of DRS with the proposed microcamera setup in this study, might provide an accurate tool for resection margin assessment in BCS, by means of examining the excised tumor, as well as the tumor cavity for residual tumor/microcalcifications.

Due to the fact that suspicious microcalcifications are also located at the border of the tumor, they can provide an interesting target for intraoperative margin assessment *(4)*. Moreover, when microcalcifications are present in the resection plane after excision of the tumor, they are a strong indication that tumor cells are left behind in the patient. Therefore, visualizing microcalcifications in the resection plane during surgery can be pivotal in assessing resection margins intraoperatively, allowing surgeons to excise extra tissue in the same procedure when indicated.

Conclusion

The presented novel cross-polarized DOI microcamera setup provides a non-invasive technique for fast and real-time assessment of microcalcifications in superficial breast tissues. Through a robust registration method, accurate correlations were made between the microcamera images and corresponding slice mammography regions. By focusing on the context of the region of interest (superficial 2 mm), the current approach provides both promising results as well as considerable anticipation for future studies and applications.

Acknowledgements

Walter Messina assisted considerably in designing the microcamera assembly. This is gratefully acknowledged. Lisanne de Boer

References

1. M. M. Eberl, C. H. Fox, S. B. Edge, C. A. Carter, M. C. Mahoney, BI-RADS classification for management of abnormal mammograms. *J. Am. Board Fam. Med.* **19**, 161–164 (2006).

2. T. Q. H. Ho, M. C. S. Bissell, C. I. Lee, J. M. Lee, B. L. Sprague, A. N. A. Tosteson, K. J. Wernli, L. M. Henderson, K. Kerlikowske, D. L. Miglioretti, Prioritizing Screening Mammograms for Immediate Interpretation and Diagnostic Evaluation on the Basis of Risk for Recall. *J. Am. Coll. Radiol.* **20**, 299–310 (2023).

3. IKNL, RIVM, Monitor bevolkingsonderzoek borstkanker 2018/2019. , 1–6 (2020).

4. T. Sharma, J. A. Radosevich, G. Pachori, C. C. Mandal, A Molecular View of Pathological Microcalcification in Breast Cancer. *J. Mammary Gland Biol. Neoplasia* **21**, 25–40 (2016).

5. A. Bane, Ductal Carcinoma In Situ : What the Pathologist Needs to Know and Why. *Int. J. Breast Cancer* **2013**, 1–7 (2013).

6. G. Rauch, B. Hobbs, H. Kuerer, M. Scoggins, A. Benveniste, Y. Mi Park, A. Caudle, P. Fox, B. Smith, B. Adrada, S. Krishnamurthy, W. T. Yang, Microcalcifications in 1657 Patients with Pure Ductal Carcinoma in Situ of the Breast: Correlation with Clinical, Histopathologic, Biologic Features and Local

Recurrence. *Annu. Surg. Oncol.* **23**, 482–489 (2016).

7. B. Barreau, I. De Mascarel, C. Feuga, G. MacGrogan, M. H. Dilhuydy, V. Picot, J. M. Dilhuydy, C. T. De Lara, E. Bussières, I. Schreer, Mammography of ductal carcinoma in situ of the breast: Review of 909 cases with radiographic-pathologic correlations. *Eur. J. Radiol.* **54**, 55–61 (2005).

8. S. Hofvind, B. Iversen, L. Eriksen, B. Styr, K. Kjellevold, K. Kurz, Mammographic morphology and distribution of calcifications in ductal carcinoma in situ diagnosed in organized screening. *Acta Radiol.* **52**, 481–487 (2011).

9. P. L. Arancibia Hernández, T. Taub Estrada, A. López Pizarro, M. L. Díaz Cisternas, C. Sáez Tapia, Breast calcifications: Description and classification according to BI-RADS 5th edition. *Rev. Chil. Radiol.* **22**, 80–91 (2016).

10. R. Smithuis, R. Pijnappel, Differential of Breast Calcifications*Radiologyassistant.nl* (2008) (available at https://radiologyassistant.nl/breast/calcifications/differential-of-breast-calcifications).

11. F. Cardoso, S. Kyriakides, S. Ohno, F. Penault-Llorca, P. Poortmans, I. T. Rubio, S. Zackrisson, E. Senkus, Early breast cancer: ESMO Clinical Practice Guidelines for diagnosis, treatment and follow-up. *Ann. Oncol.* **30**, 1194–1220 (2019).

12. S. G. Brouwer de Koning, M. J. T. F. D. Vrancken Peeters, K. Jóźwiak, P. A. Bhairosing, T. J. M. Ruers, Tumor Resection Margin Definitions in Breast-Conserving Surgery: Systematic Review and Meta-analysis of the Current Literature. *Clin. Breast Cancer* **18**, e595–e600 (2018).

13. F. Meric, N. Q. Mirza, G. Vlastos, T. A. Buchholz, H. M. Kuerer, G. V. Babiera, S. E. Singletary, M. I. Ross, F. C. Ames, B. W. Feig, S. Krishnamurthy, G. H. Perkins, M. D. McNeese, E. A. Strom, V. Valero, K. K. Hunt, Positive surgical margins and ipsilateral breast tumor recurrence predict disease-specific survival after breast-conserving therapy. *Cancer* **97**, 926–933 (2003).

14. R. Rulaningtyas, A. S. Hyperastuty, A. S. Rahaju, Histopathology Grading Identification of Breast Cancer Based on Texture Classification Using GLCM and Neural Network Method. *J. Phys. Conf. Ser.* **1120** (2018), doi:10.1088/1742-6596/1120/1/012050.

15. L. L. De Boer, T. M. Bydlon, F. Van Duijnhoven, M. J. T. F. D. Vranken Peeters, C. E. Loo, G. A. O. Winter-Warnars, J. Sanders, H. J. C. M. Sterenborg, B. H. W. Hendriks, T. J. M. Ruers, Towards the use of diffuse reflectance spectroscopy for real-time in vivo detection of breast cancer during surgery. *J. Transl. Med.* **16**, 1–14 (2018).

16. L. L. de Boer, E. Kho, K. K. Van de Vijver, M. J. T. F. D. Vranken Peeters, F. van Duijnhoven, B. H. W. Hendriks, H. J. C. M. Sterenborg, T. J. M. Ruers, Optical tissue measurements of invasive carcinoma and ductal carcinoma in situ for surgical guidance. *Breast Cancer Res.* **23**, 1–15 (2021).

17. F. Geldof, B. Dashtbozorg, B. H. W. Hendriks, H. J. C. M. Sterenborg, T. J. M. Ruers, Layer thickness prediction and tissue classification in two-layered tissue structures using diffuse reflectance

spectroscopy. *Sci. Rep.* **12**, 1–12 (2022).

18. E. Kho, B. Dashtbozorg, L. L. de Boer, K. K. Van de Vijver, H. J. C. M. Sterenborg, T. J. M. Ruers, Broadband hyperspectral imaging for breast tumor detection using spectral and spatial information. *Biomed. Opt. Express* **10**, 4496 (2019).

19. E. Kho, L. L. De Boer, K. K. Van De Vijver, F. Van Duijnhoven, M. J. T. F. D. V. Peeters, H. J. C. M. Sterenborg, T. J. M. Ruers, Hyperspectral imaging for resection margin assessment during cancer surgery. *Clin. Cancer Res.* **25**, 3572–3580 (2019).

20. R. Vanna, C. Morasso, B. Marcinno, F. Piccotti, E. Torti, D. Altamura, S. Albasini, M. Agozzino, L. Villani, L. Sorrentino, O. Bunk, F. Leporati, C. Giannini, F. Corsi, Raman spectroscopy reveals that biochemical composition of breast microcalcifications correlates with histopathologic features. *Cancer Res.* **80**, 1762–1772 (2020).

21. M. Alsheh Ali, K. Czene, P. Hall, K. Humphreys, Association of Microcalcification Clusters with Short-term Invasive Breast Cancer Risk and Breast Cancer Risk Factors. *Sci. Rep.* **9**, 1–8 (2019).

22. A. J. Watras, J. J. Kim, J. Ke, H. Liu, J. A. Greenberg, C. P. Heise, Y. H. Hu, H. Jiang, Large-field-of-view visualization with small blind spots utilizing tilted micro-camera array for laparoscopic surgery. *Micromachines* **11**, 1–14 (2020).

23. N. Modir, M. Shahedi, J. D. Dormer, B. Fei, Development of a real-time spectral imaging system using in-site micro-LED-based illumination and high-speed micro-camera for endoscopic applications. , 40 (2021).

24. L. Niemitz, S. D. van der Stel, S. Sorensen, W. Messina, S. Konugolu, V. Sekar, H. J. C. M. Sterenborg, S. Andersson-engels, T. J. M. Ruers, R. Burke, Microcamera Visualisation System to Overcome Specular Reflections for Tissue Imaging. *Micromachines* **14**, 1062 (2023).

25. L. Feenstra, S. D. van der Stel, M. Da Silva Guimaraes, B. Dashtbozorg, T. J. M. Ruers, Point projection mapping system for tracking, registering, labeling and validating optical tissue measurements. *J. Biomed. Opt.* **Under revi** (2023).

26. M. Alsheh Ali, M. Eriksson, K. Czene, P. Hall, K. Humphreys, Detection of potential microcalcification clusters using multivendor for-presentation digital mammograms for short-term breast cancer risk estimation. *Med. Phys.* **46**, 1938–1946 (2019).

27. I. Willekens, E. Van de Casteele, N. Buls, F. Temmermans, B. Jansen, R. Deklerck, J. de Mey, High-resolution 3D micro-CT imaging of breast microcalcifications: A preliminary analysis. *BMC Cancer* **14** (2014), doi:10.1186/1471-2407-14-9.

28. M. Pilewskie, M. Morrow, Margins in breast cancer: How much is enough? *Cancer* **124**, 1335–1341 (2018).

29. L. L. de Boer, B. H. W. Hendriks, F. van Duijnhoven, M.-J. T. F. D. V. Peeters-Baas, K. Van de

Vijver, C. E. Loo, K. Jóźwiak, H. J. C. M. Sterenborg, T. J. M. Ruers, Using DRS during breast conserving surgery: identifying robust optical parameters and influence of inter-patient variation. *Biomed. Opt. Express* **7**, 5188 (2016).

Paper III

Towards a flexible polarimetric camera-on-tip miniature endoscope for 3×3 Mueller matrix measurements of biological tissue

Niemitz, Lorenzo and Sørensen, Simon and Wang, Yineng and Messina, Walter and Burke, Ray and Andersson-Engels, Stefan.

1262733– (2023) *European Conference on Biomedical Optics*.

Best Student Paper

Towards a flexible polarimetric camera-on-tip miniature endoscope for 3x3 Mueller matrix measurements of biological tissue

Lorenzo Niemitz[a], Simon Sorensen[a], Yineng Wang[a], Walter Messina[a], Ray Burke[a], and Stefan Andersson-Engels[a, b]

[a]Biophotonics@Tyndall, IPIC, Tyndall National Institute, Cork, Ireland
[b]Department of Physics, University College Cork, Cork, Ireland

Keywords: camera-on-tip, micro camera, polarimetry, Mueller matrix, endoscope

1. INTRODUCTION

The interrogation of polarisation state of light is a developing technique in biomedical imaging. As polarised light interacts with structural changes in tissue, it has seen use in differentiation between (pre)cancerous and non-cancerous tissue, for example.[1] In biomedical imaging rapid diagnostics using minimally invasive techniques is desirable. Endoscopy is already very prevalent in medicine and therefore miniaturisation of polarimetry systems onto endoscopic platforms is a natural development. Flexibility of such a device allows navigation to more complicated parts of the body. All polarimetric systems consist of a polarisation state generator (PSG) and a polarisation state analyser (PSA) which need to be integrated into such a system.

A rigid endoscope capable of imaging a full 4x4 Mueller matrix has been developed by Qi et al.[2] This endoscope achieves the polarisation state generation a rigid rotating sheath. Partial polarimetric endoscopy which captures a 3x3 Mueller matrix has also been demonstrated and is easier to achieve since it does not require quarter wave plates in the generator or analyser. Clancy et al and Qi et al both demonstrate a rigid polarimetric endoscopy using a stereo endoscope and a standard rigid endoscopy, respectively.[3, 4] Integration of polarisation state analyser and generator into the tip has been demonstrated using complex mechanical designs.[5] However questions have been raised regarding the electromagnetic compatibility of such a system due to the presence of motors in the tip.[6] Forward et al present a flexible 3x3 fibre based probe that uses diced polarisers orientated at the horizontal, vertical, and -45 degree positions to generate and acquire the necessary polarisation states.[7]

This work presents an imaging probe designed to enable *in-vivo* polarimetry measurements using a micro camera on the tip as a sensor. A 3x3 Mueller matrix image of crossed linear polarisers, captured using a micro camera is demonstrated. This device demonstrates the potential of micro camera sensors in providing 2-dimensional polarimetry data in a flexible endoscopic system. For a device to be used in a clinical setting it needs to be capable of providing data rapidly when it is needed, as well as being navigable to the target location. A fibre optically illuminated endoscope with micro-camera sensor allows for rapid switching of illumination fibres using backend illumination systems as well as rapid acquisition of data. Optical fibres enable the probe to be rigid or flexible depending on application, and the camera at the tip ensures consistent image quality regardless of application area. An idealised system and its potential future of polarimetry in translational biophotonic devices is also discussed.

2. DESIGN

The design in Figure 1 utilises diced polarisers mounted in front of six illumination fibres that act as the PSG. These fibres are concentrically arranged around a central camera with opposite pairs of fibres illuminating with the same polariser orientation to provide an even illumination over the field-of-view of the camera. The camera sits fixed within core component (indicated grey). The inner sheath (indicated in cyan) is allowed to rotate freely

Further author information: (Send correspondence to Lorenzo Niemitz)
Lorenzo Niemitz: E-mail: l.niemitz@student.ucc.ie, Telephone: +353 21 234 6624

Translational Biophotonics: Diagnostics and Therapeutics III, edited by Zhiwei Huang, Lothar D. Lilge, Proc. of SPIE Vol. 12627, 1262733
© 2023 SPIE · 0277-786X · doi: 10.1117/12.2670607

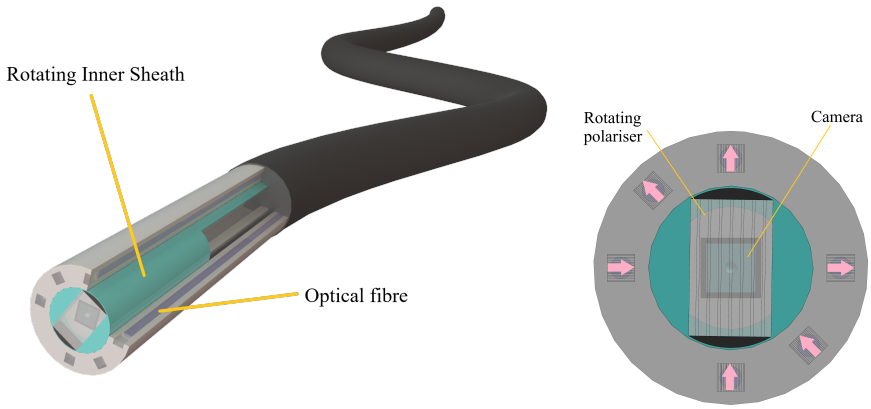

Figure 1. Probe design with sectioned view of the outer sheathing (L) and close up view of the distal end (R). The outer shell is part of a core component (indicated grey) which also connects to the camera housing in the center. The inner sheath (indicated cyan) is allowed to rotate freely within a limited range of motion inside this core component. In the close up view the polariser orientations are indicated using the pink arrows, the camera can be seen in the centre with the PSA polariser mounted in front of it on the inner sheath.

between angles of 0 and 90 degrees within this core component. This inner sheath includes a mount for a larger polariser that sits in front of the camera.

The probe tip is designed to be is 7 mm in length, and 5 mm in diameter, with mechanical validation to follow. In theory the length of this distal end is variable and must at minimum support the length of the camera and more importantly secure attachment to the rotating inner sheath. Rotation will be achieved using a stepper motor, integrated proximally with a torque coil to transfer rotation along the length of the device. The initial design however, includes a rigid rotation mount to more accurately control the rotation at the distal end.

3. METHODS

Linear glass polarisers (Edmund Optics 12-649) are diced using a mechanical dicing saw to the required dimensions and mounted in front of the fibres. The polarisers are orientated at 0, 45, and 90 degrees with respect to the zero axis of the probe as shown in Figure 1. All components are integrated into a 3D printed components and secured using UV cure epoxy (Norland NOA68). A monochrome AMS NanEYE image sensor, with 90 degree field-of-view (FOV) and F2.7, is used as the sensor. Six illumination fibres 400 μm with numerical aperture of 0.5 are arranged concentrically around the micro-camera, ensuring that the FOV of the camera is illuminated sufficiently. Two illumination fibres are active for each polarisation state generated to ensure an even illumination over the FOV of the camera for each image captured.

Figure 2 shows a microscope image of the assembled tip of the system with a 5 mm diameter. The large central polariser is allowed to rotate freely around the camera by rotating the back of the innner sheath. Optical fibres are mounted behind the polarisers. Tolerances will be tightened in future iterations of the design.

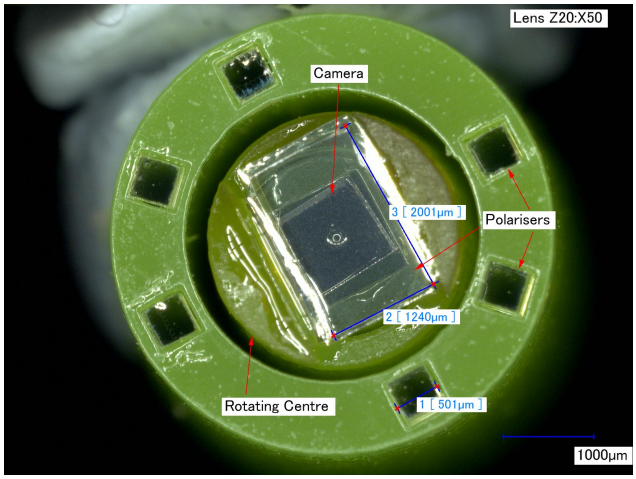

Figure 2. Image of the 3D printed holder with integrated polarisers concentric around the camera, and the rotating centre piece with larger linear polariser.

4. RESULTS

Figure 3 shows results captured using a micro camera with rotating polarisers. To the best of the authors' knowledge these are the first Mueller matrix images captured using a micro camera.

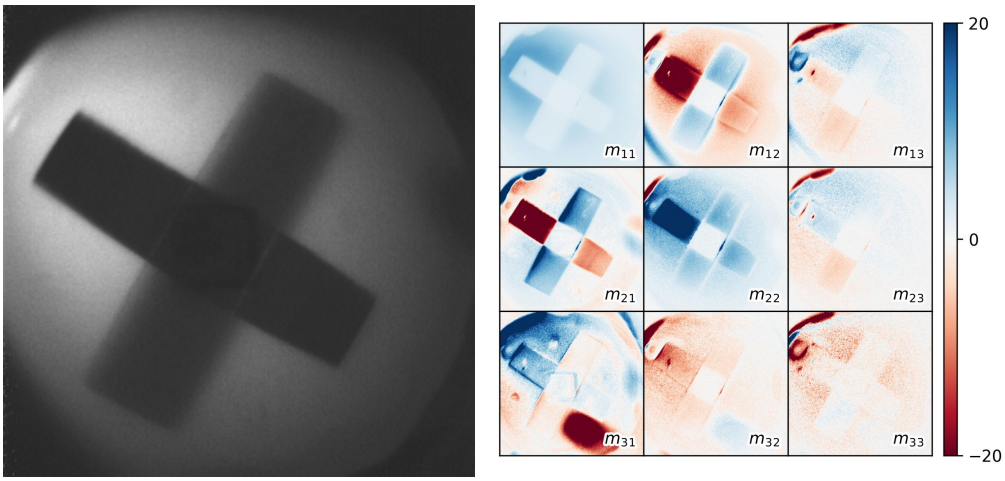

Figure 3. Image of crossed plastic polarisers on a white tissue phantom acquired using AMS NanEYE camera, PSG set to 90 degrees and PSA set to 0 degrees (L) and 3x3 Mueller matrix images of the same region (R). Analysis code used.[8]

5. DISCUSSION AND CONCLUSION

A design for a miniaturised camera on the tip endoscope with 3x3 polarimetric capability is presented. With Figure 3 demonstrating the ability to resolve a polarimetric measurement using a micro-camera. Another proposed design uses a MEMS device to rotate the polarisation optic in front of the camera.

A monochrome image sensor allows for the full utilisation of the pixels per measurement run, and since polarimetry is usually performed at a single wavelength at a time makes the most sense for the device. Illumination

fibres are preferred over LEDs in illumination as they provide flexibility in the delivered illumination as well as remove concerns of heating effects and electrical safety in the body. Fibre illumination also allows for potential extension of the system to the broadband system using multiple illumination wavelengths. Illumination with fibre bundles can allow for greater numerical aperture to improve the illumination if overlap is problematic in the final probe.

An idealised device would use a polarised camera sensor (such as the Sony IMX250MZR) in the micro camera format. However currently a sensor like this is not commercially available. The disadvantage of such a sensor in the small footprint would be the pixel utilisation, with only a quarter of the pixels available for each image. An alternative is a polarisation rotator in the micro format mounted in front of the camera and electrically controlled. With the inclusion of variable retarders of sufficiently small footprint mounted in front of two of the illumination fibres and in front of the camera, a 4x4 mueller matrix imaging system would be theoretically possible at this scale.

In conclusion we have demonstrated acquisition of a 3x3 Mueller matrix using a micro camera system, as well as the integration of such a system into a small footprint endoscope tip.

ACKNOWLEDGMENTS

The authors would like to thank Paul Tassie for his help with the polariser dicing, Noreen Nudds for help with the integration of components, and Guangbo Hao with his advice regarding mechanical actuation.

The authors would like to acknowledge funding from Science Foundation Ireland Grant SFI/12/RC/2276_P2 as well as SFI/15/RP/2828.

REFERENCES

[1] Singh, M. D., Ghosh, N., and Vitkin, I. A., [*Mueller Matrix Polarimetry in Biomedicine: Enabling Technology, Biomedical Applications, and Future Prospects*], 61–103, Springer International Publishing, Cham (2023).

[2] Qi, J. and Elson, D. S., "A high definition mueller polarimetric endoscope for tissue characterisation," *Scientific reports* **6**(1), 1–11 (2016).

[3] Clancy, N. T., Arya, S., Qi, J., Stoyanov, D., Hanna, G. B., and Elson, D. S., "Polarised stereo endoscope and narrowband detection for minimal access surgery," *Biomedical optics express* **5**(12), 4108–4117 (2014).

[4] Qi, J., Ye, M., Singh, M., Clancy, N. T., and Elson, D. S., "Narrow band 3× 3 mueller polarimetric endoscopy," *Biomedical optics express* **4**(11), 2433–2449 (2013).

[5] Huang, Z., Fu, Y., Li, Z., and Wu, J., "A portable 3× 3 mueller matrix polarimeter prototype for cancer detection ex vivo," in [*Proceedings of the 3rd International Conference on Biomedical Signal and Image Processing*], 92–97 (2018).

[6] Qi, J. and Elson, D. S., [*Polarimetric Endoscopy*], 179–204, Springer International Publishing, Cham (2023).

[7] Forward, S., Gribble, A., Alali, S., Lindenmaier, A. A., and Vitkin, I. A., "Flexible polarimetric probe for 3× 3 mueller matrix measurements of biological tissue," *Scientific Reports* **7**(1), 1–12 (2017).

[8] Ryota, M., "Polanalyser v1.2.0." https://github.com/elerac/polanalyser (2022).

Paper IV

Camera-on-tip Angioscope for in-vivo Cardiovascular Diagnostics and Surgical Guidance

Sørensen, Simon and Messina, Walter, and Niemitz, Lorenzo, and O'Dowling, Claire, and Buszman, Piotr and Andersson-Engels, Stefan, and Burke, Ray.

– (submitted: Mar 2024) *Submitted to Journal of Biomedical Optics.*

Camera-on-tip Angioscope for *in vivo* Cardiovascular Diagnostics and Surgical Guidance

Simon T. Sørensen[a], Walter Messina[a], Lorenzo Niemitz[a], Claire O'Dowling[a,b], Piotr Buszman[d], Stefan Andersson-Engels[a,c,*], Ray Burke[a]

[a]Biophotonics@Tyndall, IPIC, Tyndall National Institute, Lee Maltings, Dyke Parade, Cork, Ireland
[b]Centre for Research in Vascular Biology, APC Microbiome Ireland, University College Cork, Cork University Hospital, Cork, Ireland
[c]University College Cork, School of Physics, Cork, Ireland
[d]Center for Cardiovascular Research and Development, American Heart of Poland, Poland

Abstract. Cardiovascular imaging with camera-on-tip catheters has the potential to provide physiologically relevant data on the tissue state and device placement that can improve the clinical outcomes. In this work, we review the unmet clinical need for image based *in vivo* cardiovascular diagnostics and guidance for minimally invasive procedures. We present a 7 Fr camera-on-tip catheter with fibre-coupled multi-spectral illumination including methods for imaging in a blood-filled field-of-view (FOV). We demonstrate that the imaging catheter can be navigated from the femoral artery to cardiac regions such as the left atrium and left ventricle in a porcine model, where *in vivo* images of the cardiac walls are recorded. We further show that physiologically relevant parameters such a heart rate and respiration can be extracted from the images and that the changes to tissue state can be inferred from the imaging data. Finally, a methodology is outline for merging the imaging data with Diffuse Reflectance Spectroscopy (DRS) recorded through optical fibre.

Keywords: camera-on-tip, cardiovascular imaging, diffuse imaging, biophotonics, catheterisation, diffuse reflectance spectroscopy.

*Stefan Andersson-Engels, stefan.andersson-engels@tyndall.ie

1 Introduction

Recent advances in highly sensitive detectors and novel light sources across the visible and near-infrared spectrum have opened up new possibilities in particular in biomedical sensing. Furthermore, camera CMOS technology with a reduced footprint derived from the enormously high-volume smartphone market have been repurposed, and such micro image sensors with sub-mm dimensions are now commercially available for endoscopy applications.[1] From a spectroscopy point of view, Diffuse Reflectance Spectroscopy (DRS) has seen extensive use in tissue differentiation research, distinguishing healthy tissue for tumor tissue, for example.[2–5] This allows for simple integration requiring two spatially separated optical fibres and is a modality that is integrated into a catheter system in this work. It also lends itself to combination with other systems

such as a camera imager, since illumination fibres can be switched to be used as DRS excitation and collection fibres using an optical switch.

Imaging the cardiovascular space has become part of the standard of care for cardiovascular illnesses. The scale of this imaging can range from very large magnetic resonance imaging (MRI) and computed tomography (CT) devices[6,7] to millimetre sized intravascular imaging in intravascular-ultrasound (IVUS),[8] optical coherence tomography (OCT),[9,10] or scanning fibre endoscope (SFE) systems.[11] Imaging wavelengths and technologies span a similarly broad spectrum from X-ray[12] through the visible to the infrared.[13] With ultrasound systems playing an important role, both external, transesophageal, and intravascular.[14] Each of these optical and acoustic modalities provides different penetration depth, spatial and spectral resolution. Camera systems and CMOS technology promise to play a greater role as the technology develops further and is adopted more in biomedical research[15–17] and clinical applications.[13] Angioscopy based on fibre optics has already been demonstrated as a potentially powerful adjunctive tool in cardiovascular medicine with applications such as bypass and thromboembolectomy procedures, endovascular neurosurgery procedures, and general peripheral vascular operations.[18,19] Autofluorescence has been demonstrated as an indicator of RF lesions in cardiac tissue captured through imaging fibre.[20] The goal in each case is to provide real-time intravascular image data to a clinician, while minimising the use of harmful fluoroscopy, and providing information in-situ that would otherwise be impossible to obtain. As imaging technologies develop further, they promise to provide unprecedented information that can drive life-saving decisions.

Recent work has investigated transthoracic systems based on micro CMOS imagers. Karimov *et al.* performed a transapical and percutaneous cardiac procedure to visualise intracardiac structures in bovine models with two different cardioscopic systems.[21] Fagogensis *et al.* applied

autonomous intracardiac navigation using haptic vision to navigate an imaging catheter to the cardiac walls in animal models.[22] Alotaibi *et al.* used a commercial bronchoscope with a diameter of 5-6 mm to visualise the intracardiac anatomy in an *ex-vivo* porcine heart.[23] Opfermann *et al.* demonstrated a novel videoscope to percutaneously access the pericardial space under direct visualisation in porcine models.[24]

Despite the rapid technological advancements of CMOS technology, challenges remain, especially regarding the integration, to fully meet the clinical needs required for *in vivo* diagnostics and surgical guidance deep within the human body. In this paper, we present a multimodal catheter integrated micro image sensor for *in vivo* cardiac applications. As an example of the clinical potential, we demonstrate *in vivo* imaging of the cardiac walls of a beating heart of a porcine model over a duration of several minutes with the imaging catheter inserted through the femoral artery. We further show that physiological parameters such as heart and respiration rate can be extracted directly from these images. By occluding the left anterior descending artery, we show that changes to the tissue state can be inferred from the imaging data. Finally, we demonstrate that combining endoscopic imaging with DRS is a promising technique that can provide additional physiologically relevant information about tissue composition and state. It is well known that tissue with different levels of oxygenation, i.e., a different ratio of oxygenated and deoxygenated hemoglobin present, will have a different spectral response.[25,26] In cardiac tissue, monitoring tissue ischemia, that is areas of reduced or restricted blood flow, is of clinical significance. For example, direct imaging of tissue vascularisation can potentially provide clinical validation of circumferential ablation of the left atrial appendage for the treatment of persistent atrial fibrillation.

2 Methods

2.1 Micro camera catheter

The sensor used in this work is the AMS NanEYE2D RGB fitted with a grated index (GRIN) lens with a field of view (FOV) of 120 degrees in air, and F number of 2.8. Due to operation in a liquid field, the effective FOV *in vivo* is reduced to approximately 90 degrees. The GRIN lens system provides a simple and effective general lens system for the micro image sensor, with effective focus from 3.0 mm to infinity and an optimal focus at 8.0 mm. However, a custom lens solution is expected to be able to further improve image quality, especially when the design is application specific.

The image sensor is integrated into a 3D printed alignment holder along with two 200 um optical fibres and a saline flush channel. The flush channel consists of 1.20 mm OD braided polyimide tubing (Nordson medical, USA). The system is manually operated using a syringe which also acts as the saline reservoir. The system sits within a 2.30 mm OD catheter tubing, the dimensional requirement of which was informed by the target cardiovascular application. And image of the probe and drawing of the distal module can be seen in Figure 1. The detailed mechanical design, assembly, and integration of the system is being disseminated separately. Illumination can be coupled to the two illumination fibres at the proximal end and is delivered using custom-built light sources. Delivering the illumination via fibre rather than from emitters mounted at the distal end near the camera, gives the advantage of flexibility in illumination to beyond traditional RGB imaging.

Due to the lack of low-cost commercial multispectral sources with high customisability, sources are built in house. The endoscope backend system is designed to be portable and compact to accommodate the working environment of the operating theatre. Laser illumination allows for

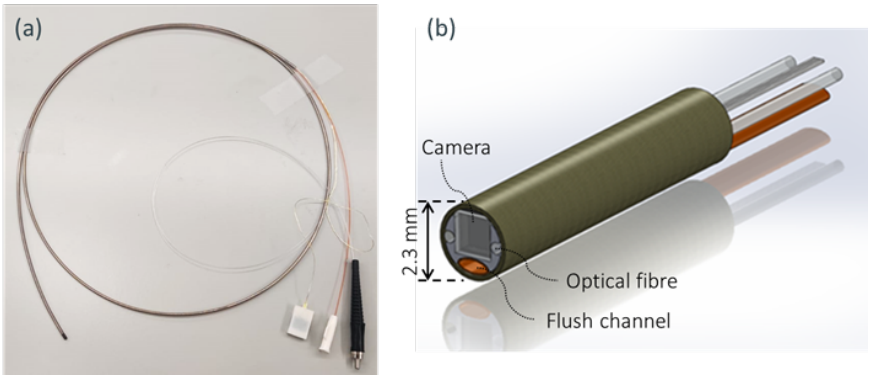

Fig 1 (a) Image of the catheter-integrated imaging sensor. The proximal end has three connectors for the camera communication, fibre connector and saline flush channel, respectively. (b) CAD drawing showing camera-on-tip sensor at the distal end of the catheter. The catheter outer diameter is 2.3 mm which includes the 1 mm^2 imaging sensor, two Ø200 µm illumination fibres and flush channel. The rigid tip length is 5 mm.

narrow bandwidth illumination targeted to probe specific spectral regions of interest as well as allowing for recombination of the illumination wavelengths, or for sequential or synthetic white-light illumination, to reconstruct colour image.[27] Laser also provides a high coupling efficiency for fibre coupling. The source used primarily in this work is a laser source combining 6 wavelengths from the VIS to NIR. The coherent nature has shown some limitations which will be discussed later.

2.2 Multimodal and multispectral biomedical imaging

Broadly speaking, the micro camera captures diffusely reflected light from a wide field-of-view and spectral information can be gained either using multispectral illumination or Bayer spectral filters on the sensor. In contrast, DRS is a contact measurement and reflection data is collected from a sampling volume that typically penetrates a few mm into the tissue depending on wavelength and tissue type and inter fibre distance. In other words, where the camera sensor records many spatial sampling points with a relatively coarse spectral resolution, the DRS system collects data from a 3-dimensional sampling volume with excellent spectral resolution. This is illustrated in Figure 2.

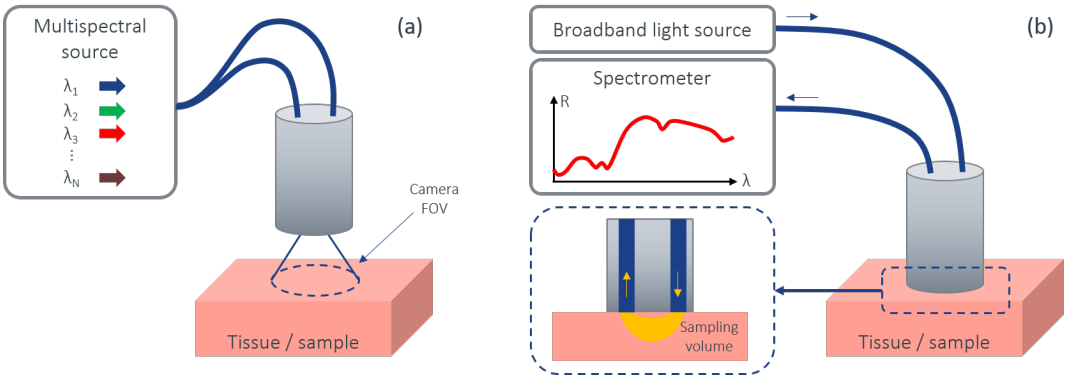

Fig 2 Schematic of sensing modalities of the system, with (a) wide-field non-contact diffuse imaging using multi-spectral or broadband illumination giving good spatial resolution and (b) DRS providing excellent spectral resolution. Diffuse imaging can either capture a colour image in a single frame using white-light illumination with an RGB image sensor, or stacking of sequentially acquired frames under monochromatic illumination for a multi-spectral approach. In contrast, DRS uses a spectrometer to measure broadband light that has diffusely propagated between the two fibres, thus probing a sampling volume with higher spectral resolution.

The two sensing modalities are complementary and a dual modality system has the potential to provide simultaneous high-resolution spectral and spatial information. The camera assists in the navigation and determining the region of interest, and the DRS can provide diagnostic information in this region. The camera probe presented in this work is designed for dual operation with the camera and DRS in mind, as previously discussed.

At the core of the DRS system developed used in this work is a high-performance spectrometer (Wasatch Photonics, WP-VISNIR-R2-IC, 400-1080 nm, 1 nm resolution) with a temperature-controlled detector array for low-noise and stability. The illumination source is a fibre-coupled halogen (Thorlabs, SLS201L/M, 360 - 2600 nm) with -132 mireds colour temperature balancing filter (Thorlabs, FGT165M). The filter flattens the emission spectrum to ensure a significant SNR improvement across the measurement range. A fibre-only probe was designed to evaluate the DRS system separately to the camera. However, it is important to notice that the same functionality can be achieved using the fibres in the camera probe which can be put in contact with the tissue

when required. The probe consists of a 400 μm 0.39 NA source fibre (Thorlabs, FT400EMT) and a 365 μm, 0.22 NA detector fibre (Thorlabs, FG356LEC). The cleaved fibres were positioned with a separation of 2.0 mm using a 3D printed housing. The system allows a contact measurement to be made on tissue with data acquired in 80 ms. Calibration is performed using a spectralon target (SphereOptics, SG 3052). The next research step is the integration of both modalities, imaging and DRS, into a multimodal system using an optical switch. This system will be able to use the image data for guidance and navigation, with spatially resolved spectral data highlighting regions of interest. The system can be navigated to these regions and a DRS contact measurement can be conducted for verification.

2.3 Pseudo-colour for intuitive data presentation

In this section, we describe a novel approach to convert a full DRS spectrum to a single colour, which offers an intuitive way to interpret the complex DRS spectra to clinicians in an intuitive format that aligns with what is seen by the human eye and a camera sensor. There is no unambiguous way to convert a spectrum to RGB space. However, the CIE 1931 colour matching functions x, y, z match the chromatic response of the cone cell in the human eye and offer one possible way to calculate the tri-stimulus values X, Y, Z of a spectrum S(λ) similar to response of human eye.[28] These values can further be converted to RGB using standard functions in e.g. MATLAB for a given white point, such as D65 cold white illumination. Using these values the spectral data obtained by the DRS system is colour mapped to different shades of red, indicating higher or lower amounts of oxygenation in the tissue. In this way, we convert a full spectrum to a single pseudo-colour, which can be tracked over time. Whitenening of the colour corresponds to a change in oxygenation in the spectrum.

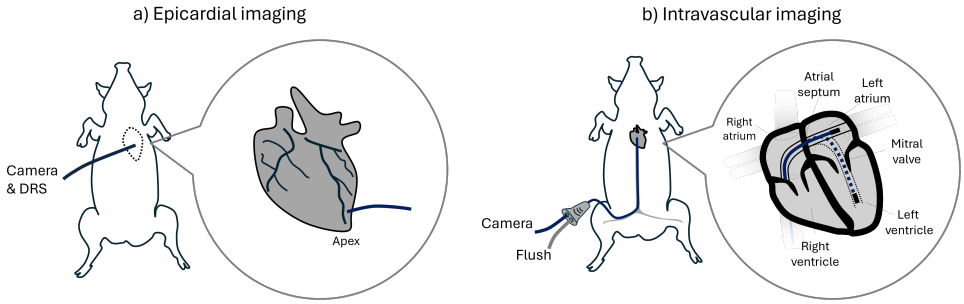

Fig 3 Schematic of study protocol. a) A left thoracotomy procedure was performed to image and perform DRS measurements of the epicardium. The probe was held near the apex. b) Using standard femoral artery catherisation, the image catheter was navigated to the right atrium and further through the septum to the left atrium and ventricle. The camera-on-chip system was operated inside the guiding catheter with saline flush applied to clear the blood-filled FOV in front of the camera. A separate balloon catheter was inserted into the LAD to control vessel occlusion in both animal models.

2.4 Study protocol

The porcine model was selected because of the anatomical and physiological similarities with the human heart and vascular system. Two adult animals were used in the study, which was conducted under approval of the protocol and ethics review board (Center for Cardiovascular Research and Development, American Heart of Poland Inc, TYN 2407-20). The animals were sedated with intramuscular ketamine (10 mg/kg) and xylazine (0.05 – 0.2 mg/kg) and anesthetised with inhaled isoflurane (1–3%). Heparin (150-200 IU/kg) was administered for systemic anticoagulation. The animals were placed in dorsal recumbency and electrocardiography was established.

After induction of anaesthesia, vascular access was obtained through the femoral artery. Guidewires and catheters were navigated using standard techniques and angiography, and the imaging catheter was introduced through a large bore 9 Fr venous sheath. A balloon catheter was introduced into the left anterior descending artery (LAD), where inflation and deflation were used to control vessel occlusion and reperfusion to achieve hypoxia.

A illustration of the study protocol is shown in Figure 3. A left thoracotomy procedure was

performed in the first animal to give access to the epicardium. Imaging the epicardium eliminates the challenge of a blood filled FOV and images were recorded of the area of the apex while inducing hypoxia. DRS data was recorded from the same area with a separate probe in contact with the tissue.

In the second animal, the 9 Fr venous sheath was inserted into the right atrium and images were acquired of the interatrial spectrum before performing a transseptal cross. The imaging catheter was navigated to the left atrium before passing through the mitral valve to the left ventricle. Images of the pericardium were recorded at relevant stages in the procedure. In particular, images were acquired continuously of a fixed FOV to observe the tissue colour change while inducing myocardial ischemia. Flushing was provided both through the larger guiding catheter using an automatic pump. As will be discussed in the following, holding the guiding catheter against pericardium provides an efficient way to clear the FOV from blood and provide tissue image data over a duration of minutes. The study was carried out in December 2020 during the COVID-19 pandemic. As a consequence, the procedure was performed by the surgical team in Poland with a video link to Ireland showing the operating theatre and fluoroscopy imaging. The imaging and DRS systems were designed for remote control and troubleshooting.

3 Results

3.1 Surgical guidance and cardiovascular imaging

The camera-on-tip system was successfully tested with extensive imaging of the epicardium and with real-time intracadiac of the cardiac walls. Insertion of the imaging catheter through the femoral artery and navigation to atria was performed with ease, and images and video were recorded throughout the procedure.

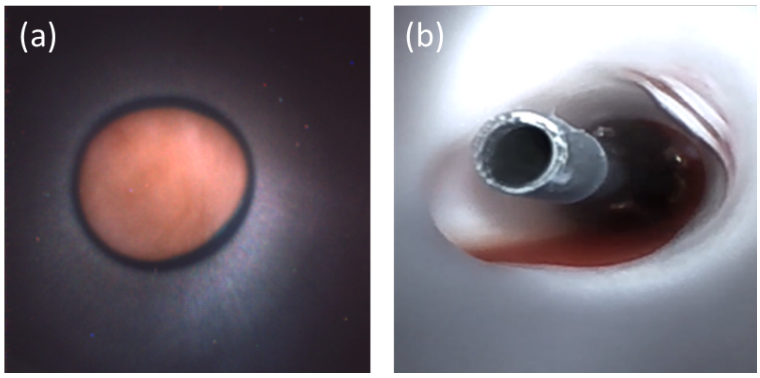

Fig 4 Two methods for clearing the field of view of the camera. (a) uses a catheter held against the heart wall with saline flush to clear the blood field. (b) uses a balloon catheter to clear the blood field. Note that the balloon catheter image only was captured in a porcine model in a different study.

The camera system cannot image through the blood field in a meaningful way. In order to clear the field of view two methods are demonstrated. In Figure 4 (a) a guiding catheter is placed in contact with the heart wall, and a saline flush clears the field of view, effectively isolating a region of tissue for imaging. The camera system can then be positioned spatially along the longitudinal direction of the guiding catheter to obtain live video of the isolated region with appropriate focus. In Figure 4 (b), a balloon catheter is inflated to isolate the region of interest from the blood field similarly through obstruction. The camera is then able to image the tip of the balloon catheter and other areas of interest. The camera system also has an integrated flush channel that allows for clearing the FOV immediately in front of the camera and removal of debris obstructing its FOV. In this study, the flushing was predominantly provided through the guiding catheter. With the guiding catheter positioned against the cardiac wall, this method gave a clear field-of-view over a duration of several minutes.

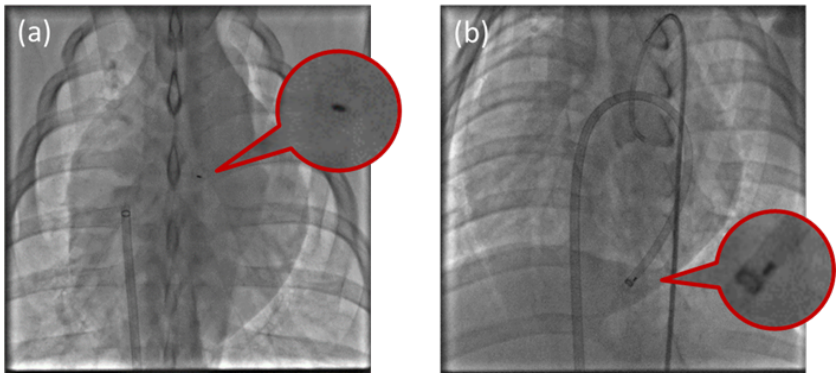

Fig 5 Fluoroscopy images of catether-integrated imaging probe. The catheter is inserted through the right femoral artery and arrives in the right atrium through the inferior vena cava. (a) Transseptal puncture has been performed and the system is now located in the left atrium. b) the microcamera catheter has been bent, passed through the mitral valve and now located in the left ventricle and approximately at the apex.

196 The fluoroscopy images in Fig. 5 (a) and (b) show fluoroscopic images mid procedure. The
197 guiding catheter is clearly visible. In Fig. 5 (a) the transeptal puncture has been performed. The
198 system with marker band can be seen crossing from the right side of the heart to the left side.
199 In Fig. 5 (b) the catheter has been bent further and has been navigated past the mitral valve and
200 navigated to the apex of the heart.

201 In Fig. 6 (a) and (b) images of the septum were acquired under reconstructed white-light laser
202 illumination. Note that the camera can be maneuvered closer to the tissue filling a greater field of
203 view if desired. This can be seen in Fig. 6 (c) and (d). In these images the left ventricle is imaged.
204 The system allows for flexibility in imaging modalities and Fig. 6 (d) shows the imaging under
205 NIR illumination. The NIR light has a greater penetration depth in tissue and allows for imaging at
206 some depth. Figure 6 (c) and (d) are imaging the same tissue region and the large diagonal feature
207 is visible in both images. Video data of the procedure is included in the supplementary online
208 material. In the video data there is an occasional blood flow incursion into the guiding catheter.
209 This can be quickly cleared with saline flush through the guiding catheter.

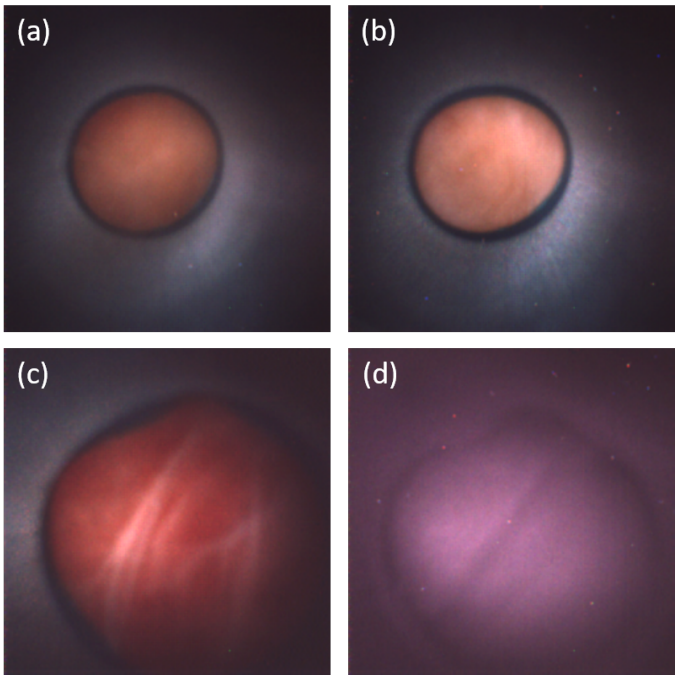

Fig 6 Examples of images acquired *in vivo* in the second porcine model in different chambers of the heart. The camera-on-tip catheter was first inserted into the right atrium where images were captured of the septum in (a)-(b). After performing a transseptal puncture, images were recorded of the left ventricle under (c) visible and (d) near-infrared illumination. A video recording is available online (Video 1, MP4, 8.38 MB) showing continuous imaging of the cardiac walls of the beating heart over 2 minutes with white-light laser illumination. The image in (c) is a still from the video.

3.2 Imaging plethysmography

The field of view can be changing rapidly with motion. By using the guiding catheter to exclude the blood field the camera image is stabilised and a region of interest (ROI) can be collected in the centre of the image that is not obscured by the catheter. To this end, we have developed an algorithm to capture only this central region, which works as follows: Firstly, we select the red channel as it has a good contrast between the tissue and catheter. This layer is then binarised using a standard adaptive algorithm with a sensitivity of 0.6. To enhance the contrast of the circular ROI of the catheter, the binary image is convoluted (closed) with a Gaussian blur using a disk with 3-pixel diameter. The resulting binary image clearly shows the circular diameter of the catheter,

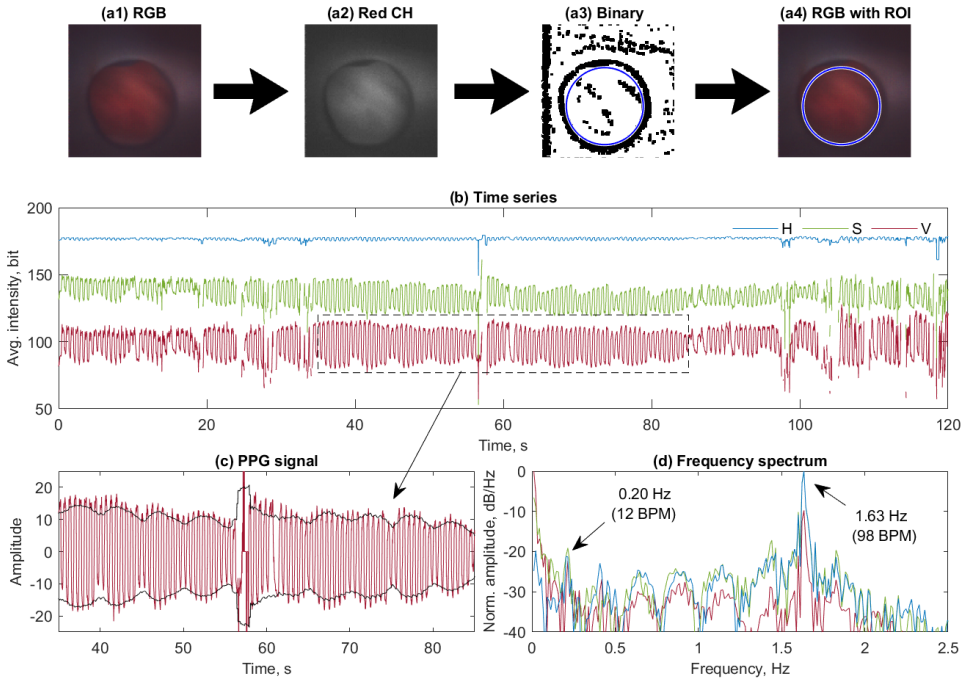

Fig 7 Data analysis of video captured inside of the left ventricle. Images (a1)-(a4) show the circle fitting algorithm which detects the relevant tissue pixels, using the outer guiding catheter as a reference. The red channel (a2) is used and the image is binarised. The largest circle is detected in the binary image (a3), and this results in the circular ROI (a4). This process is repeated for each frame. Frames where no circle is detected are discarded. Using this data a time series of each of the HSV channels is plotted (b) showing the variations in average intensity of the region in each frame. A section of the time series is selected for analysis (c) with the average subtracted and and envelope function added to show the respiration rate. The normalised Fourier transform of each channel over this time segment revels features in frequency space (d). This shows a sharp peak at the heart-rate of the animal at 98 bpm and another peak at 12 bmp, the respiratory rate of the animal.

which is fitted with a standard circle-fitting algorithm. In some cases, multiple circles are found but the fit with the best fitting parameter is chosen. When the tissue is not visible due to incursion of blood, the walls of the catheter are also not visible. Frames with poor cirlce fit are in this way disregarded. When imaging outside of the guiding catheter a central region of interest without fitting can be used.

In Figure 7 (a1)-(a4) an extracted frame is shown, from which the red channel is extracted. The previously described binarisation and ROI extraction algorithm extracts the circular region of

interest. The average H, S and V values are extracted from a 2-minute video sequence of the left ventricle. The ROI used for the calculations is chosen as a circle with 90% of the radius found in the fit to remove any boundary effects such as blood leaking into the catheter. The calculated values are shown as a time series in Figure 7 (b). This Photoplethysmogram (PPG) data is shown in Figure 7 (c). From such a time series standard physiological data, such as heart rate and respiration, can be clearly observed. The respiration is more clearly seen in the normalised data. Figure 7 (d) shows a fourier transform of the signal with peaks at both the respiratory rate of the porcine model at 12 beats per minute (BPM) and a heart rate of 98 BPM. It is highly encouraging that the values can be clearly observed over a 2 min window. It is also the first demonstration of *in vivo* and intra-vascular PPG data collection using a camera. With further development, this technique can potentially be expanded from a single averaged PPG signal to imaging PPG with spatial perfusion information.

3.3 Tissue oxygenation

To differentiate ischemic tissue from healthy tissue using the micro image sensor, we examine the distribution of pixel intensities in each of the colour channels of the imager following arterial occlusion. In order to approximate the human visual response, images are converted to the HSV colour space. Figure 8(a) shows the aggregated pseudocolour histograms of the same imaging data used in Fig. 7, averaged over 20 frames per histogram. Ischemia is induced at around 30 s in the time series. Figure 8(b) shows histograms at selected times during the occlusion cycle. It is observed that there is a shift in the distribution over the duration of the induced ischemia, most apparent in the Saturation value. This can be interpreted as a change in absorption between oxy and deoxy hemoglobin, which is in agreement with the DRS measurements analysed in the subsequent

section. The images in Fig. 8(c) show the time-averaged images used in the calculation of (b). The subtle colour changes are more clearly observed in the histograms than the images, which will be explored further in future work.

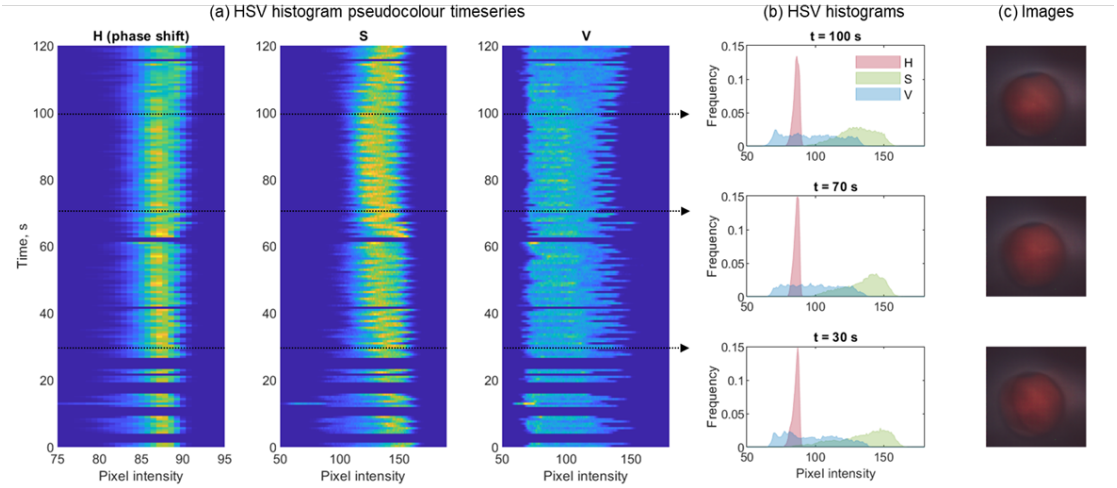

Fig 8 (a) Histogram pseudocolour timeseries of the HSV layers (Hue, Saturation, Value) from the same video used in Fig. 7. The data is averaged over 20 s to remove motion artefacts and the data is disregarded where no circle could be fitted as described in Fig. 7. (b) Histograms shown at selected times to more clearly highlight the changes in the S and V channels. (c) The corresponding images averaged over the same 20 s duration as the histograms in (a)-(b).

3.4 Merging DRS with imaging

DRS reflectance data of the epicardium was recorded continuously through several cycles of ischemia and reperfusion. Representative spectra of healthy tissue and during the occlusion are shown in Fig. 9(a). The characteristic double absorption peaks from oxyhemoglobin at 540 and 575 nm are clearly visible in the healthy DRS spectrum as a decrease in reflectance. These features disappear during the occlusion, where the spectrum is dominated by the deoxyhemoglobin absorption peak around 555 nm. The spectra further show an increased reflectance in NIR from deoxyhemoglobin (decrease in absorption). This is in agreement with what is reported in the literature.[29]

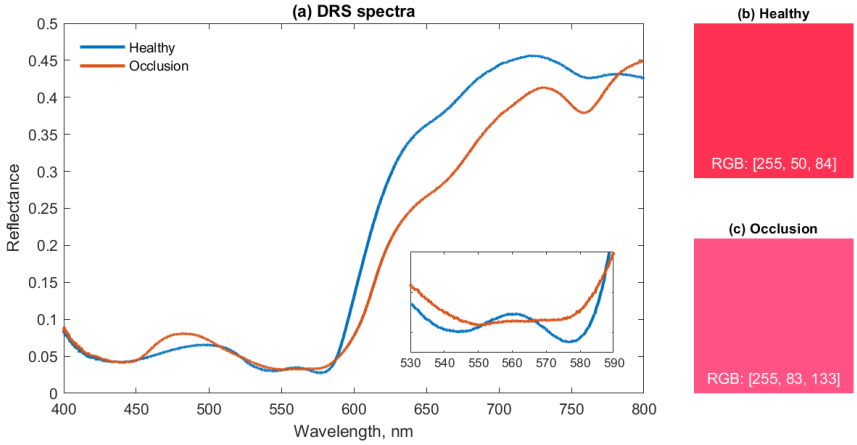

Fig 9 (a) DRS spectra of the epicardium of the first animal model. The two spectra are for healthy oxygenated tissue and with occlusion of the LAD, respectively. The spectra are averaged over 3 seconds to remove artefacts from the heart beat. (b)-(c) The DRS spectra for healthy and occluded tissue are each converted to a single RGB colour with CIE 1931 colour matching functions to match the response of the human eye, which suggests a whitening of the tissue during the occlusion.

Figure 9(b)-(c) show the spectrum-to-colour conversion described previously, where the full spectrum is converted to an RGB colour using the CIE 1931 colour matching functions that match the response of the human eye. As can be seen in the figure, the RGB colours calculated from the spectra change to a paler shade of red during the occlusion as expected from the decreased reflectance. It should be noted that the exact colour scale depends on the CIE XYZ to RGB conversion, which has not been calibrated here. This spectrum-to-colour conversion offers a potential novel and intuitive way to interpret the DRS measurements that can be merged with the camera data. Additionally, it is important to note that any colour map that portrays clinical significant difference to a clinician could be used here, and the goal is to visualize only the change. Hence, for example, with sufficient calibration ischemic tissue could be labelled “red” and healthy tissue “green”, with the intermediate values appearing in “amber”, in a traffic light approach. In the all-red colour map chosen above, the calculated colour change is strongly exaggerated but nonetheless gives clear feedback to the clinician that a change has occurred. Reflectance measurements sample

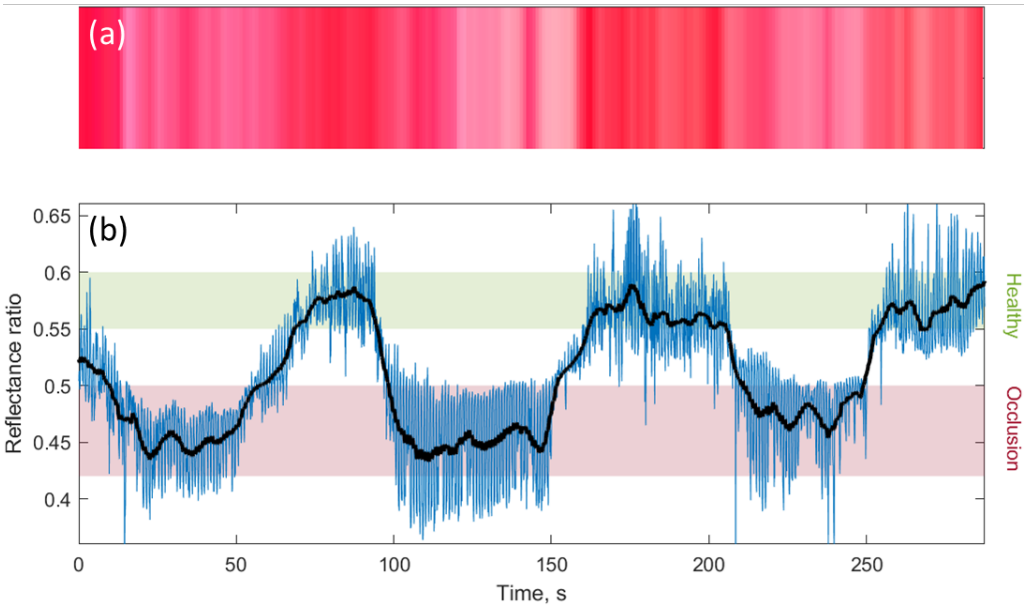

Fig 10 Time series of DRS reflectance ratios and corresponding spectrally converted RGB values. The reflectance ratio is calculated as the deoxyhemoglobin absorption peak at 555 nm divided by the sum the oxyhemoglobin absorption peaks at 540 and 575 nm, respectively. The ratio-metric regions coarsely corresponding to healthy and occlusion are indicated in (b) and the black line is a moving average low-pass filter to remove the heartbeat. The RGB values are calculated from 1-second averaged spectra to remove artefacts from the heartbeat.

a volume of tissue that, depending on the wavelength and tissue composition, can penetrate up to a few mm into the tissue. The spectral colour can therefore not be expected to be what a human eye or camera system would see.

In Fig. 10 we show a time series of the spectrum-to-colour conversion together with a reflectance ratio, calculated as $R(555nm)/(R(540nm) + R(575nm))$, where R is the average reflectance in a 5 nm band. These spectral bands are the deoxyhemoglobin absorption peak at 555 nm and the sum the oxyhemoglobin absorption peaks at 540 and 575 nm, respectively. We observe a clear change in the average DRS reflectance ratio over the course of the measurement which spans multiple occlusion cycles, where healthy tissue shows a higher reflectance ratio than when the tissue is occluded. We also observe that the tissue recovers relatively quickly once the oc-

clusion is lifted, within 10-20 seconds. There appears to be no long lasting effects due to the multiple occlusions with the levels returning to within the same range each time. These results show the sensitivity and fast response of DRS and its applicability in the *in vivo* cardiovascular space. Similar results to those captured on the epicardium are expected for DRS measurements of the endocardium.

4 Discussion

The micro imager's small footprint allows integration into miniature endoscopes as presented in this work, as well as enabling other small footprint tools to be sensorised with a camera. The main output of the micro sensor is an image, either monochrome or in colour, which is used in navigation and guidance at location *in vivo*. In cardiovascular imaging, the micro camera's footprint allows it to be integrated into 3-8 Fr (1-2.5 mm diameter) catheter devices, which can be navigated to small blood vessels through a slightly larger guiding catheter. The small footprint of the image sensor and successful integration into a 2.50 mm catheter system can be seen in Figure 2. The sensor is usually integrating in a forward facing modality but could be arranged to be side-facing. The returned image then provides a clinician with vision of an area of interest.

Applications of such a guidance image can be divided into two categories, image enhanced guidance and diagnostics. We define image enhanced guidance as navigation to a feature using an *in situ* image, and diagnostics as the ability to visualise a feature of interest *in vivo*, for example a lesion or device, and the ability to gather additional data using a DRS sensor, for example. Imaging involves recording an image of an area, which is usually difficult or impossible to visualise. The camera system allows for live vision on location. This includes the verification of correct device placement in cardiovascular procedures. More in the diagnostic direction the image inside of the

vessel can aid diagnostic tools by locating of areas of interest for further analysis such as with a contact measurement DRS probe as is presented in this work. Or the image itself can be used to obtain diagnostic information by looking at the colour change in the pixels, extracting information about colour changes which may be due to tissue oxygenation, and either correlating them to a clinically significant marker or extracting information such as heart and breathing rate from such colour changes.

Various procedures in interventional cardiology involve placing devices, such as pacemaker leads, stents, and valves, under fluoroscopic guidance. During minimally invasive valve repair interventions, such as Transcatheter Aortic Valve Implantation (TAVI), a new valve is delivered through the blood vessels to location in the heart for example to treat aortic stenosis.[30–32] While stent placement has been verified using OCT and IVUS technology, often the surgeon lacks vision inside the vasculature and relies on repeated fluoroscopic imaging. A front mounted camera can give directional information about where the catheter is pointing to. During a transeptal cross procedure locating the correct puncture spot is critical; when navigating to a particular region in the heart the angle of this puncture spot may want to be adjusted. Image guidance and sensing *in situ* has the potential to reduce the reliance on fluoroscopy during this procedure. During a Pulmonary Vein Isolation procedure (PVI) tissue is ablated in order to treat arrhythmia. Electrodes may not capture incomplete or partial ablation. In these cases a camera and DRS system in combination can be used to validate transmural ablation and have the potential to reduce radiation exposure for doctors and patients and to speed up the procedure. The technology may also see use in recording procedures and verifying the efficacy and success of an intervention. A possible application of intra-catheter sensing technology may be in imaging the infected heart: Endocarditis is a clinical problem that progresses rapidly and modern imaging techniques have been limited in their ability

to diagnose, especially early.[33] It can occur as a complication after device placement, and affects 0.5%-3% of patients within one year of the TAVI procedure alone,[31] for example. The ability to guide navigation and deploy sensing tools inside of the heart may prove useful in verifying infection, and locating it, when non-invasive technologies fail to be conclusive.

Recent work has investigated the many advantages of micro CMOS imagers for cardiac applications,[21–24] but these studies have generally focused on visualisation only with no quantitative information derived from the imaging sensor. Here we have demonstrated that physiological parameters can be calculated from the imaging sensor, which we expect will provide additional value to clinicians. For example, it has been demonstrated that imaging PPG can provide information on the perfusion status of tissues during surgery.[34] In this work, we used the full FOV to calculate a PPG signal, but this can potentially be extended to generate PPG perfusion maps from a micro CMOS sensor with improved image analytics. Similarly, we are expecting that multi-spectral imaging will add additional quantitative insights such as spatial mapping of the tissue oxygenation state and can further significantly enhance the image contrast to highlight, e.g., vasculature. This can potentially be used to evaluate the success of cardiac ablation procedures.

Operation of a camera in a vessel comes with the additional challenge of clearing the blood field. Two methods are generally adopted for clearing the FOV. The first involves inflation of a balloon catheter within the blood vessel clearing the FOV and allowing imaging of the walls of the vessel. This is not always an optimal solution, for example in the heart where the obstruction of an area with a balloon is not necessarily possible or could be detrimental to the patient. The second method involves the guiding catheter being used to shield the sensor from continuous blood flow. A saline flush can then be used to clear the FOV making imaging possible. We distinguish between two methods of flushing, the macro-flush where the guiding catheter is used as the flush channel,

and the micro-flush where the flush channel is integrated into the chip on tip imaging probe.

Specular reflections are direct reflections that occur on glossy uneven surfaces of biological tissue and can cause problematic image artefacts that detract from the image quality on an already resolution limited sensor by creating bright spots where the underlying features are obscured. Movement of the sensor during a procedure can help identify these reflections since they will move, however removal, reduction and prevention is preferred. We have previously demonstrated two methods of specular reflection removal using micro image sensors, using an algorithmic approach and a static cross-polarisation approach.[35] In a cardiovascular application due to frequent movement within the body a static polarization approach would be preferred and may be implemented in a future design. All aspects, from illumination wavelength and delivery, to mechanical integration, and lensing at the tip of the device, will be considered and improved further in future work.

For general imaging, the coherent nature and resulting speckle pattern have been found to interfere with image quality in this application space, even though the speckle seems to be reduced due to Brownian motion in the liquid field. As a result an LED-based source is currently preferred for illumination, however future work is looking at using a de-speckling system in the laser-based illumination pipeline.[36]

The output image lends itself to various image-processing techniques, many of which can be implemented in real or near real-time. The camera operates at around 40 frames per second (FPS), and the low resolution allows for rapid processing. The addition of a field-programmable gate array (FPGA) scan help to further optimize image processing algorithms in a clinical systems.[37]

5 Conclusion

In conclusion, we present a 7 Fr (Ø2.3 mm) camera-on-tip catheter system for cardiovascular guidance and diagnostics applications. The system uses fibre-coupled multi-spectral illumination methods to image in a blood-filled field of view. We demonstrate that the imaging catheter can be navigated to challenging cardiac regions through the femoral artery in a porcine model. Specifically, we present images recorded *in vivo* of the inter-atrial septum, and cardiac walls in the left atrium and left ventricle. To the best of our knowledge, this is the first time a camera-on-tip catheter has been navigated through the femoral artery to the left atrium and ventricle with images recorded *in situ*. We further show that physiologically relevant parameters such as heart rate and respiration can be extracted from the video data. A method is outlined for measuring the tissue oxygenation state from the image data and merging with DRS data. The results presented in this work show the potential for cardiovascular imaging with camera-on-tip catheters to provide physiologically relevant data and device placement that can improve the clinical outcomes.

Disclosures

The authors declare no conflicts of interest.

Code, Data, and Materials Availability

The data and analysis code that support the findings of this study are openly available at the public repository Zenodo.org. DOI: 10.5281/zenodo.10818883

Acknowledgments

We would like to thank all the collaborators at the Center for Cardiovascular Research and Development, American Heart of Poland Inc for their contributions this study. This work was supported

393 by the European Union's Horizon 2020 Programme, Grant No. 831117, and Science Foundation
394 Ireland (SFI), Grants No. SFI/15/RP/2828 and SFI/22/RP-2TF/10293.

395 *References*

396 1 OmniVision, "Omv6948, 200x200 product brief: Miniature camera module provides high-
397 quality imaging for disposable medical guidewires, catheters and endsoscopes," (2020).

398 2 M. S. Nogueira, S. Maryam, M. Amissah, *et al.*, "Evaluation of wavelength ranges and tissue
399 depth probed by diffuse reflectance spectroscopy for colorectal cancer detection," *Scientific*
400 *reports* **11**(1), 798 (2021).

401 3 L. L. De Boer, T. M. Bydlon, F. Van Duijnhoven, *et al.*, "Towards the use of diffuse reflectance
402 spectroscopy for real-time in vivo detection of breast cancer during surgery," *Journal of trans-*
403 *lational medicine* **16**, 1–14 (2018).

404 4 I. Gkouzionis, S. Nazarian, A. Anandakumar, *et al.*, "Using diffuse reflectance spectroscopy
405 probe tracking to identify non-tumour and tumour tissue in upper gastrointestinal specimens,"
406 in *European Conference on Biomedical Optics*, ETu1A–1, Optica Publishing Group (2021).

407 5 D. Lin, S. Qiu, W. Huang, *et al.*, "Autofluorescence and white light imaging-guided endo-
408 scopic raman and diffuse reflectance spectroscopy for in vivo nasopharyngeal cancer detec-
409 tion," *Journal of Biophotonics* **11**(4), e201700251 (2018).

410 6 A. Ponsiglione, A. Stanzione, R. Cuocolo, *et al.*, "Cardiac ct and mri radiomics: systematic
411 review of the literature and radiomics quality score assessment," *European Radiology* , 1–10
412 (2022).

413 7 A. Busse, R. Rajagopal, S. Yücel, *et al.*, "Cardiac mri—update 2020.," *Der Radiologe* **60**
414 (2020).

8 J. P. Marteslo, M. S. Makary, H. Khabiri, *et al.*, "Intravascular ultrasound for the peripheral vasculature—current applications and new horizons," *Ultrasound in medicine & biology* **46**(2), 216–224 (2020).

9 H. G. Bezerra, M. A. Costa, G. Guagliumi, *et al.*, "Intracoronary optical coherence tomography: a comprehensive review: clinical and research applications," *JACC: Cardiovascular Interventions* **2**(11), 1035–1046 (2009).

10 C. P. Hendon, T. H. Lye, X. Yao, *et al.*, "Optical coherence tomography imaging of cardiac substrates," *Quantitative imaging in medicine and surgery* **9**(5), 882 (2019).

11 L. E. Savastano, Q. Zhou, A. Smith, *et al.*, "Multimodal laser-based angioscopy for structural, chemical and biological imaging of atherosclerosis," *Nature biomedical engineering* **1**(2), 0023 (2017).

12 A. C. Kwan, A. Pourmorteza, D. Stutman, *et al.*, "Next-generation hardware advances in ct: cardiac applications," *Radiology* **298**(1), 3–17 (2021).

13 M. J. Suter, S. K. Nadkarni, G. Weisz, *et al.*, "Intravascular optical imaging technology for investigating the coronary artery," *JACC: Cardiovascular Imaging* **4**(9), 1022–1039 (2011).

14 E. Wali and S. Nathan, "What is the clinical utility of intravascular ultrasound?," *Current cardiology reports* **20**, 1–11 (2018).

15 M. R. Gaab, "Instrumentation: endoscopes and equipment," *World neurosurgery* **79**(2), S14–e11 (2013).

16 G. Matz, B. Messerschmidt, W. Göbel, *et al.*, "Chip-on-the-tip compact flexible endoscopic epifluorescence video-microscope for in-vivo imaging in medicine and biomedical research," *Biomed. Opt. Express* **8**, 3329–3342 (2017).

Paper V

Design and assembly of miniature diagnostic catheter imaging systems based on an angioscope study

Messina, Walter and Niemitz, Lorenzo and Sørensen, Simon and O'Dowling, Claire and Buszman, Piotr and Andersson-Engels, Stefan and Burke, Ray.

– (to be submitted: Mar 2024) *Target journal: IEEE Transactions on Biomedical Engineering.*

Design and assembly of miniature catheter imaging systems based on an angioscopy study.

Walter Messina*, Lorenzo Niemitz, Simon Sorensen, Claire O'Dowling, Piotr Buszman, Stefan Andersson-Engels, Ray Burke

***Abstract*— In this paper, we present the design and fabrication of a novel chip-on-tip catheter, which uses a microcamera and optical fibres to capture in-vivo in a beating porcine heart. We discuss some of the challenges and discuss system requirements associated with developing a miniature prototype for such a study and present design iterations and assembly instruction. Methods of clearing the blood field are discussed, including an integrated flush channel at the distal end. This permits capture of images of the endocardial walls. The device was navigated under fluoroscopic guiding, through a guiding catheter to various locations of the heart, where images were successfully acquired. Images have been captured at the intra-atrial septum, in the left atrium after a trans-septal cross procedure, and in the left ventricle.**

***Index Terms*— microcamera, cardiovascular imaging, biophotonics, catheterisation, prototyping.**

I. Introduction

Since the early days of the 19th century with the invention of endoscopes, clinicians across different medical fields have relied upon images captured directly inside the patient for accurate diagnostics and treatment. During the last decades, there has been a constant drive to reduce the size of imaging devices for medical use and endoscopy techniques are now routinely used for accurate diagnosis and minimally invasive surgeries (MIS) [1–4]. Increasingly smaller and more flexible [5] devices mean a reduced negative impact on the patient upon introduction allowing the clinicians to reach sites and very small cavities that were previously inaccessible.6 Laparoscopes, fiberscopes and micro cameras mounted on flexible catheters have gained widespread use in multiple fields including otolaryngology [7,8], ophthalmology [9], gastroenterology [10,11], bronchoscopy [12], urology [13], angioscopy, cardioscopy [14–16] and arthroscopy [17,18]. Due to their small size, these surgical tools enable MIS, diagnosis, procedure evaluation and monitoring, and can further be combined with a biopsy tool [19]. Additional optical and ultrasound techniques have been integrated onto surgical tools for improved detection efficiency, including spectrophotometry [20] fluorescence imaging [21] optical coherence tomography (OCT) [22,23] and intravascular ultrasound (IVUS) [24]. There are several companies that offer microcamera optical sensors for endoscopic applications for different medical fields. Among these, the most popular ones are AMS OSRAM and OmniVision. Many other companies have packaged them in full systems ready to be used by clinicians. The smallest camera systems available on the market have a range of resolution from 200 x 200 pixels to 720 x 720 pixels and they have a footprint ranging from 0.65 mm x0.65 mm to 1.00 mm x 1.00 mm. Integrated systems including illumination can have an overall diameter around 2-3 mm and they are usually equipped with a simple white LED light, installed directly at the distal end (on systems with larger footprint) or carried at the camera location thanks to optical fibres [8,9], [25–27]. Despite these efforts, so far, no imaging systems designed for sophisticated clinical diagnostic procedures in compact spaces have been presented.

This paragraph of the first footnote will contain the date on which you submitted your paper for review. It will also contain support information, including sponsor and financial support acknowledgment. For example, "This work was supported in part by the U.S. Department of Commerce under Grant BS123456."

W. Messina*, L. Niemitz, S. Sorensen and R. Burke are with the Biophotonics group at Tyndall National Institute, Cork, Ireland (University College Cork).

C. O'Dowling is with the Centre for Research in Vascular Biology, APC Microbiome Ireland (University College Cork) and collaborated with Tyndall National Institute.

P. Buszman is with Centre for Cardiovascular Research and Development of American Heart of Poland, Katowice, Poland.

S. Andersson-Engels is a professor at the School of Physics, University College Cork, and head of the Biophotonics group at the Tyndall National Institute.

Corresponding author Walter Messina (walter.messina@tyndall.ie).

II. Study aim

In this paper, we present and discuss methodologies for designing and fabricating a novel chip-on-tip catheter that uses a microcamera, optical fibres for illumination, and a flush/irrigation system to clear the field of view off blood for in-vivo intracardiac applications.

Cardiac catheterisation is a very common procedure, and micro-i2mage sensors such as the AMS NanEye and

Omnivision sensors may prove a valuable tool for cardiovascular imaging through a guiding catheter, and the execution of a trans-septal cross. The system itself is therefore 2.00 m in length with a diameter of 2.3 mm to allow for navigation to take place. Small-scale integration of such a compact device requires robust prototype design and assembly processes which were developed as part of this work. These processes are adaptable to different small footprint applications beyond cardiovascular imaging as discussed in this paper. Two in-vivo studies were conducted on a porcine animal model with the goal of assessing acute performance characteristics of the intra-vascular camera, and to assess ease and convenience to deliver to the various treatment sites.

III. Imaging System Design

For our system, we used a NanEye microcamera (AMS OSRAM, NE2D RGB V120F2.8 2m). This camera was selected for its small footprint combined with image quality. The body of the imaging sensor is a parallelepiped that has nominal dimensions of 1.10x1.10x1.50 mm. There are four thin shielded electrical wires going from the back of the camera to the proximal end of the catheter system in a flat edge connector for powering and communicating with the interface board (BAPIS AC62KUSB, Germany). Illumination at the distal end of the catheter, at the camera's face, is provided by two 200 µm diameter glass fibres (Thorlabs, FT200EMT) flat polished to ensure maximum light transmission and finish. Fibre illumination allows for flexibility in wavelength delivery, small footprint, and eliminates heating concerns due to distally mounted LEDs. The presence of the two optical fibres creates a platform for other sensing modalities in addition to white-light imaging, such as diffuse reflectance spectroscopy (DRS). It also helps to deliver a better illumination profile, since the NA of the fibre is quite limited, and no lensing was added in these design iterations. Navigation during cardiac catheterisation is performed under fluoroscopic guidance. To detect devices such as catheters, they are often fitted with a marker band which is visible on the x-ray image. The importance of radio-opacity of the system was highlighted by the collaborating clinicians, who found the design of the first-generation devices difficult to see during fluoroscopic imaging. Initially, we used a catheter tubing with a fluoroscopy opaque band at the distal end. However, since the manufacturer (Creganna Medical, Galway, Ireland) had discontinued this product, two 1.50 mm platinum-iridium wires had to be integrated behind the camera in later iterations. The system is guided to location by pushing it through a guiding delivery catheter.

III.A Alignment

The distal alignment piece, shown in Figure 1, serves during system assembly for component alignment in the x and y directions, as well as the z direction (along the length of the catheter). It also controls the distance between the fibres and other components for repeatability, ensures optical isolation of the camera sensor, and helps to provide a seal with the sheathing lumen. It consists of a custom 3D printed header piece that can accommodate the sensing, illumination, and flush channels. The printed parts were designed to be larger than the actual dimensions of the parts to account for shrinkage in the printing process. As per normal technological limitations of the printer and materials, some small details could not be achieved. Several iterations were carried out to finalise the design and the most suitable off the shelf material for the support. Some manual post processing of the parts was required to eliminate some unwanted resin residues and small stubs originated from the supporting structures created by the printer setup.

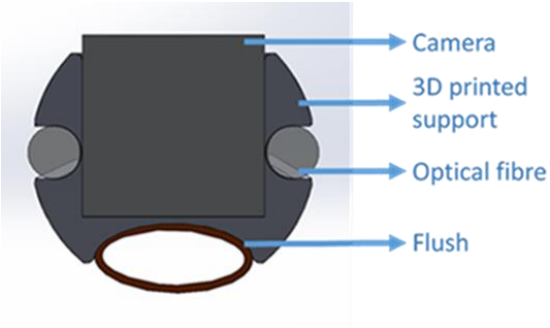

Fig 1. Front view of the final distal alignment holder design which aligns camera, optical fibres, and flush channel using a 3D printed holder which can be press fit and glued into the outer sheathing lumen.

A small selection of the design iterations is shown in Figure 2. The early experimental layouts served to test the limitation of the 3D printing technology used, and to investigate materials. One of the early designs also included a prototype for a side facing imaging system. This design is possible and may have advantages depending on the intended application however was discarded for this study. All design iterations had similar assembling processes, varying slightly from one model to the other.

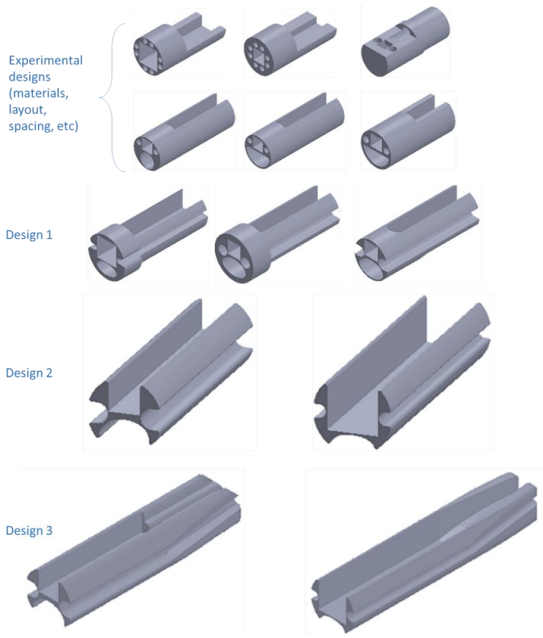

Fig 2 A selection of design iterations for the distal alignment holder are shown. They are categorised into groups with experimental and preliminary designs shown in the first row, and subsequent design iterations which were assembled successfully shown in subsequent rows, labelled Design 1-3.

III.B Imaging in a blood field

In order to image within the cardiovascular system, the blood field needs to be cleared. Several methods were investigated to achieve this, most involving some form of saline flush. One of the biggest challenges lies in continuous inflow of blood into the imaging area. Therefore, some isolation procedure needs to be used to keep the cleared area free from blood. In a vessel a balloon catheter inserted in front of the image sensor can be used to temporarily occlude a vessel to keep the field of view clear. Using the side facing imaging inserted into a balloon catheter was also an idea that was explored, which may allow imaging through the balloon to examine vessel walls, for example. However, given the goal of imaging within the heart, this method was discarded in favour of a more traditional flush. By far the most effective method we found in this study was placing the guiding catheter against the tissue to act as a seal. An internal flush channel integrated into the device can introduce saline to clear the field of view. A separate flush can be introduced through the guiding catheter should more flow be required. An important feature of our imaging system is this high-volume flush at the distal end of the catheter. A 1.20 mm outer diameter (1.00 mm inner diameter) braided polyimide tubing (Nordson medical, USA) was used to deliver the saline solution flush to clear the field of view in front of the camera. While compressed into an oval shape to fit into the distal end catheter, the proximal end of the tubing keeps its circular shape and is encapsulated, using biocompatible adhesive, into a female luer that can be connected to syringes filled with saline solution. To the best of our knowledge, this is the first demonstration of a catheter integrated imaging system with a flush channel. As a test, a 3.00 mL syringe was completely emptied in less than 1 second by manual operation at full speed, demonstrating that this system can provide a fast and efficient clearance of the camera's field of view.

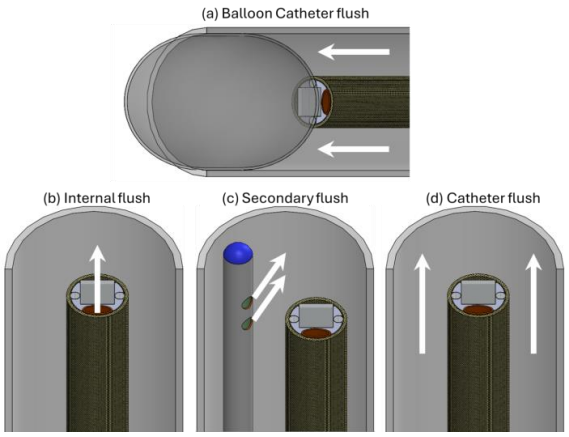

Fig 3. Schematic of blood field clearing methods. (a) shows a balloon catheter blocking the blood flow and saline flush clearing the field of view. In (b), (c), and (d), the guiding catheter is pushed against the endocardium and different flushing methods are employed to fill the area surrounding the camera sensor with saline. In (b) the internal flush is used, in (c) another flush catheter is introduced, and in (d) the guiding catheter itself is used to flush.

Preliminary in-vivo testing showed that the standard irrigation systems used in the catheters were too weak for our purpose and were flushing sideways a few centimetres away from the camera front face, making clearing the field of view challenging. An example of method to clear up the blood field is shown in Figure 3 (c). Flushing using the outer guiding catheter, as in Figure 3 (d), resulted in sufficient volume to easily clear the field of view. The internal flush's directional approach, Figure 3 (b), assisted in clearing the field of view in front of the sensor. In practice a combination of the different flush approaches may be necessary. Most important, however, remained the isolation of the flushed area from inflowing blood using the guiding catheter.

IV. Assembly Methods

Each prototype device was assembled manually in-house. Due to the small dimensions, much of the assembly is performed under a microscope. Fixing is achieved using a USP Class IV biocompatible UV curing adhesive (NOA68, Norland Jamesburg, NJ, USA). The adhesive remains a liquid until cured and so allows for manipulation until it is cured. Temporary fixing can be achieved with only a small amount of the adhesive which can be touched up later. Placing the glue is performed manually. Small amounts of the glue can be picked up and placed using a micro-applicator. This can also be sharp instrument such as a needle, or if scratching the optical components is a concern, a sharpened piece of wood,

such as a whittled toothpick. Translation stages may be helpful in the assembly process, however, were not needed for the work conducted in this study. An adjustable microscope arm also proves helpful.

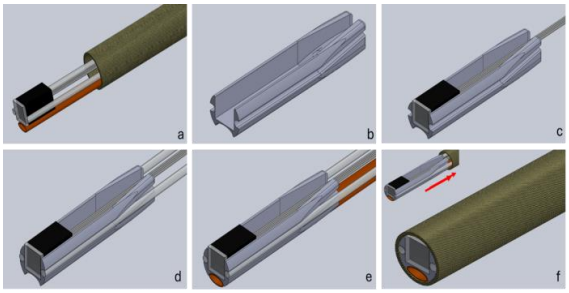

Fig 4 Assembly workflow of a distal end catheter-based imaging system. Cell (a) shows the components threaded through the sheathing lumen, (b) shows the 3D printed alignment holder. In step (c) the camera is inserted into the holder, followed by the fibres in step (d), and the flush channel in step (e). Finally in step (f) the distal part is pulled back into the sheathing lumen and secured in place.

The assembly process of the distal alignment piece is seen in Figure 4 as is described in detail below. The multi-step process is adaptable to different small scale integration challenges, and separates the assembly process into two parts, aligning all the components using the distal alignment piece, and then marrying the lumen and the alignment piece along with proximal connectors to form a finished system. (a) The camera and optical fibres, and flush are threaded through the sheathing by temporarily attaching them to a guidewire with a weak adhesive, which is pushed through the lumen. The camera should be inserted first as it is the most cumbersome and difficult part to push through, due to very flexible wires. The components now protrude through the front of the lumen. Here they can be fixed to the distal alignment piece, in what is the first primary step of the assembly process. The fibres are cleaved prior to fixing, to ensure a good termination. The flush channel is compressed into an oval shape prior to fixing it into the holder end to ensure it fits into the assembly. (b) Prior to assembly, supports are removed from the 3D printed alignment part, and the part is post processed to remove excess material using thing files and needles. This ensures a smooth finish in the areas where parts are placed. The small dimensions lead to tight tolerances, and this step ensures all the parts fit the lumen. (c) The camera is now ready to be fitted into the square shaped allotment. Deposit a thin layer of UV curable adhesive at the distal end of the 3D printed support on the three sides of the rectangular shape. Fit the camera in ensuring that no glue overflows in front of the lens and cure it in place. If needed, a light clamping system can be used to keep the camera in place and flat and flush with the distal end of the support. Finally, add a few drops of UV adhesive at the back of the camera to pot the camera with the support and strengthen the wires connection to the unit. During this step the platinum-iridium wires for x-ray guidance can be also fitted behind the camera body and above its wires. (d) In order to fix the optical fibres, deposit a very thin layer of UV glue at the distal end of the support dedicated to the optical fibres. Place the fibres at the distal end of the support and cure paying attention that they are aligned flat on the top of the camera and no glue is overflowing in front of them. A small clamp system is advisable to keep the fibres in place. Additional glue can be used at the tapered end of the support to give additional strength to the bonding. It is also advised to proceed with one fibre at a time. (e) Same procedure used for the fibres applies to the flushing system. However, being that the material is different from the fibres, it is advised not to use UV glues but a cyanoacrylate-based glue instead. It has been noticed that the bonding using UV glues with polyimide is much weaker compared to other types of adhesives. Also, due to the front shape of the support, it is important to flatten the front part of the flush, making it become slightly oval. The tapered end of the support offers some space to put some additional glue to increase the bonding strength. (f) Coat the outside of the assembled camera support heads with a thin layer of glue. While press fitting the part inside the catheter, be careful of any overflowing glue. Should this get in front of any of the assembled parts, clean immediately and proceed slowly with the insertion of the part. If the catheter is UV transparent this should be done easily and once happy with the position, the curing can start. Using alternative types of glues may be necessary in this step, although this could introduce timing difficulties.

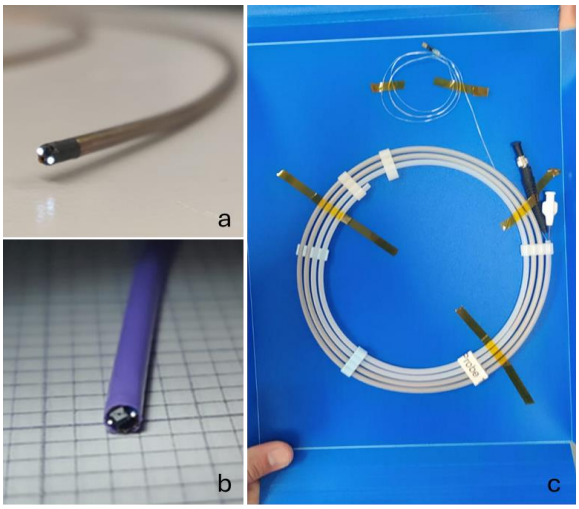

Fig 5 Finished 2.30 mm OD devices with the first iteration using braided polyimide tubing in (a), the final iteration with the Pebax tubing in (b), and the device securely packaged in a protective sleeve with the proximal terminations for the fibre, camera, and flush visible in (c).

The optical fibres are terminated at the proximal end using a standard SMA connector. Multiple fibres can be inserted into one connector, or if sensing is the goal separated into multiple end connectors. A spliced fibre can be used to drive the illumination, or separate channels can be used for contact DRS sensing. Images of the physical integration, back-end

termination, and final system are shown in Figure 5.

V. Angioscopic Imaging

The assembled device was successfully constructed and shipped to the study clinic in American Heart of Poland (Katowice, Poland) were imaging of the endocardium at multiple locations was achieved. The device is navigated through the vascular of the porcine animal with images captured in the right atrium, left atrium, and left ventricle of the animal's heart. A sealing technique using the guiding catheter lightly pressed against the cardiac walls and saline flush was used to clear the field of view in all cases. Best quality images were achieved when the device was slight recessed in the guiding catheter, the latter of which shields the device from additional blood flow after the field of view is flushed. This camera positioning can be seen well in Figure 6 (c) and (e), where the two marker wires embedded in the camera system are seen positioned inside of the guiding catheter, the tip of which has its own circular marker band. In the camera images, Figures 6 (b), (d), and (f), the guiding catheter can also be seen as it creates an annular feature in the image. Part of the imaging field of view is occupied by the catheter, with the boundary between catheter and tissue indicated by a dark ring, and the tissue visible in the centre of the image. This is displayed white in (b) and (f) and appears more similar to the colour of the endocardium in (d).

The device is able to successfully image the septum as demonstrated in Figure 6 (b). The transseptal cross is performed and the imager is successfully navigated through it into the left atrium where it can continue with image acquisition in Figure 6 (d). The device is navigated further through the valve into the left ventricle where it is able to acquire further images.

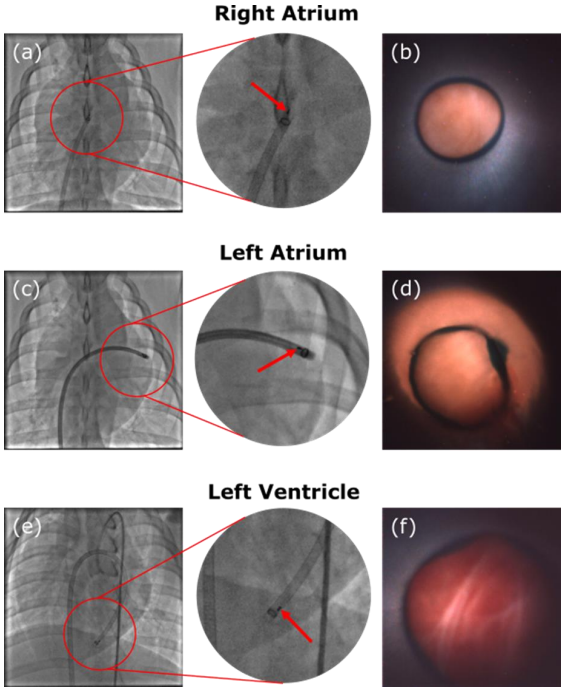

Fig 6 Images of the fluoroscopy showing the guiding catheter and device at location, and corresponding camera images. The red arrow indicates the platinum-iridium marker bands attached to the distal end of the device. A circular marker band at the tip of the guiding catheter is also visible. The device was navigated to the right atrium in (a) and images the intra-atrial septum in (b). The device sits in the left atrium in (c) where an image of the endocardium in the left atrium is displayed in (d). Finally, the device is located in the left ventricle with its position visible in (e) and an image of the endocardium of the apex of the heart can be seen in (f).

VI. Discussion

One of the primary issues were thin features on the parts breaking easily due to their limited structural thickness. At these small dimensions, through-holes can be challenging, especially over longer parts where the through-holes can fill in, requiring delicate post processing or can present uneven internal surfaces which made it difficult to pass components such as optical fibres through. The initial designs, Figure 2 Design 1, were successfully used to assemble some devices, however insertion into the sheathing catheter lumen proved difficult and parts broke during the assembly due to the closed design of some of the holes. Later designs therefore see a more open design, with the components slotted into the alignment holder from the sides, where they can easily be glued in place. The outer sheathing lumen then creates the circular seal around them. This design has the added benefit of being more space efficient. Designs in the second design iteration, Figure 2 Design 2, show the open boundary design into which components can be laid in for simpler assembly. In the third design iteration, Figure 2 Design 3, the insertion into the sheathing lumen is improved by shaping the support with a smaller and filleted back tail. These designs also include fillets that improve the attachment of the flush channel, and the taper allows for more secure attachment of the fibres to the back of the piece without impinging the insertion into the catheter. In addition to assembly considerations, designs were heavily influenced by clinician feedback. Two in-vivo studies were conducted using the devices, and the increase in the flush channel diameter, as well as switch from one sheathing material to another were all influenced by lessons learned from the first run of experiments. The saline delivery had to be improved to deliver more volume. Therefore, some designs in Figure 2 feature a larger space allotted to the flush channel. The earlier designs also had a lower resistance to kinking of the catheter while being pushed into the cardiovascular system through the guiding lumen, with revisions dictating a new material choice for outer lumen. This in turn affected the dimensions of the distal alignment holder.

Since the device is navigated through the curving structure of the cardiovascular system, it must be designed with this requirement in mind. One important consideration is the material choice for the outer sheathing. The guiding catheter delivers the device to location; however, the material must have both the flexibility to allow for easy navigation around bends, the rigidity to allow for it to be pushed through the

catheter, and the kink resistance to prevent it becoming stuck. This was a problem encountered in the first study use of the device and was revised after feedback from the clinicians. A new Pebax sleeve was used (Nordson Medical) in favour of the previously used braided polyimide. The thicker wall of the new tubing also increased the whole stiffness of the catheter assembly while still maintaining the desired very good flexibility. The push ability issue was satisfactorily resolved by the material change.

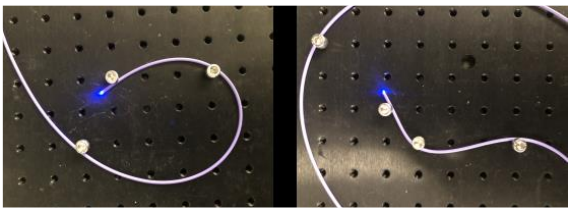

Fig 7 Light is delivered distally even through tight and complex bends.

Optical fibres, especially glass optical fibres, as were used in these iterations of the system, can negatively impact the stability of the device as it navigates bends. Figure 7 shows that light delivery is not affected dramatically even through tight bends. Losses through bending the fibres are not critical as long as enough light is delivered to the tissue and reflected back into the camera sensor. The purple Pebax material recovers well even after bending. However, breaking fibres is a common occurrence with the forces exerted on the devices. Hence it may be desirable to switch to fibre bundles, or plastic optical fibres, in future design iterations. Note that when using polymer, a high intensity UV curing lamp has been found to melt the plastic and different adhesion methods such as cyanoacrylate glue may have to be used, and the assembly workflow adjusted slightly. These devices are single use prototype devices for animal studies, and as such stringent sterilisation requirements have not been taken into consideration, which may require some revision of the design [28].

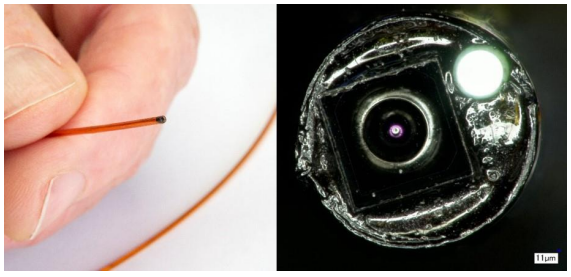

Fig 8 Assembled 1.20 mm outer diameter imaging catheter using OV6948 sensor, with illumination fibre. Shown held in hand for scale, alongside close-up microscope imaging showing camera sensor and illuminated optical fibre.

Smaller integration has also been explored and achieved by opting for a smaller camera sensor (OV6948), omitting the flush channel, and using only one illumination fibre (Figure 8). Here a similar workflow to the one above is employed. We were able to achieve a footprint of 1.20 mm outer diameter using a braided polyimide tubing. While such a system was not preferred for this cardiovascular application, due to the absence of the flush, and inability to perform DRS measurements due to only one illumination fibre, it does demonstrate the feasibility of reducing the dimensions even further. In this instance assembly was performed manually and without a distal alignment holder. This was due to the 3D printing limitation at the time making a 3D printed stable holder difficult to source. Instead, the fibre and camera were carefully aligned, and potted, before being drawn back into the lumen using a similar pull-back technique, and gaps filled using UV cure adhesive. Adhesive is deposited using a micro deposition tool and cured in stages.

VII. Conclusion

We report here the design and assembly process of a chip-on-tip catheter that has been used to successfully image in-vivo cardiac tissues thanks to a micro-camera sensor, an optical fibre-based illumination system and the possibility to clear the field of view using a flush a channel situated at the camera lens. We present design considerations and iterations and provide detailed assembly instructions for this device. These design considerations and fabrication methods are transferable to other miniature catheter-based applications. The 3D printed support allows for adequate alignment of parts, and packaging of the system in a 2.1mm diameter catheter. It can be used as an adjunct tool for guidance in many different cardiac procedures. Images collected directly inside the heart could give the clinicians and surgeons vital information on the procedure and inform on the success of the same. Further diameter reduction of the catheter footprint to reach smaller features could be possible by using more miniaturised imaging systems like the OV6948 sensor and integration at a 1.19 mm footprint has been demonstrated, though omission of the flush channel in this system may require additional engineering. The system was used to capture images in an in-vivo study on porcine models, which are, to the best of our knowledge, the first images captured using a micro-camera sensor inside of a beating heart.

Acknowledgment

This work was supported by the European Union's Horizon 2020 Programme, Grant No. 831117, and Science Foundation Ireland (SFI), Grant No. SFI/15/RP/2828.

References

[1] H. Li, X. Hou, R. Lin, et al., "Advanced endoscopic methods in gastrointestinal diseases: a systematic review," Quantitative imaging in medicine and surgery 9(5), 905 (2019).

[2] S. Shaikh and C. Deopujari, "The endoscope and instruments for minimally invasive neurosurgery," Mini Invasive Surg 4, 89 (2020).

[3] H. Jiang, "Bio-inspired micro-optical imaging for biomedical applications," in 2018 International Conference on Optical MEMS and Nanophotonics (OMN), 1–5, IEEE (2018).

[4] M. Wäny, P. Santos, E. G. Reis, et al., "Octagonal cmos image sensor for endoscopic applications," Electronic Imaging 2017(11), 46–51 (2017).

[5] M. A. Ahmad, M. Ourak, C. Gruijthuijsen, et al., "Design and shared control of a flexible endoscope with autonomous distal tip alignment," in 2019 19th International Conference on Advanced Robotics (ICAR), 647–653, IEEE (2019).

[6] J. Edelmann, A. J. Petruska, and B. J. Nelson, "Estimation-based control of a magnetic endoscope without device localization," Journal of Medical Robotics Research 3(01), 1850002 (2018).

[7] J. Gafford, M. Freeman, L. Fichera, et al., "Eyes in ears: a miniature steerable digital endoscope for trans-nasal diagnosis of middle ear disease," Annals of biomedical engineering 49, 219–232 (2021).

[8] L. A. Kahrs, T. R. McRackan, and R. F. Labadie, "Intracochlear visualization: comparing established and novel endoscopy techniques," Otology & Neurotology 32(9), 1590–1595 (2011).

[9] B. Gorissen, M. De Volder, and D. Reynaerts, "Chip-on-tip endoscope incorporating a soft robotic pneumatic bending microactuator," Biomedical microdevices 20, 1–7 (2018).

[10] F. Quader and C. P. Gyawali, "7recent advances in endoscopic treatments for gastroesophageal reflux disease," Current Treatment Options in Gastroenterology 18, 504–517 (2020).

[11] X. Ye, J. J. Cabibihan, and W. J. Yoon, "Design and verification of a flexible device for steering a tethered capsule endoscope in the stomach," in 2017 14th International Conference on Ubiquitous Robots and Ambient Intelligence (URAI), 550–555, IEEE (2017).

[12] G. Fai, S. Ostlie, M. Greminger, et al., "Tool for transbronchial biopsies of peripheral lung nodules," in Frontiers in Biomedical Devices, 41037, V001T06A006, American Society of Mechanical Engineers (2019).

[13] R. Hejj, M. McNulty, and J. G. Calleary, "Urology: the home of endoscopy," in Advances in Endoscopic Surgery, IntechOpen (2011).

[14] M. Padala, J. H. Jimenez, A. P. Yoganathan, et al., "Transapical beating heart cardioscopy technique for off-pump visualization of heart valves," The Journal of thoracic and cardiovascular surgery 144(1), 231–234 (2012).

[15] A. Alotaibi, G. Al-Dossari, and P. T. Roughneen, "Cardioscope: A new innovation for visualization of intracardiac pathology," Structural Heart 3, 27 (2019).

[16] G. Fagogenis, M. Mencattelli, Z. Machaidze, et al., "Autonomous robotic intracardiac catheter navigation using haptic vision," Science robotics 4(29), eaaw1977 (2019).

[17] H. C. Chang and W. Y. Chiu, "A single-pore knee arthroscopy system for injured athletes," in 2018 IEEE International Conference on Applied System Invention (ICASI), 1086–1087, IEEE (2018).

[18] C. J. Payne, G. Gras, M. Hughes, et al., "A hand-held flexible mechatronic device for arthroscopy," in 2015 IEEE/RSJ International Conference on Intelligent Robots and Systems (IROS), 817–823, IEEE (2015).

[19] M. Al-Akhras, H. Ali, K. Aljarrah, et al., "Influence of extremely low energy radiation on artificial tissue: Effects on image quality and superficial dose," Spectroscopy 22(5), 419–428 (2008).

[20] N. T. Clancy, G. Jones, L. Maier-Hein, et al., "Surgical spectral imaging," Medical image analysis 63, 101699 (2020).

[21] S. M. Bae, D. J. Bae, E. J. Do, et al., "Multi-spectral fluorescence imaging of colon dysplasia in vivo using a multi-spectral endoscopy system," Translational oncology 12(2), 226–235 (2019).

[22] J. Li, S. Thiele, B. C. Quirk, et al., "Ultrathin monolithic 3d printed optical coherence tomography endoscopy for preclinical and clinical use," Light: Science & Applications 9(1), 124 (2020).

[23] S. Coda, P. D. Siersema, G. W. Stamp, et al., "Biophotonic endoscopy: a review of clinical research techniques for optical imaging and sensing of early gastrointestinal cancer," Endoscopy international open 3(05), E380–E392 (2015).

[24] F. Darmoch, M. C. Alraies, Y. Al-Khadra, et al., "Intravascular ultrasound imaging–guided versus coronary angiography–guided percutaneous coronary intervention: a systematic review and meta-analysis," Journal of the American Heart Association 9(5), e013678 (2020).

[25] T. Al Abbas, O. Almer, S. W. Hutchings, et al., "A 128× 120 5-wire 1.96 mm 2 40nm/90nm 3d stacked spad time resolved image sensor soc for microendoscopy," in 2019 Symposium on VLSI Circuits, C260–C261, IEEE (2019).

[26] J. Hermanowski, "High intensity illumination from small fibers for in-vivo medical lighting." (Ushio Medical, formerly Nathaniel Group).

[27] M. Ahmadi, R. H. Hassani, G. Kosa, et al., "Endocat: An ethercat-based articulated rear view endoscope for single port surgery," in 2018 7th IEEE International Conference on Biomedical Robotics and Biomechatronics (Biorob), 1070–1075, IEEE (2018).

[28] A. D. Rocha, W. K. Drake, P. F. Rice, et al., "Iterative prototyping based on lessons learned from the falloposcope in vivo pilot study experience," Journal of Biomedical Optics 28(12), 121206–121206 (2023).

Paper VI

Open-source compact and customisable multi-LED platform for biophotonics applications

Yavari, Hasti and Niemitz, Lorenzo and Wang, Yineng, and Burke, Ray, and Andersson-Engels, Stefan, and Sørensen, Simon.

(Manuscript in editing process. To be submitted: 2024) *Target journal: Biomedical Optics Express.*

Open-source compact and customizable multi-LED platform for biophotonics applications

HASTI YAVARI[1,3], LORENZO NIELMITZ[1], YINENG WANG[1], RAY BURKE[1], STEFAN ANDERSSON-ENGELS[1,2], AND SIMON SORENSEN[1]

[1] *Tyndall National Institute, University College Cork, T12 R229 Cork, Ireland*
[2] *Department of Physics, University College Cork, T12 K8AF Cork, Ireland*
[3] *Hasti.yavari@tyndall.ie*

https://github.com/hastiy/MultispectralLEDEngine

Abstract: Multispectral illumination facilitates a wide range of biophotonics applications including tissue characterization. In this work, we present a comprehensive, open-source guide for constructing a compact multispectral LED platform that is coupled to a single multi-mode fiber or a liquid light guide, offering a cost-effective and reconfigurable alternative to commercially available options. The light source comprises of blue (455 nm), green (530 nm), red (660 nm), and two infrared (IR) LEDs (850 nm and 940 nm); however, it can readily be reconfigured to accommodate different wavelengths depending on the particular application. Blueprints, assembly instructions, parts list, and GUI software are made available online, allowing any research group to build their own instrument. Lastly, the light source is validated on biological samples to demonstrate its clinical value.

1. Introduction

Biophotonics techniques are commonly employed in clinical settings to assist clinicians in a wide range of applications ranging from screening and diagnosis to surgical assistance [1]. In-vivo non-invasive diagnostic imaging methods such as multispectral imaging [2-4], diffuse optical imaging [5,6], diffuse reflectance spectroscopy [7, 8], fluorescence imaging [9-11] and in-vivo microscopy [12,13] are enabling the clinicians to make faster and more evidence-informed decisions. Adapting these techniques in real-life clinical settings requires reasonably compact and easy to use instrumentation. In the recent years, we have seen emergence of various handheld or endoscopic integrated probes used in clinical settings for applications such as surgical guidance [11, 14], wide-field imaging [15], and cancer-monitoring [16, 17].

Seamless integration of biophotonics techniques into clinical workflows requires robust, portable and reasonably compact instrumentation. In the case of endoscopy, small footprint devices not only potentially improve patients' comfort and minimize costs associated with wound recovery and revision surgeries, but also enable previously unachievable applications such as accessing the cecum at the proximal end of the large intestines [18]. Miniaturized endoscopes must provide high-resolution images while complying with challenging form factors, opto-mechanical and illumination requirements. With the advancement of semiconductor technology, wide ranges of compact and functional detectors, e.g. AMS NanEye (1 x 1 mm^2 footprint) and Omnivision OV6948 (0.575 x 0.575 mm^2 footprint) micro-cameras, is readily available in the market. However, there is a noticeable absence of comparable sophistication in commercial illumination systems, compelling numerous research groups to independently construct their own devices.

Spectrally resolved light is commonly used in a variety of in-vivo imaging techniques to detect pre-malignant cells and differentiate between various types of lesions [19-21]. The basic principle behind these techniques is the unique information that the interaction of light with

tissue provides depending on the tissue's chromophores and biomolecular composition. Biological tissue's key biomarkers; namely, oxy- and deoxyhaemoglobin, water, lipid, collagen, oxy-, deoxy- haemoglobin, and met-myoglobin, exhibit unique absorption and fluorescence properties. For example in the case of oxy- and deoxyhaemoglobin, red and infrared wavelengths are particularly of interest as oxygenated haemoglobin absorbs more infrared light and allows more red light to pass through, while deoxyhaemoglobin behaves oppositely. From a visual point of view, shorter blue and green wavelengths tend to highlight tissue's microvasculature while longer red and infrared wavelengths are used to probe higher penetration depths.

A well-designed light source can enable multiple biophotonics application. For example, wide-field illumination is made possible by combining red, green and blue channels. Narrow-band illumination is made possible by using channels that enhance tissue feature visualization. Topographic imaging is made possible by sequentially illuminating the target from different angles. Opting for either light-emitting diodes (LEDs) or lasers for illumination presents distinct sets of advantages and disadvantages. LEDs generally require less stringent operation and safety protocol in clinical settings and do not produce unwanted speckle pattern when coupled through a multi-mode fiber. On the other hand, lasers offer significantly higher coherency and luminosity. The parasitic speckle pattern of fiber-coupled laser illumination introduces noise and impedes the quality of the captured images but can be utilized in itself for techniques such as laser speckle contract imaging or flow imaging [22]. Apart from applications when speckle pattern is intentionally utilized, much effort has been made to eliminate it from the illumination profile [23]. However, in practice speckle pattern elimination remains a challenge for in-vivo clinical applications. Enticed by the higher coherency of lasers, most research groups opt for building laser-based light sources. Chen et. al. demonstrates a laser-based narrow-band illumination system made of RGB lasers for miniature endoscopes using a monochrome camera and an acoustic frequency mechanical stress modulation speckle reduction technique [24]. The illumination system provides promising results, however; the mechanically vibrating speckle reduction mechanism proposed is not robust and imposes practical challenges in a clinical setting. Bobrow et al. has developed a similar light source made of RGB lasers and a diffusing laser speckle reducer [25]. Clancy et al. has developed an LED endoscopic light source made of red, green, blue and violet ($\lambda <$ 430 nm) LEDs and compares it's illumination with xenon lamp commonly used in endoscopy application [14]. Gryko et al. has developed a LED source comprised of 13 LEDs and investigated the spectral power distribution of the LEDs from a color feature recognition perspective [26].

In the interest of open science, research groups are sharing their instruments and scientific data online. A recent example is Schröder et al. 's cost-efficient open-source laser engine for microscopy [27]. We present a cost-effective, portable and open-source multi-LED system with a multi-mode fiber or a liquid light guide (LLG) output that suits both miniature and larger footprint multispectral imaging applications. The coupled light offers several advantages compared to a tip mounted illumination that generally suffers from undesired heating effects, inflexible design and large footprint [28]. The proposed LED module can be reconfigured to wavelengths of choice depending on the application of interest. Moreover, the LEDs can potentially be replaced by lasers should lasers have a particular advantage for an application. Sequential acquisition of the spectral images is facilitated through a user-friendly LABVIEW interface designed to accommodate both technical and non-technical users. Blueprints, parts list, assembly instructions and GUI software are available on Github, hastiy/MultispectralLEDEngine allowing any research group to build their own light source.

2. Materials and Method

2.1 LED illumination platform

The illumination platform comprises of blue (455 nm, 1150 mW), green (530 nm, 370 mW), red (660 nm, 940 mW), as well as 2 IR LEDs (850 nm, 900 mW and 940 nm 800 mW). Each LED can be powered individually or simultaneously to produce a tunable spectrum, allowing for highlighting different features and probing deeper penetration depth. Light from each LED passes through a condenser lens (f=16 mm, NA=0.79) and is directed using long-pass dichroic filters (495 nm, 600 nm, 735 nm and 900 nm). Lastly, all the beams are combined using another condenser lens and focused to a single multimode optical fiber of choice. The fiber is subsequently coupled to a larger multi-mode fiber to scramble the optical modes from each LED. Liquid light guides can readily replace the light platform's fiber optic output as well depending on the particular application. There are no moving parts in the optical path. The optics are arranged on a custom 190 x 290 mm^2 plate fitted inside an enclosure box. The power intensity of each LED is controlled using an individual driver through an acquisition device and a custom-built GUI. The optical components are off-the-shelf products from Thorlabs and Edmund Optics. The light source is customizable in terms of wavelength to a reasonable degree. Fewer LEDs and/or LEDs with other wavelengths can replace the proposed wavelengths with considerations to the optical design. Fig. 1 (a) and (b) show the built and schematics of the multi-spectral LED platform, respectively. The optical layout of the light source is shown in Fig. 1 (c).

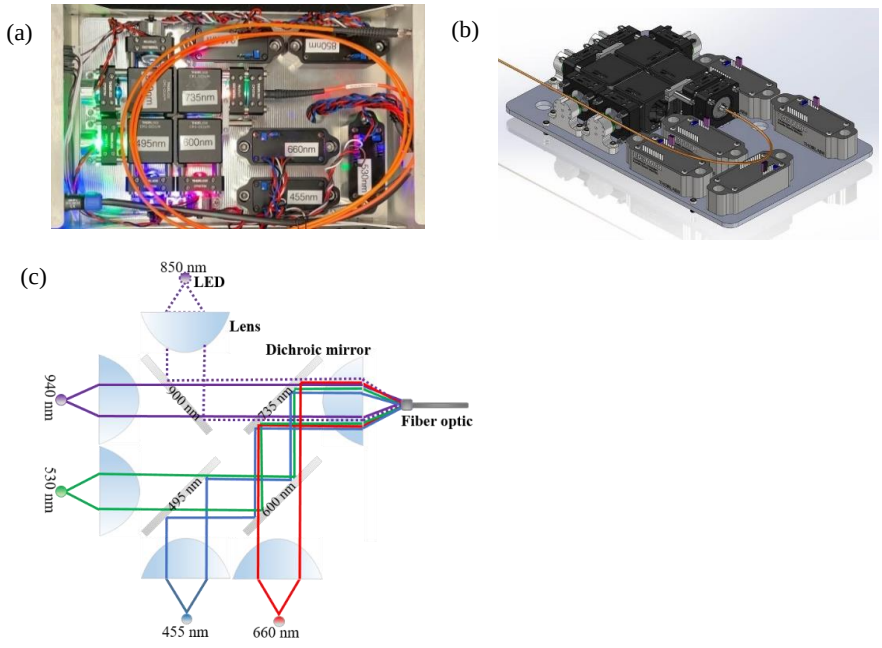

Fig. 1. (a) Built multi-spectral LED platform. (b) Mechanical schematics of the LED platform. (c) Optical layout of the LED platform.

Besides each individual channel, the GUI offers a "white" light channel which is a combination of red, green and blue LEDs producing a near-continuous spectrum. From a clinical point of view, white light illumination enables potential real-time viewing of the target with colors close to what a human eye would perceive. Color temperature of reconstructed white light is produced by relating each of the RGB channels with a corresponding blackbody

radiation [29]. Here the voltage versus intensity of the red, green and blue LEDs are measured (using a PM100D Thorlabs optical power meter) and RGB coefficients are extracted by comparing the emitted light with the corresponding intensity at that particular wavelength of a blackbody radiator.

2.2 Biophotonics application

To demonstrate the illumination capability of the LED platform, two applications have been chosen using the multispectral illumination source and a monochromatic camera. The first one is endoscopy using a custom-built probe with a monochrome micro-camera and 4 optical fibers delivering the light to the tissue. The main goal with this application is to show-case the benefit of using fibers in size-constraint applications like endoscopy. For the second application, we have chosen to highlight the illumination capability of the light source, when not restrained by size, using a monochrome camera with higher resolution and a light-guide delivering light to the tissue. The experimental setups for these applications are shown in F. 2. In Fig. 2 (a) a custom designed handheld probe is used to integrate illumination with the micro-camera (monochrome AMS NanEYE, 90 FOV, F 2.7, 62 kP). The probe has been previously validated for tissue imaging ex-vivo [30]. The micro-camera has a footprint of 1.0 x 1.0 mm^2 and is run by a frame-grabber connected to the laptop. The probe design comprises of the micro-camera placed in the center of the probe surrounded with four fiber optics on its sides for a more uniform illumination. In Fig. 6 (b) a monochrome camera (FLIR Blackfly S BFS-U3-51S5P, 5 MP) and lens (Navitar NMV-50M23 50 mm F/2.8) are used for imaging and a light guide (Thorlabs LLG5-4Z, 5 mm Core, 420 - 2000 nm) is used for illumination. The biological sample is a fresh ovine's heart and bovine's leg muscle sourced from a local butcher shop.

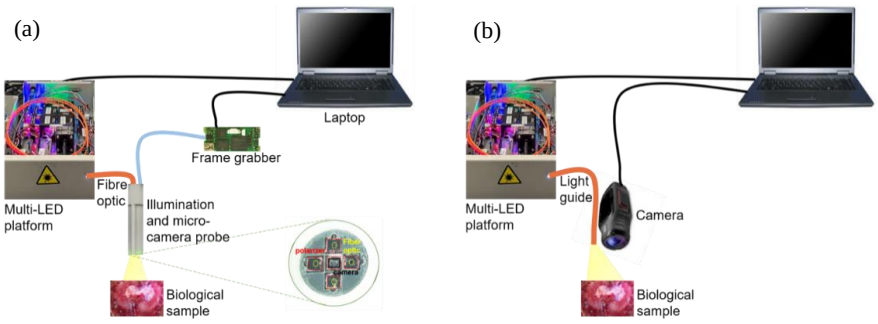

Fig. 2. Experimental setup for multispectral imaging of biological tissue using a (a) micro-camera packaged with optical fiber in a custom design probe, (b) camera of higher resolution and light guide illumination delivered from the multispectral light platform.

The sample is illuminated sequentially using the custom-built LabVIEW interface. An image is captured for a cycle of minimum to maximum intensity for each LED. The illumination duty cycle of each LED can be controlled using their respective high speed driver (Thorlabs LD3000R) and is capable of synchronizing with high frame rate cameras. In both setups, the biological sample, camera and illumination channel are fixed to ensure minimum motion artefacts. Specular reflection in both applications is dealt with using polarizers. In Fig. 2 (a), cross polarizers are used in front of the camera as well as the fibers (Edmund Optics linear P-transmitting polarizer diced using a mechanical dicing saw to 2.0 x 2.0 mm^2). Fig. 2 (b), the camera itself uses a polarized sensor providing four sets of polarized images, with polarization angles at 90°, 45°, 135° and 0° and a cross-polarizer (Edmund Optics linear P- transmitting polarizer) is placed in front of the light guide. The relevant polarization is then extracted from the images using a simple demosaicing algorithm.

In a color CMOS camera, a portion of the light reaching the sensor is filtered out by RGB filters, i.e. Bayer filter. Color image is then generated using a demosaicing algorithm [31, 32]. Monochrome cameras do not have such filters and therefore higher photon counts are reaching the pixel area, effectively improving the low-light performance and resolution for the same construction geometry. Moreover, common demosaicing artifacts, namely, Moiré and color artifacts are naturally absent in monochrome images. By using a monochrome camera, higher spatial resolution can be achieved, especially for applications limited by size. More information on the imaging principle behind a color versus monochrome CMOS can be found in the Appendix. When using monochrome cameras as the detector, the images captured using different wavelength illumination can be combined to produce a color image. The contrast of subtle features can be manipulated in the color reconstruction process depending on the approach used. Flexible Spectral Color Enhancement (FICE) is a powerful technique used to highlight features that are not evident when using simple white light endoscopy. Real-time enhanced endoscopy images are produced either using purely digital image-processing techniques (e.g. i-scan technology) or through combining digital image-processing with physical use of band pass filters (e.g. i-scan OE technology) [33, 34]. We have employed a similar approach to highlight vasculature features when reconstructing a color image digitally.

3. Validation and Results

3.1 LED illumination platform

Fig. 3 shows the spectrum of the LED platform at 4500 K color temperature measured with a reflection target and a spectrometer (VIS-NIR Wasatch Photonics).

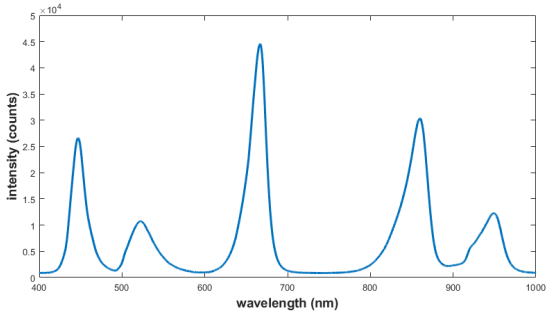

Fig. 3. LED platform spectrum at color temperature of 4500 K.

The optical output power for each individual LED when transmitted through multimode fibers of different core diameters (d_{core}) and numerical apertures (NA) is shown in Table 2.

Table 2. Optical output power for each individual LED using various multimode fiber optics.

	Power [mW]			
Wavelength [nm]	d_{core} = 200 um NA = 0.22	d_{core} = 200 um NA = 0.39	d_{core} = 400 um NA = 0.39	d_{core} = 400 um NA = 0.5
455	2.98	8.23	30.01	34.40
530	0.44	1.25	4.64	6.15
660	1.81	5.84	20.95	27.43
850	1.14	4.67	20.06	28.25
940	1.39	3.67	15.07	21.39

Stability of the light output for each LED was measured by recording optical power of LEDs at half of their respective max voltage for the duration of 20 minutes. CV is the

(a) (b)

coefficient of variation. Fig. 4 (a) shows the result for the first 5 minutes and Fig. 4 (b) shows the results for the remaining 15 minutes.

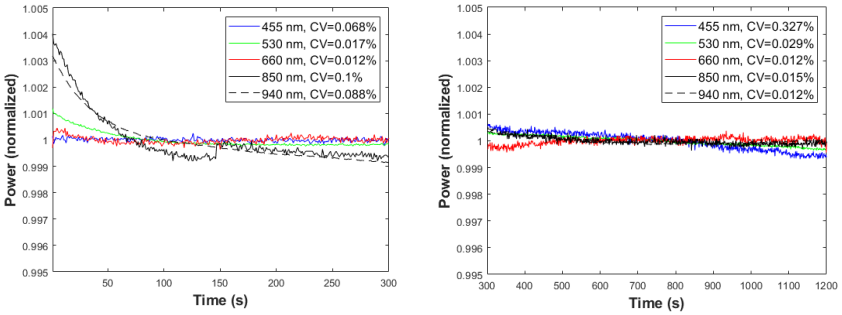

Fig. 4. Stability measurement of the light source by recording optical power of LEDs at half of their respective max voltage for the (a) initial five minutes and (b) Between five to twenty minutes. CV is the coefficient of variation.

3.2 Biophotonics application

The light source is validated on biological tissue using the setups shown in Fig. 2. Fig. 4 (a) shows monochrome images recorded using the micro-camera probe when the ovine's heart is sequentially illuminated using optical fibers with blue (455 nm), green (530 nm), red (625 nm) LEDs. The images are then linearly combined digitally to reconstruct a color image as shown in Fig. 4 (b). In the photo to the left (reconstructed 1), the image is reconstructed with the goal of providing a color resemblance closest to the tissue perceived by human eye. Whereas in the photo to the right (reconstructed 2), the image is reconstructed in such a way that it enhances the features of the tissue. Fig. 4 (c) shows monochrome images recorded using the FLIR camera when the bovine slice is sequentially illuminated using a light guide with blue (455 nm), green (530 nm), red (625 nm) and infrared (850 nm and 940 nm) LEDs. In Fig. 4 (d), image reconstruction is done by linearly combining the blue and green channel with red (R+G+B) in the photo to the left and combining the blue and green channel with 850 nm infrared (IR+G+B) in the photo to the right.

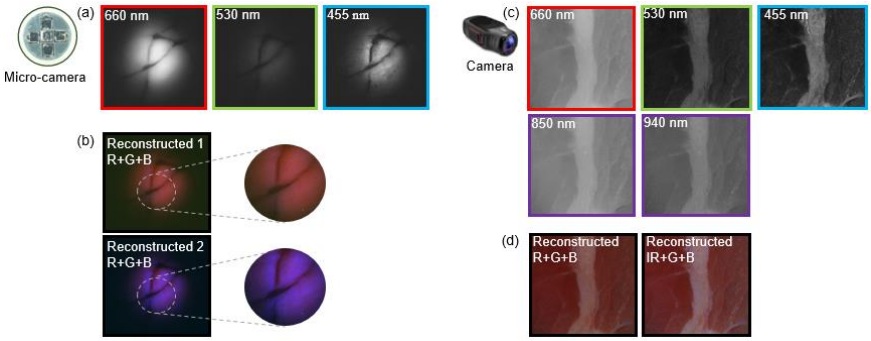

Fig. 5. (a) Ex-vivo monochrome images collected by sequentially illuminating an ovine's heart with blue (peak at 455 nm), green (peak at 530 nm), and red (peak at 625 nm) light using the setup shown in Fig. 2 (a). (b) Color reconstructed images; Reconstructed 1: resembling the real-life colors of the sample, Reconstructed 2: utilizing image-recombination techniques to maintain visual features evident in the monochrome images. (c) Ex-vivo monochrome images collected by sequentially illuminating bovine tissue with blue light (peak at 455 nm), green light (peak at 530 nm), and IR light (peak at 850 and 940 nm) taken with a FIR camera using the setup shown

in Fig. 2 (b). (d) Color reconstructed images created by linearly combining the blue and green channel with red (R+G+B) or infrared (IR+G+B) images. 850 nm is used for the infrared channel in the image to the right.

In Fig. 5 (a) and (b), an area of roughly 5 mm is imaged from 7 mm distance with the exposure time kept at a fixed value for all channels. The presence of dark corners stems from constraints inherent in the design of the miniature probe, in particular with the AMS micro-camera's sensor light sensitivity (ISO sensitivity) and the micro-camera lens's ability to collect the light. This limitation becomes more evident at higher object-camera distances. Infrared images taken with the probe had to be discarded due to light leakage into sensor as a result of mechanical limitations in the material used for printing the holder. The sample features, i.e. blood vessel and colored spots, are highlighted with blue illumination, while red light fails to show the more subtle details. As expected, the green image looks darker than the rest due to the green LED's low output power. In Fig. 5 (b), two color reconstructed images are presented namely; Reconstructed 1 and Reconstructed 2. In Fig. 5 (b) Reconstructed 1, the focus of reconstruction is to achieve the color reconstruction resembles closest to that of the tissue in real-life which compromises much of the details evident in the blue channel. In Fig. 5 (b) Reconstructed 2, spectral imaging color enhancement concept is demonstrated by producing a color image which preserves maximum amount of features using digital image reconstruction techniques. Here we can observe that despite the limited resolution of the micro-camera, discernible subtle features persist in the color reconstructed image.

In Fig. 4 (c) and (d), an area of roughly 5 mm is imaged from 10 mm distance using a 5MP sensor camera. The light guide illuminates the target uniformly with no dark corners. Despite the camera sensor's low extinction ratio at higher wavelengths, the infrared channels at higher exposure time capture similar feature information as the red channel at lower exposure. The reconstructed images look nearly identical for the image reconstructed using the red channel compared to infrared channel. This is expected since the blue and green channel are offering the most visual information. Infrared light can potentially highlight features beneath the tissue surface but we were not able to demonstrate that with our sample.

4. Discussion

We introduce a compact and customizable fiber-coupled LED platform, comprising five LEDs, designed for easy assembly by other research groups. Fiber coupling is achieved using a standard SMA port, allowing users to utilize various fibers based on the specific requirements of their applications. The optical and opto-mechanical parts cost add up to approximately €1500 EUR. This price is excluding the drivers and readout boards, electronics components and the custom mechanical parts, which can be purchased from a range of distributors (Thorlabs, RS, Arduino and National Instruments). This cost is significantly lower than commercial multi-wavelength fiber-coupled LED sources available in the market, which typically cost several thousands of euros with limited customizability. Heat management in the light source is navigated through use of aluminum material for the custom lens holders as well as application of heat-conducting paste behind the LED PCBAs. In this way, even without an additional dedicated cooling system the LED platform exhibited a highly stable output power with maximum 1% variation from the mean (Fig. A3 in the Appendix). For detectors with limited sensitivity, i.e. micro-cameras, the power requirements of the light source increases, which in turn highlights the importance of ensuring that the intensity of each individual LED to be as high as possible. In our light source, the relatively lower output power of the green LED is evident in the images captured by both the micro-camera and the larger camera. Although unfavorable, green LEDs naturally exhibit lower power due to their solid state design. Therefore, the bottle-neck in achieving high power RGB LED illumination lies with the green channel.

The choice of using LEDs over lasers proved to be advantageous despite the inherent lower fiber optic coupling efficiency of LEDs (Table 2). In this way, we naturally circumvent unwanted speckle patterns and the need for devising a speckle-reduction technique. Furthermore, we can achieve a near-continuous spectrum, which can be used for spectroscopy techniques such as Diffuse Reflectance Spectroscopy (DRS). From a practical point of view, LEDs have the additional advantage of requiring less stringent operating guidelines and safety protocols, making them more suitable for use in clinical settings for both ex-vivo and in-vivo applications. In theory, besides the choice of replacing the proposed LEDs with LEDs of choice, any LED in the system can be replaced with a laser with minor redesign. Compared with other biophotonics light sources presented in the literature [14 & 24-26], our light source is the first one made available online. Our design is versatile and customizable. Rather than making an exact duplicate, we encourage the researchers to adapt the design to their particular application.

An important factor to consider when performing sequential imaging in-vivo is synchronization between the light source and the camera. In our light source, the illumination duty cycle of each LED is controlled using their respective high-speed driver (Thorlabs LD3000R) which is capable of synchronization with high frame rate cameras. This synchronization will be different for the light source with each camera and is outside the scope of this paper. The images shown in this work are taken ex-vivo using a hand-held probe which was fixed in place. In an in-vivo clinical setting, motion artifacts can arise from maneuvering the endoscope as well as the natural movement of the target area inside the body due to respiration, heartbeat or peristalsis. Fast wavelength switching and high speed intensity modulation of the light source, high frame rate or readout speed and the auto-exposure algorithm of the detector as well as good synchronization between the two are imperative for demanding applications such as real-time in-vivo imaging, flow cytometry, microscopy and etc.

5. Conclusion

We demonstrate an open-source multispectral LED platform that can deliver relatively higher coupling efficiencies through a single multimodal fiber optic or liquid light guide of choice. Each LED can be powered individually or simultaneously to produce a tunable spectrum, allowing for highlighting different features and probing deeper penetration depth in various biophotonics applications. To facilitate reproducing the instrument, blueprints, assembly instructions, parts list, and GUI software are made available on Github (https://github.com/hastiy/MultispectralLEDEngine,).

Appendix

Color versus monochrome camera

Fig. A1 shows the imaging principle behind a color and monochrome CMOS.

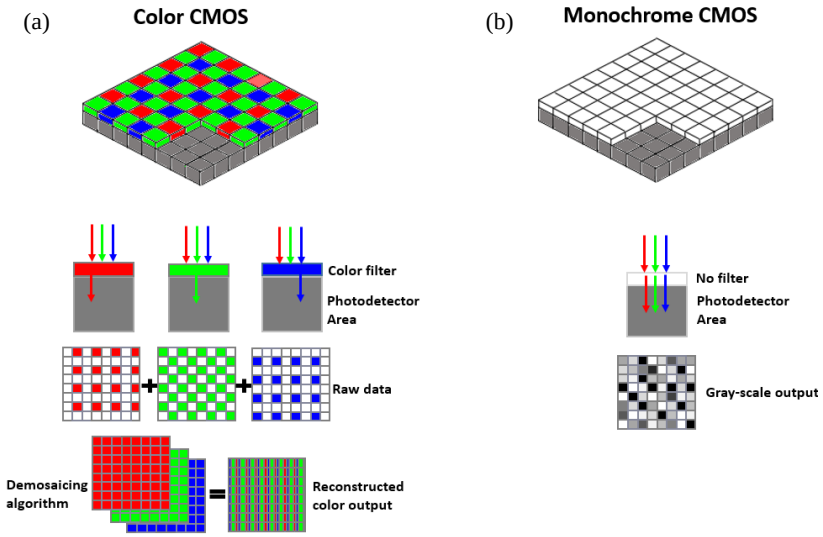

Fig. A1. Imaging principle behind (a) color and (b) monochrome CMOS cameras.

Lens choice

Coupling the emitted light from LEDs to the multimode optical fiber is done through using two identical 1" aspheric condenser lens placed as shown in Fig. A2. These lenses offer the advantage of easier mounting while providing a reasonable coupling efficiency.

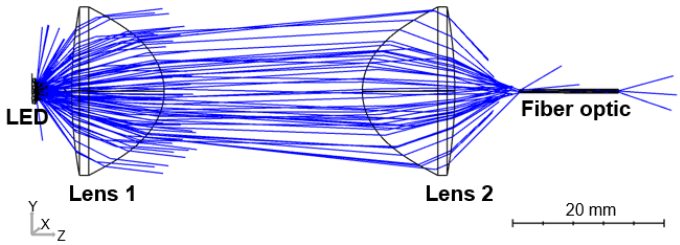

Fig. A2. Coupling of light emitted from LED to a 400 um fiber NA 0.39 fiber optic.

Table A1 shows the coupling efficiency calculated for different lenses using Zemax non-sequential modelling.

Table A1. Coupling efficiency from lens to fiber optic for various lens types.

Lens type	Lens 1 focal length [mm]	Lens 2 focal length [mm]	Coupling efficiency [%]
Aspheric condenser 0.5”	8	8	
Aspheric condenser 1”	16	16	
Aspheric condenser 2”	32	32	
Achromatic 1”	30	30	
Achromatic 1”	30	50	

Table A2 summarizes the characteristics of the LEDs used in the LED platform.

Table A2. Light-source LEDs characteristics.

Nominal Wavelength [nm]	Thorlabs Item #	Output Power [mW]		Irradiance [μW/mm^2]	Max Current (CW) [mA]	Forward Voltage [V]	Viewing Angle (Full Angle at Half Max) [deg]	Emitter Size [mm x mm]
		Minimum	Typical					
455	M455D3	1150	1445	32	1000	3.25	80	1x1
530	M530D3	370	480	9.46	1000	3.6	80	1x1
660	M660D2	940	1050	20.9	1200	2.6	120	1.5x1.5
850	M850D2	900	1100	22.9	1200	2.95	90	1x1
940	M940D2	800	1000	19.1	1000	2.75	90	1x1

Funding. This work is financially supported by Science Foundation Ireland (SFI/15/RP/2828 & SFI-22/RP-2TF/10293) and IPIC2 Biomedical theme (Grant number: SFI-12/RC/2276_P2 **).**

Disclosures. The authors declare no conflicts of interest.

Liability. The open-source LED platform is a class 3 light source. Caution must be carried out when aligning and using the light source. The authors assume no liability in case of negligence of user to adhere to safety protocols when dealing with the light source proposed in this work.

References

1. S. H. Yun and S. J. Kwok, "Light in diagnosis, therapy and surgery." Nat Biomed Eng 1, 0008 (2017).
2. R. M. Levenson, and J. R. Mansfield. "Multispectral imaging in biology and medicine: slices of life." Cytometry Part A: the journal of the International Society for Analytical Cytology 69.8 748-758 (2006).
3. L. Qiu, L. Zhang, V. Turzhitsky, et al., "Multispectral Endoscopy with Light Gating for Early Cancer Detection." IEEE J Sel Top Quantum Electron. 25(1):7201309 (2019).
4. D. J. Waterhouse, S. Bano, W. Januszewicz, et al., "First-in-human pilot study of snapshot multispectral endoscopy for early detection of Barrett's-related neoplasia." J Biomed Opt. 26(10):106002 (2021).
5. A. Gibson and H. Dehghani. "Diffuse optical imaging." Philosophical Transactions of the Royal Society A: Mathematical, Physical and Engineering Sciences 367.1900 (2009).
6. B. Jung, B. Choi, A. J. Durkin, et al., "Characterization of port wine stain skin erythema and melanin content using cross-polarized diffuse reflectance imaging." Lasers Surg. Med., 34, 174–181 (2004).
7. L. L. D. Boer, T. M. Bydlon, F. V. Duijnhoven, et al., "Towards the use of diffuse reflectance spectroscopy for real-time in vivo detection of breast cancer during surgery." J. Transl. Med. 16, 1–14 (2018).
8. J. W. Spliethoff, W. Prevoo, M. A. Meier, et al., "Real-time in vivo tissue characterization with diffuse reflectance spectroscopy during transthoracic lung biopsy: a clinical feasibility study." Clinical cancer research 22.2 357-365 (2016).
9. E. M. Sevick-Muraca, "Translation of near-infrared fluorescence imaging technologies: emerging clinical applications." Annual review of medicine 63 217-231 (2012).
10. A. Refaat, Ahmed, M. L. Yap, G. Pietersz, et al., "In vivo fluorescence imaging: success in preclinical imaging paves the way for clinical applications." Journal of Nanobiotechnology 20.1 1-22 (2022).
11. H. L. Stewart, D. J. Birch, "Fluorescence Guided Surgery." Methods Appl. Fluoresc. 9, 042002 (2021).
12. K. W. Bishop, K. C. Maitland, M. Rajadhyaksha, et al., "In vivo microscopy as an adjunctive tool to guide detection, diagnosis, and treatment." J. Biomed. Optics 27, 040601 (2022).
13. W. A. Wells, M. Thrall, A. Sorokina, et al., "In vivo and ex vivo microscopy: moving toward the integration of optical imaging technologies into pathology practice." Archives of pathology & laboratory medicine 143.3, 288-298 (2019).

14. N. T. Clancy, S. Arya, J. Qi, et al., "Polarised stereo endoscope and narrowband detection for minimal access surgery." Biomed. Opt. Express, 5, 4108–4117 (2014).
15. C. M. Lee, C.J. Engelbrecht, T. D. Soper, et al., "Scanning fiber endoscopy with highly flexible, 1 mm catheterscopes for wide-field, full-color imaging." J. Biophotonics, 3, 385–407, (2010).
16. C. Martelli, A. L. Dico, C. Diceglie, et al., "Optical imaging probes in oncology." Oncotarget 2016, 7, 48753.
17. B. Jayachandran, J. Ge, S. Regalado, et al., Design and development of a hand-held optical probe toward fluorescence diagnostic imaging. J. Biomed. Opt. 12, 054014 (2007).
18. J. Westerhof, R. K. Weersma, J. J. Koornstra, "Risk factors for incomplete small-bowel capsule endoscopy." Gastrointestinal Endoscopy, V. 69, 1, 74-80 (2009).
19. N. D. Tan, Y. Q. Lin, Z. Y., et al., "White-light endoscopy is insufficient to distinguish between types of esophageal white lesions." J Dig Dis. 22(9):520-528 (2021).
20. A. P. Dhawan, B. D'Alessandro, S. Patwardhan, et al., "Multispectral optical imaging of skin-lesions for detection of malignant melanomas." 2009 Annual International Conference of the IEEE Engineering in Medicine and Biology Society, 5352-5355 (2009).
21. J. R. Mansfield. "Multispectral Imaging: A Review of Its Technical Aspects and Applications in Anatomic Pathology." Veterinary Pathology. 51 185-210 (2014).
22. W. Heeman, W. Steenbergen, G. van Dam, et al., "Clinical applications of laser speckle contrast imaging: a review." J Biomed Opt. 1-11 (2019).
23. J. Jaybhay, and S. Rajveer., "A study of speckle noise reduction filters." signal & image processing: An international Journal (SIPIJ) 6.3 71-80 (2015).
24. Z. Y. Chen, A. Gogoi, S. Y. Lee, et al., "Coherent narrow-band light source for miniature endoscopes." IEEE Journal of Selected Topics in Quantum Electronics 25, no. 1 1-7 (2018).
25. T. Bobrow, N. Durr, "An adaptive-coherence light source for hyperspectral, topographic, and flow-contrast imaging." Proc. SPIE 10871, Multimodal Biomedical Imaging XIV, 108710Y (2019).
26. L.Gryko, U. J. Blaszczak, J. Lewandowski, et al., "Visualisation of biological tissues with the use of LED source illumination." Proc. SPIE 11176, Photonics Applications in Astronomy, Communications, Industry, and High-Energy Physics Experiments 2019, 111762Y (2019).
27. D. Schröder, J. Deschamps, A. Dasgupta, et al., "Cost-efficient open source laser engine for microscopy." Biomed. Opt. Express 11, 609-623 (2020).
28. D. Brüggemann, B. Blase, F. Bühs, et al., "Endoscope with distal LED for illumination." InWorld Congress on Medical Physics and Biomedical Engineering May 26-31, pp. 2107-2110 (2013).
29. E. Y. Lam, "Combining gray world and retinex theory for automatic white balance in digital photography." Proc. 9th Int. Symp. Consum. Electron., 134–139 (2005).
30. L. Niemitz, S. D. van der Stel, S. Sorensen, et al., "Microcamera Visualisation System to Overcome Specular Reflections for Tissue Imaging." Micromachines 14, 1062 (2023).
31. E. R. Fossum, "CMOS image sensors: Electronic camera-on-a-chip." IEEE Trans. ElectronDevices, vol. 44, no. 10, pp. 1689–1698 (1997).
32. S. Mendis, S. E. Kemeny, and E. R. Fossum, "CMOS active pixel image sensor." IEEE Trans. Electron Devices, vol. 41, no. 3, pp. 452–453 (1994).
33. H. Neumann, M. Fujishiro, CM. Wilcox, et al., "Present and future perspectives of virtual chromoendoscopy with i-scan and optical enhancement technology." Digestive Endoscopy 26 43-51 (2014).
34. P. Pal, A. P. Singh, N. D. Kanuri, et al., "Electronic chromo-endoscopy: technical details and a clinical perspective." Translational Gastroenterol Hepatology 7 (2022).

Paper VII

Multi-spectral in-vivo FPGA-based surgical imaging

Alsharari, Majed and Niemitz, Lorenzo and Sørensen, Simon and Woods, Roger and Burke, Ray and Engels, Stefan Andersson and Reaño, Carlos and Mai, Son T.

International Symposium on Applied Reconfigurable Computing
LNCS 13569, 103–117 (2022).

Multi-spectral In-Vivo FPGA-Based Surgical Imaging

Majed Alsharari[1,5( )], Lorenzo Niemitz[2], Simon Sorensen[2], Roger Woods[1], Ray Burke[2], Stefan Andersson Engels[2,3], Carlos Reaño[4], and Son T. Mai[1]

[1] Queen's University Belfast, Belfast BT9 5AF, Northern Ireland, UK
{malsharari01,r.woods,thaison.mai}@qub.ac.uk
[2] Tyndall Institute, Lee Maltings Complex Dyke Parade, Cork T12 R5C, Ireland
{lorenzo.niemitz,simon.sorensen,ray.burke,
stefan.andersson-engels}@tyndall.ie
[3] Department of Physics, Kane Science Building, University College Cork, Cork, Ireland
[4] Universitat de València, 46100 Valencia, Spain
carlos.reano@uv.es
[5] Jouf University, Sakaka 72341, Saudi Arabia
malsharari@ju.edu.sa
https://www.qub.ac.uk/schools/eeecs/, https://www.ipic.ie/,
http://research.ucc.ie/profiles/D006/stefan.andersson-engels@tyndall.ie,
http://www.uv.es/caregon2, https://www.ju.edu.sa

Abstract. Intelligent and adaptive in-vivo, catheter-based imaging systems with enhanced processing and analytical capability have the potential to enhance surgical operations and improve patient care. The paper describes an intelligent surgical imaging system based on a 'chip on tip', which reduces the need for conventional imaging. The associated embedded system provides real-time, in-vivo imaging analysis and data display for surgeons, enhancing their ability to detect clinically significant tissue. The paper presents initial work on an field programmable gate array implementation of a contrast limited adaptive histogram equalization algorithm, Hessian matrix construction and region of interest function on the AMD-Xilinx's Kria KV260 board. It outlines optimizations undertaken to reduce the BRAMs by 38%, DSP48 blocks by 80%, flip-flops by 33% and LUTs by 36%, thus creating a design operating at 121 FPS.

Keywords: Surgical imaging · Field programmable gate array

1 Introduction

In current surgical practice, surgeons still rely heavily on external, 'gold standard' imaging systems such as X-ray, CT and MRI. In-vivo imaging systems such as endoscopes, intravascular ultrasound are standard but can be further

Partially supported by Jouf University.

© The Author(s), under exclusive license to Springer Nature Switzerland AG 2022
L. Gan et al. (Eds.): ARC 2022, LNCS 13569, pp. 103–117, 2022.
https://doi.org/10.1007/978-3-031-19983-7_8

enhanced and using smart and integrated micro cameras. This offers the potential to enhance surgical procedures and outcomes by providing high quality, diagnostic images from deep within the body using micro-scale image sensors on a micro catheter platform.

As an example, the unprocessed in-vivo images in the femoral artery, distal to proximal, of a porcine model with different illumination RGB and Near Infra-Red (NIR) are shown in Fig. 1. Fig 1(a) shows a clear field of the marker band of a balloon catheter, a commonly used medical device for cardiac procedures, and Fig 1(b) gives the same location illuminated using 940nm NIR. Commercial micro-camera integrated circuits are available, but they are not specifically designed for biophotonics applications such as surgical guidance, based on diffuse reflectance imaging, fluorescence and reflectance for specific biomarkers. Commercially available micro-cameras [8] are limited by resolution, image quality, sensitivity, field of view, etc., thus limiting their use in-vivo.

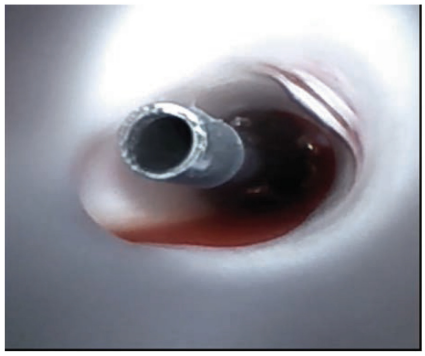

(a) RGB image showing the marker band of a balloon catheter

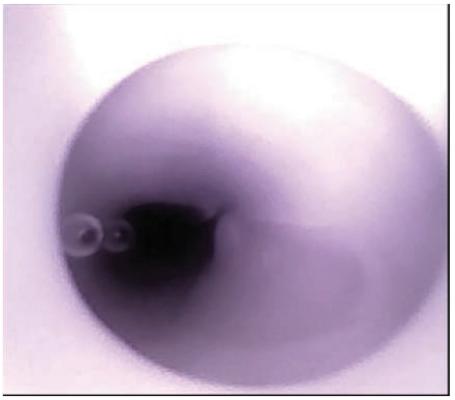

(b) 940nM NIR illumination showing a diffuse image with some ability to image through the blood field.

Fig. 1. Multispectral images from inside the femoral artery of a porcine model (Courtesy of Tyndall National Institute).

Using integrated image sensors in-vivo to successfully allow, for example, specular reflection and effective viewing of a beating heart, poses image processing and data analytics challenges. This can be resolved by employing smart, adaptive algorithms on an embedded system to enhance the image effectively, but requires adoption of a suitable low power technology and careful design. The Tyndall National Institute (TNI) in collaboration with clinicians and the medical device industry, are creating an intelligent surgical system (ISS) based on a custom CMOS image sensor and embedded processing unit which provides both image sensor power management and image processing capability to convert the detected signals at the edge or interface into clinical significant medical images, in real time. This paper describes the collaboration with Queen's University to

implement the image processing functionality on an field programmable gate array (FPGA) on the AMD-Xilinx's Kria KV260 AI board.

The work uses multispectral image processing to recover the best possible RGB images, including enhancement with at least two NIR wavelengths. A contrast limited adaptive histogram equalization (CLAHE) algorithm [5] is employed to help outline specific features such as tumours, by suppressing the contrast of each pixel based on its neighbouring values. A Region of Interest (ROI) algorithm highlights intra-operative ROIs to the clinician, by applying convolution procedures using the derivatives of Gaussian kernel to construct the Hessian matrix of each pixel with the eigenvalues used by an edginess or ROI function. In this paper, we undertake a number of optimisations for the implementation of this functionality using the AMD-Xilinx Vitis High-Level Synthesis (HLS) tools.

The paper is structured as follow: Sect. 2 briefly describes the ISS, followed by an explanation in Sect. 3 of the processes and algorithms used for the detection of blood vessels. The system architecture is then described in Sect. 4 and followed by the results in Sect. 5. Conclusions are given in Sect. 6.

2 Intelligent Surgical System

The proposed ISS consists of a front-end comprises a micro camera and light source, and a small embedded processor with intelligent image processing functionality, connected via a fiber optic cable to a transceiver (see Fig. 2). The front-end module needs to have a small footprint within a microcatether (3–6 Fr.) in order to allow surgeons to navigate to the narrow regions inside body organs. The challenge is to undertake the design of this functionality in a lower power, FPGA technology that provides the adaptive processing to support evolving requirements. The back-end comprises a high performance computing resource which, in the future, will incorporate additional intelligence (AI) capability, gleaned by surgeons from operations as they are performed.

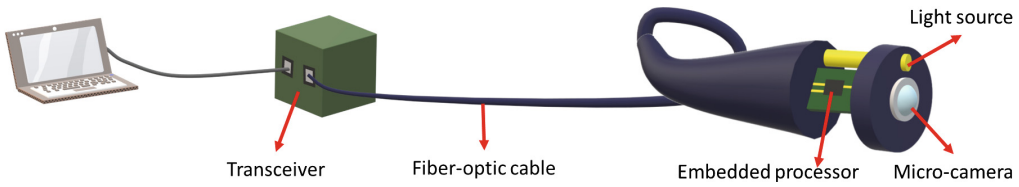

Fig. 2. Visualisation of the overall system design.

Images are captured by the micro-camera, and an automated multispectral light source helps to vary the illumination spectrum. The multispectral illumination is coupled to a single fibre and as part of the system control, the illumination wavelengths are selected and synchronised with the detection by

the imager and the video data transfer. The resulting raw video data is transmitted in a streaming-data fashion to the embedded processing unit which, in the future, will incorporate increasingly complex image analysis intelligence to assist the surgeon during the operation. Therefore, optimisation of the current implementation is essential in order to support future computation requirements.

Incorporating FPGA technology to surgical systems is an interesting choice when building innovation systems that are cost effective, have low-power consumption, and seek high performance. A multi-stage, FPGA-based customised design using similar image functionality was explored in [2] for the enhanced detection of blood vessels in retinal images. In another example, an FPGA platform was used in an endoscope imaging system [4] to provide a low-cost, high-performance implementation. A FPGA-based controller for robotic-assisted surgical system was developed in [7] to provide real-time control of a robot arms. Similar to our future plans, they aim to build the controller as a single chip, but clearly have different requirements.

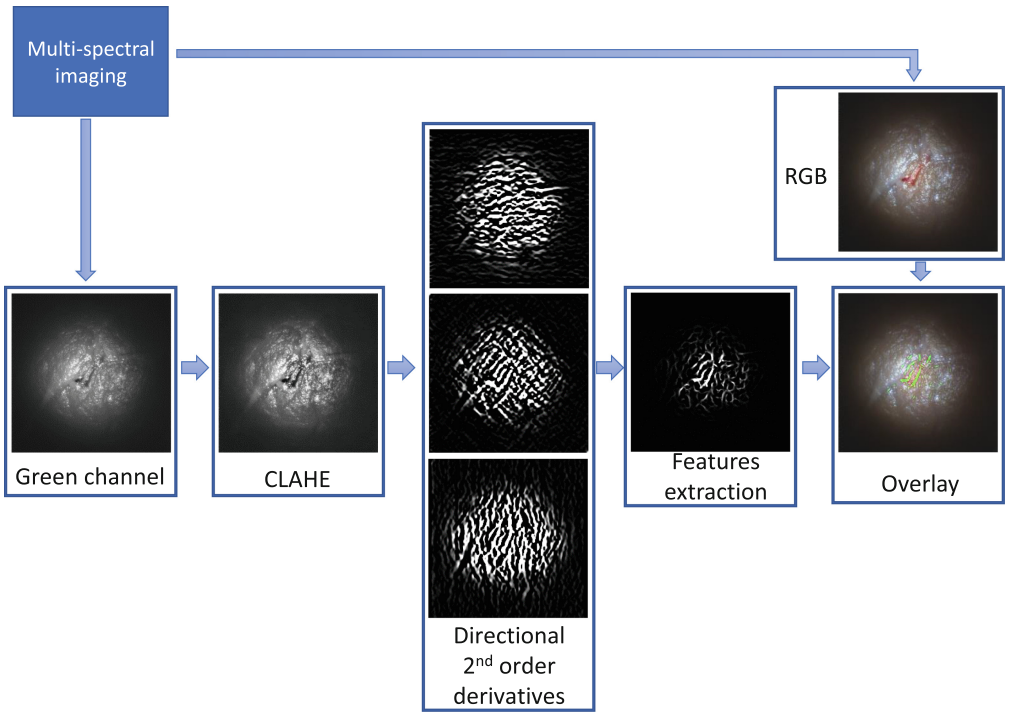

Fig. 3. Extraction of tissue features process from real imaging data captured by the multi-spectral imaging system developed by Tyndall Institute.

3 Extraction of Tissue Features

A key need is to identify key features in generated images such as in the extraction of tissue features (Fig. 3). Therefore, the proposed system employs the

widely-used CLAHE algorithm followed by a features extraction stage. It determines the directional second order derivatives of the enhanced image by computing the eigenvalues of Hessian matrix to decide whether a pixel is of interest or not. Overlying detected features on top of the hyperspectral images helps the surgeons to identify the ROIs. With the aim to incorporate future additional functionality, it is vital to minimise the FPGA resources by mapping effectively the required functionality onto the parallel FPGA resources and employing system level optimisations to produce the smallest footprint.

3.1 Image Acquisition

With conventional micro cameras, data is acquired with a rolling electronic shutter at a frame rate of 100 frames per second (FPS). By experimentation of the detection of blood vessels, it was determined that only the green channel needed to be extracted, because it has unique representations of the dark background and the bright retinal blood vessels. Each pixel stores a charge proportional to the light intensity and is converted to a digital value between 0 to 255 within the imager.

3.2 CLAHE

CLAHE is applied to enhance the contrast of each pixel based on its spatial location and neighboring pixels and has been shown to map well to FPGA [3]. A key stage of the algorithm is to divide the image into predefined and equal sized tiles where each tile is independent and does not share pixels with its neighboring tiles. A histogram for each tile is then obtained with 256 bins and clipped to a threshold predefined by the user (Fig. 5). All exceeded amounts are accumulated and redistributed uniformly to each bin which prevents noisy pixels from being enhanced by the Adaptive Histogram Equalization (AHE) process [6].

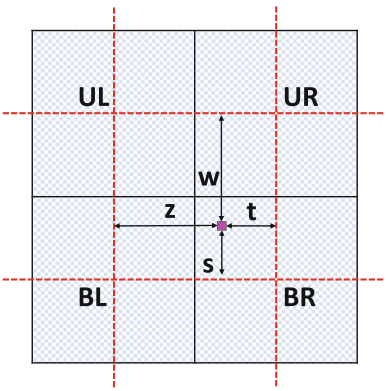

Fig. 4. Bi-linear interpolation process

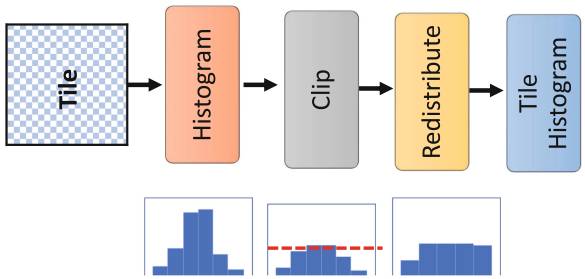

Fig. 5. Clipping, redistributing, and accumulating processes.

For each pixel value in the image, a cumulative distribution function (CDF) is generated using the cumulative sum of the redistributed histogram of each tile as below:

$$CDFt(p) = \sum_{n=0}^{p} \frac{h_t(n)}{z} \tag{1}$$

where p pixel in tile t, h_t is histogram of tile t, and z is the size of the tile. After that, a bi-linear interpolation of each pixel p, $I_{new}(p)$, is determined by three other CDFs of pixels from adjacent tiles, as shown in (2) and demonstrated graphically in Fig 4. This interpolation process reduces the impact of any interfering effects that will be generated at the framed boundaries.

$$\begin{aligned} I_{new}(p) = & \frac{s}{s+w}\left(\frac{t}{z+t}cdf_{UL}(p) + \frac{z}{z+t}cdf_{UR}(p)\right) \\ & + \frac{w}{s+w}\left(\frac{t}{z+t}cdf_{BL}(p) + \frac{z}{z+t}cdf_{BR}(p)\right) \end{aligned} \tag{2}$$

3.3 Convolution with Derivatives of Gaussian Kernel

Convolution with the second-order derivative of 2D Gaussian kernel estimates the directional gradients of the image and involves the construction of a Hessian matrix, H, of the image. The second-order partial derivative of 2D Gaussian kernels in x-direction, G_{xx}, xy-direction, G_{xy}, and y-direction, G_{yy}, are described in Eqs. (3), (4) and (5) respectively.

$$\frac{\partial^2 G(x,y)}{\partial x^2} = \frac{1}{2\pi\sigma^4}\left[\frac{x^2}{\sigma^2} - 1\right] e^{-\frac{x^2+y^2}{2\sigma^2}} \tag{3}$$

$$\frac{\partial^2 G(x,y)}{\partial xy} = \frac{xy}{2\pi\sigma^6} e^{-\frac{x^2+y^2}{2\sigma^2}} \tag{4}$$

$$\frac{\partial^2 G(x,y)}{\partial y^2} = \frac{1}{2\pi\sigma^4}\left[\frac{y^2}{\sigma^2} - 1\right] e^{-\frac{x^2+y^2}{2\sigma^2}} \tag{5}$$

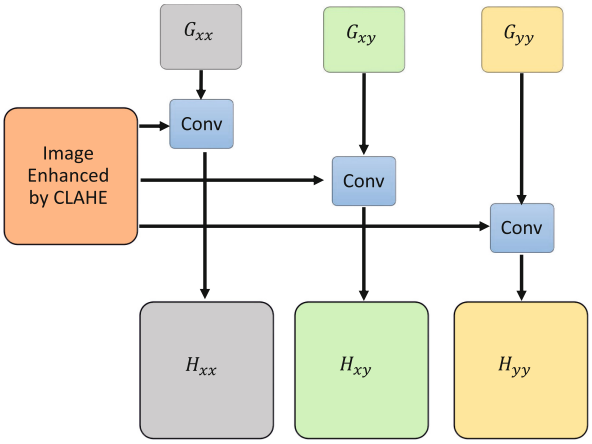

Fig. 6. Convolution with second-order derivatives of 2D Gaussian kernel

where x and y are integer values between $[-K, K]$, $K = 4\sigma + 1$ and σ is a scaling constant which affects the size and intensity of the Gaussian kernel. Any order derivative of a Gaussian kernel is also separable. This can be computation efficient since separable $(N \times N)$ kernels can be decomposed into horizontal and vertical kernels of size $(N \times 1)$ and $(1 \times N)$ respectively.

3.4 Constructing the Hessian Matrix

H is a square matrix which holds the directional second-order derivatives of an image, I, such as in Eq. (6). Each directional derivative of I can be determined by the convolution with the directional derivatives of Gaussian kernel (Fig. 6).

$$H = \begin{bmatrix} H_{xx} & H_{xy} \\ H_{yx} & H_{yy} \end{bmatrix} \tag{6}$$

The second-order derivative of I in the x-direction H_{xx} is given as Eq. (8) where $H_{xx} = I * G_{xx}$, $H_{xy} = I * G_{xy}$ and $H_{yy} = I * G_{yy}$. The Hessian matrix is symmetric since H_{xy} and H_{yx} are equal.

3.5 Eigenvalues of Hessian Matrix

For a given pixel point (x, y), the $H(x, y)$ is a 2×2 symmetric matrix which has two real eigenvalues. Therefore, determining eigenvalues at point (x, y) can be simplified using linear algebra as the following:

$$H(x, y) = \begin{bmatrix} h_{xx} - \lambda & h_{xy} \\ h_{xy} & h_{yy} - \lambda \end{bmatrix} = 0 \tag{7}$$

where $\lambda = \frac{h_{xx} + h_{yy} \pm \sqrt{(h_{xx} - h_{yy})^2 - 4h_{xy}^2}}{2}$, and $H_{xx}(x, y)$, $H_{xy}(x, y)$, and $H_{yy}(x, y)$ are represented as h_{xx}, h_{xy}, and h_{yy} respectively. From (7), it can be seen that

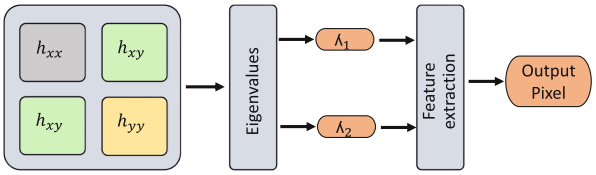

Fig. 7. Eigenvalues calculation and feature extraction

the two eigenvalues might be positive or negative real values and might be equal. Therefore, the inequality $|\lambda_2| \geq |\lambda_1|$ should always be satisfied for the purpose of this application before proceeding for a further process.

3.6 Feature Extraction or ROI Function

For images with darker features than the background, the edginess function, $F(x, y)$ in (8), is used to discriminate. It uses the eigenvalues of the corresponding Hessian matrix of a pixel (Fig. 7) to produces a value between [0,1], where values close to zeros are associated with the background and vice-versa. This gives,

$$F(x,y) = \begin{cases} (e^{-\frac{R_B^2}{2\beta^2}})(1 - e^{-\frac{S^2}{2c^2}}) & \lambda_2 > 0 \\ \\ 0 & otherwise \end{cases} \tag{8}$$

where $R_B = \lambda_2/\lambda_1$, $S = \sqrt{\lambda_2^2 + \lambda_1^2}$, $\beta = 0.5$, and $c = 15$ are used. We only implemented the traditional Hessian multi-scale filtering in [2] since the improved Hessian multi-scale enhancement filter requires calculations that involve all pixels of the image which impact the overall throughput and memory usage.

4 FPGA-Based Image Processing System Architecture

The AMD-Xilinx's Kria KV260 AI board and associated Vitis HLS 2021.2 toolset was used for initial implementation and design exploration. To optimise the image processing implementation, the data flow (DF) optimization was employed as it leads to solutions with lower memory usage and is applied by adding the DATAFLOW pragma in HLS. This ensures flawless data transfer from one function to the other and will support seamless integration of future, real-time functionality, as yet undefined.

Each processing step inside the system has to be linked to the next and/or previous processing step by internal streaming interfaces which will act as FIFO channels after C-synthesis. When using FIFOs, it is important to avoid deadlock, which can occur when depth is not specified correctly. A baseline system architecture was therefore established to allow stable system functionality and

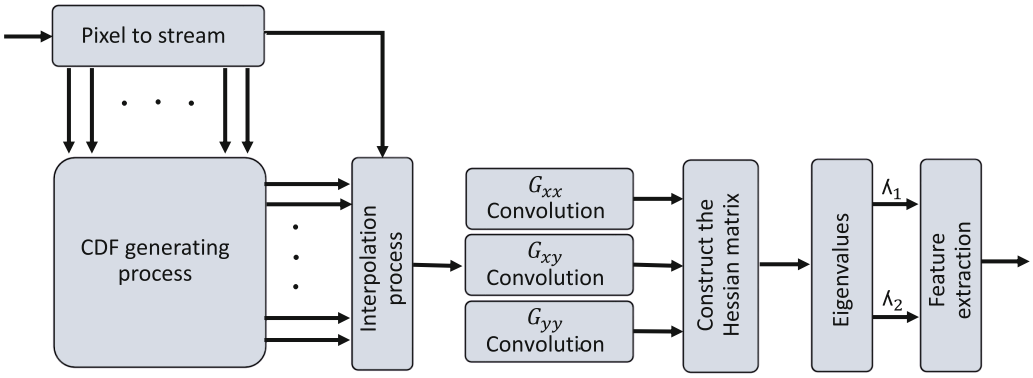

Fig. 8. Proposed FPGA-based image processing system architecture

then used as a reference design to evaluate the effectiveness of the applied optimisation techniques.

The baseline image processing system architecture (Fig. 8) comprises cascading processing elements (PEs) connected by streaming interfaces. The CLAHE is organised into the CDF generating processes, comprising large look-up tables (LUTs) which is connected to interpolating processes. The convolution process is applied as one PE, but it has small internal FIFO channels which help the separable convolution and border replication loops to be in-line when specifying the INLINE pragma in the DF optimisation flow. Finally, the Hessian matrix, determination and sorting of the eigenvalues, and the feature extraction functions, are combined into one PE, and termed the feature extraction process.

4.1 Experimental Setup

Vitis HLS 2021.2 is used for resource estimation and exporting RTL designs of the IP core while for place and route, we used Vivado 2021.2. For on-chip power, we used linux command "platformstats" and "timeit" package for timing analysis. The target FPGA platform is the Kria KV260 AI board (XCK26-SFVC784-2LV-C). For CPU/GPU evaluation, we used the Jetson Nano development kit which has a 1.43 GHz Quad-core ARM A57 as the CPU and 128-core Maxwell as the GPU. We chose to operate on 5W mode, and we used OpenCV/OpenCV-Cuda 4.1.1 implementations realised using Python on Jupyter notebook. For power analysis, we used "jetson-stats" package while for time analysis, we used "timeit" package. Both are imported as Python code to measure the performance for OpenCV implementations.

5 Evaluation

This section provides details of the baseline design and changes in resource utilisation and throughput after system- and algorithmic-level optimisations are applied. These are critical to ensure that sufficient FPGA real estate is available

for future improved image analysis functionality and possible AI intelligence. The performance of the optimisations were investigated by assessing their impact in Matlab (Sect. 5.3).

As the CMOS sensor will be 240 × 240 pixels and the system will need to operate at 100 FPS, each frame needs to be executed in 10 ms. If every pixel is executed for each clock cycle, this suggested a design with a 160 ns period time will need 9.216 ms for one 240 × 240 frame to satisfy the design requirements.

Loops are pipelined using PIPELINE pragma with the minimum initiation interval (II) to satisfy period time by the HLS tool. Floating-point data types with single precision is the default for mathematical operations and variables in the baseline design. For CLAHE, the image is divided into a 8 × 8 tile grid size, giving 64 independent regions. For the convolutions, we specify σ to be 2 which gives a (19 × 19) filter size, based on Sect. 3.3.

5.1 Baseline Design

The main hardware units in the FPGA are comprised of: a dedicated processing DSP48 (DSP) blocks including a 25-bit x 18-bit multiplier, a 48-bit adder and a 48-bit accumulator; a block RAM (BRAM) unit with 36 Kbits of data, configured as either two independent 18 Kb RAMs, or one 36 Kb RAM; a single bit flip-flip (FF) unit with pre-set/pre-clear functionality and; a 5-bit Lookup Table (LUT) which can be configured as logic, memory, or a shift register.

The baseline design of Fig. 8 was coded into three main functions, namely the CLAHE, convolution and the feature extraction processes. FIFOs were implemented as different dataflow objects. The resource breakdown resulted from the synthesis is given in Table 1.

Table 1. Utilization estimates of baseline design on the Kria KV260 SOM involving a Zynq UltraScale+ (% of the resource is listed)

Process	BRAM	DSP	FF	LUT
FIFO	12 (4.2%)	0 (0.0%)	2836 (1.2%)	2695 (2.3%)
CLAHE	26 (9.0%)	76 (6.1%)	6179 (2.6%)	26689 (22.8%)
Convolutions	57 (19.8%)	565 (45.3%)	10209 (4.4%)	40141 (34.3%)
Feature ext,	0 (0.0%)	58 (4.6%)	1043 (0.4%)	5811 (5.0%)
Total	95 (32.0%)	699 (56.0%)	20267 (8.7%)	75336 (64.3%)

The convolution process has the highest resource allocation as a lot of processing is required. It uses the majority of DSP blocks and in addition, a large amount of BRAMs in order to implement the buffers used for the FIFOs and the efficient separable convolution processes. FIFOs consume almost 4.2% of BRAMs since a large depth is specified to avoid deadlock issues which can cause FIFOs with a small depth size between these loops and functions to be filled and thus blocking writing or reading to the FIFOs.

5.2 Convolution Optimisations

In this section, optimisations were identified at the system level and algorithmic level with the aim of reducing the FPGA resources. At algorithmic level, we focused around exploiting common coefficients to employ common factor optimisation (CFO) to reduce the computational complexity [1,9] and also change the order of the computation (re-ordering).

Hardware Sharing: With flip-flops readily available in both the programmable logic and DSP48 blocks, pipelining can be used to increase the speed beyond that required and folding then applied to reduce the resources usage. This optimisation is available within the Vitis tools and was employed in the convolution function by applying feature II of pipelined loops. The unroll function produces multiple copies of the same function which are then folded onto one PE, leading to a reduction in the resources. This reduces the number of DSPs to 15%, FFs to 6%, and LUTs to 38% of the baseline design. However it also results in a reduction in the clock rate well below the desired value, in this case 27 MHz.

Common Factor Optimisation: The Hessian matrix requires the computation of three second-order directional derivatives of enhanced image (Fig. 9) requiring $3N$ multiplications and $3(N-1)$ additions and associated row buffers. The coefficients of $(N \times N)$ Gaussian kernels are determined by Eqs. (3), (4) and (5) and can be decomposed into $(1 \times N)$ horizontal and $(N \times 1)$ vertical kernels. These coefficients will be fixed for the convolution process. If we expand the horizontal convolution expression in X direction, then for N is 19, this gives,

$$\begin{aligned} h_{xxh}x_n &= h_{xxh1}x_1 + h_{xxh2}x_2 + h_{xxh3}x_3 + h_{xxh4}x_4 + h_{xxh5}x_5 + h_{xxh6}x_6 \\ &+ h_{xxh7}x_7 + h_{xxh8}x_8 + h_{xxh9}x_9 + h_{xxh10}x_{10} + h_{xxh9}vx_{11} + h_{xxh8}x_{12} + h_{xxh7}x_{13} \\ &+ h_{xxh6}x_{14} + h_{xxh5}x_{15} + h_{xxh4}x_{16} + h_{xxh3}x_{17} + h_{xxh2}x_{18} + h_{xxh1}x_{19} \end{aligned} \tag{9}$$

This will require 19 multiplications and 18 additions. However, we can exploit the separability and symmetrical proprieties of Gaussian kernels and eliminate zero values. For the specific xx direction, $h_{xxh6} = h_{xxh7}$ and $h_{xxh8} = 0$. Exploiting this and exploiting the symmetry in Eq. (9), we can reorganise this specific computation into Eq. (10) as follows:

$$\begin{aligned} h_{xxh}x_n &= h_{xxh1}(x_1 + x_{19}) + h_{xxh2}(x_2 + x_{18}) + h_{xxh3}(x_3 + x_{17}) \\ &+ h_{xxh4}(x_4 + x_{16}) + h_{xxh5}(x_5 + x_{15}) + h_{xxh6}(x_6 + x_{14} + x_7 + x_{13}) \\ &+ h_{xxh9}(x_9 + x_{11}) + h_{xxh10}x_{10} \end{aligned} \tag{10}$$

This optimisation reduces the computation by 50% as only eight multiplications and sixteen additions are needed. When this is applied to the other horizontal and vertical directional convolutions, h_{xy} and h_{yy}, it reduces the number of DSPs by 50% compared to baseline process in Table 2 while still providing a throughput of 114 FPS. The figures for this revised implementation are listed as **CFO** in Table 2.

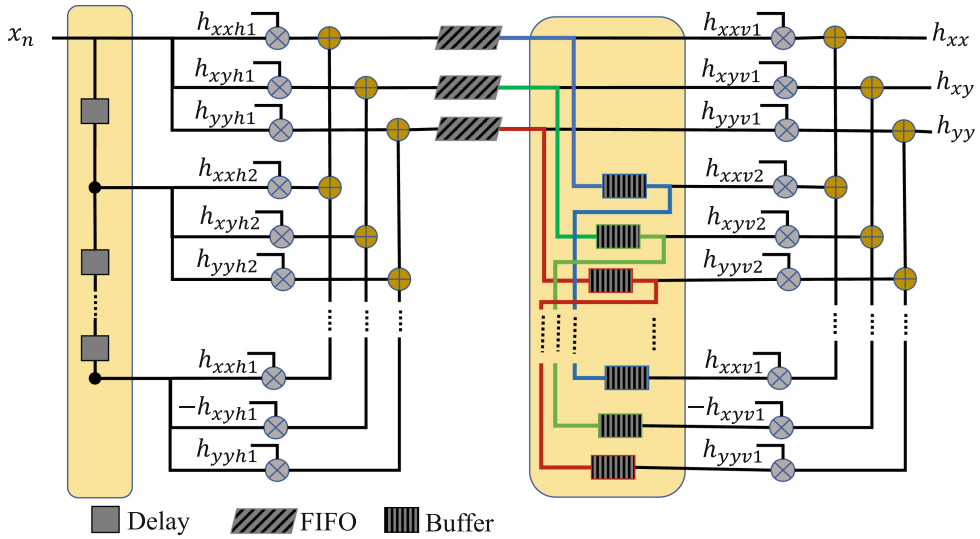

Fig. 9. Baseline separable convolution design for three different kernels combined

Re-ordering: The separable 2D convolutions can be decomposed into a horizontal followed by a vertical 1D-convolution each involving N multiplications and $N-1$ additions. The baseline design computes the horizontal followed by the vertical 1D-convolution, requiring the intermediate storage of $(3(N-1))$ buffers of length equal to an image row (Fig. 9), corresponding to $(N-1)$ buffers for each of the three different intermediate results produced by the horizontal convolutions. However, if we reverse the order of operation such that we start with vertical convolution, this will require only $(N-1)$ buffers since enhanced pixels coming from CLAHE process are shared between the different directional derivatives (Fig. 10). For (19×19) kernels, the number of BRAMs are reduced from 54 to 18 which more than 60% saving in convolution process. This **Reorder** design provides a 40% overall reduction in the baseline design in Table 2.

5.3 Combined Designs

In this section, we explore more about combined optimisations that would eventually build efficient designs that achieve high performance with minimal resource usage.

Combined: A more efficient design can be achieved by combining a number of these algorithmic optimisations. We first apply the **Re-order** optimisation to save in BRAMs usage and then the **CFO** option to reduce the complexity of the convolution function. This provides an additional saving in DSPs usage. The combined design (shown as **Combined** in Table. 2) achieved a 114 FPS which fulfils the design requirement of 100 FPS and with a lower BRAMs and DSPs resource usage. However, we expect a higher throughput after hardware implementation due to high-level optimisations by the Vivado tool.

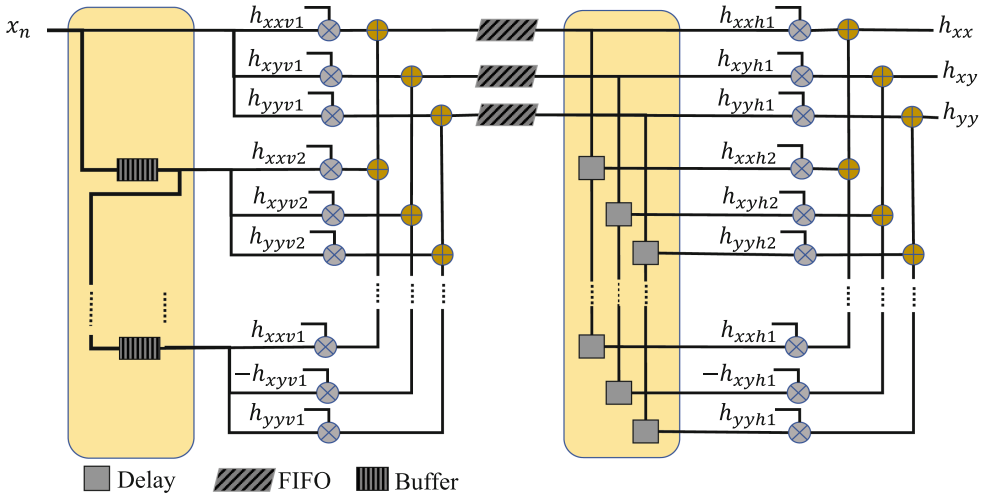

Fig. 10. Re-ordered separable convolution implementation for three kernels

Combined$^+$: Another obvious optimisation is to trade-off wordlength against resolution due to the small size of the original image. It is clear that a floating-point representation is unnecessarily large for circuit parts of the processing chain. For this reason, we changed the data type for the **Combined** design from 32-bit floating-point to 18-bit fixed-point arithmetic in the convolution only. This is organised into a 10-bit integer with the remaining 8 bits used for the fractional part.

Sufficient performance quality or quality of results (QoR) was ensured by assessing experimentally the visual impact and also measuring the structural similarity index measure (SSIM) and image quality degradation by peak signal-to-noise ratio (PSNR). Our results indicate that the 18-bit fixed-point representation scored on average 0.985 SSIM index and 40dB PSNR value compared to 32-bit floating-point results. The resource utilization labelled as **Combined$^+$** is presented in Table 2 with the biggest saving is in DSP units where the 5 DSPs of the floating-point can be reduced to a single DSP for the 18-bit fixed-point representation. There is also been a small reduction in the number of flip-flops and LUTs needed. As expected, there has only been a minimal change in throughput, 121 FPS, due the consistent use of pipelining.

5.4 Implementation Comparison

It is worth considering the performance issues when compared to a GPU implementation. For this reason, the same design was implemented on GPU and initial results generated and compared to the best FPGA realisation. In the GPU realisation, all optimisations were applied to ensure a high quality design. For example, conditional statements used for sorting eigenvalues and in feature extraction function had to be implemented solely using OpenCV-Cuda commands as it does not have ready-to-use functions for this. This allowed the GPU implementation to have a very fast execution compared to CPU.

Table 2. Resource utilization of optimized designs on (Kria KV260 SOM)

Design	BRAM (288)	DSP (1248)	FF (234240)	LUT (117120)	FPS
Baseline	95 (32%)	699 (56%)	20507 (8%)	76704 (65%)	114
CFO	95 (32%)	417 (33%)	14879 (6%)	58623 (50%)	114
Re-order	59 (20%)	684 (54%)	25055 (10%)	76240 (65%)	114
Combined	59 (20%)	422 (33%)	19479 (8%)	59480 (50%)	114
Combined^{+}	59 (20%)	142 (11%)	13687 (5%)	49426 (42%)	121

The resulting performance figures are shown in Table 3. As expected, the GPU outperforms the CPU. However, the optimisation implemented in mapping the design to FPGA has resulted in higher throughput when compared to the GPU. The solid FPGA performance is largely achieved due to small image size. The smaller size has resulted in an effective utilisation of the on-board FPGA resources and avoided having to undertake off-chip memory accesses which would compromised the performance. Use of the efficient design allows a throughput rate that is nearly 1.4× as fast as the GPU. The lower power performance of the FPGA device comes to the fore, but the overall System-on-Module (SoM) power consumption results in comparable GPU FPS/W figure. This would be much better if we use the single FPGA figure.

Table 3. Throughput and power comparison

	Image size	Jetson nano developer kit		Kria vision AI starter kit	
		ARM A57 (CPU)	Maxwell (GPU)	Zynq UltraScale+MPSoC (FPGA)	
				Baseline	Combined^{+}
Time (ms)	240 × 240	20.50	12.10	8.73	8.26
FPS	240 × 240	48.85	82.41	114.4	121
FPS/W	240 × 240	17.0	29.42	30.59	33.15

6 Conclusions

The paper presents details of an FPGA implementation of an intelligent surgical imaging system based on a 'chip on tip' camera system. The key challenge is to be able to implement a low power embedded processing unit to be able to enhance the image quality and in the future, provide increased intelligence.

Results were presented on the implementation of the contrast limited adaptive histogram equalization to suppress the contrast of each pixel based on its neighbouring values, convolution procedures using the derivatives of Gaussian and the construction of the Hessian matrix of each pixel with the eigenvalues used by a ROI function. We are able to demonstrate savings in DSP processor resources by up to 80% without a non-discernible loss in image quality. The work to date has been important in ensuring that available FPGA real estate is created so that the user can incorporate future functionality. Future work is targeted at providing much more intelligence into the embedded system which will provide detection capability for the surgeon. This will focus around building up a knowledge of existing operations and providing embedded training on the device.

References

1. Bailey, D.G.: Design for Embedded Image Processing on FPGAs. Wiley, Hoboken (2011)
2. Elbalaoui, A., Fakir, M., Taifi, K., Merbouha, A.: Automatic detection of blood vessel in retinal images. In: 2016 13th International Conference on Computer Graphics, Imaging and Visualization (CGiV), pp. 324–332 (2016). https://doi.org/10.1109/CGiV.2016.69
3. Honda, K., Wei, K., Arai, M., Amano, H.: CLAHE implementation and evaluation on a low-end FPGA board by high-level synthesis. IEICE Trans. Inf. Syst. **E104D**(12), 2048–2056 (2021). https://doi.org/10.1587/transinf.2021PAP0006. Publisher Copyright: Copyright 2021 The Institute of Electronics, Information and Communication Engineers
4. Liu, X., Li, L.: FPGA-based three-dimensional endoscope system using a single CCD camera. In: 2015 IEEE International Conference on Information and Automation, pp. 614–618 (2015). https://doi.org/10.1109/ICInfA.2015.7279360
5. Pizer, S., Johnston, R., Ericksen, J., Yankaskas, B., Muller, K.: Contrast-limited adaptive histogram equalization: speed and effectiveness. In: 1990 Proceedings of the First Conference on Visualization in Biomedical Computing, pp. 337–345 (1990). https://doi.org/10.1109/VBC.1990.109340
6. Pizer, S.M., et al.: Adaptive histogram equalization and its variations. Comput. Vis. Graph. Image Process. **39**(3), 355–368 (1987)
7. Taghizadegan, A., Piltan, F., Sulaiman, N.B.: Design high frequency surgical robot controller: design FPGA-based controller for surgical robot manipulator simscape modeling. Int. J. Hybrid Inf. Technol. **9**(5), 431–474 (2016)
8. Wäny, M., Voltz, S., Gaspar, F., Chen, L., Tecnopolo, A.L.M.: Ultrasmall digital image sensor for endoscopic applications. In: Proceedings of International Image Sensor Workshop, pp. 1–3 (2009)
9. Woods, R., McAllister, J., Lightbody, G., Yi, Y.: FPGA-Based Implementation of Signal Processing Systems. Wiley, Hoboken (2008)